Mechanobiology of tissue differentiation during osteochondral defect repair

by

Daniel John Kelly, BA, BAI, MSc

A thesis submitted to the University of Dublin in partial fulfilment of the requirements for the degree of

Doctor in Philosophy

Trinity College Dublin

October 2003

Supervisor
Professor P.J. Prendergast

External Examiner
Dr. I. Martin
(University of Basel)

Internal Examiner
Dr. V.A. Campbell

DECLARATION

I declare that I am the sole author of this thesis and that the work presented in it, unless otherwise referenced, is my own. I also declare that the work has not been submitted, in whole or in part, to any other university or college for a degree or other qualification.

I authorize the library of Trinity College Dublin to lend or copy this thesis on request.

Daniel Kelly

October, 2003.

ACKNOWLEDGEMENTS

I have been extremely fortunate to work for a man whose enthusiasm for his research is infectious. My sincerest thanks to my supervisor Prof. Patrick Prendergast for his constant guidance and inspiration over the last five years.

I would like to thank everyone who worked with me on the BITES and SCAFCART projects over the past four years. It has been challenging and enjoyable throughout.

Many thanks also to everybody in the workshop, particularly Gabriel Nicholson and Peter O'Reilly. I would also like to thank Paul Normoyle for his help with the temperature-controlled bath.

I have really enjoyed working with everyone in the Bioengineering group. Thanks to Laoise, Linda, Bruce, Adriele, John B, John V, Laura, Louise, Conor, John G, Matteo, Triona, Suzanne, Alex, Kevin, Paul, Damien, Seosamh, Fergal and all the other postgrads, I'm sure we'll drink again together at some stage.

I would also like to thank Joan Gillen and Nicole Byrne for their assistance whenever it was necessary.

Finally I want to thank Katie for always being there, my brother Jack and sister Caroline, and my parents for all their support throughout my college years.

This work was funded by the EU projects BITES and SCAFCART:

'Biomechanical Interactions in Tissue Engineeering and Surgical Repair'
Contract No: QLK3-1999-00559

'Novel bioresorable scaffolds and culture methods for cartilage tissue engineering'
Contract No: G5RD-CT-1999-00050

CONTENTS

Abstract i

List of Figures ii

List of Tables ix

Chapter 1 Introduction 1
The concepts of mechanobiology and in particular mechano-regulated tissue differentiation are introduced. The importance of developing a mechano-regulation model for tissue differentiation in order to improve cartilage repair is argued.

Chapter 2 Literature Review 8
Current theories for mechano-regulated tissue differentiation are presented. Because a mechano-regulation model will be applied to osteochondral defect repair the biomechanical properties of cartilage are outlined, and studies of cartilage repair are reviewed. Tissue engineering strategies for cartilage repair are described.

Chapter 3 Methods 44
The development of a mechano-regulation model for tissue differentiation is described. A finite element model of an osteochondral defect is presented. A rig to test tissue engineered cartilage is described.

Chapter 4 Results 76
The patterns of tissue differentiation within the defect under each of the conditions simulated are graphically illustrated. The mechanical stimuli responsible for the differentiation process are presented. The results of the mechanical tests of tissue engineered cartilage are presented, and used to simulate if engineered cartilage or scaffolds can improve the repair in defects.

Chapter 5 Discussion 153
The assumptions and limitations of this study are first discussed. An attempt to validate the results of the model is then made by comparing the predictions of the model with that observed experimentally. A hypothesis for why the spontaneous repair tissue that forms in osteochondral defects ultimately degrades is presented. The predictions of the mechano-regulation model relating the mechanical properties of a scaffold or engineered tissue to the quality of the repair are discussed. A blueprint for the optimal scaffold for osteochondral defect repair is presented.

Chapter 6 Conclusions 174
The main results of this study are listed and recommendations for future work are given.

References 177

Appendices 185

ABSTRACT

Differentiation can be thought of as a process by which cells and tissues undergo a change in phenotype toward a more specialized form or function. It is the contention of this thesis that tissue differentiation is in some way regulated by the mechanical environment of the cells within the tissue.

A theoretical model was developed which relates the dispersal, proliferation, and death of cells, and their subsequent differentiation, to their mechanical environment. In an attempt to confirm this mechano-regulation hypothesis, an algorithm based on the theoretical model was developed and used to simulate tissue differentiation during spontaneous osteochondral defect repair, where the mechanical environment within the defect was determined using finite element modelling. The influence of a number of physical factors, such as defect size and loading, were studied by altering these parameters in the finite element model. Furthermore, the influence of implanting a scaffold or engineered cartilage tissue on osteochondral defect repair was examined, where the mechanical properties of tissue engineered cartilage was determined experimentally.

The mechano-regulation model successfully predicted the main patterns of tissue differentiation observed during osteochondral defect repair. An increased amount of fibrous tissue formation, and reduced bone formation, was predicted as the size of the defect was increased. Only by implanting a scaffold or engineered tissue with mechanical properties approaching that or normal articular cartilage was the quality of repair predicted to significantly improve over spontaneous repair.

The ability of this model to simulate different aspects of tissue differentiation provides evidence to confirm our original hypothesis of mechano-regulated tissue differentiation. It is proposed as a tool to be used in the design of orthopaedic implants and to evaluate future tissue engineering strategies.

LIST OF FIGURES

1.1 It is hypothesised that connective tissue cells differentiate from the mesenchymal cell pool in response to the local mechanical and biochemical stimuli, adapted by van der Meulen and Prendergast (2000) from Caplan (1994). **2**

1.2 Effect of octahedral shear stress and hydrostatic stress on cell shape. **3**

1.3 A schematic representation of the hypothesised influence of mechanical stimuli on tissue differentiation proposed by Pauwels. Taken from Weinans and Prendergast (1996). **4**

1.4 A schematic drawing of a chondral (partial-thickness) and an osteochondral (full-thickness) defect. The bone marrow mesenchymal stem cells cannot access the defect until the subchondral bone is penetrated. **5**

2.1 (a) Pauwels' illustration of an angulated fracture, consisting of a tension side (Z) where cells were thought to be elongated, and a compression side (D) where the cells were thought to be hydrostatically stressed. (b) Histological section of an angulated fracture callus, consisting of small chondrocytes on the compressive (right) side of the callus, and a more fibroblast like cells on the tension (left) side of the callus. Adapted from Pauwels (1980). **10**

2.2 (a) Pauwels' representation of cartilage been squeezed between the regenerating bony tissue. In the centre the regenerating tissue is elongated transversely. (b) Callus from a fracture of the forearm of a mouse, showing collagen fibers have developed in the area of maximum elongation. Adapted from Pauwels (1980). **10**

2.3 Strain tolerance of repair tissues. A tissue cannot exist in an environment where the interfragmentary strain exceeds the strain tolerance of the extracellular matrix of the tissue. Taken from Perren and Cordey (1980). **11**

2.4 (a) Carter and colleagues (2001) view of the role of hydrostatic stress history and distortational strain (octahedral shear strain) history on tissue differentiation. (b) Carter and colleagues (2001) view of the role of hydrostatic stress history and maximum principal stress history on tissue differentiation. **12**

2.5 Top: Finite element mesh of a chondral defect used by Carter and Beaupré (2001). Left: The distribution of hydrostatic stress and tensile strain in normal articular cartilage. Right: The distribution of hydrostatic stress and tensile strain in the articular cartilage and regenerating tissue in the chondral defect. **14**

2.6 Mechano-regulation pathway hypothesised to control tissue differentiation based on the tissue strain and fluid flow. Both tissue strain and interstitial fluid flow are hypothesised to cause cell deformation. A region of high cell deformation causes fibrous tissue formation, intermediate deformations allow cartilage formation and low strains allow bone formation. After Prendergast et al. (1996). **15**

2.7 The effect of stain amplitude on cell proliferation. Only periosteal-derieved osteoblasts respond significantly to 3000 μstrains. All cell types respond significantly to 10000 μstrains. Taken from Jones et al., 1991. **18**

2.8 The influence of applied load on cell death in a centrally loaded region of a cartilage explant (solid circles) and in the adjacent partially loaded region (open circles). Left: below 250 N (which corresponded to an applied stress of 6MPa), cell viability was described as independent of the applied load. Right:

above 250 N, cell death increased in proportion to the applied load. Taken form Clements et al. (2000). **19**

2.9 Cellular and collagen fibre arrangement in articular cartilage. Left: light microscope overview of adult articular cartilage from femoral chondyle, adapted from Hunziker et al. (2002). Schematic representation of articular cartilage, adapted from Carter and Beaupré (2001). **21**

2.10 Schematics of load-deformation visceoelastic behaviors of articular cartilage. Adapted from Mow and Guo, 2002. **23**

2.11 Characteristic stress-strain relationship for articular cartilage in a steady state strain-rate experiment. Adapted from Mow and Guo, 2002. **24**

2.12 A simplified sectional view of the knee joint. Adapted from Martini, 2001. **30**

2.13 Photographs of osteochondral repair tissue, from Shapiro et al., 1993. **31**

2.14 Photographs of osteochondral repair tissue, from Shapiro et al., 1993. **31**

2.15 Photographs of osteochondral repair tissue, from Shapiro et al., 1993. **32**

2.16 Photographs of osteochondral repair tissue, from Shapiro et al., 1993. **32**

2.17 Photographs of osteochondral repair tissue, from Shapiro et al., 1993. **32**

2.18 Photographs of osteochondral repair tissue, from Shapiro et al., 1993. **33**

2.19 Autoradiographic analysis of osteochondral defect repair. 1 dot: 5 % or less of cells are labelled. 2 dots: 5 to 10 % of cells labelled. 3 dots: 10 to 15 % of cells labelled, and so on. The confines of the original defect defect are enclosed in the red dotted line. Adapted from DePalma et al., 1966. **34**

2.20 Repair tissue in a goat model of ACI. Adapted from Dell'Accio et al., 2003. **36**

2.21 Immunohistochemical staining for type II collagen in a rabbit model of osteochondral defect repair. Adapted from Rahfoth et al. (1998). **39**

2.22 Histological appeareance near the center of an osteochondral defect in the chondyle (a & b) and patellar groove (c & d) after 16 weeks. (a) and (c): Safranin-O staining more intense in chondyle repair tissue compared to the patellar groove repair tissue. (b) and (d): Cross-polarized light micrographs showing a more articular–like collagen structure in the chondyle repair tissue compared to the patellar groove repair tissue. Adapted from Niederauer et al. (2000). **40**

2.23 Chondrocyte-PGA constructs cultured for 6 weeks in either static flasks or rotating vessels. Constructs grown statically contained more extracellular matrix peripherally than centrally. Adapted from Freed et al. (1998). **42**

3.1 Quadratic relationship assumed between shear strain and cellular mitosis and death. **47**

3.2 The mechano-regulation concept first proposed by Prendergast et al (1997), and adapted by Lacroix and Prendergast (2002) to account for bone resorbtion and two separate bone fields, immature woven bone and mature woven bone. **49**

3.3 A region containing granulation tissue. **50**

3.4 A region containing both cartilage and granulation tissue. **50**

3.5 A region containing fibrous, cartilage and granulation tissue. **50**

3.6 A region containing all cartilage tissue after n iterations. **51**

3.7 The mechano-regulation diagram controlling tissue differentiation (not drawn to scale). **53**

3.8 Flow chart diagram of computational algorithm to model cell dispersal, proliferation, differentiation and death. **55**

3.9 Axi-symmetric finite element model of the knee with an osteochondral defect. Right: Finite element mesh illustrating loading and boundary condition. Left: 5mm defect (box) showing origin of mesenchymal stem cells (arrows). **58**

3.10 Axi-symmetric finite element mesh of the 5 mm, 7 mm and 9 mm osteochondral defects. **61**

3.11 Schematics of three testing configurations frequently used to study the compressive behaviour of articular cartilage. (a) In the confined compression test, the sample is radially confined and compressed via a porous indenter. (b) In the unconfined compression test, the sample is free to bulge radially and is compressed via two impermeable platens. (c) An indentation test, which is commonly used to test articular cartilage in vivo. **63**

3.12 (a) Confined compression rig, complete with bath and temperature control device. (b) 3 different grades of porous filter elements. (c) Close-up picture of unconfined compression pieces. (d) Close-up picture of confined compression pieces. **65**

3.13 Punched samples of normal bovine nasal cartilage. **66**

3.14 (a) A 10% ramp displacement and hold, followed by two more 5% ramp displacement and holds, are applied to each sample.(b) The force rises during the compression phase, and relaxes during the hold phase until it reachs an equilibruim value. (c) The equilibruim stress for each loading is determined by dividing the equilibruim force by the area of the sample. Hence a stress strain curve can be plotted for each sample, the slope of which gives the aggregate modulus. **67**

3.15 Aggregate modulus plotted against GAG content for each sample tested. (Red markers – articular cartilage. Blue markers – nasal cartilage). **69**

3.16 Schematic of multiphase scaffold. **72**

4.1 Colour scaling used in plots of tissue differentiation. 77

4.2 Predicted patterns of tissue differentiation in 5 mm defect during simulation. **79**

4.3 Percentage of each tissue type predicted to form within the defect over the course of the simulation – (a) coarse mesh (b) intermediate mesh (c) fine mesh. For the purposes of this illustration granulation tissue is assumed to persist within an element until the total cell concentration exceeds 50. **80**

4.4 Comparisons of the amounts of bone tissue, cartilage tissue and fibrous tissue predicted to form with the coarse, intermediate and fine mesh densities. **81**

4.5 Location of elements in 5 mm defect mesh used in detailed analysis of mechanical stimuli and cell concentration. **82**

4.6 Predictions of octahedral shear strain in different elements within the defect throughout the simulation for the coarse, intermediate and fine mesh density finite element models. **84**

4.7 Predictions of interstitial fluid flow in different elements within the defect throughout the simulation for the coarse, intermediate and fine mesh density finite element models. **85**

4.8 Predictions of cell concentration in different elements within the defect throughout the simulation for the coarse, intermediate and fine mesh density finite element models. **86**

4.9 Prediction of octahedral shear strain in the very bottom left element for the coarse, intermediate and fine mesh density models. No averaging is applied. **87**

4.10 Predicted patterns of tissue differentiation in 5 mm, 7 mm and 9 mm defects during simulation. **88**
4.11 Comparisons of the amounts of bone tissue, cartilage tissue and fibrous tissue predicted to form in the 5 mm, 7mm and 9 mm defects. **89**
4.12 Location of elements in (a) 7 mm and (b) 9 mm defect meshes used in detailed analysis of mechanical stimuli and cell concentration. **90**
4.13 Predictions of octahedral shear strain in different elements within the defect throughout the simulation for the 5 mm, 7 mm and 9 mm defect. **92**
4.14 Predictions of interstitial fluid flow in different elements within the defect throughout the simulation for the 5 mm, 7 mm and 9 mm defect. **93**
4.15 Predictions of total cell concentration in different elements within the defect throughout the simulation for the 5 mm, 7 mm and 9 mm defect. **94**
4.16 Predicted patterns of tissue differentiation in 7 mm defect during simulation of different loading conditions. **96**
4.17 Comparisons of the amounts of (a) bone tissue (b) cartilage tissue and (c) fibrous tissue predicted to form in the 7 mm defect under different loads. For the purposes of this illustration granulation tissue is assumed to persist within an element until the total cell concentration exceeds 50. **97**
4.18 Predictions of octahedral shear strain in different elements within the 7 mm defect throughout the simulation for the 500 N, 800 N and 1100 N loading condition. **98**
4.19 Predictions of interstitial fluid flow in different elements within the 7 mm defect throughout the simulation for the 500 N, 800 N and 1100 N loading condition. **99**
4.20 Predictions of total cell concentration in different elements within the 7 mm defect throughout the simulation for the 500 N, 800 N and 1100 N loading condition. **100**
4.21 Influence of granulation tissue diffusion coefficient on the amounts of bone tissue, cartilage tissue and fibrous tissue predicted to form in the 7mm defect. For the purposes of this illustration granulation tissue is assumed to persist within an element until the total cell concentration exceeds 50. **102**
4.22 Predicted patterns of tissue differentiation in 7 mm defect during simulation of different repair tissue integration conditions. **104**
4.23 Comparisons of the amounts of bone tissue, cartilage tissue and fibrous tissue predicted to form in the 7 mm defect under different repair tissue integration conditions. **105**
4.24 Predictions of octahedral shear strain in different elements within the 7 mm defect throughout the simulation assuming either complete or no integration between the repair tissue and the surrounding tissue. **106**
4.25 Predictions of interstitial fluid flow in different elements within the 7 mm defect throughout the simulation assuming either complete or no integration between the repair tissue and the surrounding tissue. **107**
4.26 Predictions of cell concentration in different elements within the 7 mm defect throughout the simulation assuming either complete or no integration between the repair tissue and the surrounding tissue. **108**
4.27 Comparisons of the amounts of (a) bone tissue (b) cartilage tissue and (c) fibrous tissue predicted to form in the 7 mm defect under different cell mitosis conditions. **111**
4.28 Predictions of octahedral shear strain in different elements within the 7 mm defect throughout the simulation assuming either concentration dependent

mitosis, concentration independent mitosis or no mitosis after 30 iterations. **112**

4.29 Predictions of interstitial fluid flow in different elements within the 7 mm defect throughout the simulation assuming either concentration dependent mitosis, concentration independent mitosis or no mitosis after 30 iterations. **113**

4.30 Predictions of total cell concentration in different elements within the 7 mm defect throughout the simulation assuming either concentration dependent mitosis, concentration independent mitosis or no mitosis after 30 iterations. **114**

4.31 Mean equilibrium aggregate modulus of tissue engineered cartilage constructs seeded with different numbers of cells. (Error bars: ± Standard deviation. A second order polynomial is fitted to the data). **116**

4.32 Comparison of the equilibrium aggregate and Young's modulus of normal articular cartilage and 12-week tissue engineered cartilage constructs. (Error bars: ± Standard deviation. Values for normal cartilage taken from Mow et al., 1980). **117**

4.33 Comparison of the equilibrium aggregate modulus of tissue engineered cartilage constructs pre-cultured in different media after 6 weeks in vivo. **118**

4.34 Comparison of the equilibrium aggregate modulus of tissue engineered cartilage constructs pre-cultured in different media after 8 weeks in vivo. **118**

4.35 Predicted patterns of tissue differentiation in 7 mm defect during simulation of repair after implantation of an engineered tissue. **121**

4.36 Comparisons of the amounts of (a) bone tissue (b) cartilage tissue and (c) fibrous tissue predicted to form in a 7 mm defect implanted with tissue engineered cartilage. **122**

4.37 Predictions of octahedral shear strain in different elements within the 7 mm defect throughout the simulation with tissue engineered cartilage implanted. **123**

4.38 Predictions of interstitial fluid flow in different elements within the 7 mm defect throughout the simulation with tissue engineered cartilage implanted. **124**

4.39 Predicted patterns of tissue differentiation in 7 mm defect with and without an implanted homogenous scaffold. **126**

4.40 Comparisons of the amounts of bone tissue, cartilage tissue and fibrous tissue predicted to form in the 7 mm defect implanted with a homogenous scaffold. **127**

4.41 Predictions of octahedral shear strain in different elements within the 7 mm defect throughout the simulation with and without an implanted homogenous scaffold. **128**

4.42 Predictions of interstitial fluid flow in different elements within the 7 mm defect throughout the simulation with and without an implanted homogenous scaffold. **129**

4.43 Predictions of total cell concentration in different elements within the 7 mm defect throughout the simulation with and without an implanted homogenous scaffold. **130**

4.44 Predicted patterns of tissue differentiation in 7 mm defect with and without an implanted homogenous scaffold. **132**

4.45 Comparisons of the amounts of bone tissue, cartilage tissue and fibrous tissue predicted to form in the 7 mm defect implanted with a homogenous scaffold.

(a) Influence of reducing the Young's modulus of the scaffold. (b) Influence of increasing the Young's modulus of the scaffold. **133**

4.46 Location of elements in 7 mm defect mesh used in detailed analysis of mechanical stimuli and cell concentration in the presence of a scaffold. **131**

4.47 Predictions of octahedral shear strain in different elements within the 7 mm defect throughout the simulation with and without an implanted homogenous scaffold. **134**

4.48 Predictions of interstitial fluid flow in different elements within the 7 mm defect throughout the simulation with and without an implanted homogenous scaffold. **135**

4.49 Predicted patterns of tissue differentiation in 7 mm defect after implantation of a homogenous scaffold. **137**

4.50 Comparisons of the amounts of bone tissue, cartilage tissue and fibrous tissue predicted to form in the 7 mm defect implanted with a homogenous scaffold of various permeabilities. **138**

4.51 Predictions of octahedral shear strain in different elements within the 7 mm defect throughout the simulation with and without an implanted homogenous scaffold. **139**

4.52 Predictions of interstitial fluid flow in different elements within the 7 mm defect throughout the simulation with and without an implanted homogenous scaffold. **140**

4.53 Predicted patterns of tissue differentiation in 7 mm defect after implantation of a multiphase scaffold. Influence of Young's modulus of superficial phase. **142**

4.54 Comparisons of the amounts of bone tissue, cartilage tissue and fibrous tissue predicted to form after implantation with a multiphase scaffold, where the material properties of superficial phase are varied. **143**

4.55 Predictions of octahedral shear strain in different elements within a defect implanted with a multiphase scaffold, where the material properties of the superficial phase of the scaffold are varied. **144**

4.56 Predictions of interstitial fluid flow in different elements within a defect implanted with a multiphase scaffold, where the material properties of the superficial phase of the scaffold are varied. **145**

4.57 Predicted patterns of tissue differentiation in 7 mm defect after implantation of a multiphase scaffold. Influence of Permeability of superficial phase. **146**

4.58 Comparisons of the amounts of bone tissue, cartilage tissue and fibrous tissue predicted to form after implantation with an multiphase scaffold, where the permeability of the superficial phase is varied. **147**

4.59 Predicted patterns of tissue differentiation in 7 mm defect after implantation of a multiphase scaffold. Influence of material properties of bony layer. **149**

4.60 Comparisons of the amounts of bone tissue, cartilage tissue and fibrous tissue predicted to form after implantation with an inhomogenous scaffold, where the material properties of the bone phase is varied. **150**

4.61 Predicted patterns of tissue differentiation in 7 mm defect after implantation of a multiphase scaffold. Influence of material properties of chondral layer. **151**

4.62 Comparisons of the amounts of bone tissue, cartilage tissue and fibrous tissue predicted to form after implantation with an inhomogenous scaffold, where the material properties of the chondral phase is varied. **152**

5.1 Illustration of the hypothesised differentiation processes in large and small defects, depicting the failure of the spontaneous repair process to satisfactory fill a large defect with the appropriate tissue types. **161**

5.2 Prediction of octahedral shear strain and interstitial flow in two different elements with and without cell mitosis after 30 iterations of the model for a 1100N loading. **163**

5.3 Illustration of the hypothesised degradation process that occurs in osteochondral defects. **164**

5.4 The influence of varying either (a) Young's modulus or (b) the permeability of the scaffold on the amounts of fibrous tissue predicted within the defect after 50 iterations of the simulation. **168**

5.5 Fissure in an osteochondral defect implanted with a scaffold. Adapted from Niederauer et al. (2000). **169**

5.6 Variation in the Young's modulus and permeability of a computer optimised scaffold. **171**

5.7. Comparison of the predicted patterns of tissue differentiation in 7 mm defect during spontaneous repair, repair in the presence of a homogenous scaffold, and repair in the presence of a computer optimised scaffold. **172**

LIST OF TABLES

2.1 Comparison of average compliance values for normal articular cartilage with the repair tissue in empty defects or defects implanted with cell-seeded collagen gels 24 weeks post-operatively. A lower compliance value indicates a stiffer tissue. Adapted from Wakitani et al. (1994). **38**

3.1 Material properties of tissues. **57**

3.2 Diffusion co-efficient (in mm^2/iteration) parametric variation study. **58**

3.3 Aggregate modulus, GAG (as a percentage of dry weight) and collagen II (as a percentage of dry weight) content for normal bovine nasal cartilage. Biochemical analysis performed at the University of Bristol Academic Rheumatology Department. **67**

3.4 Aggregate modulus, GAG (as a percentage of dry weight) and collagen II (as a percentage of dry weight) content for normal bovine articular cartilage. Biochemical analysis performed at the University of Bristol Academic Rheumatology Department. **67**

3.5 Aggregate modulus plotted against GAG content for each sample tested. (Red markers – articular cartilage. Blue markers – nasal cartilage). **68**

3.6 Material properties of superficial layer of inhomogenous scaffold. **72**

3.7 Material properties of cartilage layer of inhomogenous scaffold. **72**

3.8 Material properties of bone layer of inhomogenous scaffold. **72**

3.9 The material properties of tissue engineered cartilage used in simulation of osteochondral defect repair. **73**

4.1 Equilibrium aggregate modulus of tissue engineered cartilage constructs seeded with different numbers of cells. **116**

Chapter 1

Introduction

Contents

1.1	**Mechanobiology**	**2**
1.2	**Articular cartilage repair**	**4**
1.3	**Objectives of the thesis**	**6**

1.1 Mechanobiology

The fundamental tenant of mechanobiology is that biological processes are regulated, in part, by stimuli to cells generated by mechanical loading (van der Meulen and Husikes, 2002). This coupling between mechanics and biology begins during early development when the primordial cellular structure first experiences deformations and pressures, and continues throughout growth, development and ageing of the organism. Of particular interest is understanding how the loads applied to cells within connective tissues affect the health of the musculoskeletal system. For example, it has been hypothesised that mechanical forces considerably influence the mesenchymal stem cell differentiation pathway and hence the patterns of tissues appearing within developing or repairing tissues (Fig. 1.1).

Consistent patterns of tissue differentiation are found during growth, development and regeneration of tissues, as well as during remodelling of tissues surrounding implants. One of the aims of mechanobiology is to determine what types of mechanical stimuli regulate tissue differentiation, and to express quantitatively the relationship between this mechanical stimulus and the resulting cellular

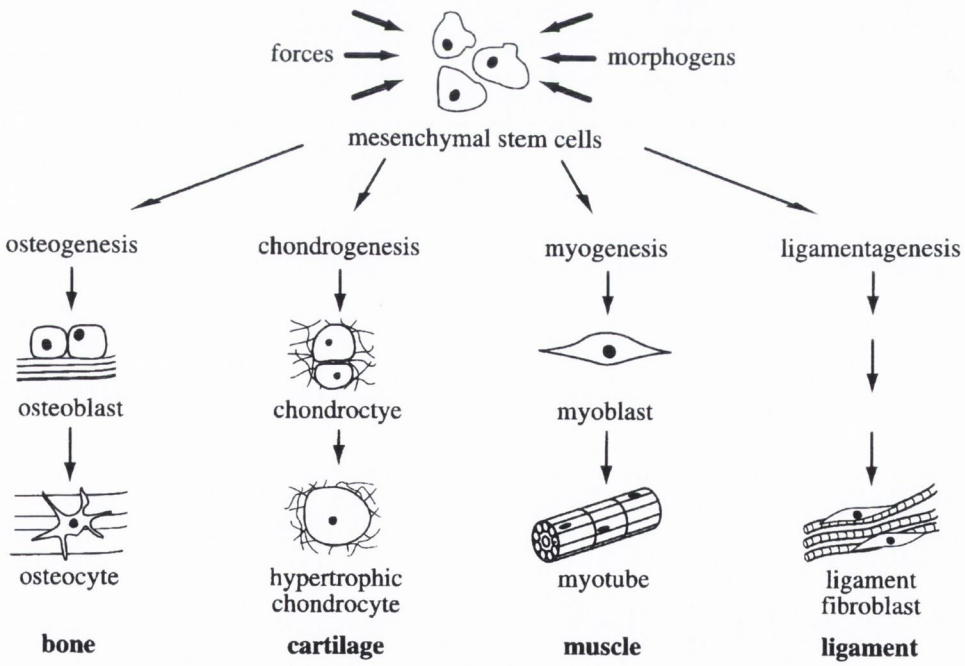

Fig. 1.1 *It is hypothesised that connective tissue cells differentiate from the mesenchymal cell pool in response to the local mechanical and biochemical stimuli, adapted by van der Meulen and Prendergast (2000) from Caplan (1994).*

(a) Octahedral shear stress. Causes a change in cell shape, but no change in volume.

(b) Hydrostatic stress. Causes a change in cell volume, but no change in shape.

Fig. 1.2. *Effect of octahedral shear stress and hydrostatic stress on cell shape.*

differentiation. Pauwels (1941) proposed the first theoretical model of mechano-regulated tissue differentiation. He proposed that two invariants of the stress tensor, the octahedral shear stress (which causes a change in cell shape, see Fig. 1.2a) and the hydrostatic stress (which causes a change in cell volume, see Fig. 1.2b), regulated the cell differentiation pathway such that granulation tissue containing mesenchymal cells would differentiate to produce fibrous, fibrocartilage or cartilage tissue as follows: high levels of hydrostatic stress and low levels of octahedral shear stress induced chondrogenesis, whereas high levels of octahedral shear stress and low levels of hydrostatic stress induced fibrous tissue formation (ligamentagenesis), see Fig. 1.3. No specific stimulus for bone formation was proposed. Instead he concluded that bone formation occurred once cartilage or connective tissue provided a framework rigid enough for ossification to occur. Pauwels' ideas were based on solid mechanics theory, radiographs of bone fractures and logic, but were limited by the fact that the capacity to measure or compute tissue stresses and strains accurately did not exist in the 1940s.

In the years since Pauwels published his ideas on mechano-regulated tissue differentiation, the finite element method has developed into a tool capable of accurately determining stresses and strains in complex biological systems (Huiskes and Chao, 1983; Prendergast, 1997). Along with modern histological and biochemical techniques to characterise tissue differentiation, this has led to development of a number of new theories of mechano-regulated tissue differentiation (Carter *et al.*, 1988; Prendergast *et al.*, 1997; Claes and Heigele, 1999; Kuiper *et al.*, 2000). None of these theories has yet become widely accepted. Discovering exactly how tissue differentiation is regulated by its mechanical environment will be a major step forward in orthopaedics, as this new knowledge may well prove essential in making informed decisions regarding tissue-engineering treatments for cartilage and bone defects, or help devise new implant designs which do not provoke adverse tissue adaptations, and ultimately to cure diseases such as osteoporosis and osteoarthritis.

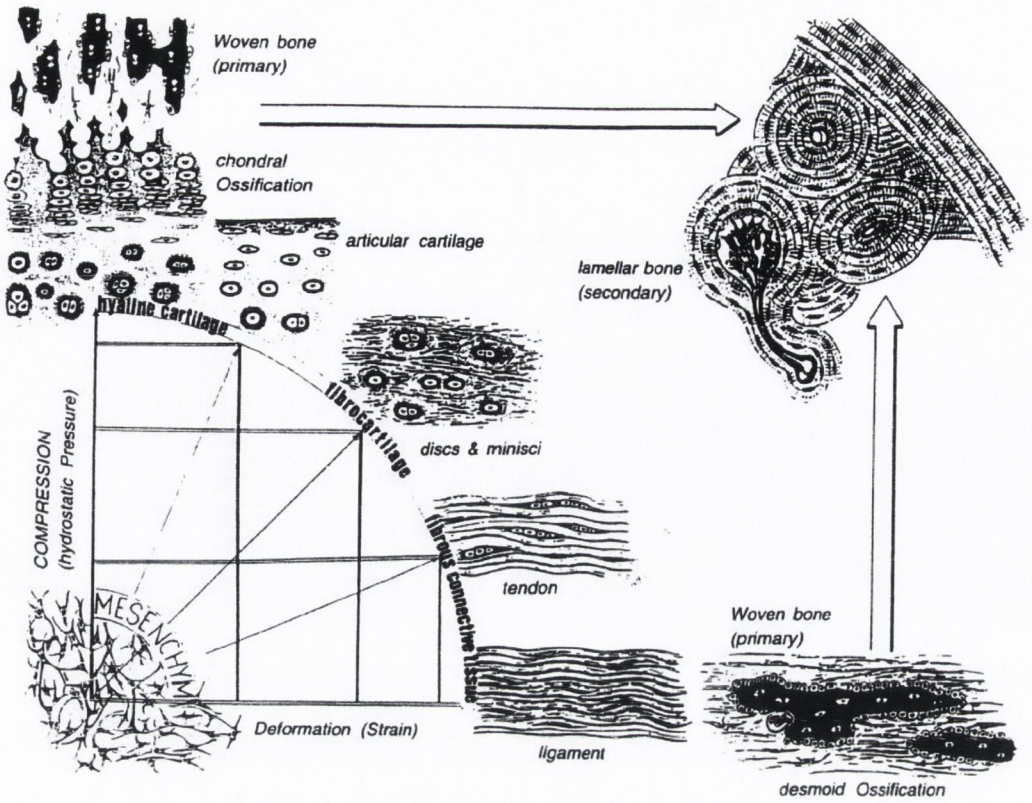

Fig. 1.3. *A schematic representation of the hypothesised influence of mechanical stimuli on tissue differentiation proposed by Pauwels (1941). Figure taken from Weinans and Prendergast (1996).*

1.2 Articular cartilage repair

Articular cartilage has limited reparative abilities. Articular cartilage defects are generally classified as either chondral (partial) or osteochondral (full-thickness) defects (Hunziker, 1999). Chondral defects are in the cartilage layer alone whereas osteochondral defects extend into the subchondral bone, see Fig 1.4. Since chondral defects do not penetrate the subchondral bone they cannot be easily reached by the mesenchymal stem cells located within the underlying bone marrow. Hence, when a chondral defect is created, a short-lived tissue response is observed which fails to provide sufficient cells or matrix to repair even small defects (Mankin, 1982; Wakitani, 1994). When a full-thickness or osteochondral defect is artificially created, a fibrin clot is formed within the defect that is invaded by mesenchymal cells from the bone marrow (Shapiro *et al.*, 1993). These cells differentiate and form a repair tissue characterised as fibrous, fibrocartilage, or hyaline-like cartilage (Shapiro *et al.*, 1993; Metsaranta *et al.*, 1996; Furukawa *et al.*, 1980). This tissue is biomechanically

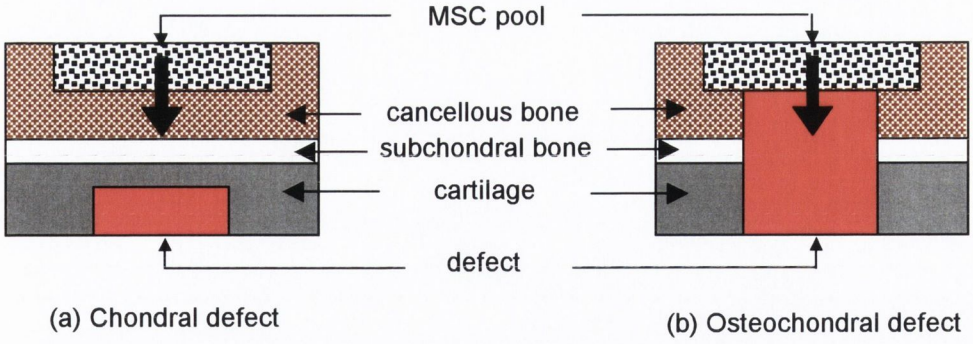

Fig. 1.4. *A schematic drawing of a chondral (partial-thickness) and an osteochondral (full-thickness) defect. The bone marrow mesenchymal stem cells do not have easy access the defect until the subchondral bone is penetrated.*

inferior to normal articular cartilage, and usually starts to degenerate within six to twelve months (Shapiro *et al.*, 1993; Furukawa *et al.*, 1980). Despite the poor outcome, this mesenchymal stem cell based spontaneous repair process is the basis for a number orthopaedic techniques (subchondral abrasion, microfracture, spongialization) commonly used to treat articular cartilage defects or diseases of articular cartilage such as osteoarthritis (OA). Osteoarthritis is the most prevalent disorder of the musculoskeletal system, and is a consequence of mechanical and biological events that destabilize tissue homeostasis in articular joints. It can either be caused by an age-related loss of ability of the tissue to respond to normal forces (primary OA) or the inability of the tissue to respond to excess loading (secondary OA) (Risbud and Sittinger, 2002).

The mechanobiology of osteochondral defect repair is complex. Successful repair depends on the migration and proliferation of mesenchymal stem cells into the defect, the formation of bone through both intramembranous and endrochondral ossification, and finally the differentiation of mesenchymal stem cells into chondrocytes that produce and maintain a functional hyaline-like repair tissue. Unsuccessful repair is characterised by fibrous tissue formation and eventually degradation of the repair tissue.

Currently no orthopaedic repair technique has been developed which fully meets this definition of 'successful' articular cartilage repair. Tissue engineering strategies for cartilage repair involve the implantation of a cell-free or cell-seeded gel or scaffold, or a more mature *in vitro* engineered-tissue, into the damaged or diseased cartilage. It offers a promising alternative to traditional orthopaedic techniques. *In*

vitro studies have shown that agarose gels (Benya and Brown, 1986) or scaffolds such as fibrous polyglycolic acid (Vunjak-Novakovic *et al.*, 1999; Martin *et al.*, 2000) can maintain the chondrogenic phenotype and support cell proliferation, viability and the synthesis of cartilage matrix moloecules. When used to treat osteochondral defects in animal models, these cell-carriers have improved the repair tissue compared to untreated controls (Schaefer *et al.*, 2002; Schreiber *et al.*, 1999; Rahfoth *et al.*, 1998); however the repair tissue is still inferior to normal articular cartilage, with morphologically stable hyaline cartilage reported in fewer than half of all defects after 18 months (Rahfoth *et al.*, 1998). It would seem therefore that, even if a scaffold or gel promotes chondrogenesis *in vitro,* it does not necessarily produce a functional repair tissue *in vivo*.

1.3 Objectives of the thesis

> "*The purpose of computational mechanobiology is to determine the quantitative rules that govern the effects of mechanical loading on tissue differentiation, growth, adaptation and maintenance by trail-and-error...Computational mechanobiologists hypothesize a potential rule and determine if the outcome of this hypothesis produces realistic tissue structures and morphologies, hence trial-and-error*" ~ van der Meulen and Husikes (2002)

The aim of this thesis is to develop a theory capable of predicting tissue differentiation due to the biophysical stimuli experienced by mesenchymal stem cells. This theory will be incorporated into a computational model and tested by attempting to simulate tissue differentiation during osteochondral defect repair based on the mechanical environment within the defect. In order to simulate tissue differentiation, other aspects of cell behaviour involved in the tissue differentiation process, which may also be regulated by mechanical forces, such as migration, proliferation, and cell death will be incorporated into the model.

If the mechano-regulation model succeeds in predicting the patterns of tissue differentiation observed experimentally, then the proposed theory will have been

strengthened to the extent that it could be used to evaluate tissue-engineering strategies used in osteochondral defect repair.

Current tissue engineering strategies involve implanting either an *in vitro* tissue-engineered cartilage construct or a scaffold into the defect, yet little is known about how the mechanical properties of these constructs will influence the quality of the repair tissue. A mechano-regulation model for tissue differentiation could be used to determine the optimal mechanical properties for such a construct to induce chondrogenesis rather then fibrous tissue formation within the defect. The utility of a mechano-regulation model capable of realistic predictions of tissue differentiation do not end at simulating osteochondral defect repair. One could envisage such a model being used to optimise any tissue-engineering implant that incorporates mesenchymal stem cells, or to design orthopaedic implants that do not provoke adverse tissue adaptations and, perhaps most importantly, to understand the mechanisms behind debilitating musculoskeletal diseases such as osteoporosis and osteoarthritis.

Chapter 2

Literature review

Contents

2.1 Introduction **9**

2.2 Mechanobiology of cells of the mesenchymal lineage **9**

2.2.1 Tissue differentiation *9*

2.2.2 Cell dispersal *16*

2.2.3 Mitosis and cell death *17*

2.3 Composition, structure, and biomechanics of articular cartilage **20**

2.3.1 The solid and fluid phases of articular cartilage *20*

2.3.2 The cellular level of articular cartilage *21*

2.3.3 The biomechanical properties of articular cartilage *22*

2.3.4 Biot's general theory of three-dimensional consolidation *25*

2.4 In vivo studies of cartilage defect repair **30**

2.4.1 Anatomy and physiology of the knee joint: A brief introduction *30*

2.4.2 Spontaneous repair of osteochondral defects *31*

2.4.3 Physical factors influencing repair *34*

2.4.4 Repair of cartilage defects using tissue-engineering *35*

2.5 Conclusions **42**

2.1 Introduction

This chapter begins with a review of the existing theories for mechano-regulation of tissue differentiation. Other aspects of cell behaviour that influence the tissue differentiation process (cell dispersal, mitosis and cell death) are also discussed. As this thesis will use cartilage defect repair as a model to study stem cell mechanobiology, the second section of this chapter will examine the composition, structure and biomechanics of articular cartilage. The theory of poroelasticity commonly used by bioengineers to model articular cartilage will be introduced. The chapter will conclude with a review of *in vivo* studies of cartilage defect repair.

2.2 Mechanobiology of cells of the mesenchymal lineage

2.2.1 Tissue differentiation

According to Bianco and Robey (2000) the concept of a stem cell originates in the early 20th century, yet as early as 1895 Roux suggested that mechanical stresses were responsible for the differentiation of connective tissues (Roux, 1895). Therefore research into how the mechanical environment influences the differentiation of pluripotential mesenchymal stem cells into chondrocytes, fibroblasts or osteoblasts precedes the discovery of the mesenchymal stem cell itself.

Fracture healing became an early model for studying mechano-regulated tissue differentiation, as the mechanical loading of the fracture callus was known to influence healing. As described in the Introduction, the modern treatment of this subject begins with Pauwels (1941, 1980). He proposed that two stress invariants, namely the octahedral shear stress and the hydrostatic stress, regulated the type of soft tissue formed within the fracture callus. Octahedral shear stress causes material deformation, but no change in volume, and was proposed as a specific stimulus for fibrous tissue formation, while hydrostatic stress causes a change in material volume, but no change in distortion, and was proposed as a specific stimulus for chondrogenesis (Fig. 1.3). Pauwels's ideas on tissue differentiation were based on comparisons of histological patterns in oblique pseudarthroses (false joint) and angulated fractures with the state of stress and strain in the tissue as determined by simple mechanical models, see Fig. 2.1 and Fig. 2.2. He noted that areas of cartilage

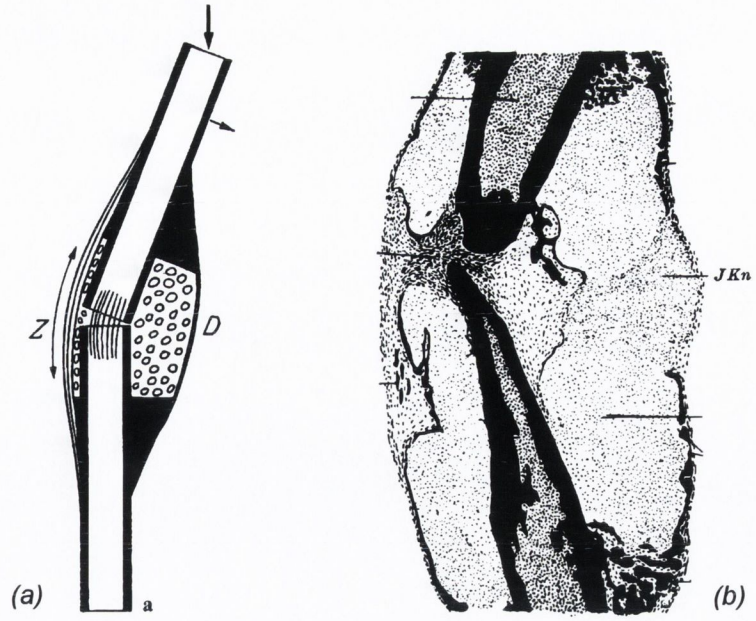

Fig. 2.1. *(a) Pauwels' illustration of an angulated fracture, consisting of a tension side (Z) where cells were thought to be elongated, and a compression side (D) where the cells were thought to be hydrostatically stressed. (b) Histological section of an angulated fracture callus, consisting of small chondrocytes on the compressive (right) side of the callus, and a more fibroblast like cells on the tension (left) side of the callus. Adapted from Pauwels (1980).*

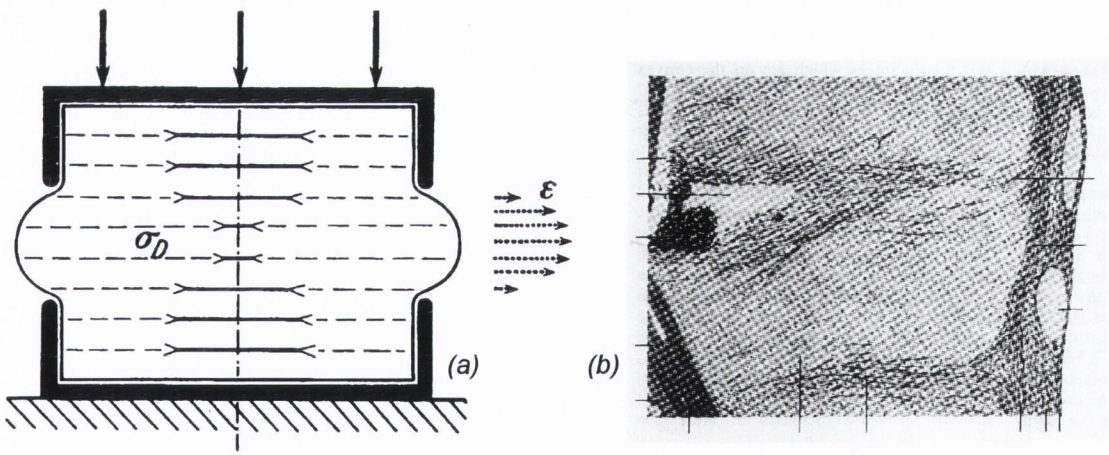

Fig. 2.2. *(a) Pauwels' representation of cartilage been squeezed between the regenerating bony tissue. In the centre the regenerating tissue is elongated transversely. (b) Callus from a fracture of the forearm of a mouse, showing collagen fibers have developed in the area of maximum elongation. Adapted from Pauwels (1980). Black lines in figure have no significance here.*

formation consistently developed in certain locations within the fracture, which he believed coincided with areas of hydrostatic pressure. Similarly parallel collagen fibres or fibrous tissues were hypothesised to develop in areas of tissue elongation. Pauwels did not propose a specific stimulus for bone formation. Instead he concluded that bone formation occurred once cartilage or connective tissue provided a rigid enough template on which ossification could occur.

Perren and Rahn (1980) proposed a simple model for tissue differentiation based on a qualitative analysis of fracture healing. They proposed that a certain tissue phenotype would not form in a fracture callus if the strain level in the fracture callus caused that tissue to fail, see Fig. 2.3. This idea was termed the 'interfragmentary strain theory'. Interfragmentary strain was defined as the interfragmentary motion divided by the fracture gap size. Based on the strength of different tissue phenotypes, and the measured interfragmentary strain, tissue differentiation can be predicted. Initially the fracture site is filled with granulation tissue, which begins to differentiate towards cartilage, gradually increasing the strength of the regenerating tissue. As the tissue stiffens, the interfragmentary strain decreases, allowing the formation of stiffer and stronger tissues at the fracture site. This process continues until full function is restored in the bone. Although easy to understand, this model is limited because it assumes that only a single tissue type exists within a fracture callus at any one point in time, which is obviously a simplification.

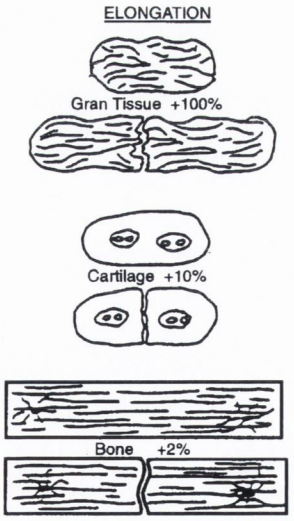

Fig. 2.3. *Strain tolerance of repair tissues. A tissue cannot exist in an environment where the interfragmentary strain exceeds the strain tolerance of the extracellular matrix of the tissue. Taken from Perren and Cordey (1980).*

Carter and colleagues (1988, 2001) expanded on Pauwels' ideas for mechano-regulated tissue differentiation by including the influence of the magnitude and direction of hydrostatic stress and the octahedral shear (distortional) strain history. Octahedral shear stress was replaced with octahedral shear strain due to the belief that biological events at the tissue level are often related to changes in cell shape and local matrix deformation. This mechano-regulation model is based on the hypothesis that bone formation occurs in regions of low octahedral shear strain and hydrostatic stress where a good vascular supply exists, chondrogenesis occurs in regions of compressive hydrostatic stress and low octahedral shear strain, fibrous tissue formation occurs in regions of high octahedral shear strain and fibrocartilage occurs in regions of high octahedral stress with a superimposed compressive hydrostatic stress, see Fig. 2.4 (a). A second diagram of mechano-regulated tissue differentiation was also hypothesized by Carter and colleagues based on the maximum principal strain rather that the octahedral shear strain, see Fig. 2.4 (b). This alteration was made based on studies that suggested the magnitude of the intermittently applied maximum principal strain regulates intermembranous ossification (Perren and Rahn, 1980) and collagen type I synthesis (Giori *et al.*, 1993). Both these diagrams introduce the idea of "Pressure lines" and "Tension lines", which are critical values above or below which tissue differentiation occurs.

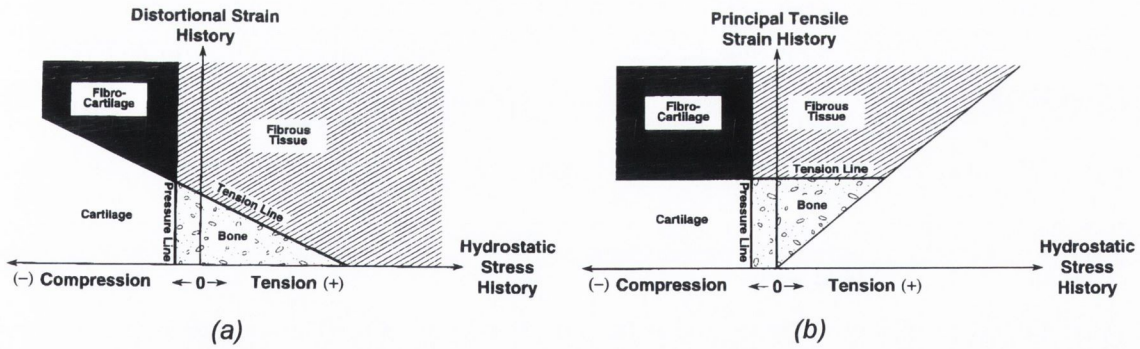

Fig. 2.4 *(a) Carter and colleagues (2001) view of the role of hydrostatic stress history and distortational strain (octahedral shear strain) history on tissue differentiation. (b) Carter and colleagues (2001) view of the role of hydrostatic stress history and maximum principal stress history on tissue differentiation.*

Carter and co-workers tested their theory of mechano-regulated tissue differentiation by comparing the patterns of tissue differentiation around implants (Giori *et al.*, 1995) and during fracture healing (Carter and Beaupré, 2001; Loboa *et al.*, 2001) and osteochondral defect healing (Carter and Beaupré, 2001) with the patterns of hydrostatic stress and maximum principal tensile strain determined using finite element modelling. The latter study involved creating an idealized two-dimensional finite element model of a full-thickness cartilage defect, see Fig. 2.5 (a). The stress and strain histories within the defect were determined based on a time-varying load that was applied to the model. The hydrostatic stress within the defect was predicted to be chondrogenic, see Fig. 2.5 (c); however due to the differences between the material properties of the normal cartilage and the regenerating tissue, high tensile strains were present within the regenerating tissue that are not present in normal cartilage, see Fig. 2.5 (b). According to their mechano-regultion hypothesis (Fig. 2.4), these tensile strains could be expected to promote fibro-cartilage or fibrous tissue formation. These tests of their theory were limited in two respects:

(i) The models were static in the sense that they compared the patterns of tissue differentiation to the patterns of hydrostatic stress and maximum principal stress (or distortational strain) for one particular moment in time, usually when the repair tissue was in an early mesenchymal stage. Therefore the theory was not tested to see if it could *simulate the progression* of the tissue differentiation process over time.

(i) The tissue differentiation predictions were only semi-quantative in the sense that definite magnitudes of hydrostatic stress and maximum tensile strain that produce a certain tissue type were not explicitly defined, leading to woolly conclusions such as "the stress and strain patterns in the interfragmentary gap reveals an environment of hydrostatic pressure and tensile strain that, based on the mechanobiological tissue differentiation concept, supports the development of fibrocartilage within the region" (Loboa *et al.*, 2001). This semi-quantitive nature of the calculations renders the theory subjective, and hence difficult to falsify.

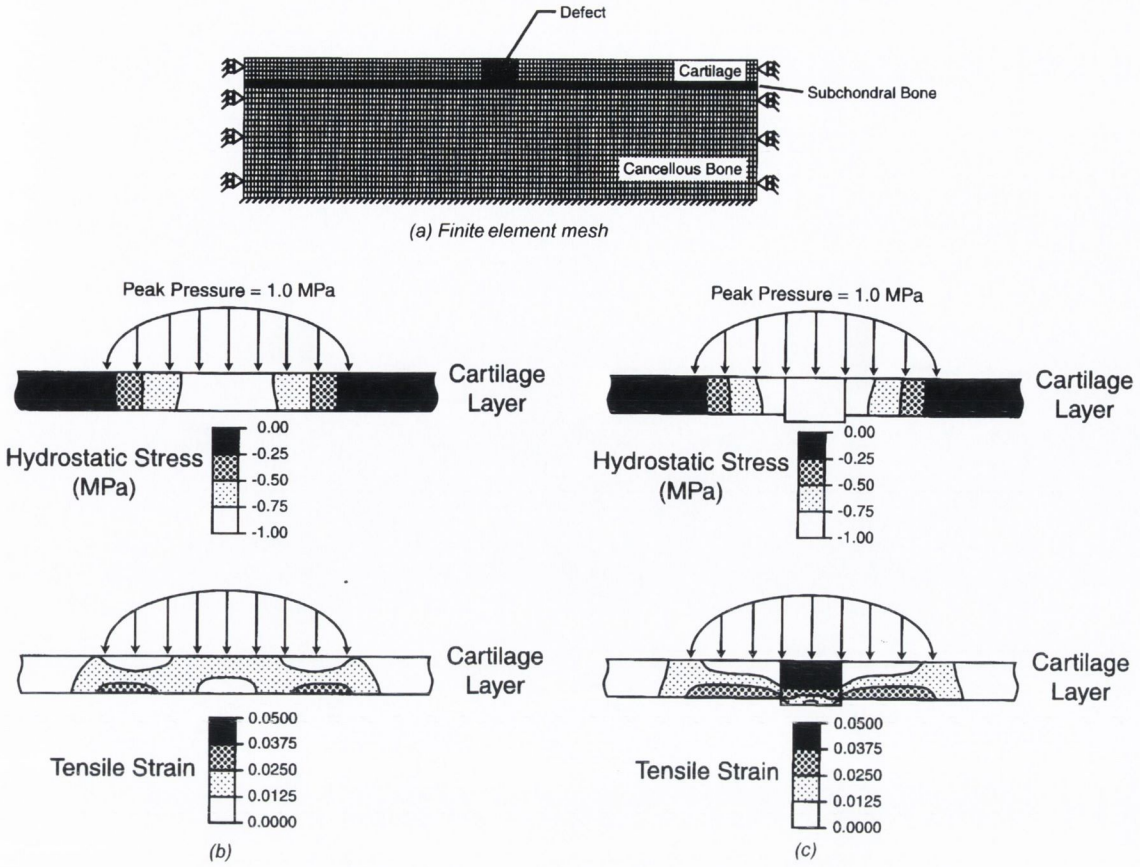

Fig. 2.5 *(a) Finite element mesh of a chondral defect used by Carter and Beaupré (2001). (b) The distribution of hydrostatic stress and tensile strain in normal articular cartilage. (c) The distribution of hydrostatic stress and tensile strain in the articular cartilage and regenerating tissue in the chondral defect.*

Prendergast *et al.* (1997) used a dynamic poroelastic finite element model to analyse the mechanical environment of differentiating cells in an experiment where a moving piston was implanted into the femoral chondyles of dogs (Søballe *et al.*, 1992). A poroelastic analysis offers the advantage of determining not only the solid matrix stresses and strains, but also the fluid pressure within the tissue and the corresponding fluid flow over time. Prendergast *et al.* (1997) found that the biophysical stimuli experienced by differentiating cells at the implant interface are not only generated by the tissue matrix, but also to a large extent by the drag forces from interstitial fluid flow. Based on this study, an alternative mechano-regulation diagram was proposed based on the octahedral shear strain and interstitial fluid flow within the regenerating tissue, see Fig. 2.6. The stimulus for differentiation S was defined as:

$$S = \frac{\gamma}{a} + \frac{v}{b} \qquad \text{(Eqn. 2.1)}$$

where γ is the octahedral shear strain and v is the fluid velocity relaive to the solid, a and b been empirical constants. Setting a = 3.75% and b = 3 ms^{-1}, bone formation is predicted to occur if S is less than 1, cartilage formation is predicted to occur if S is grater than 1 and less than 3, and fibrous tissue formation is predicted to occur if S is greater than 3 (Huiskes *et al.*, 1997). Combined with a poroelastic finite element model that predicts the strain and fluid flow acting on cells, this mechano-regulation model has successfully predicted tissue differentiation observed experimentally around implants (Huiskes *et al.*, 1997). By using a diffusion equation to describe the migration of cells through a fracture callus, Lacroix and Prendergast (2002a), Lacroix and Prendergast (2002b) and Lacroix *et al.* (2002) were also able to use this mechano regulation model to simulate the time-course of fracture healing. The same empirical constants and material characteristics were used to predict tissue differentiation around implants and during fracture healing, in order to counter any arguments that the empirical constants could be 'tweaked' to predict any particular outcome.

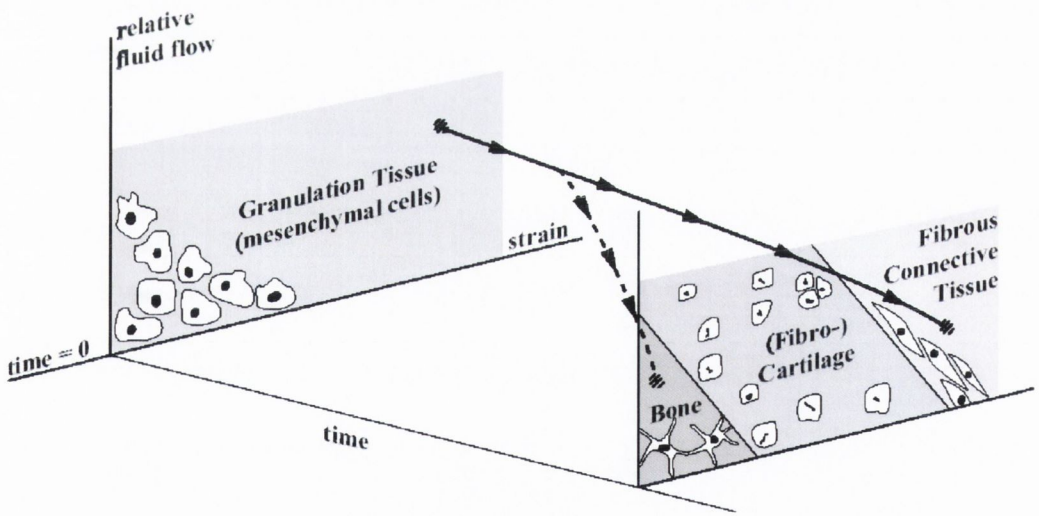

Fig. 2.6. *Mechano-regulation pathway hypothesised to control tissue differentiation based on the tissue strain and fluid flow. Both tissue strain and interstitial fluid flow are hypothesised to cause cell deformation. A region of high cell deformation causes fibrous tissue formation, intermediate deformations allow cartilage formation and low strains allow bone formation. After Prendergast et al. (1996).*

2.2.2 Cell dispersal

The majority of studies examining the movement of cells have done so on an *in vitro* substrate environment, and to the author's knowledge no study to date has investigated experimentally the movement of cells through regenerating tissues. It has been suggested that the movement of cells can be thought of as an assemblage of particles, with each particle moving around in a random way (Murray, 1989). When this random movement results in some macroscopic or gross regular movement of the group, it can be thought of as a diffusion process, where the rate of change in cell concentration c can be expressed using a simple diffusion equation:

$$\frac{\partial c}{\partial t} = D\nabla^2 c, \qquad \text{(Eqn. 2.2)}$$

where D is the diffusion coefficient coefficient and ∇ is the gradient operator. Microscopic study of leukocyte movement has measured a diffusion coefficient of 240 μm^2/min (Gruler and Bültmann, 1984). Studies of fibroblasts have reported cell velocities yielding slower diffusion coefficients of about 2-60 μm^2/min. In a mathematical model of fracture healing, Bailón-Plaza and Van Der Meulen (2001) concluded that the diffusion coefficient to represent mesenchymal cell dispersal *in vivo* should be at the higher end of these reported values, since *in vitro* substrate conditions may slow down cellular migration and growth factors released during fracture healing act as chemoattractants to increase cell speeds *in vivo*.

In a finite element analysis of fracture healing, Lacroix *et al.* (2002) used a simple reverse-engineering approach to determine the diffusion coefficient that would give a steady state cell concentration throughout the fracture callus at the end of a 16 week healing period. This gave a diffusion coefficient of 2.37 mm^2/day if mesenchymal stem cells originated from a single site, and a coefficient of 0.34 mm^2/day if the mesenchymal stem cells originated from three different sites. Including the process of mesenchymal stem cell dispersal was predicted to have a fundamental effect on the healing pattern and the healing rate. This result highlights the importance of including cellular dispersal to accurately simulate the tissue differentiation process. However this model of cellular dispersal was limited since cell dispersal was assumed to be independent of the tissue differentiation process.

Therefore the diffusion coefficient was the same regardless of the cell phenotype or the tissue the cell was moving through.

2.2.3 Mitosis and cell death

Lacroix *et al.* (2002) hypothesised that it would be necessary to take account of cellular mitosis and apoptosis (programmed cell death) to accurately simulate the tissue differentiation process. They proposed that the rate of change in cell concentration n be expressed as

$$\frac{\partial n}{\partial t} = D\nabla^2 n + ns(c) - k(n) \qquad \text{(Eqn. 2.3)}$$

where $s(c)$ is a function describing the mitosis rate per cell, and k is a constant describing cell apoptosis. Lacroix *et al.* (2002) suggested that cell mitosis would be dependant on the concentration of mitosis inducing chemicals; however mechanical loading is also known to influence the proliferation of osteoblasts, chondrocytes and fibroblasts.

Jones *et al.* (1991) studied the influence of different strain magnitudes on the proliferation of two types of osteoblast-like cells and skin fibroblasts. The proliferation of periostal-derived osteoblasts was seen to increase in response to 3000 μstrains, with no increase in proliferation observed in Haversian system-derived osteoblasts or skin fibroblasts at this strain level, see Fig. 2.7. This increase in proliferation was accompanied by an increase in collagen production; however when the amount of collagen per cell was determined, it was seen that the amount of collagen synthesis per cell was only slightly stimulated. Application of 10,000 μstrains resulted in an increase in proliferation for all cell types (Fig. 2.7); however these large strains were seen to cause de-differentiation of the osteoblasts into a fibroblast-like cell, suggesting that the proliferation of fibroblasts increases under large magnitudes of strain.

The proliferation of a particular cell type may also depend on its location within the body. For example the proliferation of osteoblasts derived from the calvaria was reported to increase in response to 400 μstrain, but not at lower (200 μstrains) or higher (1000 μstrains) strains (Brighton *et al.*, 1991). This result is unsurprising

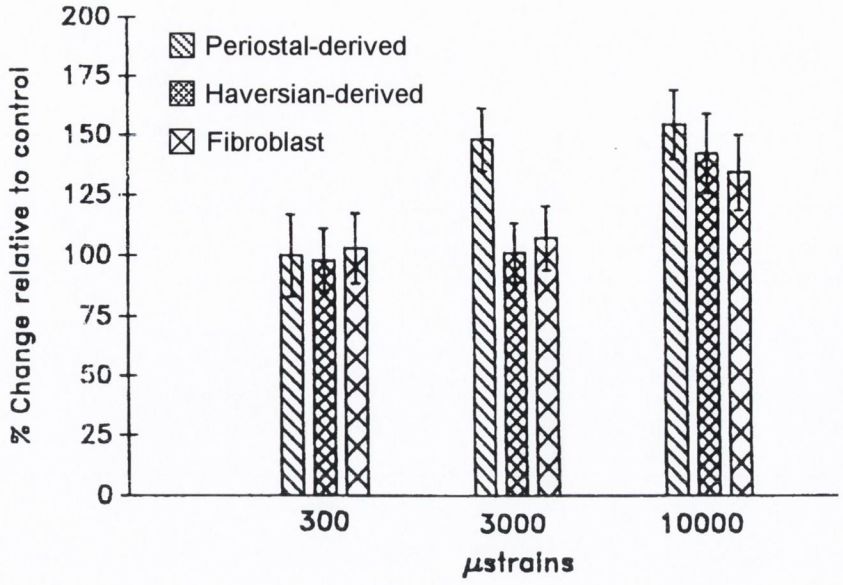

Fig. 2.7. *The effect of stain amplitude on cell proliferation. Only periosteal-derieved osteoblasts respond significantly to 3000 μstrains. All cell types respond significantly to 10000 μstrains. Taken from Jones et al., 1991.*

considering the strains observed *in vivo* are much lower in the calvaria than in the long bone (Hillam, 1994). The response of osteoblasts from different patients but from the same location within the body to applied strain has also been observed to differ significantly from patient to patient (Fermor *et al.*, 1998). Osteoblast proliferation has also been shown to depend on the number of applied loading cycles and the frequency of the loading (Kasper *et al.*, 2002). Increasing the number of applied load cycles was reported to increase cell proliferation up to a threshold cycle number, above which cell proliferation was seen to decrease. One Hz was reported as the optimal frequency for osteoblast proliferation.

Determining the influence of strain on the proliferation of chondroytes is difficult because of their tendency to de-differentiate into a fibroblast-like cell in a 2D culture system typically used to study the influence of strain on cellular proliferation (Benya and Brown, 1986). The proliferation of chondrocytes is also observed to depend on its location within the tissue. For example, subjecting chondrocytes isolated from the superficial region of articular cartilage, and cultured in three-dimensional agarose gels, to 15% dynamic strain has been reported to stimulate cell proliferation (Lee *et al.*, 1998). The proliferation of chondrocytes from the deeper

regions of articular cartilage was not influenced by the application of 15% dynamic strain.

The influence of mechanical loading on chondrocyte cell death has been studied by applying high stresses to cartilage explants in culture (Loening *et al.*, 2000; Quinn *et al.*, 2001; Kurz *et al.*, 2001). Leoning *et al.* (2000) reported chondrocyte apoptosis (programmed cell death) at peak stresses as low as 4.5 MPa, increasing in a dose dependant manner. The equilibrium compressive modulus of the loaded explants was also observed to decrease with increasing severity of the applied load. At stresses greater than 20 MPa, more than 50% of cells were reported to be apoptosed. Clements *et al.* (2000) also reported a proportional relationship between the applied load and chondrocyte cell death when the applied load was increased above 6 MPa, see Fig. 2.8. Cell death has also been shown to depend on the loading rate. Application of stress to cartilage explants at high strain rates (0.3-0.7 s^{-1}) was associated with cell death primarily in the superficial region (Quinn *et al.*, 2001). In contrast, low strain rates (3310^{-5} s^{-1}) produced cell death throughout the depth of the explant with greatest severity at the radial centre.

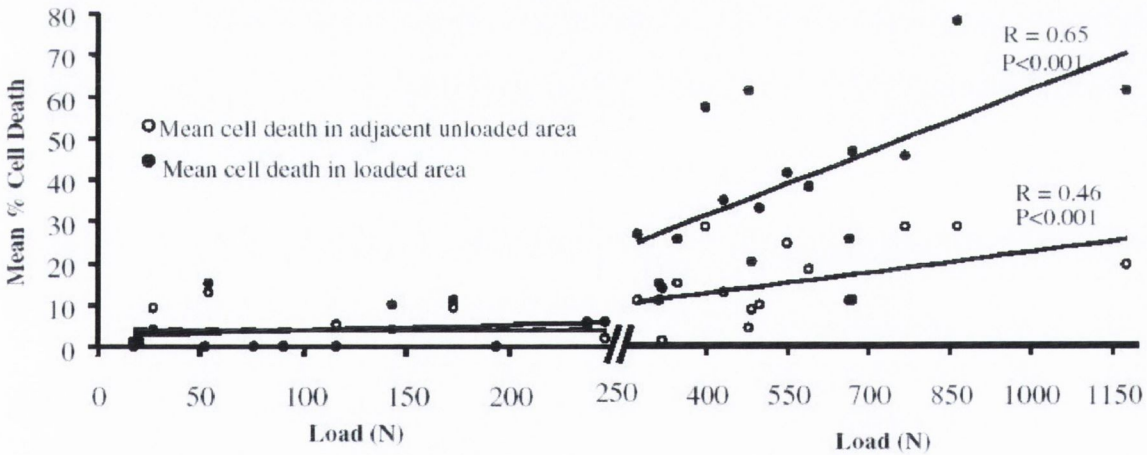

Fig. 2.8. *Applied load vs. cell death in a centrally loaded region of a cartilage explant (solid circles) and in the adjacent partially loaded region (open circles). Left: below 250 N (which corresponded to an applied stress of 6MPa), cell viability was described as independent of the applied load. Right: above 250 N, cell death increased in proportion to the applied load. Taken from Clements et al. (2000).*

2.3 Composition, structure and biomechanics of articular cartilage

2.3.1 The solid and fluid phases of articular cartilage

The bony surfaces in synovial joints are covered by a soft tissue called articular cartilage. Articular cartilage consists of a sparse distribution of chondrocyte cells embedded within an organic solid matrix that is saturated with water and mobile ions. The water phase of articular cartilage constitutes from 65 to 85% of the weight of the tissue, and it is distributed non-uniformly with depth from the tissue surface. The structural macromolecules that make up the solid matrix are synthesized by the chondrocytes. Depending on the depth from the surface, macromolecules contribute 15 to 40% of cartilage wet weight (Hasler *et al.*, 1999). The dominant molecules within the solid matrix are collagens (primarily collagen type II) and negatively charged proteoglycans. Collagen constitutes up to 75% of the dry tissue weight, and it assembles into fibrils that are inhomogenously distributed through the depth of the tissue (Mow and Guo, 2002). Proteoglycans (PGs) constitute 20 to 30% of the solid matrix of cartilage by dry weight (Mow and Guo, 2002). PGs are biomolecules composed of a central protein core with glycosaminoglycan (GAG) side chains covalently attached, a large number of which are negatively charged (Hasler *et al.*, 1999). These charged groups provide a domain with a high fixed charge density that gives rise to a large osmotic swelling pressure (Clarke, 1971). This swelling pressure contributes to the mechanical properties of the tissue. Most PG molecules bind to single hyaluronan chains to form large PG aggregates. The aggregate structure restrains the PG molecules within the collagen network, thus forming the solid matrix of articular cartilage (Mow and Guo, 2002).

The structural organisation of the solid matrix of articular cartilage varies through the depth of the tissue. In the most superficial region, commonly described as the superficial tangential zone (STZ), the collagen fibers are densely packed and orientated parallel to the articular surface (Clarke, 1971; Muir *et al.*, 1970; Clark, 1991), see Fig. 2.9. This region has a relatively low PG content and a low permeability to fluid flow, thus acting as a barrier against the large fluid flows that this region in particular experiences during compression of the tissue (Muir *et al.*, 1970). In the middle of the tissue, termed the middle or transitional zone, the collagen fibrils are larger, less densely packed, and have been reported as either randomly

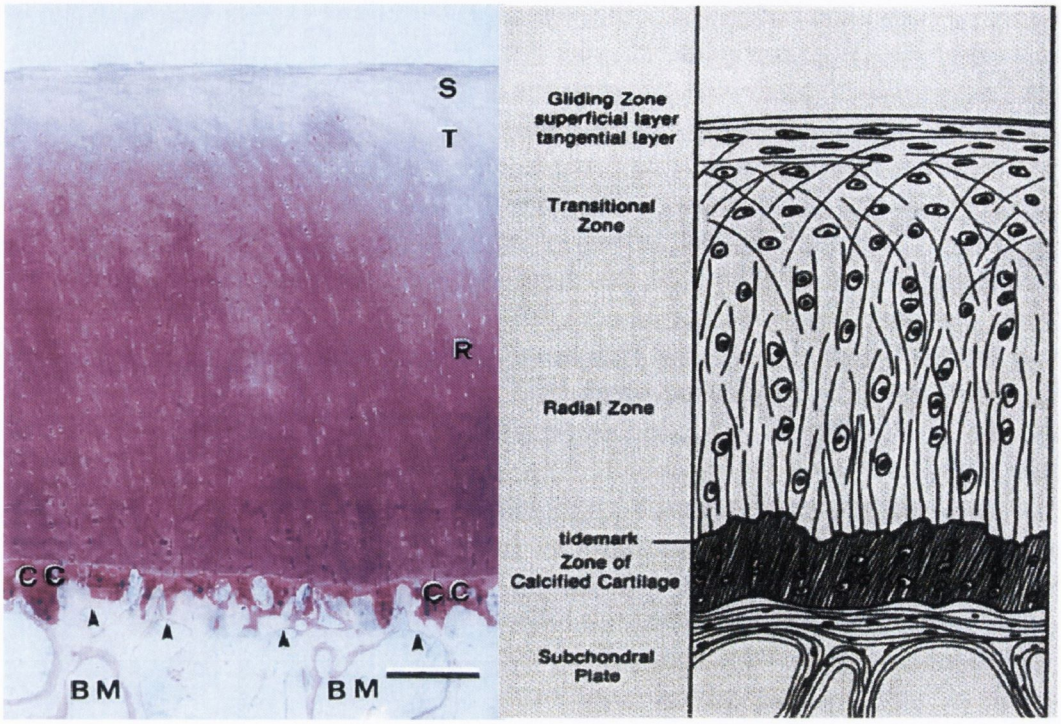

Fig. 2.9. *Cellular and collagen fibre arrangement in articular cartilage. Left: light microscope overview of adult articular cartilage from femoral chondyle, adapted from Hunziker et al. (2002). Right: Schematic representation of articular cartilage, adapted from Carter and Beaupré (2001).*

(Clarke, 1971) or radially (Clark, 1991) orientated. The PG content increases in the middle zone, giving rise to a high swelling pressure and water content (Mow and Guo, 2002). In the deepest zones the collagen fibers are longer and orientated perpendicular to the underlying calcified cartilage/subchondral bone (Clarke, 1971; Clark, 1991), anchoring the tissue to the underlying bone.

2.3.2 The cellular level of articular cartilage

The macromolecules within the tissue are synthesised, organised, and remodelled by metabolically active cells within the tissue called chondrocytes. Chondrocytes have the ability to respond to their local mechanical environment by remodelling the tissue (Hasler *et al.*, 1999). For example, in vitro dynamic compression has been shown to increase PG synthesis (Parkkinen *et al.*, 1992; Palmoski and Brandt, 1984), while static compression has been shown to reduce PG synthesis (Palmoski and Brandt, 1984). Chondrocyte size, shape and density also vary through the zones of the tissue. In the superficial zone, the chondrocytes are flattened, have a smaller volume and a

higher density when compared to the other zones of the tissue (Hunziker, 1992). In the middle zone the chondrocytes appear more rounded, larger and biosynthetically more active than in the superficial zone (Wong *et al.*, 1996). In the deep zone the chondrocytes tend to be aligned in radial columns, and the biosynthetic activity of the cells is greatest (Wong *et al.*, 1996).

2.3.3 The biomechanical properties of articular cartilage

The biomechanics of articular cartilage is best understood by viewing the tissue as having two distinct phases, a solid phase and a fluid phase. Articular cartilage is visceoealstic (i.e. the response of the tissue to an applied load varies with time), due primarily to the interaction of the solid and fluid phases during loading. During loading fluid pressure gradients are generated within the tissue, and the fluid phase is forced to flow through the solid phase, generating large drag forces as the fluid moves relative to the solid. Thus, articular cartilage will creep in response to an applied constant load and exhibit stress relaxation in response to an applied constant strain, see Fig. 2.10. These processes will continue until no pressure gradients exist within the tissue, at which point fluid will have ceased to flow within the tissue and the entire load must therefore be borne by the solid phase of the tissue. At this point, termed equilibrium, it is possible to calculate the intrinsic properties of the solid phase of the tissue using precise testing configurations.

The most common mechanical tests of cartilage in compression are the confined compression, unconfined compression, and the indention test. At equilibrium in a confined compression test, the stress-strain response of the tissue gives a measure of the aggregate modulus, H_a, of the solid phase of the tissue. The equilibrium aggregate modulus for all types of articular cartilage ranges from 0.1 - 2.0 MPa (Mow and Guo, 2002). From equilibrium in an unconfined compression test, the Young's modulus, E, of the solid phase of the tissue can be determined. The Young's modulus of articular cartilage in compression ranges from 0.41 to 0.85 MPa (Mow and Guo, 2002). Assuming articular cartilage to be homogenous and isotropic, the aggregate modulus can be related to the Young's modulus by

$$H_a = \frac{E(1-\nu)}{(1+\nu)(1-2\nu)},$$

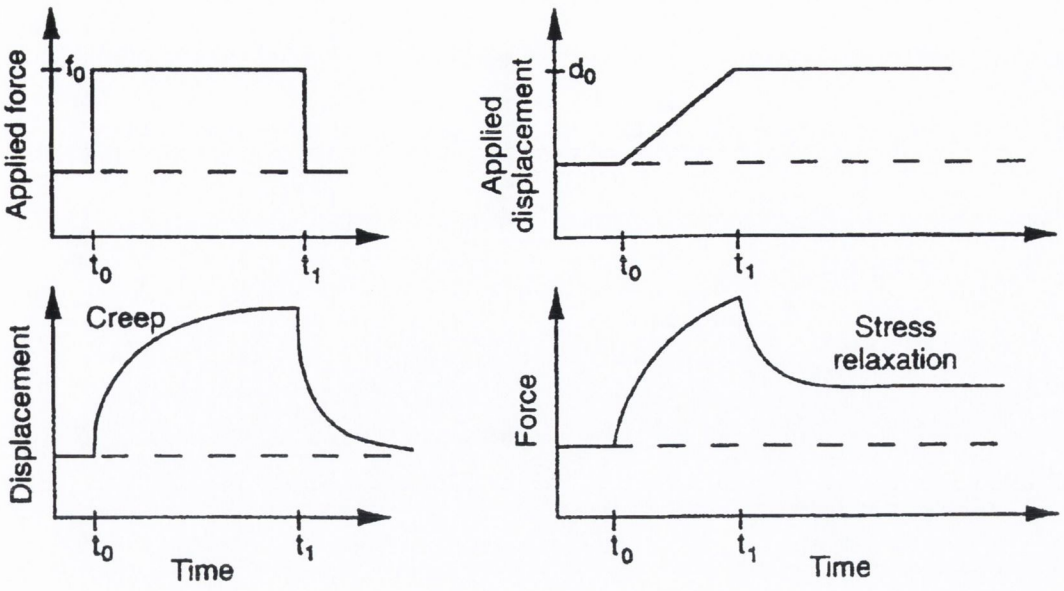

Fig. 2.10. *Schematics of load-deformation visceoelastic behaviors of articular cartilage. (a) In a creep test, a step force is applied to the sample that results in a transient increase in the measured displacement of the tissue. (b) In a stress relaxation test, a ramp displacement is applied to the sample until a desired level of compression is reached. The force rises during the ramp displacement, followed by a period of stress relaxation until the force equilibrates. Adapted from Mow and Guo, 2002.*

where v is the Poisson's ratio. However due to the zonal structure of articular cartilage, the tissue has been found to be inhomogeneous (Schingal *et al.*, 1997), with the aggregate modulus increasing from 0.079 MPa at the articular surface to 2.1 MPa in the deepest layers of the tissue.

The viscoelastic properties of the tissue are governed by its permeability. Permeability is a measure of the ease with which fluid can flow through the pores, and it is inversely proportional to the frictional drag exerted by the fluid flowing through the material (Mow *et al.*, 1994). The permeability of the tissue can be determined directly by applying a fluid pressure gradient across the tissue and measuring the corresponding volumetric discharge of fluid per unit time. The permeability of cartilage can also be determined indirectly by fitting a biphasic constitutive theory developed by Mow *et al.* (1980) to the transient stress-relaxation or creep response of a specimen loaded in confined compression. The hydraulic permeability of articular

cartilage ranges from 1.2 310^{-16} to 6.2 310^{-16} m^4/Ns (Mow and Guo, 2002). These values are very small, thus indicating that, in normal articular cartilage, large fluid pressures are generated within the tissue. For example, it has been shown that in cartilage tested in confined compression, immediately after application of the load up to 95% of the load is supported by the interstitial fluid pressure (Hunziker, 1999). This interstitial fluid pressure shields the collagen-PG solid matrix from the large loads that are generated *in vivo* (Mow and Guo, 2002).

Articular cartilage exhibits non-linear stress-strain behaviour when loaded in tension. Under low deformations a non-linear toe region is seen in the stress-strain curve due to the collagen fibrils realigning in the direction of the applied load (Fig. 2.11). As the tissue is strained further, the collagen fibers begin to be stretched, and hence generate large tensile stresses in the tissue due to the intrinsic tensile stiffness of the collagen fibers (Fig. 2.11). The slope of the linear region of the stress-strain curve gives the tensile equilibrium Young's modulus of the solid phase of the tissue. Failure of the tissue generally occurs at strains greater than 30% (Mow and Guo, 2002). Again due to the zonal structure of articular cartilage, the tissue has been found to be inhomogeneous in tension (Akizuki *et al.*, 1986), with the intrinsic tensile modulus decreasing from 20 MPa at the articular surface to 1 MPa in the deepest layers of the tissue.

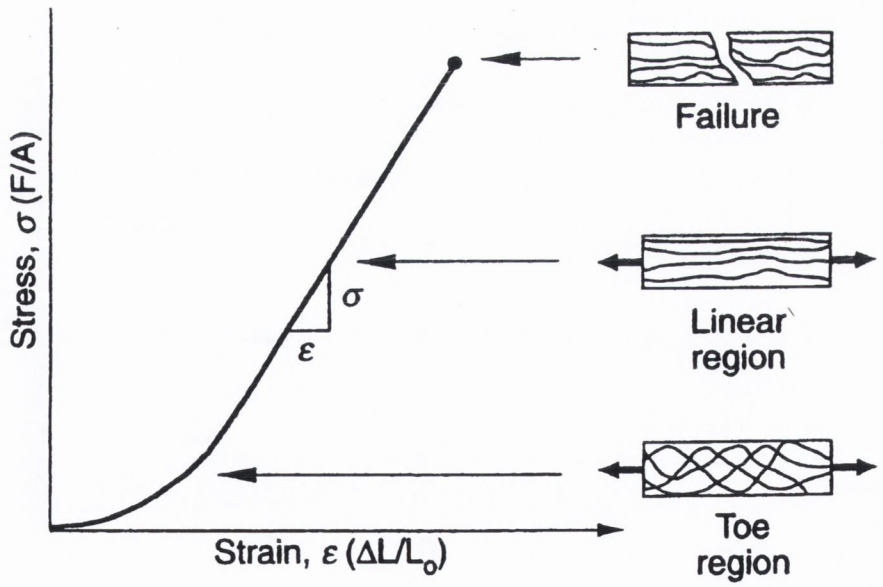

Fig. 2.11 *Characteristic stress-strain relationship for articular cartilage in a steady state strain-rate experiment. Adapted from Mow and Guo, 2002.*

3.3.4. Biot's general theory of three-dimensional consolidation

Engineering methodologies to model the bi-phasic nature of soft tissues such as cartilage have their roots in the study of consolidation – the settlement of soils under load. Consolidation was thought to be similar to the process of squeezing water out of an elastic porous medium. Trezaghi (1925) developed the first mathematical model of one-dimensional consolidation under constant load. Later Biot (1940) extended this theory to three-dimensions, valid for any time varying arbitrary load. Since the principal equations for the poroelastic theory used in many commercial finite element packages are based on this fundamental theory, a review of Biot's general theory of three-dimensional theory will be given.

According to Biot's theory, the following basic properties for the porous saturated material are assumed: (1) isotropy, (2) reversibility of the stress-strain relations, (3) linear stress-strain relations, (4) small strains, (5) fluid phase is incompressible, (6) fluid flow according to Darcy's Law.

Consider a small cubic element of such a fluid-infiltrated solid, its sides been parallel with the coordinate axes. The element is taken to be large enough compared to the size of pores so that it may be treated as homogenous, and at the same time small enough, compared to the scale of the macroscopic phenomena in which we are interested, so that it may be considered infinitesimal in the mathematical treatment. The average stress condition in the fluid-infiltrated solid is represented by forces distributed uniformly on the faces of this cubic element, which must satisfy the equilibrium conditions of a stress field.

$$\begin{aligned}
&\frac{\partial \sigma_x}{\partial x}+\frac{\partial \tau_{xz}}{\partial y}+\frac{\partial \tau_{xy}}{\partial z}=0\\
&\frac{\partial \tau_{yz}}{\partial x}+\frac{\partial \sigma_y}{\partial y}+\frac{\partial \tau_{yx}}{\partial z}=0\\
&\frac{\partial \tau_{zy}}{\partial x}+\frac{\partial \tau_{zx}}{\partial y}+\frac{\partial \sigma_z}{\partial z}=0
\end{aligned} \qquad \text{(Eqn. 2.4)}$$

Physically we may think of the stresses as composed of two parts, one that is caused by the hydrostatic pressure of the water filling the pores, the other caused by the average stress in the porous material.

The strain in the soil (e_x, e_y, e_z, γ_{xy}, γ_{xz}, γ_{yz}) can be related to the component of displacement in the material (u, v, w). In order to completely describe the macroscopic condition of the saturated material we must consider an additional variable θ, the

variation in water content. The increment of water pressure may be denoted by σ. Assuming the water pressure to be uniform throughout the element, the macroscopic conditions of the soil (e_x, e_y, e_z, γ_{xy}, γ_{xz}, γ_{yz}, θ) must be functions of the stresses in the material and water pressure (σ_x, σ_y, σ_z, τ_{xy}, τ_{xz}, τ_{yz}, σ). If the soil is assumed to be isotropic, the water pressure cannot produce any shearing strain, and for the same reason its effect will be the same on all three components of strain e_x, e_y, e_z. Therefore the stress-strain relations reduce to Hooke's law for an isotropic material, with the addition of an extra term relating the water pressure σ to the normal strain:

$$
\begin{aligned}
e_x &= \frac{\sigma_x}{E} - \frac{\nu}{E}(\sigma_y + \sigma_z) + \frac{\sigma}{3H}, \\
e_y &= \frac{\sigma_y}{E} - \frac{\nu}{E}(\sigma_z + \sigma_x) + \frac{\sigma}{3H}, \\
e_z &= \frac{\sigma_z}{E} - \frac{\nu}{E}(\sigma_x + \sigma_y) + \frac{\sigma}{3H}, \\
\gamma_{xy} &= \frac{\tau_{xy}}{G},\ \gamma_{xz} = \frac{\tau_{xz}}{G},\ \gamma_{yz} = \frac{\tau_{yz}}{G},
\end{aligned}
\qquad \text{(Eqn. 2.5)}
$$

where E is the Young's modulus, G is the shear modulus, ν is the Poisson's ratio and H is an additional physical constant. The shear modulus G can be related to the Young's Modulus and the Poisson's ratio,

$$
G = \frac{E}{2(1+\nu)}. \qquad \text{(Eqn. 2.6)}
$$

Equation 2.5 expresses the six strain components as a function of the stresses in the soil and the pressure of the water in the fluid. We still need to consider the relationship between the water content θ on these same variables. The most general relationship is

$$
\theta = a_1\sigma_x + a_2\sigma_y + a_3\sigma_z + a_4\tau_{xy} + a_5\tau_{xz} + a_6\tau_{yz} + a_7\sigma \qquad \text{(Eqn. 2.7)}
$$

Now because of isotropy the shear stress (τ_{xy}, τ_{xz}, τ_{yz}) cannot affect the water content, therefore $a_4 = a_5 = a_6 = 0$. Furthermore all three directions x, y, z must have equivalent properties $a_1 = a_2 = a_3$. Therefore equation 2.7 may be written as

$$\theta = \frac{1}{3H_1}(\sigma_x + \sigma_y + \sigma_z) + \frac{\sigma}{R}, \qquad \text{(Eqn. 2.8)}$$

where H_1 and R are physical constants. If we assume the existence of potential energy in the soil we can prove that $H = H_1$ (Proof not shown). Therefore equations 2.5 and 2.8 are the fundamental relations describing the properties of the saturated material, for strain and water content, under equilibrium conditions. They contain four distinct physical constants G, v, H and R.

We now need to establish the differential equations for the transient analysis. We can solve equation 2.5 with respect to the stresses as follows

$$e = e_x + e_y + e_z = (\sigma_x + \sigma_y + \sigma_z)\left(\frac{1-2v}{E}\right) + \frac{\sigma}{H} \qquad \text{(Eqn. 2.9)}$$

$$\Rightarrow \quad \frac{1}{E}(\sigma_y + \sigma_z) = \frac{-\sigma_x}{E} + \frac{e}{1-2v} - \frac{\sigma}{H(1-2v)} \qquad \text{(Eqn. 2.10)}$$

Substituting equation 2.10 into the first line of equation 2.5

$$e_x = \frac{\sigma_x}{E} - v\left(\frac{-\sigma_x}{E} + \frac{e}{1-2v} - \frac{\sigma}{H(1-2v)}\right) + \frac{\sigma}{3H} \qquad \text{(Eqn. 2.11)}$$

$$\Rightarrow \quad \sigma_x \frac{(1+v)}{E} = e_x + \frac{ve}{1-2v} - \frac{v\sigma}{H(1-2v)} - \frac{\sigma}{3H} \qquad \text{(Eqn. 2.12)}$$

$$\Rightarrow \quad \sigma_x = \frac{E}{1+v}\left(e_x + \frac{ve}{1-2v}\right) - \frac{E}{1+v}\left(\frac{\sigma(v+1)}{3H(1-2v)}\right) \qquad \text{(Eqn 2.13)}$$

Letting $\alpha = \dfrac{2(1+v)G}{3(1-2v)H}$ and given that $G = \dfrac{E}{2(1+v)}$ $\Rightarrow$

$$\sigma_x = 2G(e_x + \frac{ve}{1-2v}) - \alpha\sigma$$

Similarly

$$\sigma_y = 2G(e_y + \frac{ve}{1-2v}) - \alpha\sigma$$
$$\sigma_z = 2G(e_z + \frac{ve}{1-2v}) - \alpha\sigma \qquad \text{(Eqn. 2.14)}$$
$$\tau_{xy} = G\gamma_{xy},\ \tau_{xz} = G\gamma_{xz},\ \tau_{yz} = G\gamma_{yz},$$

In the same way we can express the variation in water content (equation 2.8) as

$$\theta = \alpha e + \frac{\sigma}{Q} \qquad \text{(Eqn. 2.15)}$$

where

$$\frac{1}{Q} = \frac{1}{R} - \frac{\alpha}{H}.$$

Substituting equation 2.14 for the stresses into equation 2.4, the equilibrium conditions, we find

$$G\nabla^2 u + \frac{G}{1-2v}\frac{\partial e}{\partial x} - \alpha\frac{\partial \sigma}{\partial x} = 0,$$
$$G\nabla^2 v + \frac{G}{1-2v}\frac{\partial e}{\partial y} - \alpha\frac{\partial \sigma}{\partial y} = 0, \qquad \text{(Eqn. 2.16)}$$
$$G\nabla^2 w + \frac{G}{1-2v}\frac{\partial e}{\partial z} - \alpha\frac{\partial \sigma}{\partial z} = 0,$$
$$\nabla^2 = \partial^2/\partial x^2 + \partial^2/\partial y^2 + \partial^2/\partial z^2.$$

There are three equations in four unknowns u, v, w, σ. In order to have a complete system we need one more equation. This is done by introducing Darcy's law governing fluid flow in a porous medium. According to Darcy's law the rate of flow (V_x, V_y, V_z) is related to the water pressure σ by the relations

$$V_x = -k\frac{\partial \sigma}{\partial x},\ V_y = -k\frac{\partial \sigma}{\partial y},\ V_z = -k\frac{\partial \sigma}{\partial z}, \qquad \text{(Eqn. 2.17)}$$

where k is the permeability of the soil. If the water is incompressible, the rate of change of water content must be equal to the volume of water entering per second through each of the surfaces of the element, hence

$$\frac{\partial \theta}{\partial t} = -\frac{\partial V_x}{\partial x} - \frac{\partial V_y}{\partial y} - \frac{\partial V_z}{\partial z}. \qquad \text{(Eqn. 2.18)}$$

Combining equations 2.15, 2.17 and 2.18 we obtain

$$k\nabla^2\sigma = \alpha\frac{\partial e}{\partial t} + \frac{1}{Q}\frac{\partial \sigma}{\partial t} \qquad \text{(Eqn. 2.19)}$$

We now have four equations, equations 2.16 and 2.19, satisfied by four unknowns u, v, w, σ.

Biot's formulation has been refined over the years and this approach to poroelasticity is commonly referred to as the *effective medium* approach. Another common approach to poroelasticity is the *mixture theory* approach, which stems from a fluid mechanics and thermodynamics tradition. The key difference between the *effective medium* approach and the *mixture* approach to poroelastic models is the averaging process employed to determine the material properties. In the *effective medium* approach a small but finite volume of the porous medium is used for the development of constitutive equations for a fluid-infiltrated solid. The *mixture theory* approach considers a fixed spatial point through which different materials pass. The averaging process is then density-weighted on the basis of the density of each species in the mixture, instead of being averaged over a finite volume of the porous solid as in the *effective medium* approach. An excellent comparison of the two methodologies is given by Cowin *et al.* (2001). Regardless of the differences, Mow and Lai (1980) showed that the governing equations of the "biphasic theory" (Mow *et al.*,1980), based on a *mixture theory* approach, coincide with the governing equations of the *effective medium* formulation. Computer packages have been shown to give the same results (Prendergast *et al.*, 1996).

2.4 In vivo studies of cartilage defect repair

2.4.1 Anatomy and physiology of the knee joint: A brief introduction

The majority of studies investigating cartilage defect repair do so for defects in the knee. The knee joint or tibiofemoral and patellafemoral joint is a synovial joint which transfers load between the femur and the tibia. A layer of articular cartilage covers the bony surfaces in synovial joints. The primary functions of this cartilage layer are to minimize contact stresses generated during loading and to contribute to lubrication mechanisms in the joint (Mow and Guo, 2002). Due to the unique properties of articular cartilage (as outlined in section 2.3), a healthy joint is able to withstand the large forces associated with weight-bearing and joint motion over a lifetime. A thin film of synovial fluid separates the articular surfaces (Fig. 2.12), which markedly reduces friction during articulation. During loading the pumping of synovial fluid throughout the cartilage matrix also allows for the ingress of nutrients and the removal of waste products from the tissue.

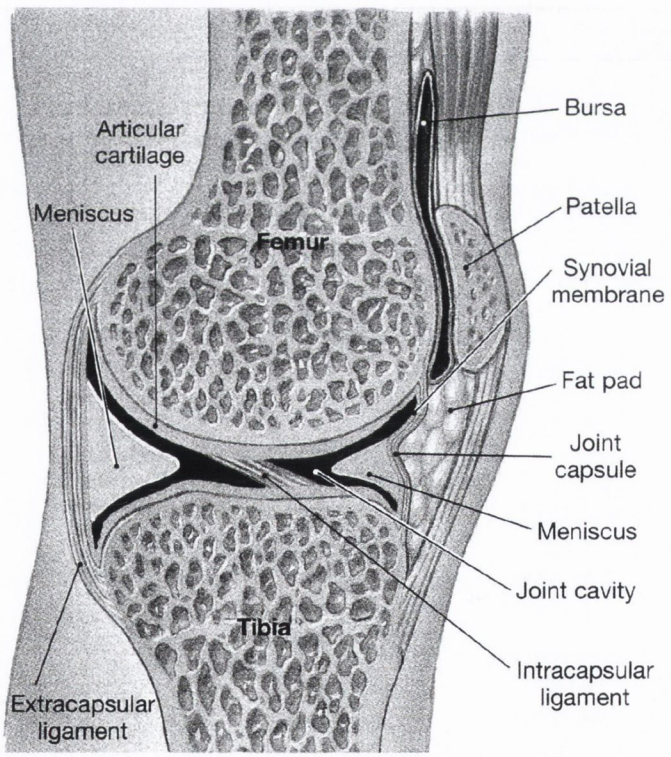

Figure 2.12. *A simplified sectional view of the knee joint. Adapted from Martini, 2001.*

Structurally the knee consists of three separate contact regions: two between the condyles of the femur and the tibia, and one between the patella and the femur. A pair of fibrocartilage pads, the menisci, lie between the peripheral surfaces of the tibial and femoral chondyles. The menisci play an important role in assisting load bearing and lubrication within the knee. The knee joint also consists of seven major ligaments that aid in stabilising the joint.

2.4.2 Spontaneous repair of osteochondral defects

Spontaneous repair in animal models of osteochondral defects consistently follows the same course (Hunziker, 1999). The patterns of cellular events has been characterised in detail using both histology (Shapiro *et al.*, 1993) and mRNA analysis (Metsaranta *et al.*, 1996). (Fig. 2.13 through to Fig. 2.18 are histology sections from Shapiro *et al.* (1993). The repair tissue is on the right, and the normal tissue is on the left, distinguished by a red dotted line added to the figures). The sequence of events can be summarised as follows:

1. Within a few hours the defect fills with a blood clot.
2. After 2-3 days the defect is filled with an organised fibrous clot, see Fig. 2.13, which is invaded by mesenchymal cells from the bone marrow. In the depths of the defect, the marrow contains many active osteoblasts synthesising woven bone (Shapiro *et al.*, 1993), although, at this time point (day 3) the yield of mRNA for type I collagen and osteonectin, a marker for bone formation, remain low (Metsaranta *et al.*, 1996).

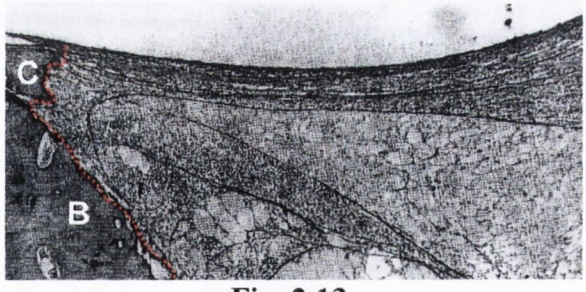

Fig. 2.13.

3. By day 7 the clot has been completely resorbed, having been replaced by a fibrous structure that, at this stage, is extensively infiltrated by undifferentiated mesenchymal cells, see Fig 2.14. The fibrous strands are orientated parallel to the articular surface suuperfically, as though acting as a scaffold which orientates the cells parallel to the articular

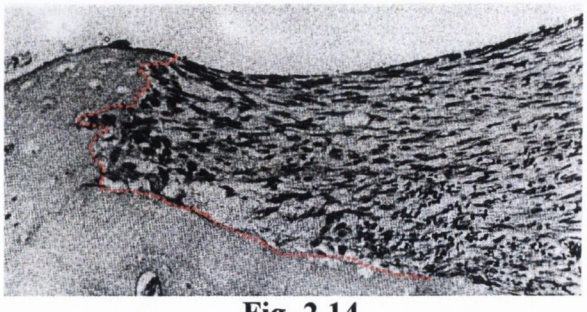
Fig. 2.14.

surface. Most of the chondrocyes in the adjacent normal articular cartilage are dead. The yield of mRNA for type I collagen increases dramatically from day 3 to day 7, staying high until day 14, and gradually declining thereafter.

4. At day 7, levels of type II collagen mRNA, a marker for chondrogenesis, are low compared to normal articular cartilage (Metsaranta *et al.*, 1996).

5. At day 14, a clear pattern of tissue differentiation becomes apparent. At the base of the defect bone formation occurs through direct intramembranous ossification. On top of this newly synthesised bone sits a layer of cartilage, see Fig 2.15, which has been shown to express type II collagen (at low levels) and has stained positive for safranin-O (Metsaranta *et al.*, 1996; Shapiro *et al.*, 1993), a marker of chondrogenesis. On top of this sits a thin layer of fibrous tissue that contains flattened, fibroblast-like cells, and which stains negative for safranin-O. The repair tissue is not well integrated with the residual cartilage (Shapiro *et al.*, 1993).

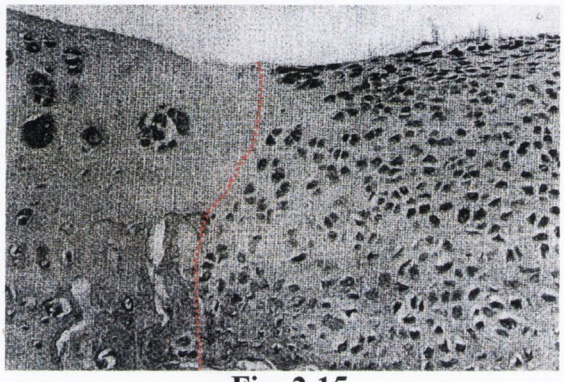

Fig. 2.15.

6. Between week 2 and week 8, bone formation and remodelling continue through both intramembranous ossification and endochondral ossification of hypertrophic chondrocyes in the deep region of the newly formed cartilage. Expression of type II collagen increases in the centre of the defect (Metsaranta *et al.*, 1996), however a well developed superficial fibrous layer persists at the articular surface, see Fig. 2.16, which can be twice as thick as the as the superficial layer in normal articular cartilage by week

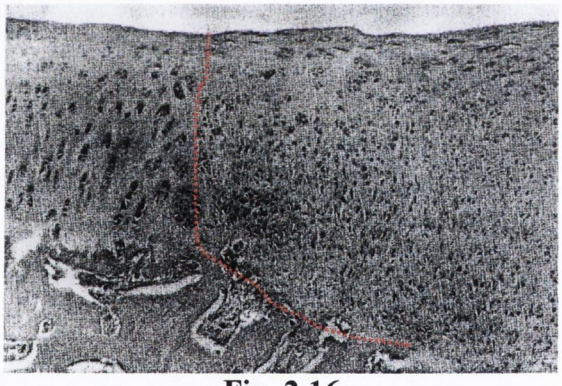

Fig. 2.16.

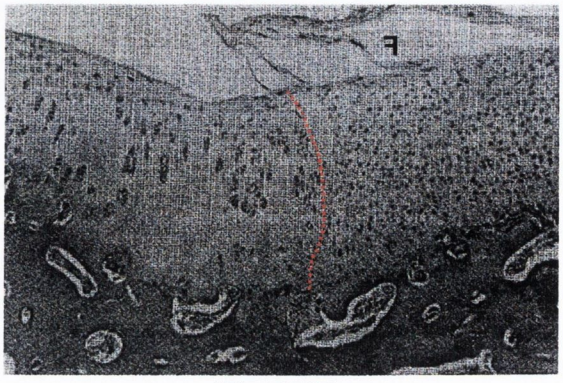

Fig. 2.17.

6 (Shapiro *et al.*, 1993). Between weeks 8 and 10, some early signs of degeneration are observed, with surface fibrillation and tears occurring in many of the defects, see Fig. 2.17.

7. From week 12 onwards, the intensity of Safranin-O staining has been observed to decrease in many defects (Shapiro *et al.*, 1993), with a reduction in intensity observed form the deep zone towards the superficial zone. The thickness of the repair tissue can often be significantly less then that of the surrounding tissue, see Fig. 2.18.

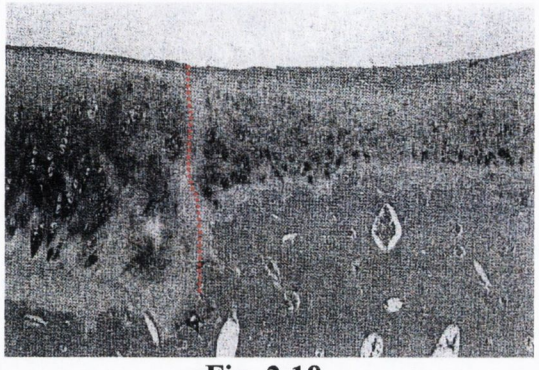

Fig. 2.18

8. By week 36, extensive acellular regions were present in the repair cartilage of many defects. The degradation process continues unremittingly with time (Shapiro *et al.*, 1993).

The proliferative ability of cells involved in the spontaneous repair of osteochondral defects has been studied by measuring the thymidine uptake at different time points (DePalma *et al.*, 1966). Thymidine becomes fixed within the nucleus of a cell during the period of DNA synthesis, thus the presence of DNA synthesis may be observed autoradiographically. No indication of cell proliferation was observed within the defect at day 2, however there was a significant increase in cell proliferation observed in the adjacent bone marrow, see Fig. 2.19 (a). At week 1, cell proliferation was first observed within the defect, with greater proliferation observed in the deeper regions of the defect compared to the upper regions, see Fig. 2.19 (b). At week 2, there is an even distribution of thymidine uptake in the reparative tissue, indicating uniform cell proliferation throughout the tissue, see Fig 2.19 (c). Cellular proliferation is seen to decrease by week 8, see Fig. 2.19 (d). At this time point the tissue is primarily cartilage-like. No significant proliferation is observed by week 32, except within the bone marrow and regions of immature cartilage. No cell proliferation is reported in the normal articular cartilage adjacent to the defect at any time point.

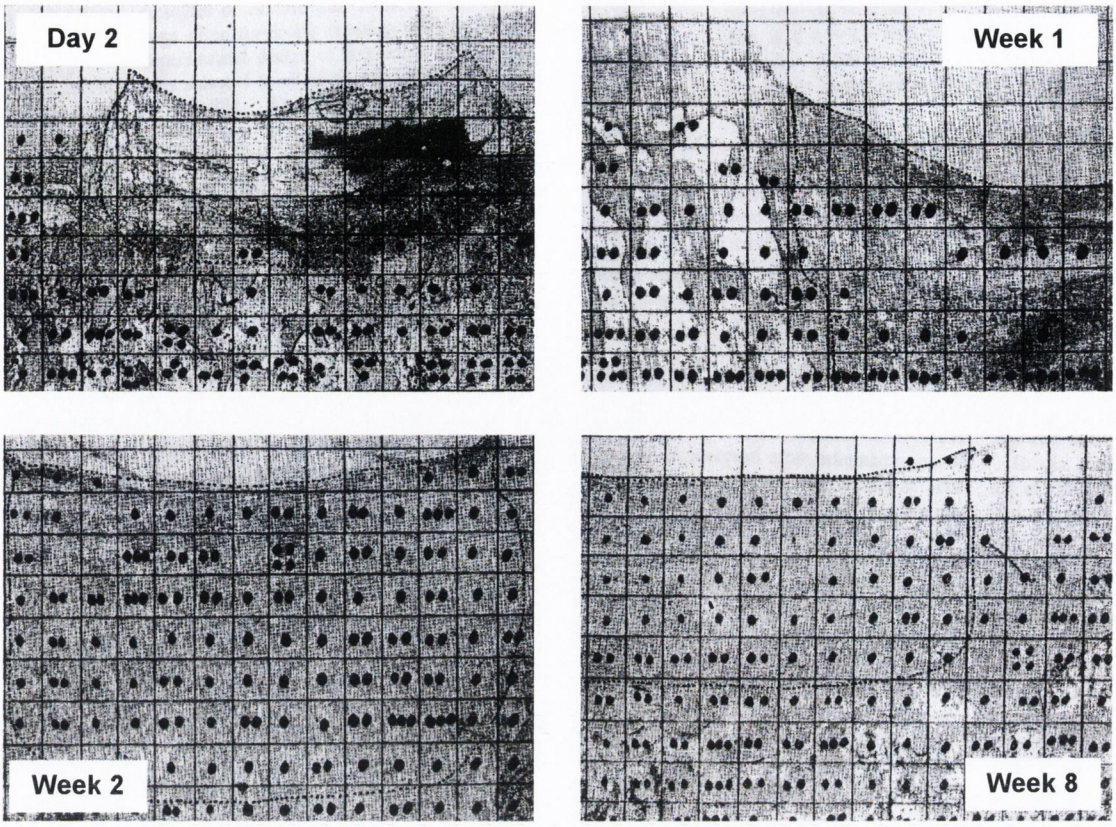

Fig. 2.19. *Autoradiographic analysis of osteochondral defect repair. 1 dot: 5 % or less of cells are labelled. 2 dots: 5 to 10 % of cells labelled. 3 dots: 10 to 15 % of cells labelled, and so on. The confines of the original defect defect are enclosed in the red dotted line. (a) Day 2: No indication of tymidine uptake in defect, with increased uptake observed in adjacent marrow. (b) Week 1: 5 to 10 % of cells labelled in upper regions, with 10 to 15 % of cells labelled in deeper regions of defect. (c) Week 2: Even distribution of thymidine uptake in the repair tissue. Labelling in upper region of defect has increased compared to the week 1. The per cent of labelled marrow cells is returning to normal levels. (d) Week 8: Thymidine uptake is only occasionally greater than 5 %. Adapted from DePalma et al., 1966.*

2.4.2 Physical factors influencing repair

The quality and extent of the repair tissue in osteochondral defects, as well as long-term survival of the repair tissue surface, depends on a multitude of factors such as the age and species of the animal, location (DePalma *et al.*, 1966) and size of the defect (Convery *et al.*, 1972), and the type of postoperative loading (Kim *et al.*, 1991). Small defects (3mm in diameter) in a horse have shown complete repair after 3 months, and

were difficult to locate after 9 months, whereas large defects (9mm in diameter) showed incomplete repair at 9 months (Convery *et al.*, 1972). The repair tissue partially replacing the large defects was a variable mixture of fibrous tissue, fibrocartilage, hypercellular cartilage and (occasionally) bone. Cartilage formation has also been observed to form at a slower and quantitatively inferior rate in defects in non-weight bearing areas compared to defects in weight-bearing areas (DePalma *et al.*, 1966), suggesting a functional loading is required for the repair of articular cartilage defects. Kim *et al.* (1991) found that every osteochondral defect in a rabbit model treated with continuous passive motion for two weeks post-operatively had mature, hyaline-like cartilage as the predominant repair tissue at 12 weeks, compared with 60% of defects treated with intermittent active motion. Different loading conditions, in combination with suturing a layer of periosteal tissue into the base of the defect, results in different repair tissues forming within the defect (O'Driscoll *et al.*, 1986). In groups of rabbits that were treated with immobilization, intermittent active motion, or two weeks of continuous passive motion, 32 to 47 % of the total collagen was type II, while the group that was treated with 4 weeks of continuous motion, 93 % of the total collagen was type II.

2.3.3 Repair of cartilage defects using tissue engineering

Tissue engineering has been defined by Nerem (2002) as:

> *"The development of biological substitutes for implantation into the body and/or the fostering of tissue regeneration and remodelling, with the purpose been to replace, repair, maintain or enhance function".*

In the context of articular cartilage defects, three possible tissue engineering approaches are possible. The first approach has been the implantation of autologous chondrocytes that have been expanded in number *in vitro* into the defect together with a periosteal flap covering the defect. This approach, termed ACI (autologous chondrocyte implantation), is used mainly in chondral defects, where the technique has been reported to contribute to the structural repair within a goat model of a purely chondral defect (Dell'Accio *et al.*, 2003). After 3 weeks a dense layer of cells persisted within the defect, see Fig. 2.20 (a), however little or no type II collagen was

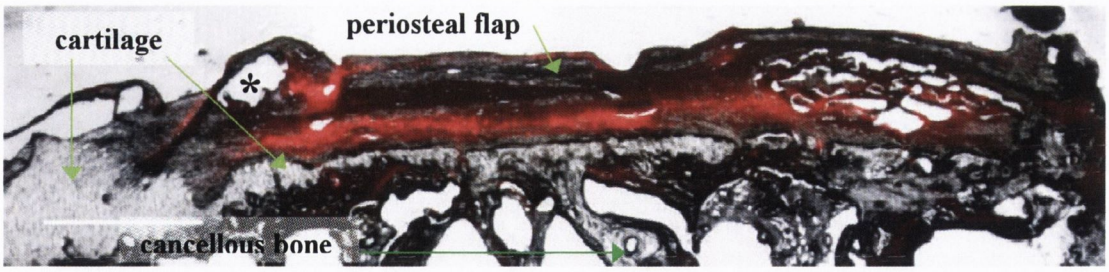

(a) Week 3: Red fluorescence indicates autologous chondrocytes are located between the underlying cartilage bed and the covering periosteal flap. Some cells are detected near a suture point (asterisk).

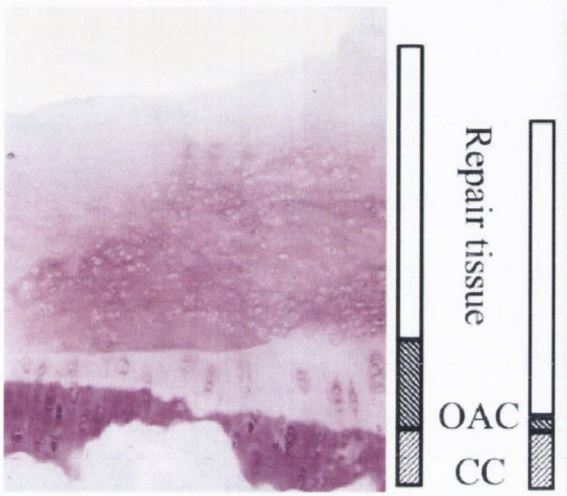

(b) Week 10: Toluidine blue staining of the repair tissue indicating the presence of sulphated proteoglycans within the repair tissue. OAC is the original articular cartilage, CC indicates calcified cartilage.

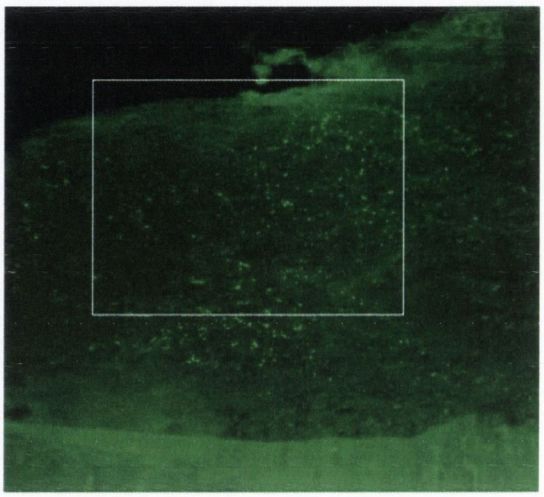

(c) Week 10: Green immunofluoresence for type II collagen. OAC is the original articular cartilage, CC indicates calcified cartilage.

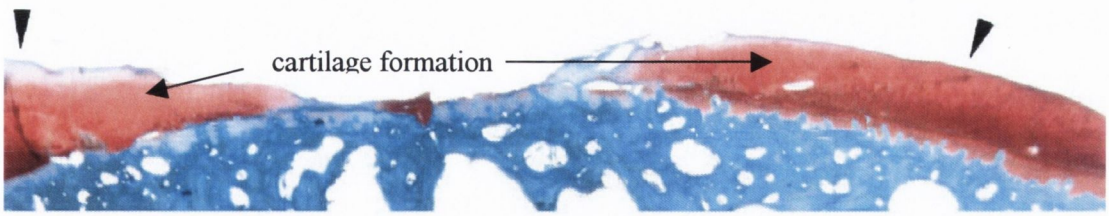

(d) Week 14: Safranin-O staining of the defect, indicating matrix formation. The black arrowheads indicate the margins of the defect.

Fig. 2.20 *Repair tissue in a goat model of ACI. Adapted from Dell'Accio et al., 2003.*

observed within the defect. However by week 10, significant amounts of proteoglycans and collagen type II was detected in the extracellular matrix, see Fig. 2.20 (b) and Fig. 2.20 (c). By week 14, partial delamination had occurred in the centre of the defect, see Fig. 2.20 (d), however the remaining repair tissue was rich inproteoglycans and the disposition of the collagen fibres was similar to that of normal articular cartilage.

The second approach involves inserting a cell-free or cell loaded scaffold into the defect with the aim of fostering the repair tissue formed by the bone marrow stem cells or the implanted cells to produce a superior repair tissue. Primarily chondrocytes (Niederauer *et al.*, 2000; Wakitani *et al.*, 1998; Rahfoth *et al.*, 1998; Liu *et al.*, 2002) or mesenchymal stem cells (Wakitani *et al.*, 1994), that have been loaded onto either collagen (Wakitani *et al.*, 1994, 1998) or agarose (Rahfoth *et al.*, 1998) gels, or a polymer material (Niederauer *et al.*, 2000; Liu *et al.*, 2002) have been employed. The results of all these studies have been variable. Mesenchymal cells loaded onto a collegen gel and inserted into an osteochondral defect were observed to differentiate into chondrocytes and produce a cartilage-like tissue, which was replaced with bone tissue over time without the loss of the overlying articular cartilage (Wakitani *et al.*, 1994). Indentation testing revealed that the repair cartilage was stiffer than the empty control defects, but less stiff than normal articular cartilage, see Table 2.1, indicating that a completely functional repair tissue was not achieved. Interestingly articular chondrocytes loaded onto the same collegen gel carrier and implanted into the same animal model resulted in a dramatically different repair tissue (Wakitani *et al.*, 1998). The chondrocytes produced a cartilage tissue; however no evidence of endochondral ossification, and hence bone formation, was observed in any region of the defect 48 weeks after transplantation. This indicated to Wakitani *et al.* (1998) that committed chondrocytes are inhibited from further linage progression; whereas mesenchymal stem cells are responsive to their biological and mechanical environment. However, in a separate study significant bone formation has been observed in smaller osteochondral defects 12 months after transplantation of chondrocytes loaded onto agarose gels (Rahfoth *et al.*, 1998). In this study a high degree of variability was observed in the results, which could be roughly classified into three groups. In the first group the repair tissue formed was similar to empty control defects, typically consisting of a narrow type II collagen positive region next to the bone, covered with

	Normal Cartilage	Defect	
		Posterior Portion	Anterior Portion
Bone marrow MSC's	5.2	11.5	15.1
Periosteum MSC's	3.8	8.9	18.8
Empty defect	4.2	21.7	41.2

Table 2.1. *Comparison of average compliance values for normal articular cartilage with the repair tissue in empty defects or defects implanted with cell-seeded collagen gels 24 weeks post-operatively. A lower compliance value indicates a stiffer tissue. Adapted from Wakitani et al. (1994).*

a type II negative connective tissue, see Fig. 2.21 (a). In the second group the repair tissue contained pronounced cartilaginous, cell-rich regions, however the superficial repair tissue was often fibrous in nature, see Fig. 2.21 (b). Surface degeneration was observed. In the third group the repair tissue was almost identical to normal articular cartilage, exhibiting the typical zonal structure of articular cartilage, see Fig. 2.21 (c).

The benifit of seeding scaffolds with cells prior to implantation is also questionable. Liu *et al.* (2002) found that seeding of polyglycolic acid scaffolds with autologous chondrocytes prior to implantation into a porcine model of an osteochondral defect improved the quality of the repair compared to defects repaired with cell free scaffolds. However Niederauer *et al.* (2000), using indentation testing and histology, revealed little differences in the repair tissues of osteochondral defects implanted with polylactide acid based scaffolds with or without pre-seeding of autologous chondrocytes. These polylactide acid based scaffolds differ mechanically from collagen or agarose gels, and polyglycolic acid scaffolds, in that they are much stiffer. In this particular study four different implants were manufactured, each consisting of two different phases, a chondral phase and a bone phase, glued together. The stiffness of the chondral phases was either 12 MPa or 32 MPa, while the stiffness of the bone phase varied from 0.3 MPa to 1080 MPa. A thin, fully dense film was glued to the articulating surface. These implants resulted in a repair tissue that is almost as stiff as normal cartilage in a goat model of the osteochondral defect (Niederauer *et al.*, 2000). Although no significant differences were observed between

(a) Control defect in the medial condyle 12 months after surgery. Fibrous tissue fills the defect with complete apposition to the residual cartilage only on the left side. Superficial degedradation and ossification protruding from the subchondral bone contribute to the loss of cartilage (arrow).

(b) Chondrocyte agarose filled defect in the medial chondyle 12 months after transplantation. On the right the cartilage has a cleft surface, and a loss of type II collagen. The black arrowheads indicate the margins of the defect.

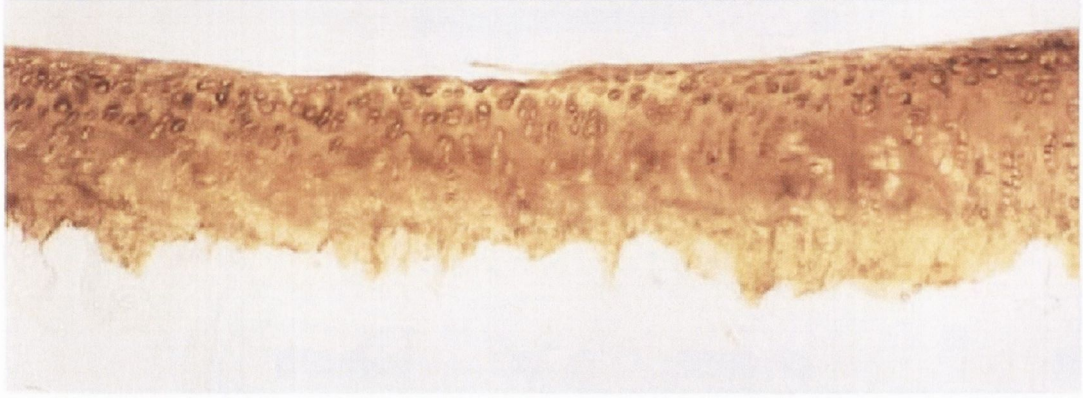

(c) Chondrocyte agarose-filled defect in the patellar groove 18 months after transplantation. Chondrocytes cluster into arrangements observed in normal articular cartilage.

Fig. 2.21 *Immunohistochemical staining for type II collagen in a rabbit model of osteochondral defect repair. Adapted from Rahfoth et al. (1998).*

the stiffness of the repair tissue for the four different implant types or for the addition/omission of chondrocytes to the scaffold prior to implantation, the implants with a stiffer cartilage phase ranked higher compared to less stiff implants when implanted into the chondyle of the knee, a high weight bearing area. In general safranin-O staining and cross-polarized light micrographs showed that a more articular cartilage-like tissue (collagen architecture etc.) formed in the chondyle than in the patellar groove, a low weight bearing area, see Fig. 2.22. Vertical fissures were often observed in the repair tissues, see Fig. 2.22 (a), however they were not accompanied by proteoglycan depletation, chondrocyte death or fibrillation of the articular surface, and were attributed to the fact that the goats were allowed to fully weight bear immediately after surgery. The relative success of this scaffold in maintaining the chondrogenic phenotype and producing a repair tissue with a zonal collagen structure similar to that in normal articular cartilage would suggest that a functional load-bearing scaffold is necessary to successfully repair osteochondral defects.

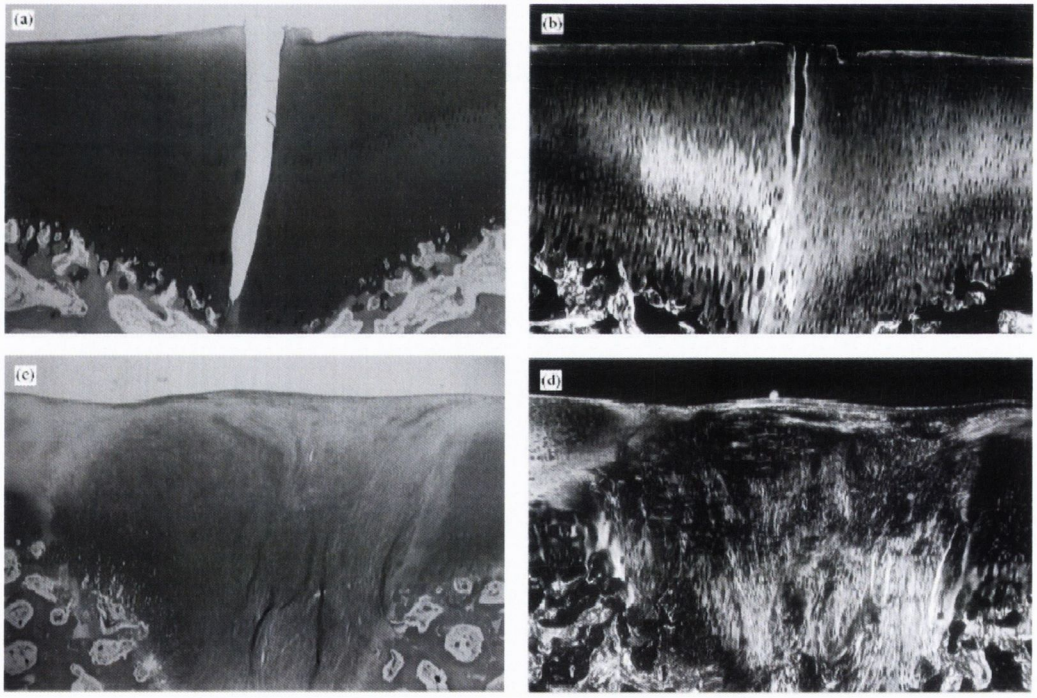

Fig. 2.22 *Histological appeareance near the center of an osteochondral defect in the chondyle (a & b) and patellar groove (c & d) after 16 weeks. (a) and (c): Safranin-O staining more intense in chondyle repair tissue compared to the patellar groove repair tissue. (b) and (d): Cross-polarized light micrographs showing a more articular–like collagen structure in the chondyle compared to the patellar groove. Taken from Niederauer et al. (2000).*

The third approach involves engineering a functional tissue *in vitro* before implantation into the defect, the idea been that such a functional tissue will be more suited to load bearing. By using scaffolds, growth factors, and bioreactors to carefully control the biochemical and biomechanical environment of cells in vitro, it has been possible to engineer a cartilage tissue that is rich in collagen type II and proteoglycans, and has mechanical properties approaching that of normal articular cartilage. For example, after 20 weeks in a static culture the aggregate modulus of engineered cartilage was reported to be 40% that of normal articular cartilage (Ma *et al.*, 1999). Rotating vessel bioreactors have been used to increase the GAG and collagen content of engineered cartilage, as well as the mechanical properties, over cartilage engineered in static culture (Vunjak-Novakovic *et al.*, 1999), see Fig. 2.23. Similar results have also been obtained with bioreactors that apply shear deformation (Waldman *et al.*, 2003a), compression (Buschmann *et al.*, 1995; Martin *et al.*, 2002) and hydrostatic pressure (Ikenoue *et al.*, 2003). These bioreactors have also been shown to produce a more homogenous tissue compared to static cultures (Vunjak-Novakovic *et al.*, 1999; Martin *et al.*, 2000). These improved properties have been attributed to enhanced mass transfer and direct mechanical stimulation of the chondrocytes to regulate their metabolism. In fact, chondrocyte matrix production has been shown to depend on both the magnitude and duration of the applied load (Ikenoue *et al.*, 2003). The specific mode of the applied force has also been shown to influence the mechanical and biochemical properties of engineered cartilage. Waldman *et al.* (2003a) demonstrated that shear forces produce a superior tissue (greater amounts of proteoglycans and collagen) compared to compression-stimulated cultures. Chondrocytes harvested from different regions of the tissue have also been shown to synthesise differing amounts of structural macromolecules (Waldman *et al.*, 2003b). Chondrocytes from the deep zone synthesised the most extracellular matrix, chondrocytes from the mid and deep zones accumulated the most amount of proteogylcan, and chondrocytes from full-thickness samples synthesised the most amount of collagen. Chondrocytes from the mid-and-deep zones produced tissue with superior mechanical properties to the tissues produced by cells from either the full thickness or deep zones of cartilage.

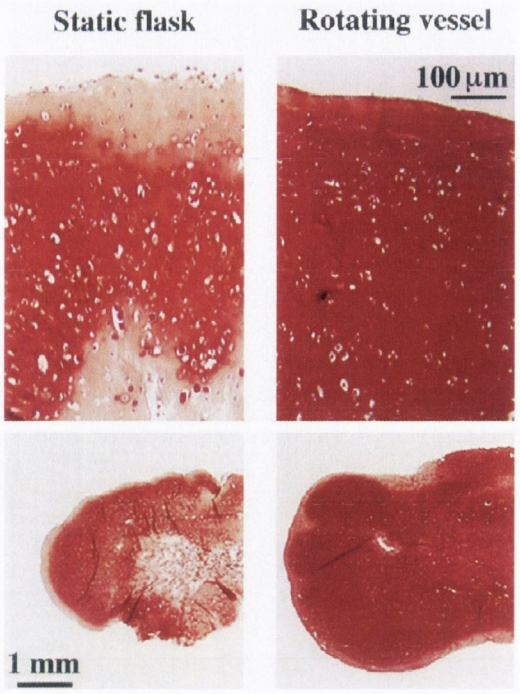

Fig. 2.23 *Chondrocyte-PGA constructs cultured for 6 weeks in either static flasks or rotating vessels. Constructs grown statically contained more extracellular matrix (stained red) peripherally than centrally. Adapted from Freed et al. (1998).*

Schaefer *et al.* (2002) implanted a tissue engineered cartilage construct, generated by bioreactor culture of chondrocytes seeded onto polyglycolic acid scaffolds, and combined with an osteoconductive support made of a ceramic/collagen sponge, into large osteochondral defects in the femoropatellar grove of adult rabbits. The engineered cartilage withstood physiological loading and remodelled into osteochondral tissue with characteristic architectural features and Young's moduli approaching that of normal articular cartilage 6 months after implantation. Whether or not such an engineered tissue will be stable in the long term has yet to be fully elucidated.

2.5 Conclusions

Many different theories have been put forward regarding mechano-regulated tissue differentiation. The contention of this thesis is that tissue differentiation is partially regulated by two mechanical stimuli - strain and fluid flow. To investigate this idea, the mechano-regulation theory of Prendergast *et al.* (1997), which has previously been used to simulate the time course of fracture healing (Lacoix *et al.*, 2002), will be

further developed to include different aspects of cellular behaviour not previously considered, and tested by attempting to simulate tissue differentiation during spontaneous osteochondral defect repair. Osteochondral defect repair is a complicated process, involving a cascade of cellular events beginning with dispersal and proliferation of mesenchymal stem cells and ending with mitosis and degradation of the repair tissue, all of which are involved in the tissue differentiation process. Only by incorporating all these different aspects of stem cell behaviour into a model of tissue differentiation can we hope to simulate osteochondral defect repair accurately. If that succeeds, the methodology could be used to evaluate tissue engineering strategies for improved cartilage repair.

Chapter 3

Methods

Contents

3.1 Introduction **45**

3.2 Development of the mechano-regulation model **45**

3.2.1 A model for cellular dispersal, mitosis and death *45*

3.2.2 A model of tissue differentiation *48*

3.2.3 Implementation of theory *51*

3.3 Modelling osteochondral defect repair **56**

3.3.1 Finite element model of an osteochondral defect *56*

3.3.2 Parameter variation study of diffusion coefficients *59*

3.3.3 Defect size and loading *59*

3.3.4 Repair tissue integration *60*

3.3.5 Cell mitosis *60*

3.4 Mechanical properties of tissue engineered cartilage **62**

3.4.1 Design and validation of rig *62*

3.4.2 Influence of tissue culture conditions *69*

3.5 Tissue engineering in osteochondral defect repair **71**

3.5.1 Modelling scaffolds used in defect repair *71*

3.5.2 Modelling tissue engineered cartilage used in defect repair *73*

3.6 Summary **75**

3.1 Introduction

Chapter 2 reviewed the computational models that have been developed to predict how mechanics can regulate tissue differentiation. In simplifying the task of modelling the tissue differentiation process, these models have neglected to include several aspects of stem cell biology that may be important in tissue differentiation. In this chapter, a theoretical model of tissue differentiation is derived which includes these aspects of stem cell biology. To test the validity of this mechano-regulation model, it will be used to simulate spontaneous osteochondral defect repair, where the mechanical stimuli are determined by finite element modelling. If successful in simulating spontaneous repair, the mechano-regulation model can then be used to evaluate how implanting an engineered tissue or a scaffold into an osteochondral defect will influence the repair process, and whether or not modulating the mechanical properties of these constructs would result in a more optimal repair.

Although the mechanical properties of normal articular cartilage and bone are well known, the mechanical properties of tissue engineered cartilage have been less well quantified. Since the accuracy of any finite element model depends upon precise knowledge of the mechanical properties, rigs to test tissue engineered cartilage in both confined and unconfined compression will be designed and fabricated, and used to determine the mechanical properties of tissue engineered cartilage.

3.2. Development of the mechano-regulation model

3.2.1 A model for cellular dispersal, mitosis and death

The exact mechanism by which mesenchymal cells disperse throughout tissues of different phenotypes remains unclear. As discussed in Section 2.2.2, Murray (1989) has suggested that cell dispersal could be approximated using a diffusion equation:

$$\frac{\partial c}{\partial t} = D\nabla^2 c, \qquad \text{(Eqn. 3.1)}$$

where c is the cell concentration, D is the diffusion coefficient, t is time and ∇ is the gradient operator. Since these mesenchymal stem cells can differentiate into cells of different phenotypes i (i.e. fibroblasts, chondrocytes and osteoblasts) that produce

different connective tissues j (i.e. fibrous tissue, cartilage and bone), a logical progression of this idea would be that the diffusion coefficient D would depend on the cell phenotype i and the tissue type j through which the cell is moving. The rate of change in the number of cells might also be expected to increase due to mitosis, or decrease due to cell death. Combining these two ideas, the dispersal of cells of a particular phenotype i can be simulated by assuming the cell population to be described by diffusive, proliferative and apoptotic processes as follows:

$$\frac{dn^i}{dt} = D^i \nabla^2 n^i + P^i(S) n^i - K^i(S) n^i, \qquad \text{(Eqn. 3.2)}$$

where n^i denotes the number of cells of type i, D^i is the diffusion coefficient for cell type i, $P^i(S)$ is a proliferation rate and $K^i(S)$ is a death rate for cell i as a function of the biophysical stimulus S. The diffusion coefficient for cell type i moving through a volume of tissue is calculated as the weighted average of the diffusion coefficients for each of the tissue types j present at that particular site, i.e.

$$D^i = \sum_{j=1}^{n_t} D_{ij} \phi_j, \qquad \text{(Eqn. 3.3)}$$

where D_{ij} is the diffusion coefficient for cell type i in tissue j, and n_t is the total number of tissue types, in this case granulation tissue, fibrous tissue, cartilage and bone. ϕ_j denotes the volume fraction of each tissue type j such that:

$$\sum_{j=1}^{n_t} \phi_j = 1. \qquad \text{(Eqn. 3.4)}$$

As the cells disperse throughout the tissue, their number will increase due to proliferation, or decrease due to cell death. The proliferative response of each cell type might be expected to be influenced by their local environment such that the rate of change in the number of cells n^i of the i^{th} type depends on $P^i(S_o)$, the proliferation rate for cell type i as a function of a mechanical stimulus S_o, and $K^i(S_o)$, the cell death rate for cell type i as a function of a mechanical stimulus S_o.

A review of the literature on mechano-regulated mitosis (Chapter 2.3) revealed no clear relationship between strain and cell proliferation. The most consistent conclusion that could be drawn from the literature review was that relatively high magnitudes of strain were seen to increase cellular proliferation, usually in combination with a dedifferentiation into a fibroblast-like cell. However the literature review also revealed that very high magnitudes of stress or strain resulted in cell death, which increased in a dose dependant manner with the applied load. Based on these findings, a quadratic relationship will be assumed between cell proliferation/death and strain S_o such that we can write:

$$P^i(S_o)n^i - K^i(S_o)n^i = a + bS_o + cS_o^2. \qquad \text{(Eqn. 3.5)}$$

This idea is presented graphically in Fig. 3.1. Equation 3.5 can then be expressed for each cell type i in matrix form as follows:

$$\frac{d}{dt}\begin{Bmatrix} n^{mesenchymal} \\ n^{fibroblast} \\ n^{chondrocyte} \\ n^{osteoblast} \end{Bmatrix} = \begin{bmatrix} a_{mesenchymal} & b_{mesenchymal} & c_{mesenchymal} \\ a_{fibroblast} & b_{fibroblast} & c_{fibroblast} \\ a_{chondrocyte} & b_{chondrocyte} & c_{chondrocyte} \\ a_{osteoblast} & b_{osteoblast} & c_{osteoblast} \end{bmatrix} \begin{Bmatrix} 1 \\ S_o \\ S_o^2 \end{Bmatrix}. \qquad \text{(Eqn. 3.6)}$$

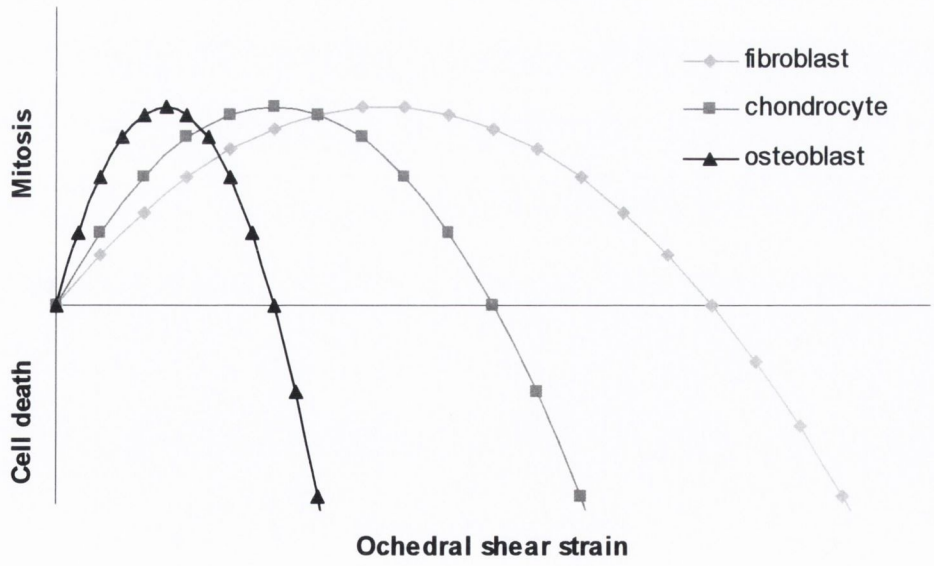

Fig. 3.1. *Quadratic relationship assumed between shear strain and cellular mitosis and death.*

3.2.2 A model of tissue differentiation

As cells disperse throughout the tissue, they will differentiate into different cell phenotypes. Prendergast *et al.* (1997) proposed that this differentiation process is regulated by two mechanical stimuli, the tissue shear strain γ and the interstitial fluid flow v. The values of these two stimuli can be combined mathematically to obtain a stimulus for differentiation S, where

$$S = \frac{\gamma}{a} + \frac{v}{b}, \qquad \text{(Eqn. 3.7)}$$

a and b are empirical constants (Huiskes *et al.*, 1997). Depending on the value of the stimulus for differentiation S, the mesenchymal stem cell pool will differentiate into different cell phenotypes. As loading is applied to the regenerating tissues, one could hypothesis four different outcomes. Firstly, if the mechanical stimulus is high, the value for S will be high, and fibrous tissue formation will occur and persist unless the regenerating region is sufficiently stabilised. Secondly if the stimulus is low, bone formation will occur through direct intramembranous ossification. Intermediate values of S will either lead to cartilage formation that persists, or merely stabilises the regenerating region of the tissue to allow for endrochondral ossification. This concept was refined by Lacroix and Prendergast (2002) by separating the bone forming field into an immature woven bone field and a mature woven bone field, and by adding a bone resorbtion field to account for the fact that low levels of loading result in bone loss. These concepts can be encapsulated into a mechano-regulation diagram (Fig. 3.2), or expressed mathematically as follows. If

$0 \; [\; S < n_{\text{resorbtion}}$	osteoclast: bone resorbtion	
$n_{\text{resorbtion}} \; [\; S < n_{\text{mature}}$	osteoblast: mature woven bone	
$n_{\text{mature}} \; [\; S < 1$	osteoblast: immature woven bone	
$1 \; [\; S < m$	chondrocyte: cartilage	
S / m	fibroblast: fibrous connective tissue	(Eqn. 3.8)

where $n_{\text{resorbtion}}$, n_{mature} and m represent boundaries of the mechano-regulation diagram.

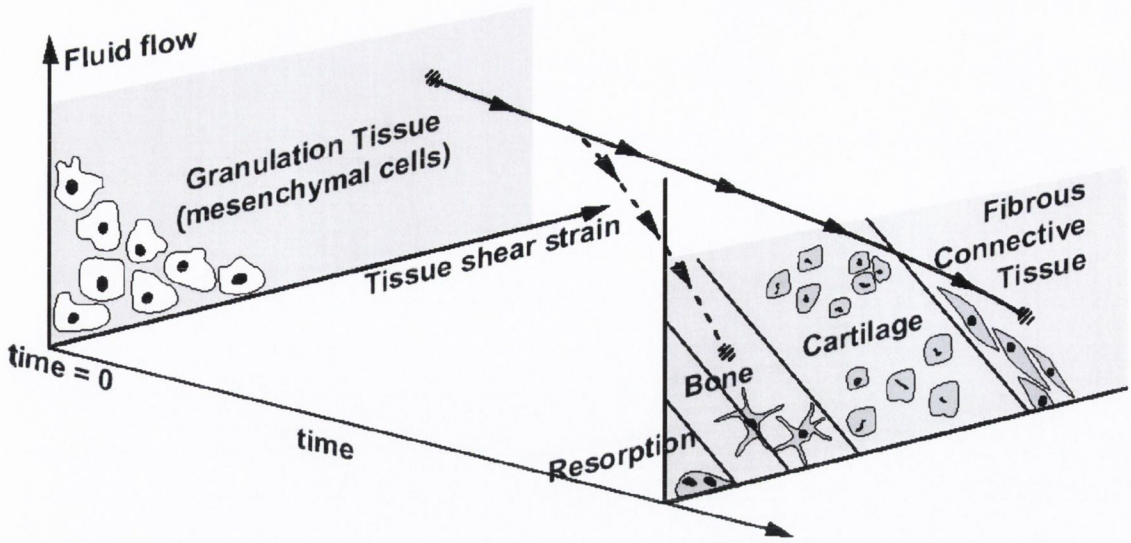

Fig. 3.2. *The mechano-regulation concept first proposed by Prendergast et al (1997), and adapted by Lacroix and Prendergast (2002) to account for bone resorbtion and two separate bone fields, immature woven bone and mature woven bone.*

Therefore mesenchymal stem cells can differentiate into fibroblasts, chondrocytes, osteoblasts or osteocytes and produce (or remove in the case of osteoclasts) fibrous tissue, cartilage tissue or bone tissue respectively based on the local mechanical stimuli. However the differentiation process is not instantaneous. For example, mesenchymal stem cells do not instantaneously differentiate into chondrocytes, replacing granulation tissue immediately with cartilage tissue. Rather this process occurs over an unknown period of time, with mesenchymal cells differentiating into chondrocytes, which gradually begin to synthesise the extracellular proteins that constitute cartilaginous tissue. Also, as the differentiated cell begins to synthesise new proteins, the material properties of the regenerating tissue will be expected to change. We can account for these phenomena by modelling the tissue differentiation process as an iterative procedure.

Schematic illustration of the tissue differentiation process

Consider a small volume of repairing tissue. At the beginning of the first iteration this volume of tissue consists entirely of granulation tissue infiltrated by mesenchymal stem cells (Fig. 3.3).

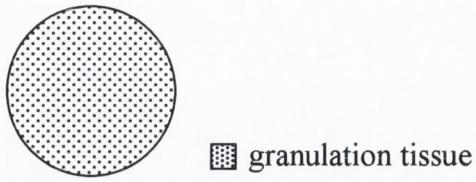

Fig. 3.3. *A region containing granulation tissue.*

Say the stimulus for differentiation after the first iteration is towards chondrogenesis. All the tissue in the region does not differentiate directly into cartilage, rather it can be thought of as a mixture of granulation tissue and cartilage tissue (Fig. 3.4).

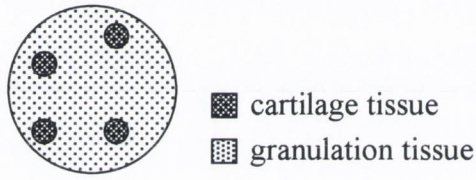

Fig. 3.4. *A region containing both cartilage and granulation tissue.*

Now say after a second iteration the stimulus within the volume of tissue is towards fibrous tissue formation. The volume of tissue can now be thought of as a mixture of granulation tissue, fibrous tissue and cartilage tissue (Fig. 3.5).

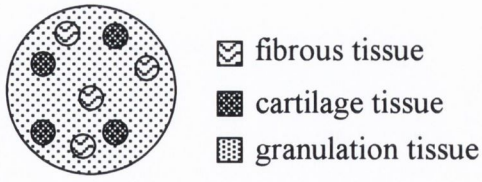

Fig. 3.5. *A region containing fibrous, cartilage and granulation tissue.*

It will be assumed here that only if the stimulus for differentiation is consistent for n iterations will all the tissue in the region completely change from one phenotype into another (Fig. 3.6).

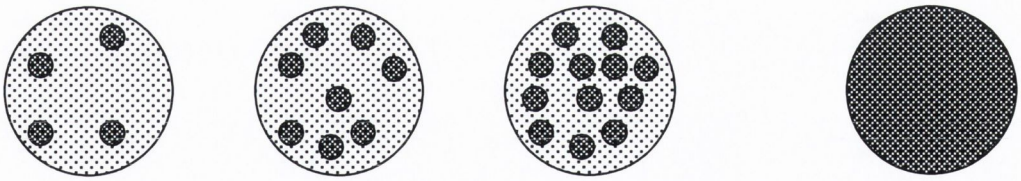

Fig. 3.6. *A region containing all cartilage tissue after n iterations.*

The tissue type predicted in the model are stored in an array T of dimension n, where the values of T are either granulation tissue, fibrous tissue, cartilage, immature woven bone or mature woven bone. At the beginning of the first iteration every value in the array is set to granulation tissue. After n iterations granulation tissue is replaced by a mixture of differentiated tissues such that

$$T = [T_1, T_2 \ldots\ldots T_{n-1}, T_n] , \qquad \text{(Eqn. 3.9)}$$

where T_n is a particular tissue phenotype j (either granulation tissue, fibrous tissue, cartilage, immature woven bone or mature woven bone). Therefore the volume fraction ϕ_j of a particular tissue type j can be expressed as

$$\phi_j = \frac{1}{n}(\text{number of times tissue type j appears in array T}). \qquad \text{(Eqn. 3.10)}$$

3.2.3 Implementation of theory

Implementing this theory required certain assumptions to be made. These assumptions will be outlined below before explaining how the theory was written into an algorithm.

Diffusion Equation

To the author's knowledge, no work to date has attempted to measure cell velocities, and hence diffusion coefficients, *in vivo*. However certain estimates can be made based on common observations. For example it is known that chondrocytes have limited diffusive abilities when embedded in mature cartilage. Comparisons of cartilage defect repair in chondral and osteochondral defects also show that

mesenchymal stem cells can travel with relative ease through granulation tissue, but cannot penetrate the subchondral bone. Obviously the mechanism by which an individual cell travels through these tissues cannot be explained by simple diffusion, rather the net outcome of the movement of a population of cells can. As a first approximation the diffusion coefficient is assumed to be the same for each cell phenotype *i* passing through a particular tissue type *j*. Therefore:

$$D_{\text{mesenchymal,j}} = D_{\text{fibroblast,j}} = D_{\text{chondrocyte,j}} = D_{\text{osteoblast,j}}.$$

The values for $D_{i,granulation}$, $D_{i,fibrous}$, $D_{i,cartilage}$, $D_{i,bone}$ are given in Table 3.1.

Mitosis and cell death

Only under the application of large strains has increased proliferation been observed in a selection of different cell types, however this was accompanied by a de-differentiation of the osteoblast-like cells into fibroblast-like cells (Jones *et al.*, 1991). As a first approximation it will be assumed that only fibroblasts will have a strain dependent relationship between proliferation and mitosis, and that the proliferation of all other cell phenotypes is independent of strain such that equation 3.6 can be written as:

$$\frac{\mathrm{d}}{\mathrm{d}t}\begin{Bmatrix} n^{mesenchymal} \\ n^{fibroblast} \\ n^{chondrocyte} \\ n^{osteoblast} \end{Bmatrix} = \begin{bmatrix} a_{mesenchymal} & 0 & 0 \\ a_{fibroblast} & b_{fibroblast} & c_{fibroblast} \\ a_{chondrocyte} & 0 & 0 \\ a_{osteoblast} & 0 & 0 \end{bmatrix} \begin{Bmatrix} 1 \\ S_o \\ S_o^{\,2} \end{Bmatrix}, \qquad \text{(Eqn. 3.11)}$$

where $a_{\text{mesenchymal}} = a_{\text{chondrocyte}} = a_{\text{osteoblast}} = 0.05$, $a_{\text{fibroblast}} = 0$, $b_{\text{fibroblast}} = 2.667$, $c_{\text{fibroblast}} = -17.778$.

Tissue Differentiation

The values of the empirical constants of equation 3.7, as well as the boundaries of the mechano-regulation diagram for tissue differentiation (equation 3.8), are taken to be the same as those used by Huiskes *et al.* (1997) in a simulation of interfacial tissue repair and Lacroix *et al.* (2002) in a simulation of fracture healing. Therefore $a = 3.75$

%, $b = 3$ μms^{-1}, $n_{resorbtion} = 0.01$, $n_{mature} = 0.53$ and $m = 3$. The corresponding mechano-regulation diagram is shown in Fig. 3.7.

As cells differentiate and produce new extracellular matrix, the material properties of the regenerating tissue will change. The material properties of a volume of tissue are calculated based on the volume fraction ϕ_j of each tissue type within the region of tissue and the total number of cells n_c within that region. The volume fraction ϕ_j (Equation 3.10) is computed based on the previous 10 iterations of the model. If this volume of tissue represented a single element in a finite element model of an osteochondral defect, the Young's modulus of any element within a finite element model would be calculated as:

$$E = \frac{(n_c^{max} - n_c)}{n_c^{max}} E_{granulation} + \frac{n_c}{n_c^{max}} \sum_{j=1}^{n_t} E_j \phi_j , \qquad \text{(Eqn. 3.12)}$$

where n_c^{max} is the maximum number of cells that can occupy any one element, and E_j is the Young's Modulus of the j^{th} tissue phenotype. Similar equations can be used to determine the permeability, Poisson's ratio, porosity and compressive moduli.

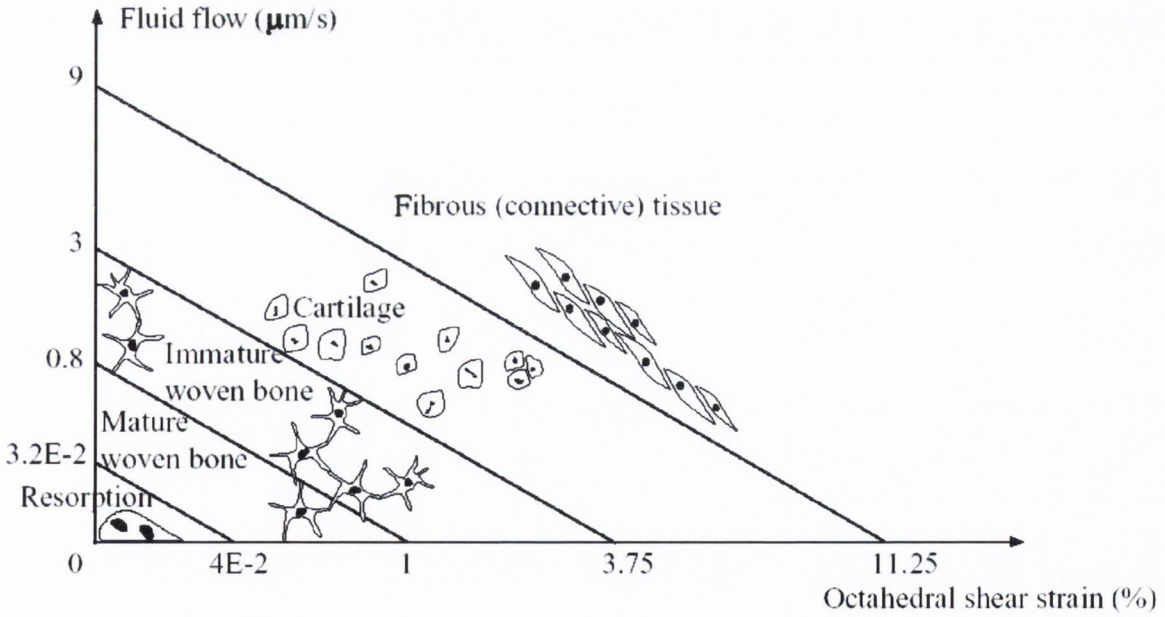

Fig. 3.7. *The mechano-regulation diagram controlling tissue differentiation (not drawn to scale).*

Algorithm

Each of these cellular events was implemented into an algorithm, a graphical summary of which is presented in Fig. 3.8. A finite element mesh is first inputted into the algorithm. Cell dispersal is determined by solving the diffusion equation based either on the initial cell distribution or from that calculated by the previous iteration of the model. Cell mitosis and cell death in any one element is then determined based on the mechanical stimuli determined from the previous iteration of the model. These stimuli are calculated by running a poroelastic structural finite element analysis. Based on the magnitudes of the octahedral shear strain and the interstitial fluid flow, a new tissue phenotype is determined for each element within the model, which is recorded into an array containing the phenotypes predicted in the previous 10 iterations of the model (Eqn. 3.9). Based on the volume fraction of each tissue type present within any one element, and the number of cells within that element, the material properties for the next iteration are determined. This algorithm is iterated until convergence of tissue phenotype is achieved.

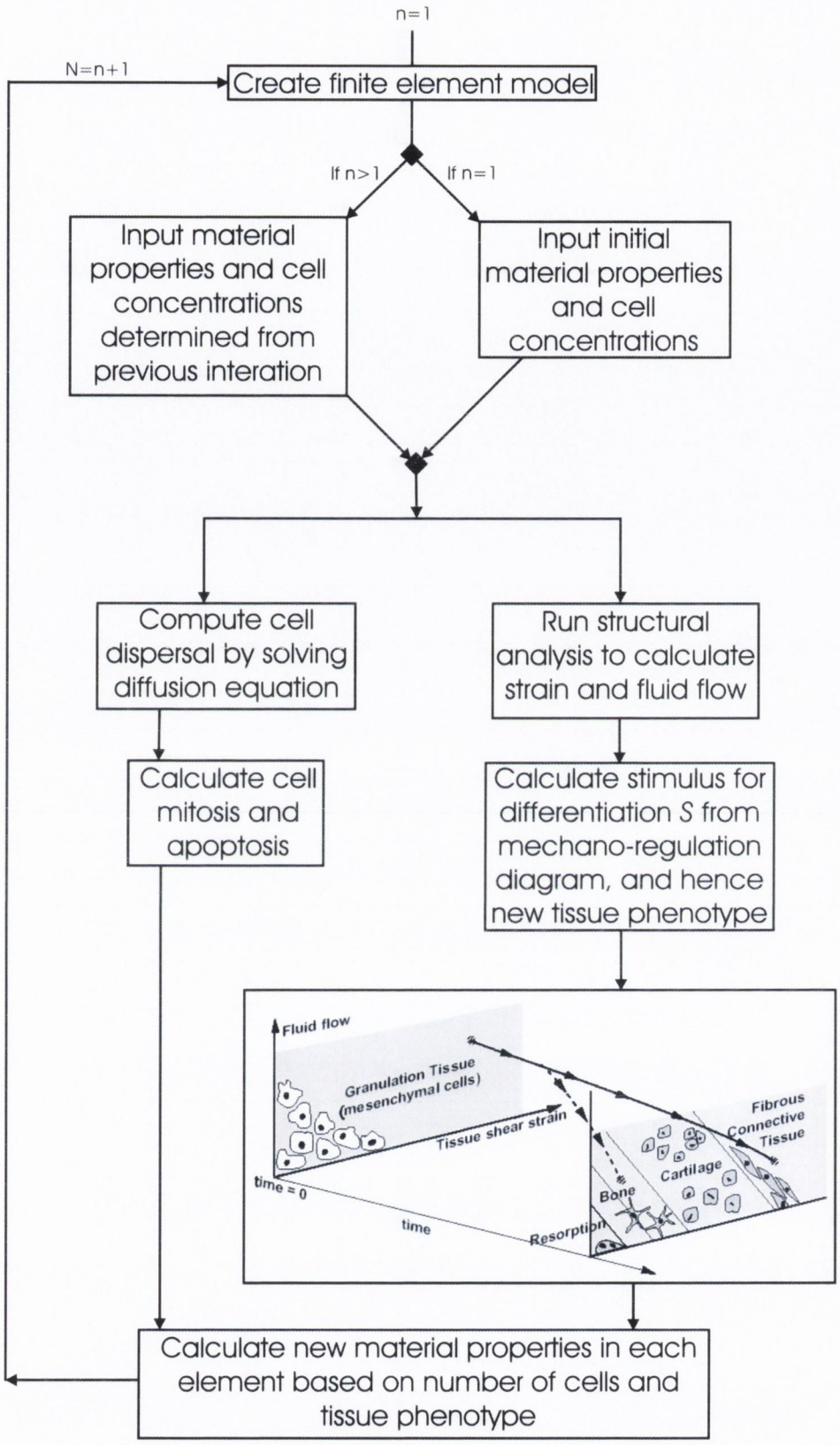

Fig. 3.8 *Flow chart diagram of computational algorithm to model cell dispersal, proliferation, differentiation and death.*

3.3. Modelling osteochondral defect repair

3.3.1 Finite element model of an osteochondral defect

As mentioned in the introduction to this chapter, the finite element method will be used to determine the mechanical stimuli within an osteochondral defect. The poroelastic theory first developed by Biot (1940) has been refined to model the viscoelastic behaviour of articular cartilage (Mow *et al.*, 1980) and bone (Cowin, 2000). A poroelastic element is available within the commercial finite element package DIANA (TNO, Delft, The Netherlands), which can be used to solve the poroelastic equations for complex geometries and loadings. Constitutive equations similar to those developed by Biot (equation 2.16 & 2.19) are used to relate the stress to the strain. Finite strain can also be implemented in DIANA by using a total or updated Lagrange formulation.

The Q term in equation 2.19 has been named the Biot material parameter. In the case of a compressible solid and fluid phase allowable in DIANA, it is related to the compressibility of the solid and fluid phases by the relation

$$\frac{1}{Q} = \frac{n}{K_f} + \frac{1-n}{K_s} \qquad \text{(Eqn. 3.13)}$$

where K_f and K_s are the intrinsic compressive modulus of the solid and fluid phases respectively. Therefore six parameters are required to completely describe a poroelastic, compressible isotropic model – the two intrinsic compressive moduli as well as the Young's modulus, the permeability, the Poissons's ratio and the porosity.

An axi-symmetric finite element model of the knee was created which included a meniscus, a femoral chondyle and an articular cartilage layer (Fig. 3.9) using Diana (TNO, Delft, The Netherlands). The cartilage layer had a thickness of 2 mm and was assumed to be uniform across the femoral chondyle. The femoral chondyle was approximated as a flattened semi-sphere of radius 20 mm, consisting of a 1 mm deep layer of cortical bone overlaying a dense cancellous bone. The tibial plateau was modelled as a rigid contact layer, the permeability of which was assumed to be the same as cartilage. The model was restrained radially along the axis of

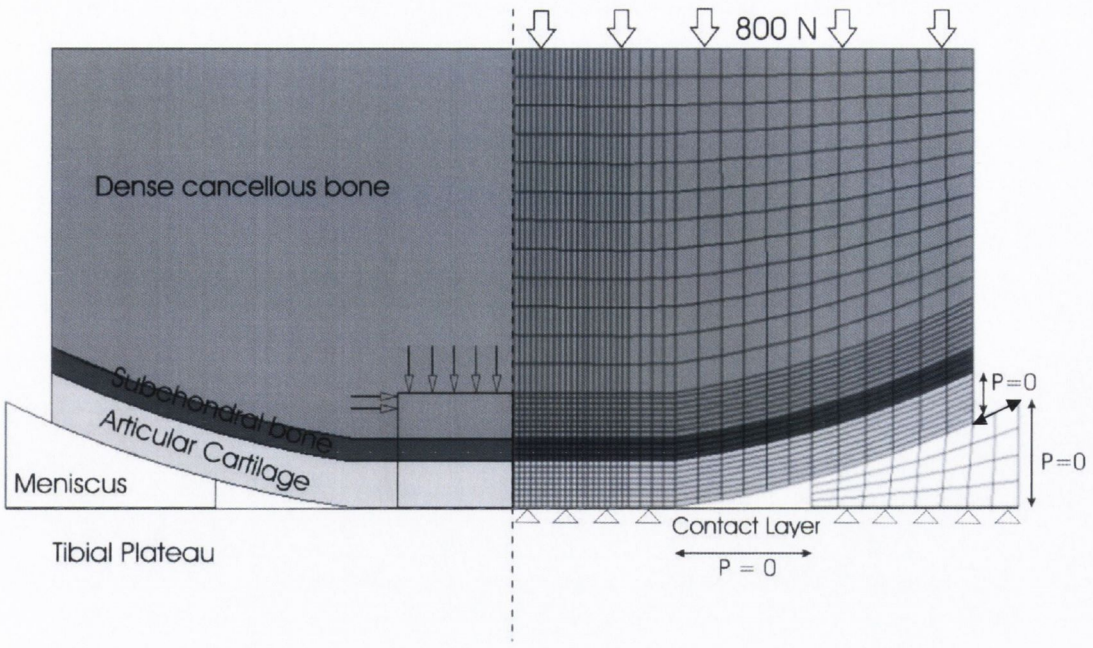

Fig. 3.9 *Axi-symmetric finite element model of the knee with an osteochondral defect. Right: Finite element mesh illustrating loading and boundary condition. Left: 5mm defect (box) showing origin of mesenchymal stem cells (arrows).*

rotation, and in the axial direction as shown in Fig. 3.9. The pore fluid pressure is set to zero at free cartilage surfaces (Fig. 3.9).

The applicability of using an axi-symmetric finite element model to study the knee has been addressed by a number of researchers. A similar axi-symmetric finite element model of the knee to the one introduced here was developed by van Lankveld (1994), whereby the meniscus and the tibial cartilage layer were modelled as bi-phasic with a linear elastic solid phase, and the femur was modelled as a rigid. The model was partially validated by comparing the results of the model to experimental results from a porous polyurethane model of the knee joint. Spilker *et al.* (1992) used an axi-symmetric transversely isotropic biphasic finite element model to determine maximum strains in the meniscus under physiological loading, and more recently a similar finite element model which also included the tibial plateau and femoral chondyle was used by Wilson *et al.* (2003) to study the effects of a meniscectomy on cartilage damage, where the finite element model was validated with data from clinical studies.

A full thickness defect is incorporated into the finite element model. The defect is 5mm in diameter and 5mm in depth. The geometry was meshed using the poroelastic elements described in the previous section.

To assess the influence of mesh density on the predicted results, three mesh densities were used to model the defect, a coarse mesh consisting of 400 elements, a intermediate mesh density consisting of 1600 elements and a fine mesh consisting of 3600 elements. Complete integration was assumed between the repair tissue and the host tissue. An axial ramp load of 800 N was applied over 0.5 seconds.

The material properties for the different tissue types used in this model are given in Table 3.1. The values are the same as those used by Lacroix and Prendergast (2002) in a model of fracture healing. The only material property that is different is the value used for the permeability of woven bone. Lacroix and Prendergast (2002) used a value of 3.7 3 10^{-13} m^4/Ns for mature woven bone, and a value of 1.0 3 10^{-13} m^4/Ns for immature woven bone. However lower values are used for both mature (3.7 3 10^{-15} m^4/Ns) and immature woven bone (1.0 3 10^{-15} m^4/Ns) in this model for two reasons. Firstly the cancellous bone in the femoral chondyles is denser than in other regions of the femur, which would reduce the permeability, and secondly the experiments used to determine the permeability of cancellous bone routinely remove the marrow before testing, which would increase the value of permeability obtained. All tissues were modelled as linear elastic, except for the meniscus which was modelled as transversely isotropic. The Young's modulus of the meniscus was set to 100MPa in the circumferential direction, and 0.5 MPa in the axial and radial directions.

Table 3.1 *Material properties of tissues.*

	Granulation tissue	Fibrous tissue	Cartilage	Immature bone	Mature bone	Cortical bone
Young's modulus (MPa)	0.2	2	10	1000	6000	17000
Permeability ($m^4/Ns \times 10^{-14}$)	1	1	0.5	0.1	0.37	0.001
Poisson's ratio	0.167	0.167	0.167	0.3	0.3	0.3
Porosity	0.8	0.8	0.8	0.8	0.8	0.04
Solid compression modulus (MPa)	2300	2300	3400	13920	13920	13920
Fluid compression modulus (MPa)	2300	2300	2300	2300	2300	2300
Diffusion co-efficient (mm^2/iteration)	0.8	0.1	0.05	0.01	0.01	-

The diffusion equation was solved using the diffusion element Q4AHT in Diana (TNO, Delft, The Netherlands). The origin of the mesenchymal stem cells was assumed to be the base of the defect (see arrows on left hand side of Fig. 3.9). A diffusion coefficient of 0.8 mm^2/iteration was chosen for the granulation tissue since it gave a steady-state cell concentration after approximately 14 iterations (or two weeks assuming each iteration corresponds to a day). The diffusion coefficients chosen for the other tissues are given in Table 3.1.

3.3.2 Parameter variation study of diffusion coefficients

In this study the diffusion coefficient for each tissue type was a best estimate, since such cell diffusion coefficients have yet to be measured. Therefore a parameter variation study will be performed to study the influence of the diffusion coefficient of each tissue type on the predictions of the mechano-regulation model[1]. A higher and lower diffusion coefficient was chosen for each tissue type, see Table 3.2. For most cases the diffusion coefficient was only changed for one material at a time.

Table 3.2 *Diffusion co-efficient (in mm^2/iteration) parametric variation study.*

	Granulation tissue	Fibrous tissue	Cartilage	Immature bone	Mature bone
Normal	0.8	0.1	0.05	0.01	0.01
High 1	1.5	0.3	0.2	0.1	0.1
Low 1	0.1	0.01	0.01	0.001	0.001

3.3.3 Defect size and loading

To investigate the influence of defect size on osteochondral defect repair, finite element models of a 7mm defect and a 9 mm defect were also created (Fig. 3.10). A load of 800N was applied to each of these models as done in the 5mm defect.

[1] A detailed parameter variation study was performed by Lacroix (2001) to study how the material properties used in a finite element model of fracture healing will influence the predictions of the mechano-regulation concept of Prendergast et al (1996). This study found that increasing the modulus or reducing the permeability of the soft tissues would reduce the mechanical stimuli during the simulation of fracture healing earlier, while reducing the modulus or increasing the permeability of the soft tissues could lead to fracture healing been prevented or the model not converging. Varying the Poisson's ratio, permeability, or the solid and fluid compression moduli had little effect on the predicted patterns of tissue differentiation.

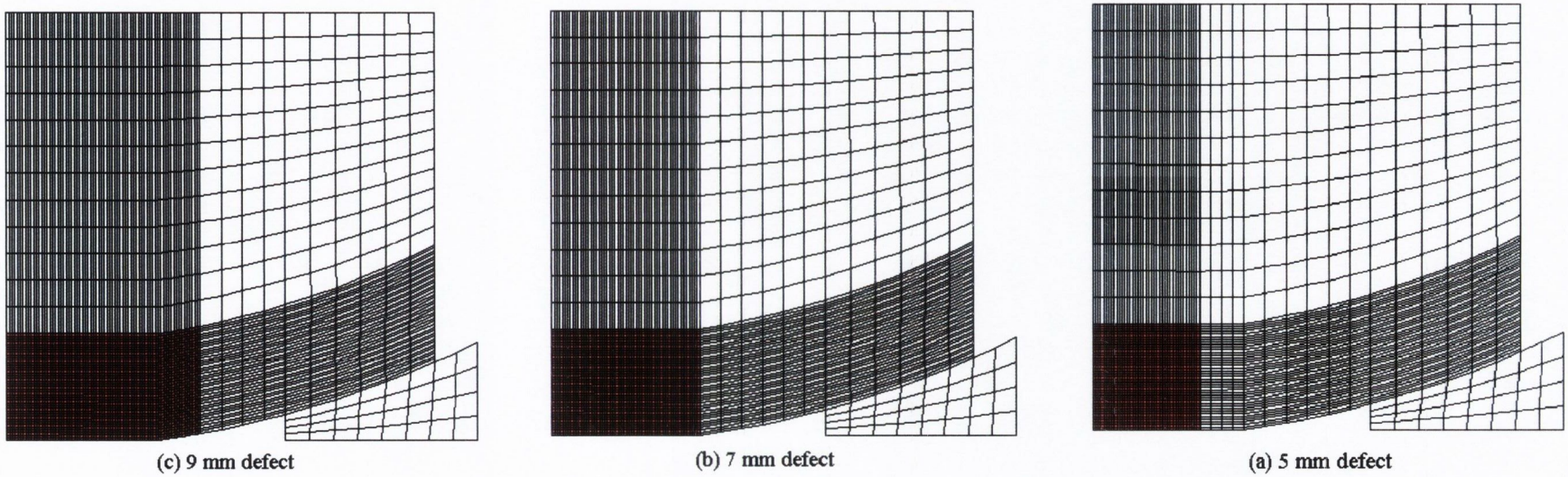

Fig. 3.10 Axi-symmetric finite element mesh of the 5 mm, 7 mm and 9 mm osteochondral defects.

The influence of loading magnitude was also examined by applying two different loads to each of the defects, a lower load of 500N, and a higher load of 1100N.

3.3.4 Repair tissue integration

The finite element model assumes complete integration between the repair tissue and the normal tissue. In osteochondral defect repair this is often not the case. To study how incomplete or partial integration between the repair tissue and the normal tissue will influence the predictions of the mechano-regulation model, the integration of the repair tissue with the normal tissue was modelled with interface elements (Diana L8IF elements). These elements require two input material properties. A normal stiffness that sets the relation between the normal traction and the normal relative displacement and a shear stiffness that sets the relation between the shear traction and the shear relative displacement. Poor integration was modelled by allowing relative displacement between the repair and normal tissue in the shear direction only. This was achieved by setting the shear stiffness set to a low value and the normal stiffness to a high value.

3.3.5 Cell mitosis

According to Murray (1989), the rate of cell proliferation would be expected to decrease in regions of high cell density due to limitations in space, nutrient diffusion or resources. To account for this expected reduction in proliferation, two different modelling approaches were investigated. Firstly the ability of cells to proliferate was removed after 30 iterations, such that Equation 3.2 reduces to:

$$\frac{dn^i}{dt} = D^i \nabla^2 n^i - K^i(S) n^i . \qquad \text{(Eqn. 3.14)}$$

The second approach involves linearly reducing cellular proliferation as the concentration of cells increases such that Equation 3.2 becomes

$$\frac{dn^i}{dt} = D^i \nabla^2 n^i + \frac{(n^{max} - n^{tot})}{n^{max}} P^i(S) n^i - K^i(S) n^i , \qquad \text{(Eqn. 3.15)}$$

where n^{tot} is the total number of cells in any one element, and n^{max} is the maximum number of cells permissible in any one element.

3.4 Mechanical properties of tissue engineered cartilage

The mechanical properties of tissue-engineered cartilage are not the same as normal articular cartilage. A review of the literature revealed that the mechanical properties of tissue-engineered cartilage vary considerably, depending on a multitude of reasons. Based on this finding it was decided to conduct a series of experiments to accurately determine the influence of culture conditions on the mechanical properties of tissue engineered cartilage. The methodologies used to determine these mechanical properties are the subject of this section of the chapter.

3.4.1 Design and validation of rig

The most common mechanical tests of normal or tissue engineered cartilage are the confined compression, unconfined compression and indentation test, see Fig. 3.11. The confined compression test consists of radially confining a sample of cartilage and compressing it using a porous indentor that allows fluid to pass through it during the compression phase. The unconfined compression test consists of compressing a sample of cartilage between two frictionless plates, where the sample is allowed to bulge radially. Both tests typically consist of applying a ramp displacement to a plug of cartilage and holding the displacement for a period of time. Under this loading condition the reaction force increases to a maximum and then relaxes to an equilibrium value. The rise and relaxation of the reaction force is measured during the test. When the force equilibrates, the aggregate or compressive modulus H_a of the tissue is defined as the equilibrium reaction force from the confined compression test divided by the area of the sample, while the Young's modulus E_s of the tissue is defined as the equilibrium reaction force from the unconfined compression test divided by the area of the sample.

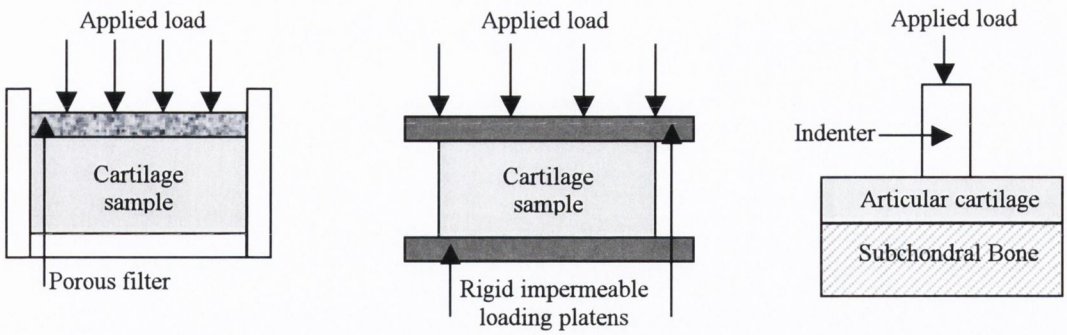

(a) Confined compression (b) Unconfined compression (c) Indentation

Figure 3.11. *Schematics of three testing configurations frequently used to study the compressive behaviour of articular cartilage. (a) In the confined compression test, the sample is radially confined and compressed via a porous indenter. (b) In the unconfined compression test, the sample is free to bulge radially and is compressed via two impermeable platens. (c) An indentation test, which is commonly used to test articular cartilage in vivo.*

A better estimate of both the aggregate modulus and the Young's modulus can be obtained by applying a series of ramp displacements to the cartilage, and determining the corresponding equilibrium reaction force after each loading increment to obtain an equilibrium stress-strain curve – the slope of this curve gives modulus. Knowing both the aggregate modulus (confined compression test) and the Young's modulus (unconfined compression) allows for a calculation of the Poisson's ratio (v_s) using the relationship (Korhonen *et al.*, 2002):

$$H_a = \frac{E_s(1-v_s)}{(1+v_s)(1-2v_s)} \qquad \text{(Eqn. 3.16)}$$

Rigs were designed and manufactured to test normal and tissue engineered cartilage in both these testing modes. Finally it is possible to estimate the permeability of normal or tissue-engineered cartilage by fitting the force vs. time curve from a confined compression test to the biphasic equations for soft tissues in confined compression, as written by Mow *et al.* (1980). For a slow compression rate problem,

defined by the inequality $t_0 >> \frac{h^2}{H_a k}$, the stress rise ($0 < t < t_0$) due to the application of a ramp displacement is given by the expression (Mow *et al.*, 1984, 1990):

$$\sigma_c(t) = H_a \varepsilon_0 \left(\frac{t}{t_0} + \frac{1}{3} \frac{h^2}{H_a k_0 t_0} e^{-M\varepsilon_0 \frac{t}{t_0}} + \ldots \right), \qquad \text{(Eqn. 3.17)}$$

while the stress response during the initial period of relaxation ($t > t_0$) is given by:

$$\sigma_c(t) = \sigma_c\big|_{t=t_0} - H_a \varepsilon_o \frac{2}{\sqrt{\pi}} \sqrt{\frac{h^2}{H_a k_0 t_0 \exp(M\varepsilon_o)} \left(\frac{t}{t_0} - 1 \right)} + \ldots \,, \qquad \text{(Eqn. 3.18)}$$

where the intrinsic permeability k is defined as

$$k = k_o \exp[M\varepsilon_o], \qquad \text{(Eqn. 3.19)}$$

t being the time and h the thickness of the sample. This model incorporates strain-dependent permeability (Eqn. 3.19). All the parameters, except the permeability k_o and the material constant M, can be determined from the confined compression test. The unknown parameters can be determined by systematically varying their values until the analytical reaction force vs. time curve (Eqn 3.17 and Eqn. 3.18) best fits the data from the experiment.

Confined Compression Rig

A 3 mm diameter chamber, 4.5 mm deep, was drilled into a cylindrical piece of stainless steel. Cylindrical porous sintered bronze filter elements, 2.9 mm in diameter and 10 mm long, were manufactured by Aegis Advanced Materials (Worcestershire, England). The maximum pore size of the filter elements could be varied from 45 microns to 205 microns. To grip the filter elements, a hole 2.9 mm in diameter and 5 mm deep was drilled into a second cylindrical piece of stainless steel. The filter element was inserted into this hole and fixed in place using grub screws. The ends of both these pieces of stainless steel were designed so that they could be mounted onto a Zwick Z005 materials testing machine. The Zwick Z005 materials testing machine

can test at speeds from 0.001 mm/min to 3000 mm/min to an accuracy of 62 μm. A 50 N load cell is used for these experiments. The whole rig is surrounded by a bath of saline solution, the temperature of which can be controlled using a thermocouple, a heating element and a temperature control device, see Fig. 3.12.

Unconfined Compression Rig

Two stainless steel cylinders were machined to a diameter of 20 mm. The top of each piece was polished in an attempt to reduce the coefficient of friction between the stainless steel surface and the cartilage sample. The ends of both pieces were designed so that they could be mounted onto the same Zwick materials testing machine used for the confined compression test. This unconfined compression rig was surrounded by the same temperature controlled bath as used in the confined compression set-up.

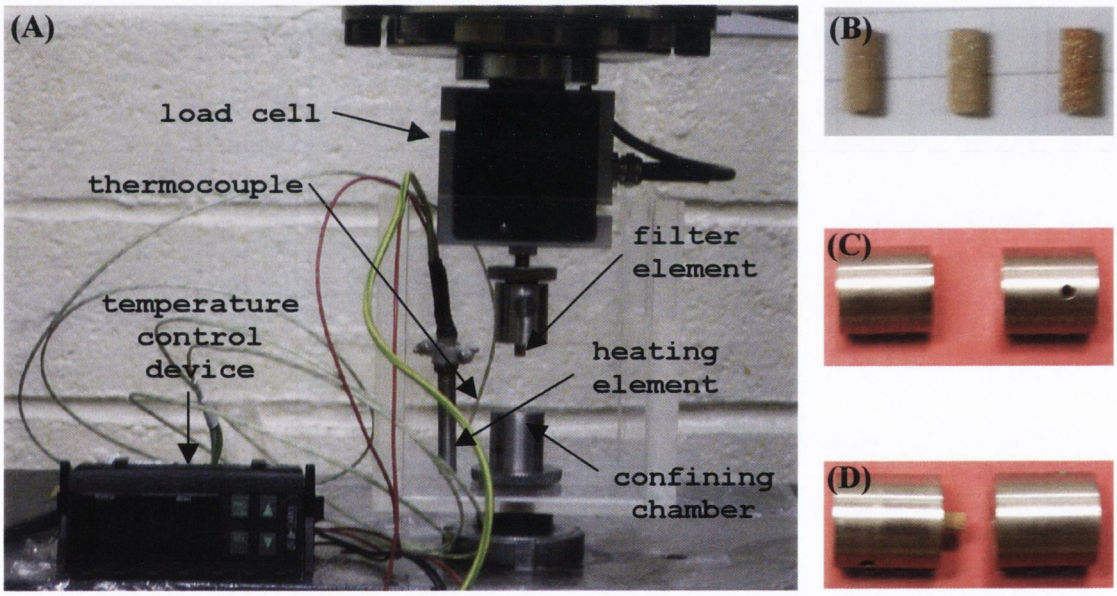

Fig. 3.12. *(a) Confined compression rig, complete with bath and temperature control device. (b) 3 different grades of porous filter elements. (c) Close-up picture of unconfined compression pieces. (d) Close-up picture of confined compression pieces.*

Validation of rig

To validate the rig, samples of normal bovine nasal (n=6) and articular cartilage (n=3) were obtained from a local abattoir and tested in confined compression. Discs 3mm diameter were punched out (Fig. 3.13). A ramp displacement corresponding to 10% strain at a ramp speed of 0.001 mm/sec was applied to each sample, which was then held until the measured reaction force equilibrated. Two subsequent ramp displacements of 5% strain each were then applied to each sample, giving a total strain of 20% (Fig. 3.14a). Based on the magnitude of the equilibrium force measured after each ramp and hold (Fig. 3.14b), a stress-strain curve for the tissue can be obtained (Fig. 3.14c). The aggregate modulus of the tissue is obtained from the slope of the stress-strain curve.

Fig. 3.13. *Punched samples of normal bovine nasal cartilage.*

The mean value obtained for the aggregate modulus of normal bovine nasal tissue was 1.49 MPa. The mean value obtained for the aggregate modulus of normal bovine articular cartilage was 0.11 MPa. This is at the lower end of values reported by Mow and Guo (2002) for normal bovine articular cartilage. It was suspected that the reason for the low value was because the articular samples were taken primarily from the superficial region of the tissue, were the concentration of proteoglycans is low, and hence the aggregate modulus of cartilage is low, as proteoglycans provide the main resistance to compression in cartilage. To test that the modulus values obtained from the confined compression test correlated with the biochemical content, each sample was sent for biochemical analysis (University of Bristol Academic Rheumatology Dept.). The total GAG (the glycosaminoglycan side chains of the proteoglycan biomolecule) and collagen II content for each sample is given in table 3.7 (nasal) and table 3.8 (articular). As expected the aggregate modulus of normal bovine cartilage is roughly correlated to the GAG content (Fig. 3.15).

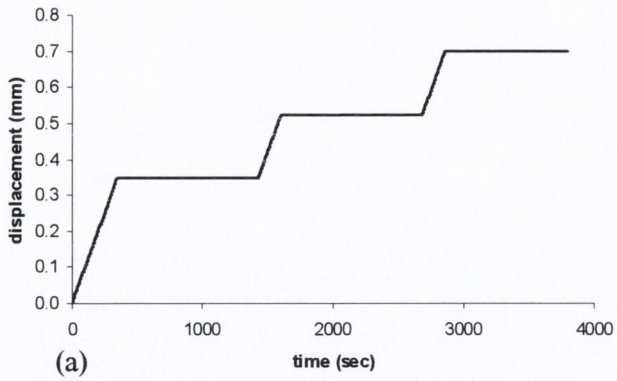

(a)

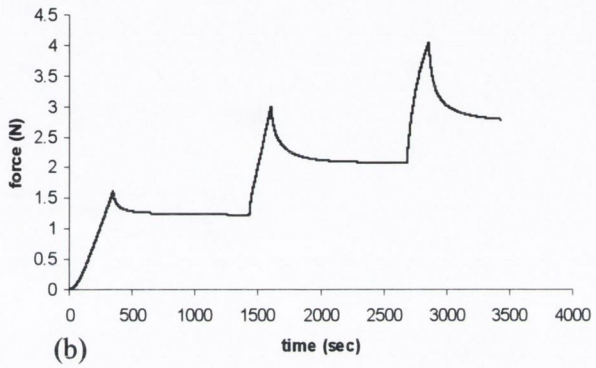

(b)

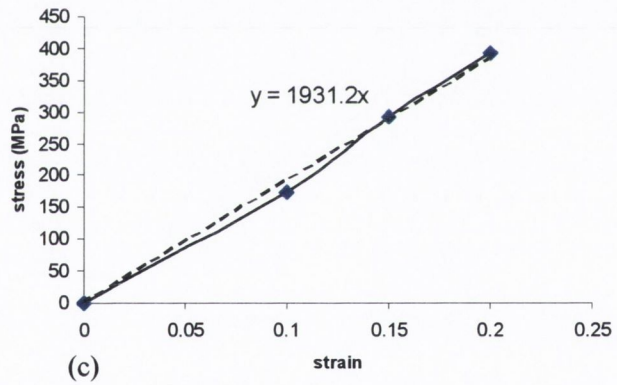

(c)

Fig. 3.14. *(a) A 10% ramp displacement and hold, followed by two more 5% ramp displacement and holds, are applied to each sample.(b) The force rises during the compression phase, and relaxes during the hold phase until it reachs an equilibruim value. (c) The equilibruim stress for each loading is determined by dividing the equilibruim force by the area of the sample. Hence a stress strain curve can be plotted for each sample, the slope of which gives the aggregate modulus.*

Table 3.3. *Aggregate modulus, GAG (as a percentage of dry weight) and collagen II (as a percentage of dry weight) content for normal bovine nasal cartilage. Biochemical analysis performed at the University of Bristol Academic Rheumatology Department.*

Normal Bovine Nasal Cartilage			
Sample #	Modulus (kPa)	GAG (% dry weight)	Collagen II (% dry weight)
1	351	30.7	43.6
2	995	35.2	55.1
3	1926	43.6	58.1
4	2160	45.1	34.2
5	1931	49.2	46.9
6	1557	47.5	41.7
Average	1486	41.9	46.6

Table 3.4. *Aggregate modulus, GAG (as a percentage of dry weight) and collagen II (as a percentage of dry weight) content for normal bovine articular cartilage. Biochemical analysis performed at the University of Bristol Academic Rheumatology Department.*

Normal Bovine Articular Cartilage			
Sample #	Modulus (kPa)	GAG (% dry weight)	Collagen II (% dry weight)
1	165	10.1	67.5
2	90	12.5	64.5
3	66	11.8	71.4
Average	107	11.4	67.8

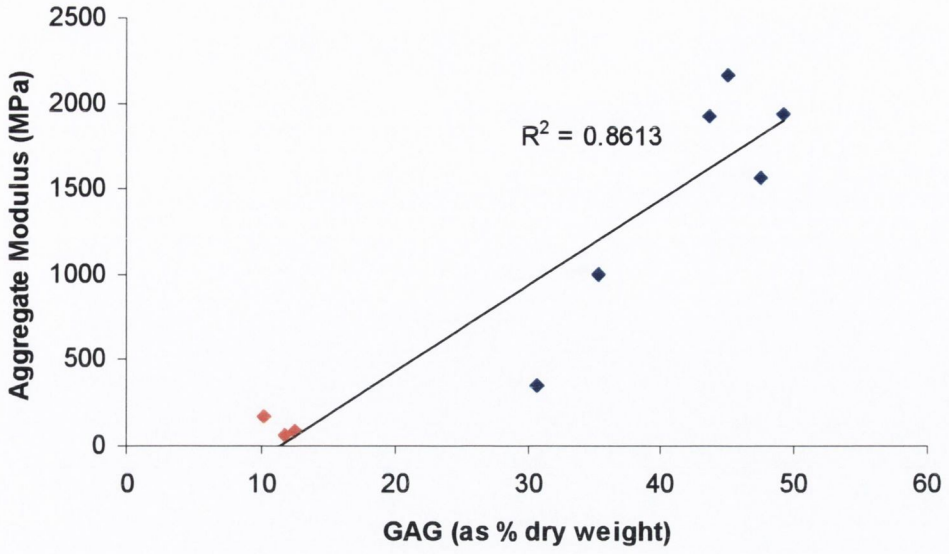

Fig. 3.15. *Aggregate modulus plotted against GAG content for each sample tested. (Red markers – articular cartilage. Blue markers – nasal cartilage).*

3.4.2 Influence of tissue culture conditions

The mechanical properties of tissue engineered cartilage is thought to be influenced by a number of culture conditions such as the time in culture, the cell seeding density, the cell source, growth factors and mechanical conditioning. To access how these factors influence the mechanical properties of tissue engineered cartilage, a number of different tissue engineering experiments were undertaken at the University of Sheffield, the University of Bristol and the University of Basel. At the end of each experiment, engineered cartilage constructs were stored in culture media and sent to Trinity College Dublin to be tested the following day. The details of each experiment are given below.

Influence of cell seeding density

Either 2 million (n=7), 4 million (n=9), 8 million (n=8) or 16 million (n=8) bovine articular chondrocyes were seeded onto 5mm diameter discs of 2mm thick non-woven Hyalograft-C® scaffolds. All scaffolds seeded on steel wires suspended in a gently stirred cell suspension for 72h and they are then transferred to culture dishes and kept on a gently shaking platform. From initiation of seeding constructs are cultured for a total of 7 days in expansion medium (DMEM + 10mM Hepes buffer + Non-essential amino acids + 10% foetal calf serum + penicillin/streptomycin antibiotic +

10ng/mlbasicfibroblast growth factor), followed by 33 days in differentiation medium (DMEM + 10mM Hepes buffer + Non-essential amino acids + 10% foetal calf serum + penicillin/streptomycin antibiotic + 1microgram/ml insulin + 50micrograms/ml ascorbic acid). Constructs were then tested in confined compression, after which samples were frozen and sent for biochemical analysis to determine GAG, collagen I and collagen II content.

Influence of long-term culture

Bovine articular chondrocytes were dynamically seeded onto Hyalograft-C® discs and put into a standard culture media for 12 weeks. After the culture period, 3 samples were tested in confined compression. Each sample was then tested in unconfined compression.

Influence of in vitro pre-culture on in vivo development

Human articular chondrocytes from two adult donors (32 and 45 years) were expanded for two passages in culture medium containing 10% FBS, 1 ng/ml TGFβ1, 5 ng/ml FGF-2, and 10 ng/ml PDGFbb. Cells were then statically seeded on Hyalograft-C® discs (5mm diameter, 2mm thick) (Fidia Advanced Biopolymers, IT) at a low ($5*10^5$ cells/scaffold) or high ($3*10^6$ cells/scaffold) cell density. Samples were implanted subcutaneously in nude mice for 6 or 8 weeks either directly after seeding or following pre-culture in vitro for 2 weeks. The in vitro pre-culture medium consisted either of a differentiating medium (10% FBS, insulin, ascorbate, 1 ng/ml TGFβ1, 5 ng/ml FGF-2, 10 ng/ml PDGF) or a proliferating medium (10% FBS, insulin, ascorbate and 10 ng/ml TGFβ1). After 6 weeks in vivo, 2 samples at each seeding density for both pre-cultures were tested in confined compression. At 8 weeks 2 samples at each seeding density for both pre-cultures and no pre-culture were tested in confined compression.

3.5 Tissue engineering in osteochondral defect repair

3.5.1 Modelling scaffolds used in defect repair

When modelling the spontaneous repair of osteochondral defects, the defect is initially filled with granulation tissue that has a very low stiffness. As described in Section 2.4.4 of Chapter 2, placing a scaffold into the defect has been shown to influence the quality and type of the repair tissue. The influence of scaffolds on osteochondral defect repair will be studied using the mechano-regulation model.

A homogenous scaffold

The defect is initially filled with a homogenous, linear poroelastic material, with mechanical properties in the same range as the reported values of porous polymers used as scaffolds in cartilage defect repair (Slivka *et al.*, 2000). Both the Young's modulus and the permeability of the scaffold were varied parametrically to assess the influence of scaffold material properties on defect repair, see Table 3.5. The other material properties for the scaffold (Poisson's ratio, porosity, solid and fluid compression modulus) were set to that of granulation tissue. In the simulation, the mechanical properties of each element in the defect remain those of the scaffold material until the properties of the regenerating tissue within the element exceeds that of the scaffold.

Table 3.5 *Material properties of homogenous scaffold.*

	Young's Modulus (MPa)	Permeability ($m^4/Ns \times 10^{-14}$)
Scaffold H1	1	1
Scaffold H2	5	1
Scaffold H3	10	1
Scaffold H4	20	1
Scaffold H5	50	1
Scaffold H6	10	0.5
Scaffold H7	10	0.1

A multiphase scaffold

A tri-phase inhomogenous scaffold was modelled in which Young's modulus and permeability of the scaffold were varied in three different layers; a superficial region,

a chondral region and a bone region. A schematic of this concept is given in Fig. 3.16. The rational behind a multiphase scaffold is that the mechanical properties required for a scaffold to induce chondrogenesis in the chondral part of the defect may be different to those that induce osteogenesis in the bony part of the defect. A superficial layer is added as it is known that the mechanical properties of the superficial layer of normal articular cartilage differ significantly from the rest of the tissue, functioning to restrict fluid exudation and thereby increase interstitial fluid pressurization. Without a superficial layer, load support in normal articular cartilage under compression shifts from the flow-dependent modes of fluid drag and pressurization towards increased solid matrix stress. Therefore it has been suggested that it is important to maintain the integrity of the articular surface in order to preserve normal compressive behaviour of the tissue and normal load carriage in the joint (La *et al.*, 1993).

The Young's modulus and permeability of each layer in the scaffold is varied systematically to access the influence of the inhomogenity of the scaffold on defect repair. The Young's modulus is set to 10 MPa and the permeability to 1e-14 m^4/Ns in two of the three layers, and then varied in the third layer. The altered properties of the superficial, chondral and bone layers are given in Tables 3.6, 3.7 and 3.8 respectively. As before, the other material properties (Poisson's ratio, porosity, solid and fluid compression modulus) for the scaffold were set to that of granulation tissue.

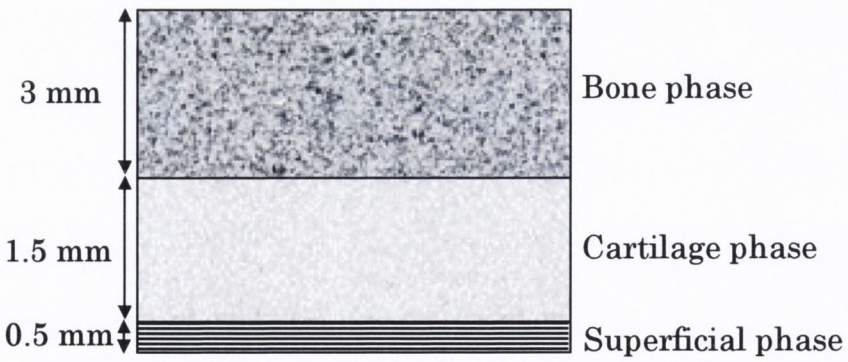

Fig. 3.16. *Schematic of multiphase scaffold.*

Table 3.6 *Material properties of superficial layer of the inhomogenous scaffold.*

	Young's Modulus (MPa)	Permeability ($m^4/Ns \times 10^{-14}$)
Scaffold M1	2	1
Scaffold M2	5	1
Scaffold M3	30	1
Scaffold M4	10	0.5
Scaffold M5	10	0.1
Scaffold M6	10	0.05

Table 3.7 *Material properties of cartilage layer of the inhomogenous scaffold.*

	Young's Modulus (MPa)	Permeability ($m^4/Ns \times 10^{-14}$)
Scaffold M7	2	1
Scaffold M8	30	1
Scaffold M9	10	0.1

Table 3.8 *Material properties of bone layer of the inhomogenous scaffold.*

	Young's Modulus (MPa)	Permeability ($m^4/Ns \times 10^{-14}$)
Scaffold M10	2	1
Scaffold M11	100	1
Scaffold M12	10	0.1

3.5.2 Influence of engineered tissues on defect repair

Engineering a cartilaginous tissue *in vitro* (e.g. in a bioreactor) before implantation into an osteochondral defect offers two benefits. Firstly the tissue is of the chondrogenic phenotype prior to implantation. Secondly the tissue will have a higher mechanical strength prior to implantation. To model the influence of an engineered tissue on osteochondral defect repair, granulation tissue was replaced with cartilage tissue in the defect at the beginning of the simulation. To account for the fact that the defect would be completely filled with chondrocytes at the beginning of the simulation, the cell concentration was set to maximum in each element at the beginning of the simulation, each cell being of the chondrogenic phenotype. Also the tissue types stored in the array of equation 3.9 were changed from granulation tissue to cartilage tissue.

Engineered cartilage modulus values used in finite element model

Normal articular cartilage is a highly non-linear, inhomogeneous material, where the Young's modulus of the tissue is much higher in tension than in compression. In the finite element model, normal articular cartilage is modelled using a linear isotropic element, with a Young's modulus equal in tension and compression. The Young's modulus of tissue-engineered cartilage was determined from compressive tests. The modulus values from the long-term culture (termed a mature engineered tissue), and the values from the short term culture with optimal seeding density (termed an immature engineered tissue), will be normalised to the *average* value used for normal articular cartilage, see Table 3.9, and used to simulate osteochondral defect repair in the presence of an engineered tissue. The influence of a hypothesised *high stiffness* engineered cartilage on defect repair was also studied.

Table 3.9. *The material properties of tissue engineered cartilage used in simulation of osteochondral defect repair. (H_a ~ Aggregate modulus; E ~ Young's modulus; v ~ Poisson's ratio; k ~ permeability).*

	Compressive Values		Finite Element Values		
	H_a (kPa)	E (kPa)	E (MPa)	v	k (mm^4/Ns)
Normal Cartilage	800	750	10	0.3	1e-15
Immature Engineered Cartilage	20	-	0.25	0.3	1e-14
Mature Engineered Cartilage	232	197	2.5	0.24	1e-14
Stiffness Engineered Cartilage	-	-	5	0.3	1e-14

It would be reasonable to assume that tissue engineered cartilage could degrade *in vivo* if cell death occurred. Therefore the Young's modulus of each element representing the engineered tissue in the finite element model will also depend on the number of cells n_c within the element. Initially the cell concentration is

set to the maximum value n_c^{max}, however if cell death occurs, the modulus of the engineered tissue will reduce according to

$$E_{updated\_engineered} = E_{original\_engineered} \frac{n_c^{max} - n_c}{n_c^{max}}. \qquad \text{(Eqn. 3.20)}$$

The modulus of each element within he model will remain as $E_{updated\_engineered}$ until such a time as it is exceeded by the modulus of the differentiated tissue E

$$E = \frac{(n_c^{max} - n_c)}{n_c^{max}} E_{updated\_engineered} + \frac{n_c}{n_c^{max}} \sum_{j=1}^{n_t} E_j \phi_j . \qquad \text{(Eqn. 3.21)}$$

3.6 Summary

A mechano-regulation theory has been developed which includes the dispersal, mitosis, death, and differentiation of cells of the mesenchymal lineage in response to their mechanical environment. The mechanical environment within the defect is determined using a poroelastic finite element model.

To test this theory, a finite element model of an osteochondral defect in the femur was created, and used to simulate spontaneous repair. The effects of physical factors, such as the magnitude of loading or the size of the defect on the tissue differentiation process, were analysed. Accurate simulation of tissue differentiation under these different conditions would justify our use of the mechano-regulation model to assess whether or not a scaffold or *in vitro* engineered tissue could improve the quality of the repair in an osteochondral defect. Since the mechanical properties of *in vitro* tissue-engineered cartilage reported in the literature vary widely, mechanical testing of tissue-engineered cartilage was undertaken after various different culture conditions. This data can be used for a simulation of osteochondral defect repair after implantation of an *in vitro* engineered tissue. Finally the mechanical properties of a scaffold can be varied in the model to search for the existence of an optimal scaffold for cartilage repair using tissue engineering. The results of these analyses are presented in the next chapter.

Chapter 4

Results

Contents

4.1 Introduction **77**

4.2 Spontaneous repair of osteochondral defects **78**

4.2.1 Influence of mesh density on model predictions *78*

4.2.2 Influence of defect size *87*

4.2.3 Influence of loading *95*

4.2.4 Parameter variation study of diffusion coefficients *101*

4.2.5 Influence of repair tissue integration *103*

4.2.6 Influence of cellular mitosis *109*

4.3 Mechanical properties of tissue engineered cartilage **115**

4.3.1 Influence of cell seeding density *115*

4.3.2 Influence of long-term culture *115*

4.3.3 Influence of in vitro pre-culture on in vivo development *116*

4.4 Influence of engineered tissues on defect repair **119**

4.5 Influence of scaffolds on defect repair **125**

4.1 Introduction

Each section of this results chapter will begin by presenting figures of the predicted patterns of tissue differentiation in the defect at different points during the simulation. In these figures an element filled with the colour green indicates ossification is predicted, an element filled with purple indicates cartilage tissue formation is predicted, and an element filled with pink indicates that fibrous tissue formation is predicted. The colour scaling used in the plots of predicted tissue types relates primarily to the number of cells within each element, and hence to the maturity and Young's modulus of the tissue. A lighter shade of colour indicates a low cell number, while a deeper shade of colour indicates a high cell number within the element, see Fig. 4.1. For bone formation, the darker shades of green indicate mature woven bone formation.

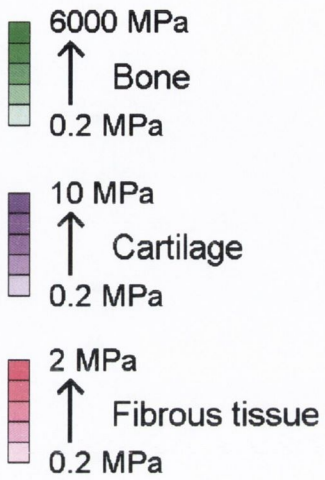

Fig. 4.1

The percentages of each tissue type predicted to form within the defect over the course of the simulation are also given. In these graphs granulation tissue is assumed to persist within an element until the total cell concentration exceeds 50%. Next the two mechanical stimuli hypothesised to regulate tissue differentiation during the simulation (i.e. octahedral shear strain and interstitial fluid flow) are plotted for 12 different locations within the defect. Finally the cell concentrations throughout the simulation are plotted for the same 12 locations within the defect.

Successful repair can be characterised by two factors:

(i) The amount of each tissue type predicted to form. Optimal repair would consist of 60% bone tissue (because that is the percentage volume of the defect that was originally bone), 40% cartilage tissue and 0% fibrous tissue.

(ii) The distribution of each tissue type within the defect. Ideally the chondral region of the defect would be completely filled by new cartilage tissue of uniform thickness, and the bony part of the defect would be completely filled with new bone tissue of uniform thickness.

Therefore to assess the quality of the repair one must consider both the plots of the predicted *pattern* of tissue differentiation and the *quantity* of each tissue type.

4.2 Spontaneous repair of osteochondral defects

4.2.1 Influence of mesh density on model predictions

As outlined in chapter 3.3.2, a low (400 elements), intermediate (1600 elements) and high (3600 elements) mesh density was used in the finite element model of the 5mm osteochondral defect. Mesh density had only a small effect on the pattern of repair predicted within the 5 mm defect, as shown in Fig. 4.2. Small differences can be observed between the patterns of repair predicted by the intermediate and fine mesh and the coarse mesh, particularly between iterations 5 and 10, suggesting that the coarse mesh may not be accurate enough for this analysis. The simulations show that, initially, the defect is partially shielded from the load by the intact cartilage adjacent to the defect, and because of this the stimulus within the defect is low. This low level of mechanical stimuli favours osteogenesis, resulting in direct intramembranous ossification in the base of the defect. As the repair tissue begins to stiffen, it starts to support load, and chondrogenesis is favoured within the centre of the defect. Fibrous tissue is predicted to form at the articular surface, as shown by the red region at the articular surface of the defect. After some time, increased bone formation is predicted to occur by endrochonrdal ossification, and regions of cartilage begin to differentiate into fibrous tissue leading to a reduction in the amount of cartilage within the defect. Fibrous or cartilaginous tissue is predicted to persist at the interface between the repair tissue and the residual tissue.

The percentage of each tissue type predicted to form within the defect varies throughout the simulation until convergence of the model is achieved after approximately 40 iterations for all mesh densities (Fig. 4.3). The amount of bone tissue formation within the defect increases throughout the simulation, initially through direct intramembranous ossification (bone tissue replacing granulation tissue), and later through endochondral ossification (bone tissue replacing cartilage tissue). The amount of fibrous tissue formation predicted within the defect remains reasonably constant after 15 iterations of the simulation.

Regarding the quantities of fibrous, cartilage and bone tissue predicted to form within the defect, it is observed that greater amounts of bone formation and less cartilage tissue formation is predicted to form using the intermediate and fine mesh density models compared to the coarse mesh density model (Fig. 4.4). The amount of fibrous tissue formation predicted with the three mesh density models is similar.

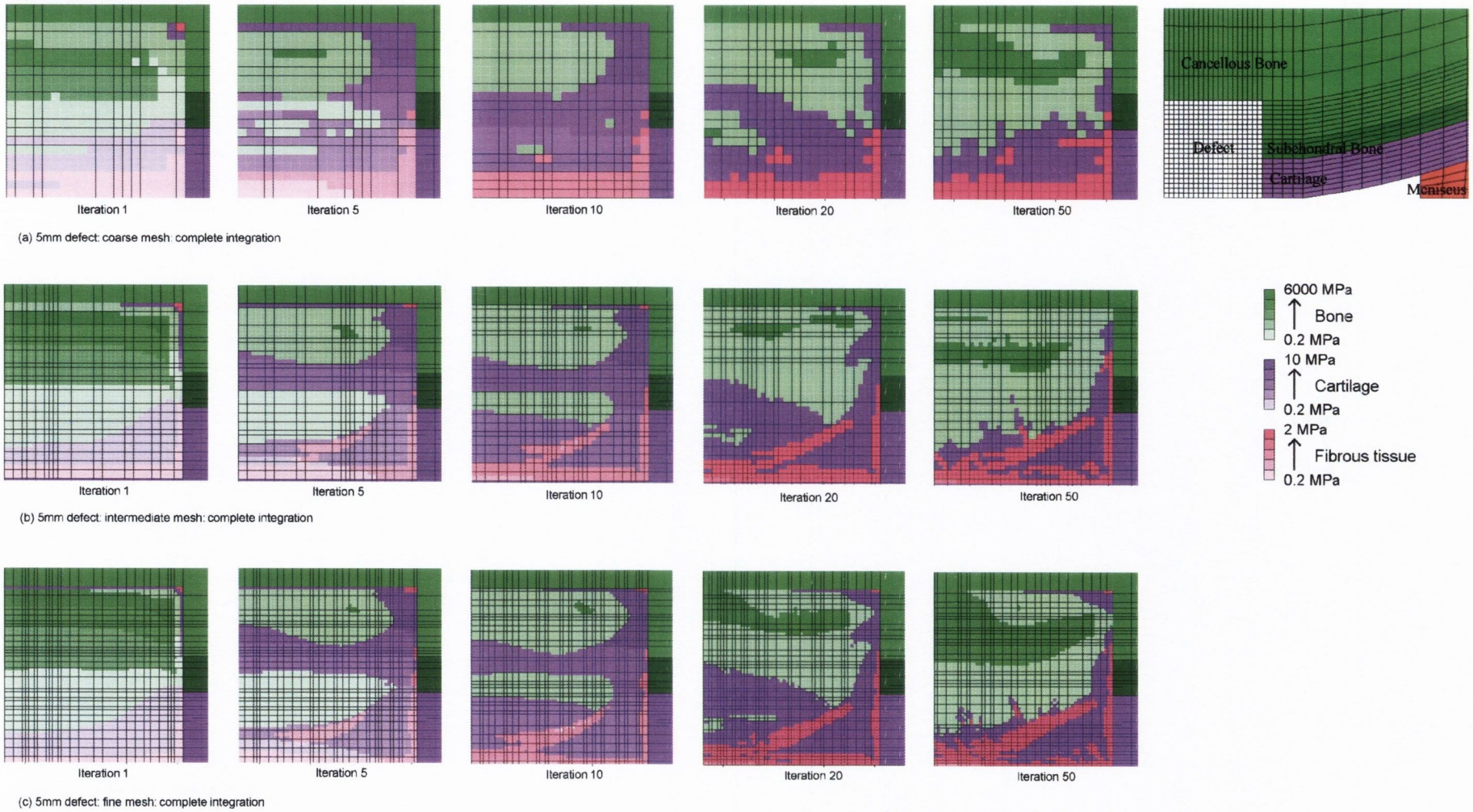

Fig. 4.2. *Predicted patterns of tissue differentiation in 5 mm defect during simulation.*

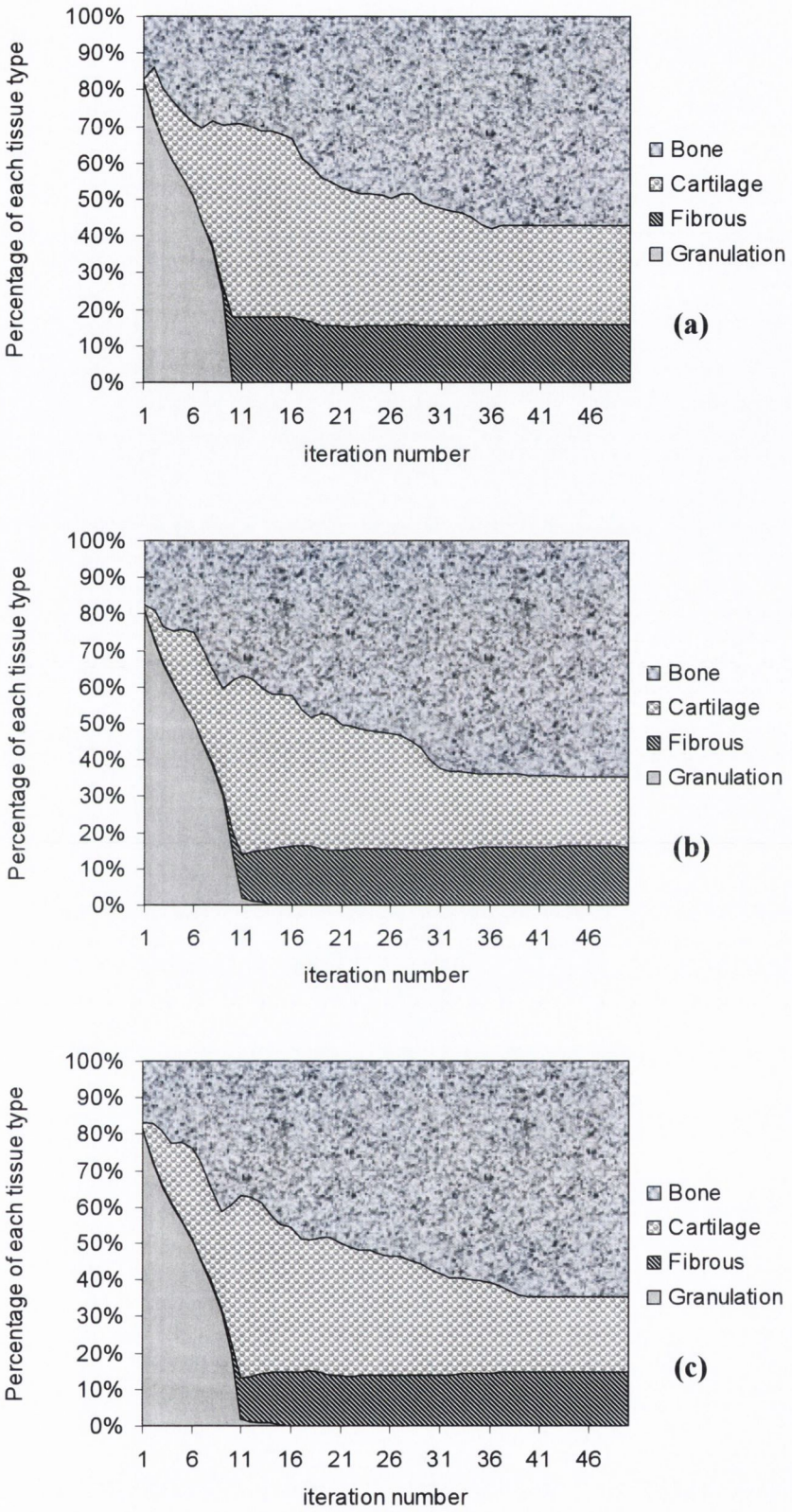

Fig. 4.3. *Percentage of each tissue type predicted to form within the defect over the course of the simulation – (a) coarse mesh (b) intermediate mesh (c) fine mesh. For the purposes of this illustration granulation tissue is assumed to persist within an element until the total cell concentration exceeds 50.*

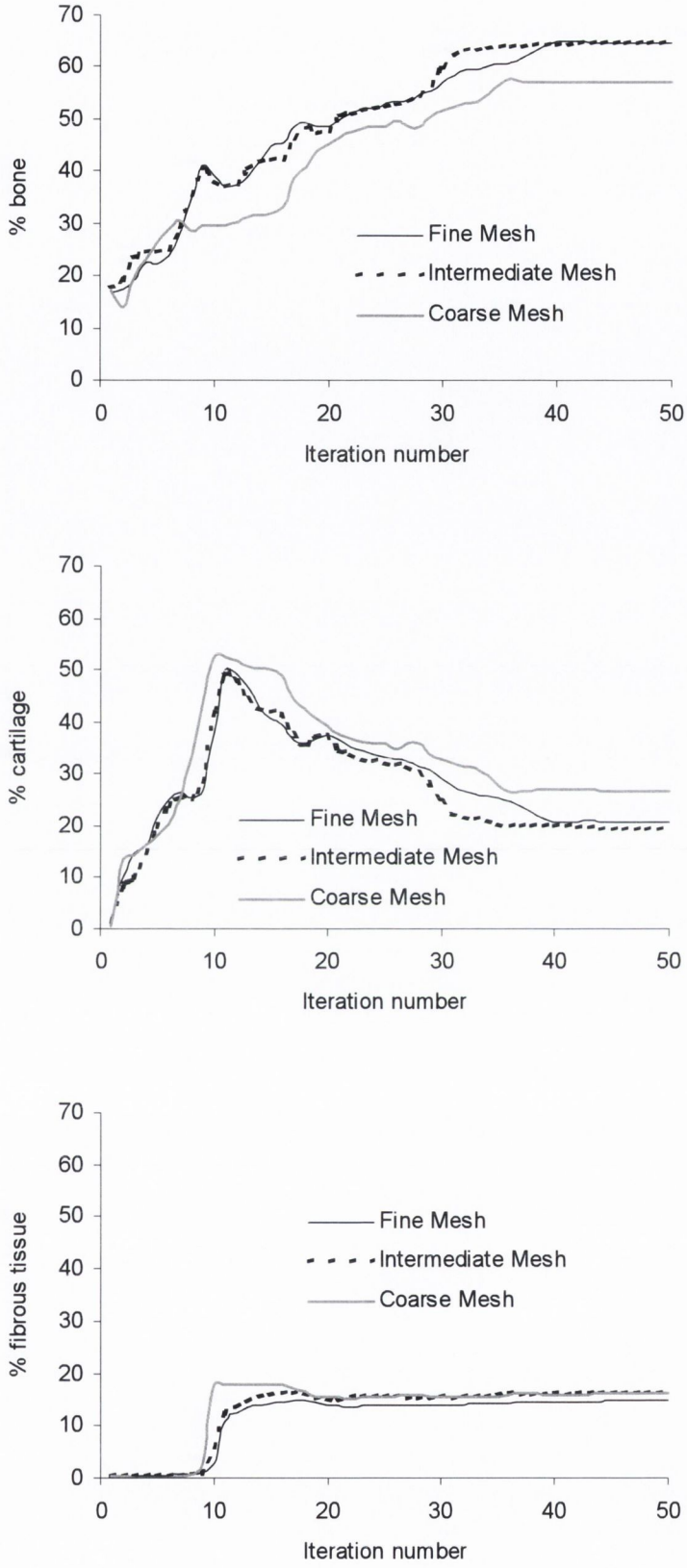

Fig. 4.4. Comparisons of the amounts of bone tissue, cartilage tissue and fibrous tissue predicted to form with the coarse, intermediate and fine mesh densities.

Mechanical stimuli

The patterns of tissue differentiation, as well as the concentration of cells, within the defect changes over time due to changes in the magnitudes of the governing mechanical stimuli, the octahedral shear strain and the interstitial fluid flow. The octahedral shear strain, interstitial fluid flow and cell concentration are plotted for 12 different locations throughout the defect, see Fig. 4.5.

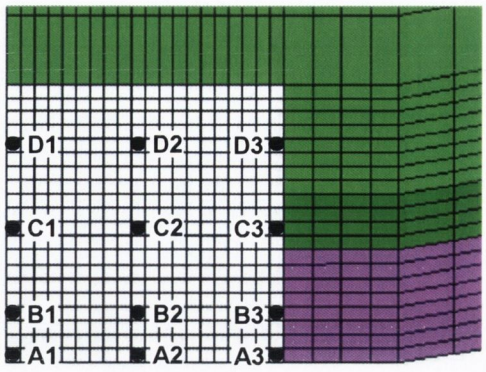

Fig. 4.5.

At the articular surface, the octahedral shear strain is predicted to rapidly increase at the centre of the defect between iterations 1-10 (Fig. 4.6 A1), after which it gradually rises before levelling off. At the edge of the defect (Fig 4.6 A3), the magnitude of the octahedral shear strain is initially high, but is predicted to fall between iteration 1-20. Throughout the rest of the repair tissue, a trend of increasing octahedral shear strain from the centre towards the periphery of the defect is predicted. The general trend in these regions is a rapid reduction in magnitude of the octahedral shear strain, except at the periphery of the defect where pattern is less definable. These predictions are reasonably consistent regardless of the mesh density chosen, except in the very centre of the defect where the predictions of the coarse mesh density model deviate from those of the intermediate and fine mesh density models.

The predicted magnitudes of interstitial fluid flow are generally greatest at the articular surface, and lowest in the base of the defect (Fig. 4.7). Larger magnitudes of interstitial fluid flow are predicted in the base of the defect towards the periphery. Differences in the predictions due to the mesh density are observed at the articular surface, and again they are between the predictions of the coarse mesh density model and the intermediate and fine mesh density models in the centre of the defect.

Cell concentration

The rate at which total cell concentration increases is greatest in the base of the defect (Fig. 4.8). Therefore total cell concentration reaches a maximum after fewer iterations of the model in the bony region of the defect compared to chondral region. Significant cell death is predicted in the centre of the defect at the articular surface (Fig. 4.8 A1) for both the intermediate and fine mesh density models. The large difference in results is surprising considering the magnitudes of octahedral shear strain predicted in this region of the defect for the three mesh densities are reasonably similar (Fig. 4.6 A1). Since the comparison of octahedral shear strain for the three mesh density models relied on averaging, it hid the fact that very large magnitudes of strain are predicted in the very superficial layer of elements in the intermediate and fine mesh density models that is not predicted by the coarse mesh density model (Fig. 4.9). These large magnitudes of octahedral shear strain are responsible for the significant cell death predicted at the articular surface in the intermediate and fine mesh density models (Fig. 4.8: A1) as mesenchymal stem cells differentiate into fibroblasts and die in the high strain environment.

In conclusion, the model predictions of tissue differentiation during osteochondral defect repair are reasonably independent of the mesh density. Small differences can be observed between the patterns of repair predicted by the intermediate and fine mesh and the coarse mesh, suggesting that the coarse mesh may not be accurate enough for this analysis. Also, the coarse mesh density model does not predict the cell death observed in the predictions of the intermediate and fine mesh density models (Fig. 4.8: A1). Therefore as a compromise between efficiency and accuracy, it was decided to use the intermediate mesh density for all remaining simulations.

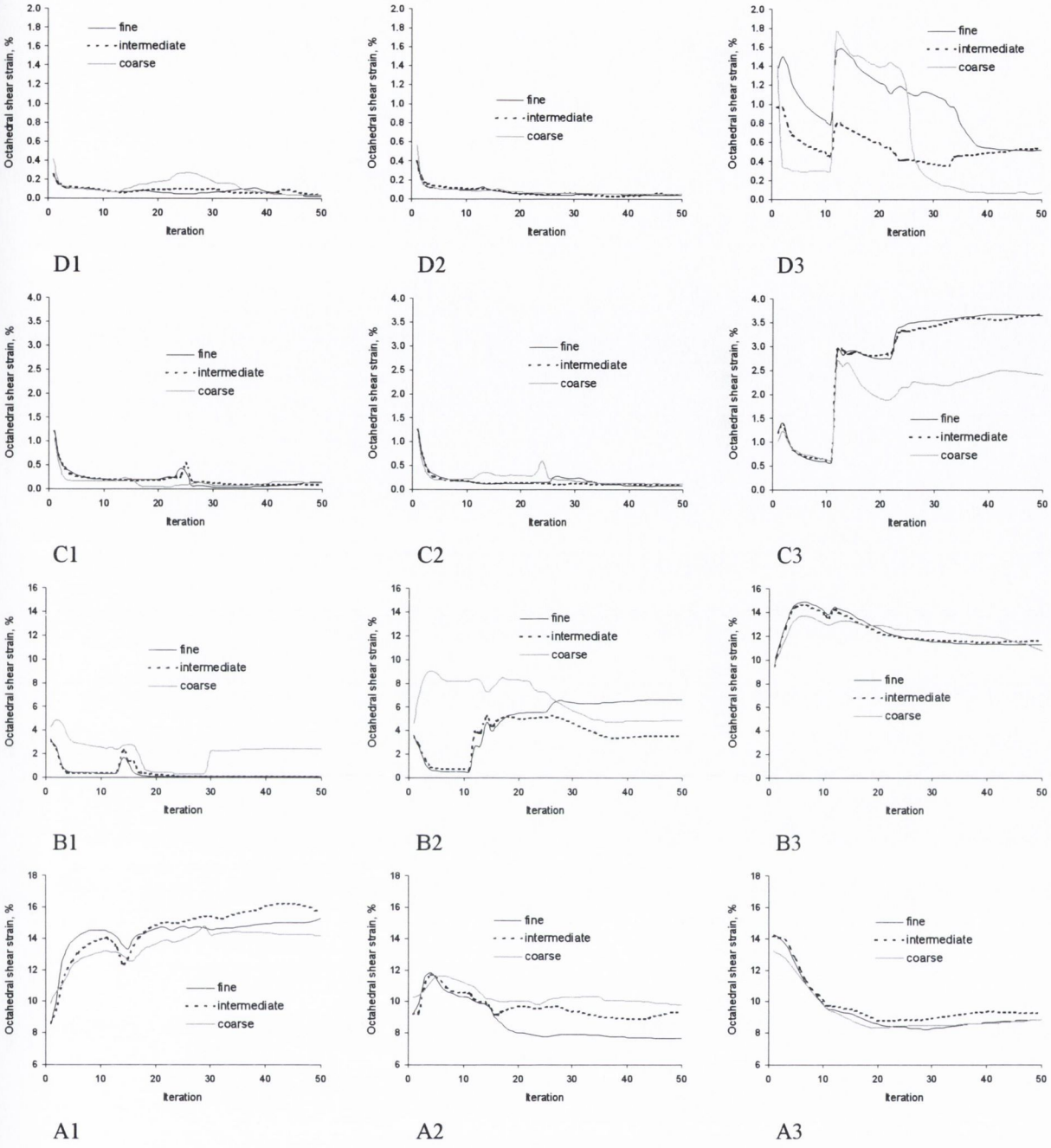

Fig. 4.6. *Predictions of octahedral shear strain in different elements within the defect throughout the simulation for the coarse, intermediate and fine mesh density finite element models. The location of each element in the mesh is indicated by the black dots in Fig. 4.5. For comparison purposes, the results from the four elements in the intermediate mesh density model that occupy the same area as a single element in the coarse mesh density model are averaged. The same averaging principle is applied to the nine elements in the fine mesh density model.*

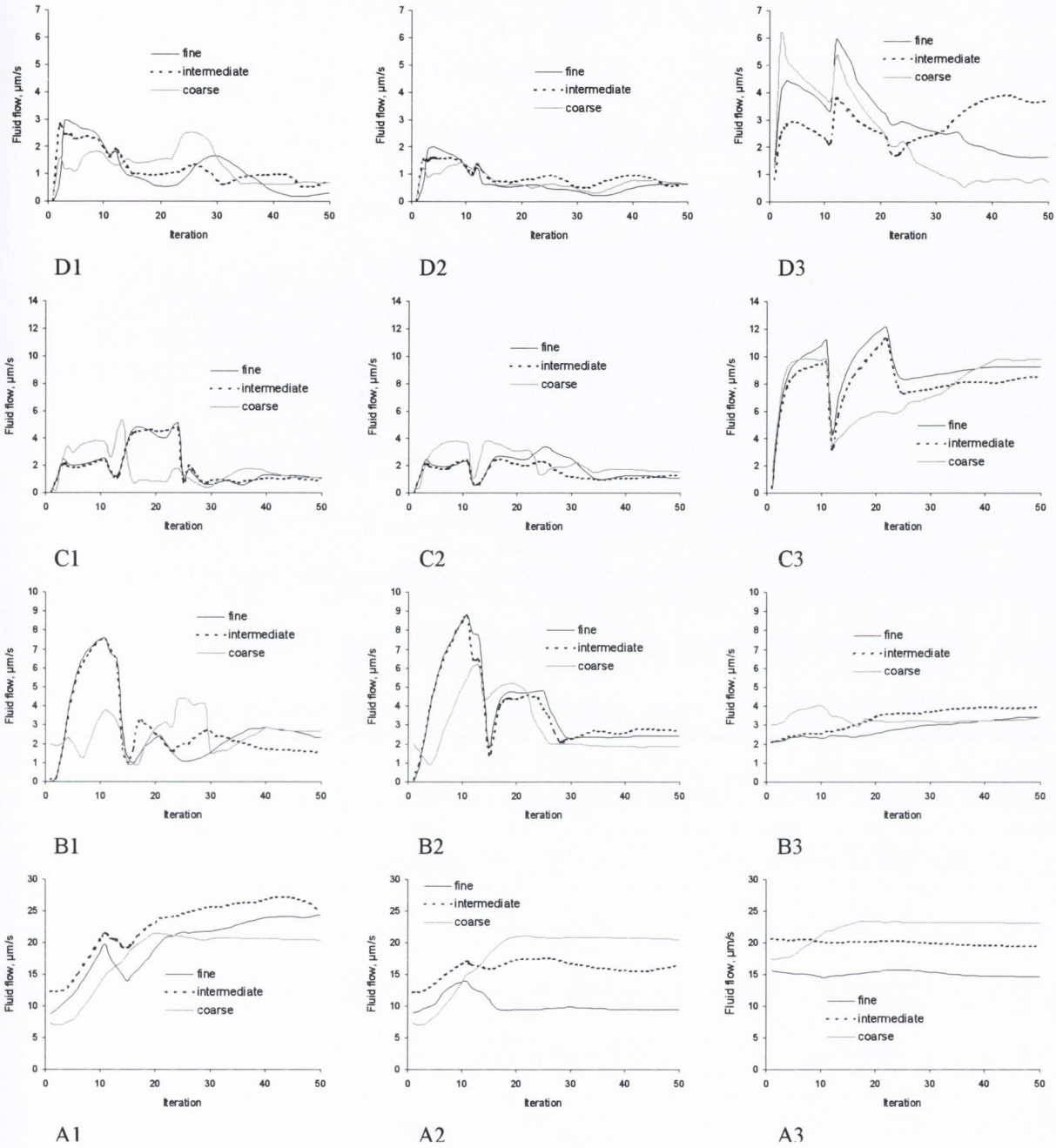

Fig. 4.7. *Predictions of interstitial fluid flow in different elements within the defect throughout the simulation for the coarse, intermediate and fine mesh density finite element models. The location of each element in the mesh is indicated by the black dots in Fig. 4.5. For comparison purposes, the results from the four elements in the intermediate mesh density model that occupy the same area as a single element in the coarse mesh density model are averaged. The same averaging principle is applied to the nine elements in the fine mesh density model.*

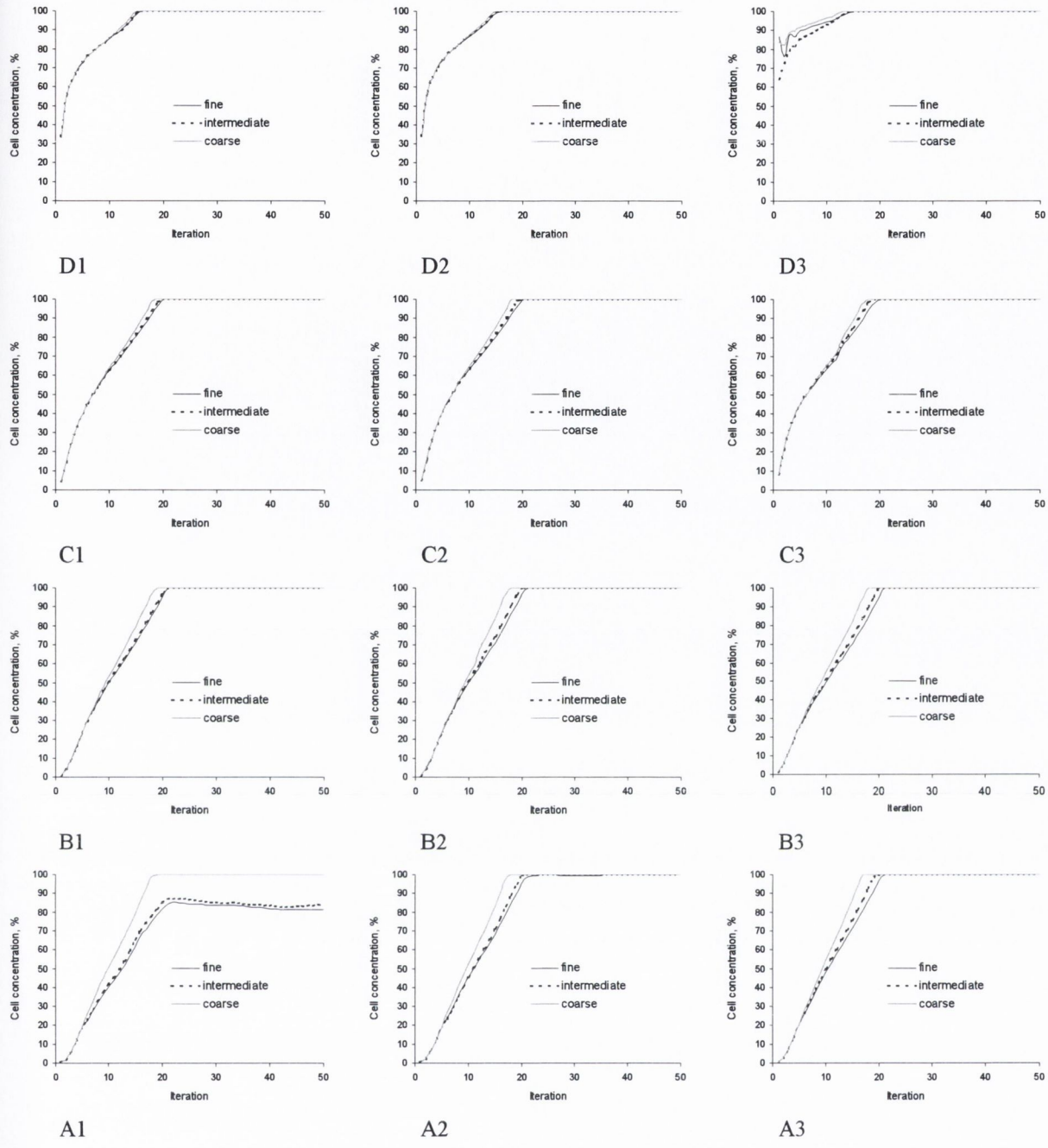

Fig. 4.8. *Predictions of cell concentration in different elements within the defect throughout the simulation for the coarse, intermediate and fine mesh density finite element models. The location of each element in the mesh is indicated by the black dots in Fig. 4.5. For comparison purposes, the results from the four elements in the intermediate mesh density model that occupy the same area as a single element in the coarse mesh density model are averaged. The same averaging principle is applied to the nine elements in the fine mesh density model.*

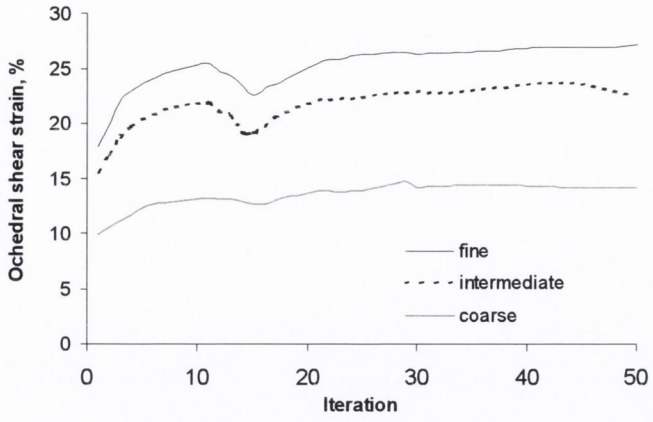

Fig. 4.9. *Prediction of octahedral shear strain in the very bottom left element for the coarse, intermediate and fine mesh density models. No averaging is applied.*

4.2.2 Influence of defect size

Significant differences in the patterns of repair are predicted in the 5 mm, 7 mm and 9 mm defects during healing (Fig. 4.10). A greater amount of fibrous tissue formation is predicted towards the periphery of the defect as the size of the defect is increased. After 50 iterations, greater amounts of fibrous tissue formation (28.2% in the 9mm defect, 19.6% in the 7 mm defect, 16% in the 5mm defect) and less bone formation (46.6% in the 9mm defect, 57.7% in the 7 mm defect, 64.6% in the 5mm defect) is predicted to form with increasing defect size (Fig. 4.11). It would seem that as the size of the defect is increased, the repair tissue becomes increasingly unstable and the stimulus for differentiation remains high, reducing the amount endochondral ossification within the defect (Fig. 4.11), leading to soft tissues persisting in a significant percentage of the bony part of the defect. Significant dedifferentiation of cartilage into fibrous tissue is also predicted as the size of the defect is increased.

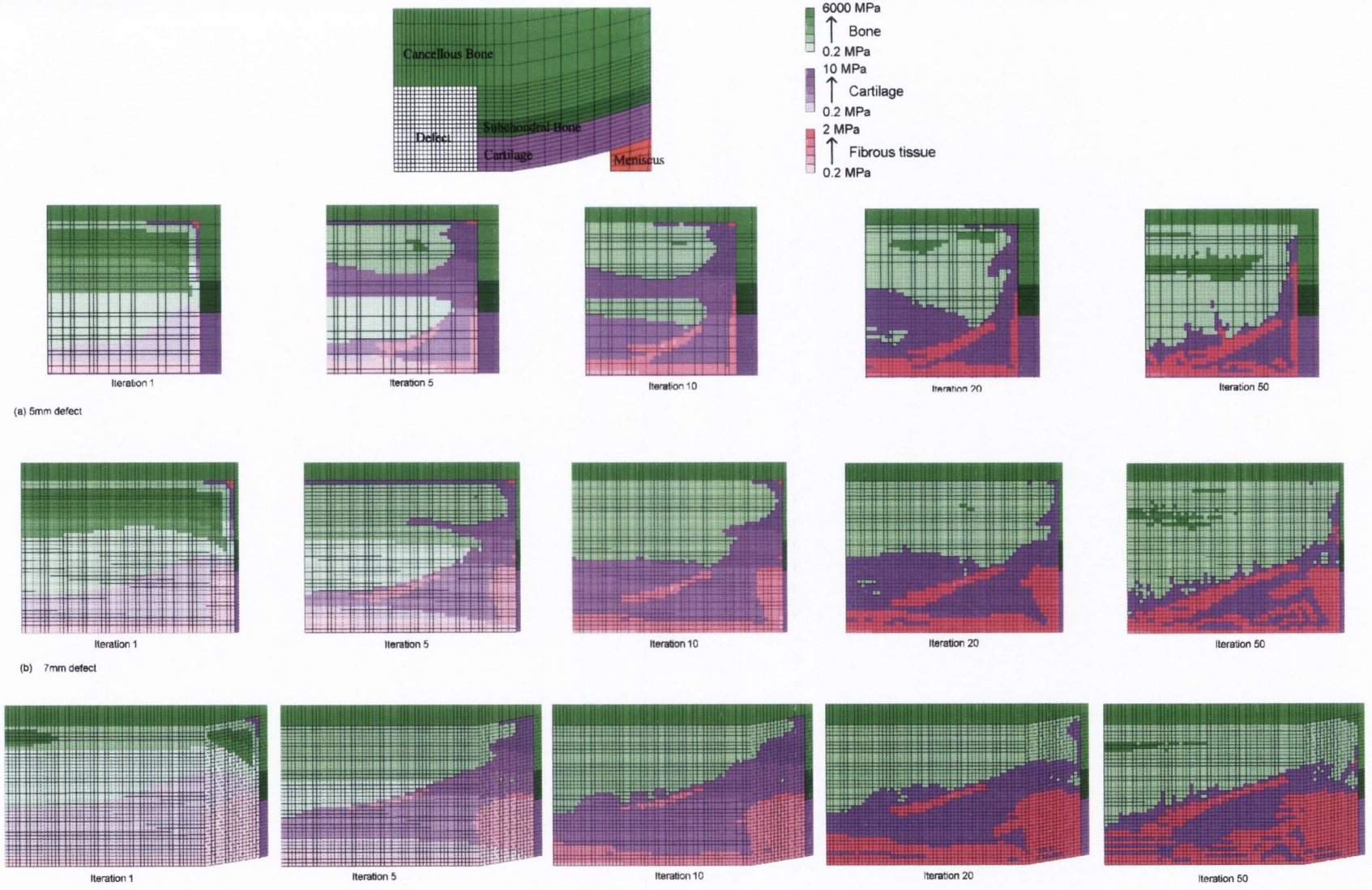

Fig. 4.10. *Predicted patterns of tissue differentiation in 5 mm, 7 mm and 9 mm defects during simulation.*

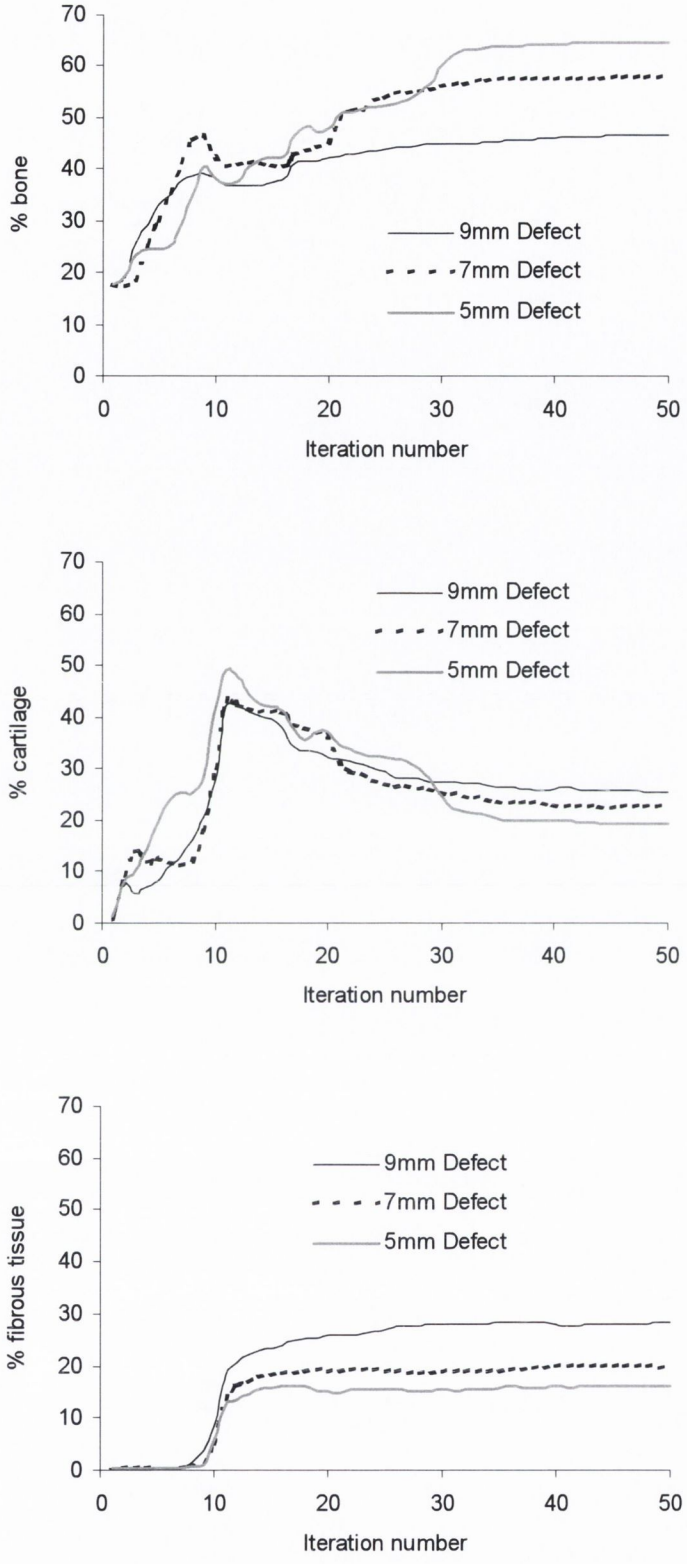

Fig. 4.11. *Comparisons of the amounts of bone tissue, cartilage tissue and fibrous tissue predicted to form in the 5 mm, 7mm and 9 mm defects.*

Mechanical stimuli

The octahedral shear strain, interstitial fluid flow and cell concentration are plotted for 12 different locations throughout the 5mm, 7 mm and 9 mm defects (see Fig. 4.4 for the 5mm defect and Fig. 4.12 for the 7mm and 9mm defects). No clear relationship emerged between the magnitude of the octahedral shear strain predicted and the size of the defect (Fig. 4.13). At the periphery of the defect it seem that increasing the size of the defect from 5mm to 9 mm actually reduced the predicted magnitude of the octahedral shear strain (Fig. 4.13 A3), while the magnitude of octahedral shear strain increased in the centre of the defect (Fig. 4.13 C1 C2 D2). Higher magnitudes of octahedral shear strain are predicted mid-way between the periphery and centre of the 9 mm defect (Fig. 4.13 C2), which correlates with a band of fibrous tissue formation predicted to form within this part of the repair tissue (Fig. 4.10). Similar regions of high octahedral shear strain are also observed in the 5 mm and 7 mm defects.

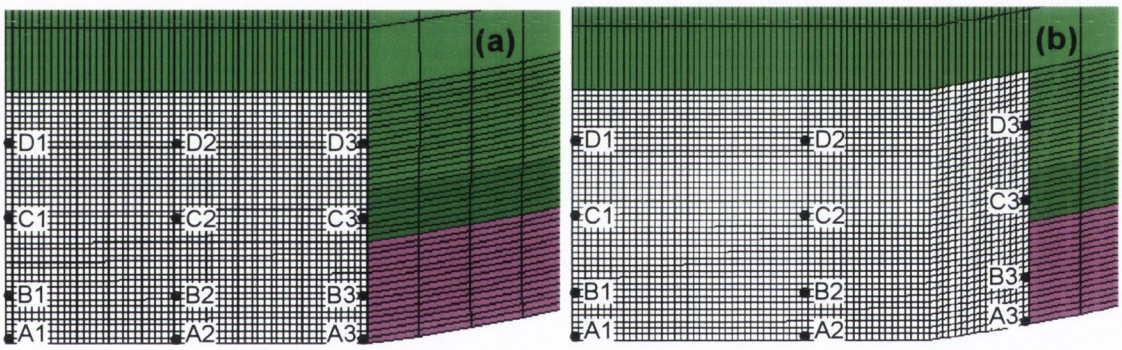

Fig. 4.12. *Location of elements in (a) 7 mm and (b) 9 mm defect meshes used in detailed analysis of mechanical stimuli and cell concentration.*

The size of the defect is predicted to have a greater effect on the magnitudes of fluid flow towards the periphery of the defect compared to the magnitudes of fluid flow in the centre of the defect (Fig. 4.14). Towards the periphery of the defect the fluid flow is generally predicted to increase with increasing defect size in the chondral part of the defect, while it is generally predicted to reduce with increasing defect size in the osseous part of the defect. The higher magnitudes of fluid flow in the chondral part of the defect would therefore seem to be the primary stimulus for the increased fibrous tissue formation predicted as the size of the defect is increased.

Cell concentration

Cell concentration throughout the defect is generally independent of defect size (Fig. 4.15). Increasing the size of the defect is not predicted to increase cell death in the high strain region at the articular surface (Fig. 4.15 A1). However cell death is also predicted in the middle of the larger 9 mm defect midway between the centre and periphery of the defect (Fig. 4.15 C2), due to the higher magnitudes of octahedral shear strain predicted within this region of the repair tissue.

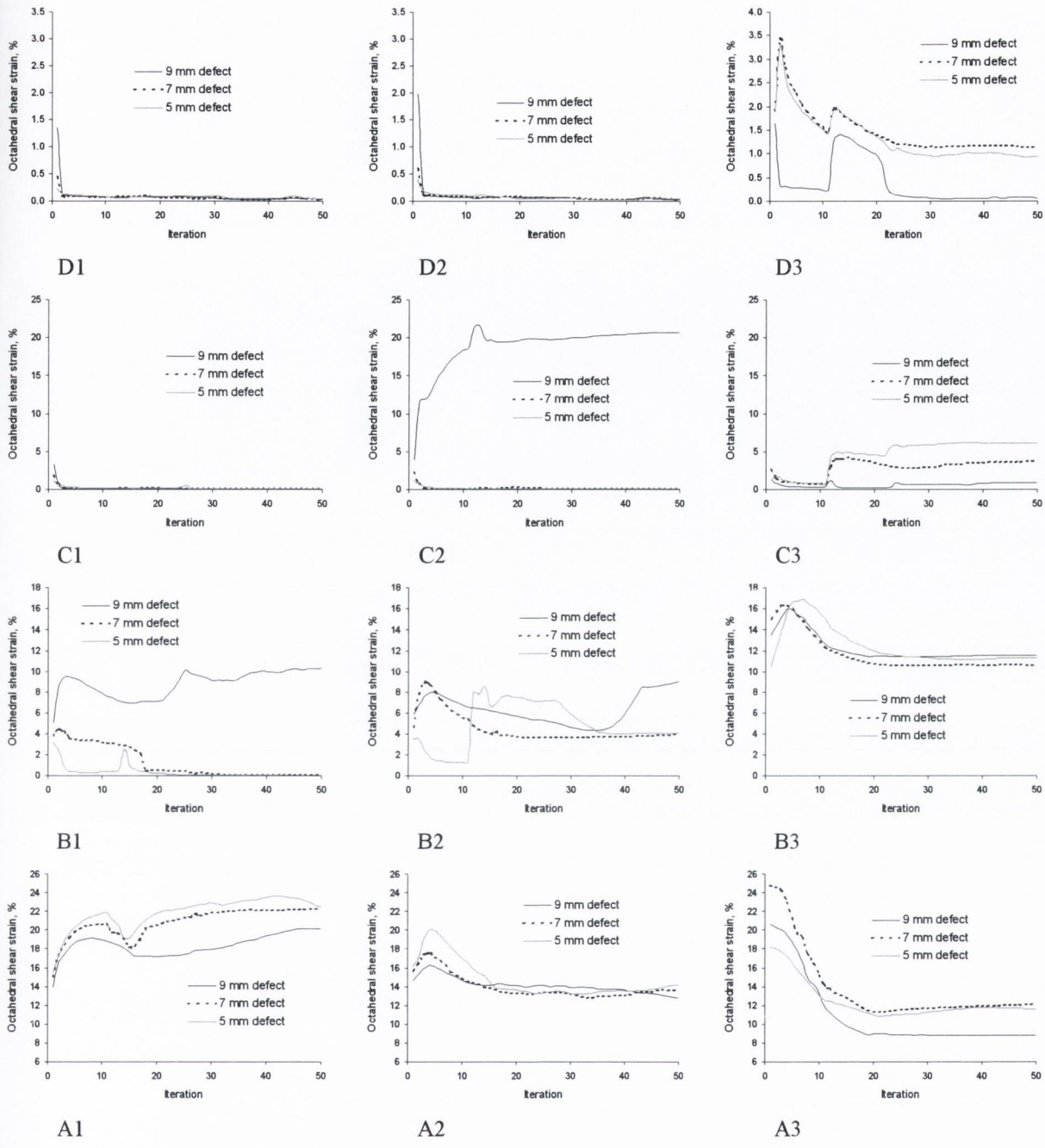

Fig. 4.13. *Predictions of octahedral shear strain in different elements within the defect throughout the simulation for the 5 mm, 7 mm and 9 mm defect. The location of each element in the 5 mm defect is indicated by the black dots in Fig. 4.5; therefore the graph in the top left hand corner represents the octahedral shear strain in the element marked by the black dot in top left hand corner of Fig. 4.5. The location of each element in the 7 mm and 9 mm defects is indicated by the black dots in Fig. 4.12.*

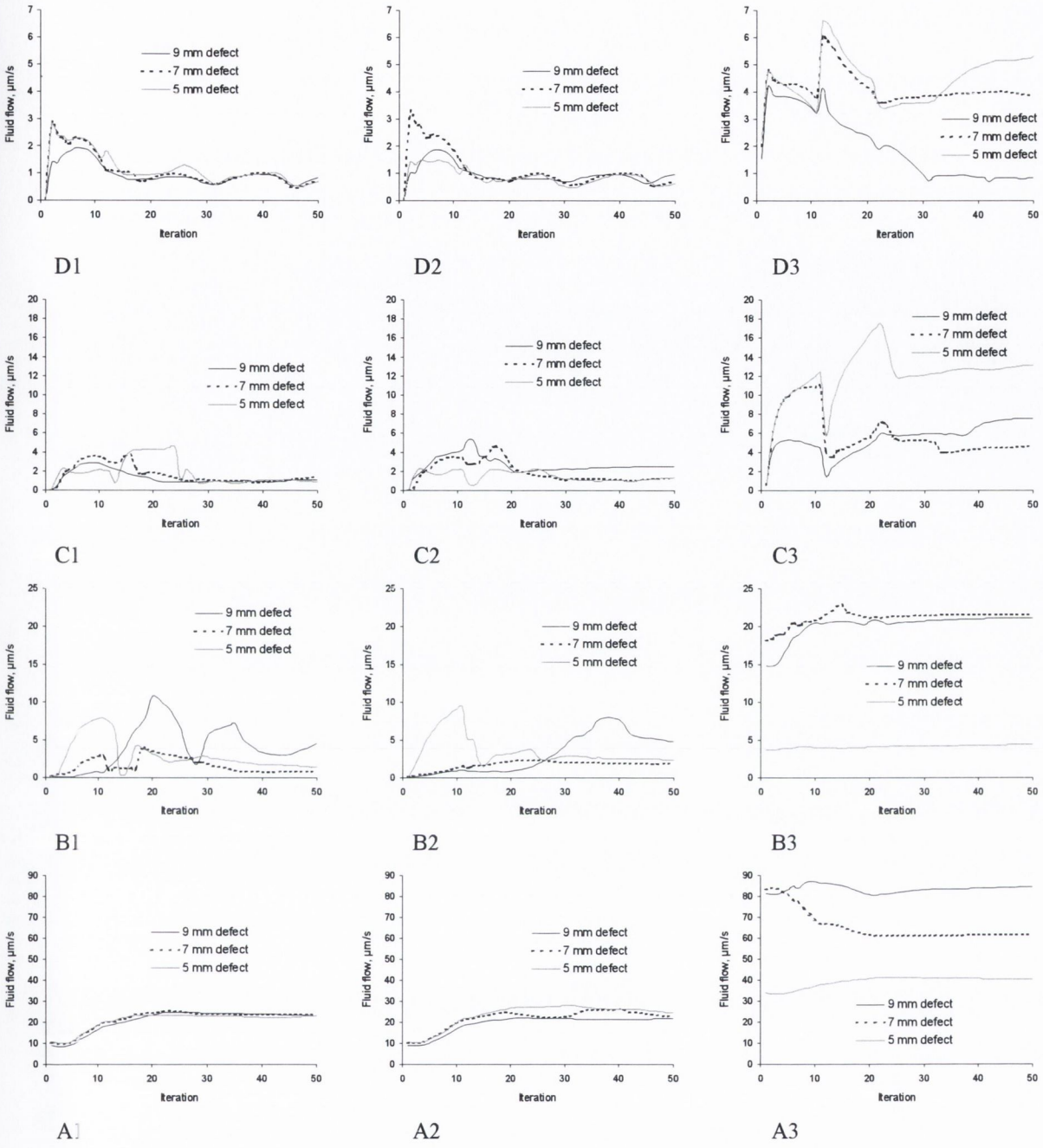

Fig. 4.14. *Predictions of interstitial fluid flow in different elements within the defect throughout the simulation for the 5 mm, 7 mm and 9 mm defect. The location of each element in the 5 mm defect is indicated by the black dots in Fig. 4.5. The location of each element in the 7 mm and 9 mm defects is indicated by the black dots in Fig. 4.12.*

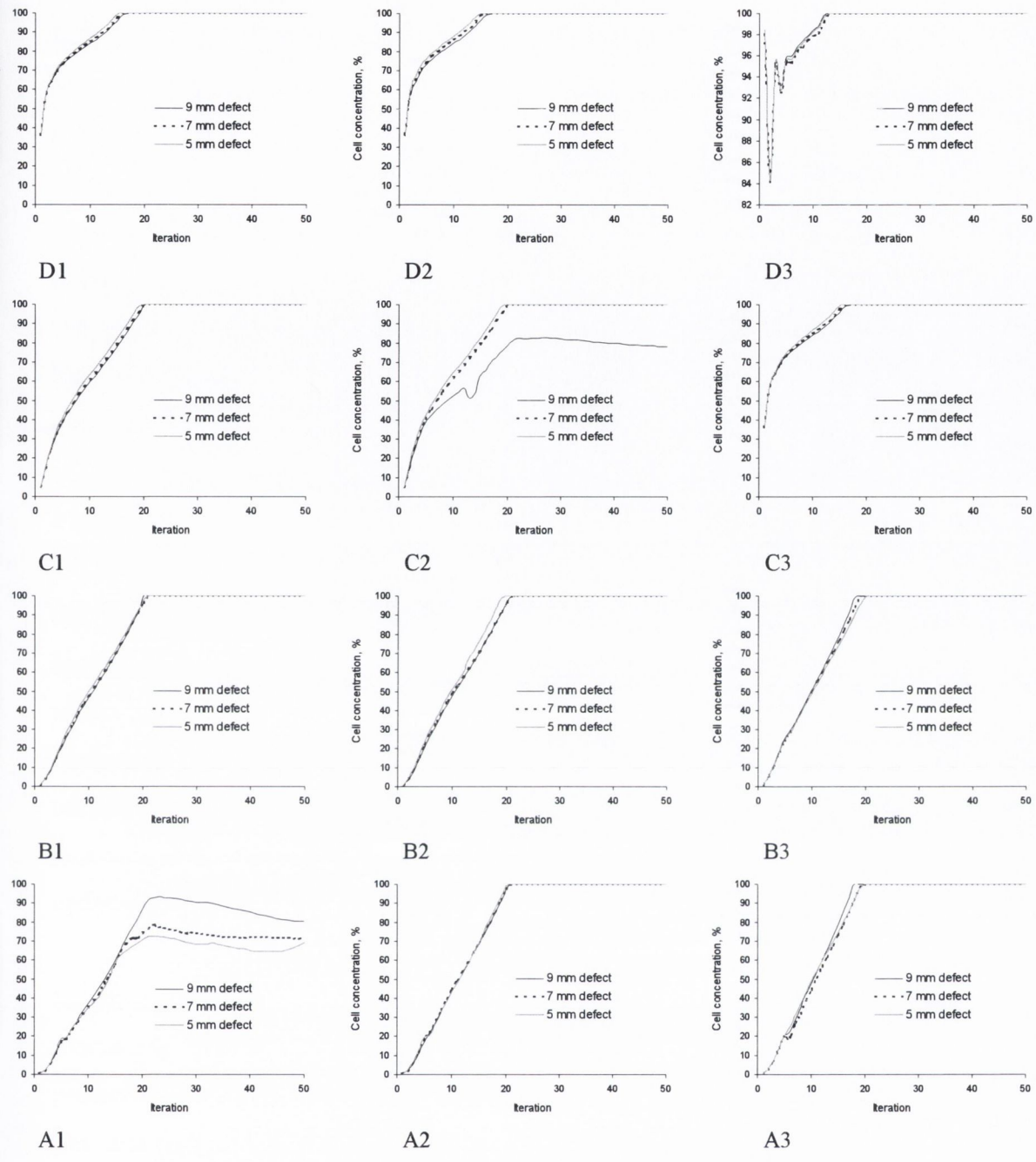

Fig. 4.15. *Predictions of total cell concentration in different elements within the defect throughout the simulation for the 5 mm, 7 mm and 9 mm defect. The location of each element in the 5 mm defect is indicated by the black dots in Fig. 4.5. The location of each element in the 7 mm and 9 mm defects is indicated by the black dots in Fig. 4.12.*

4.2.3 Influence of loading

Increasing the magnitude of the applied load from 500N to 1100N is predicted to increase in size the region of cartilage that forms in the centre of the defect between iteration 1 and iteration 10 (Fig. 4.16). Endochondral ossification occurs for all loading conditions, however progression of the osseous front reduces with increasing magnitude of applied load. Another noticeable difference between the three loading conditions is that regions of cartilage formation persists in the base of the defect for the 1100 N loading condition, suggesting that the stimulus for differentiation remains high enough in these regions to prevent complete endochondral ossification in the bony part of the defect.

After 50 iterations, greater amounts of fibrous tissue formation (25.3% for 1100N, 19.9% for 800N, 13.9% for 500N) and less bone formation (46.7% for 1100N, 59.1% for 800N, 68.2% for 500N) is predicted to form as the magnitude of the applied load is increased (Fig. 4.17). Although greater amounts of cartilage formation are predicted as the magnitude of the applied load is increased, this is accompanied by a similar increase in the predicted amount of fibrous tissue formation. For all loading conditions, the amount of bone formation is observed to initially increase due to direct intramembraneous ossification, remain steady between approximately iterations 10-20 while the defect stabilises, and then increase due to endochondral ossification (Fig. 4.17).

Mechanical stimuli

Increasing the magnitude of loading generally increases the magnitude of the predicted octahedral shear strain in the defect throughout the simulation (Fig. 4.18). The increased level of load also generally led to increases in the magnitudes of fluid flow predicted within the defect (Fig. 4.19).

Cell concentration

For the 1100 N loading condition, the increased level of strain led to cell death across nearly the whole of the superficial layer of the repair tissue (Fig. 4.20), rather than just at the centre of the articular surface, as predicted for the 500 N and 800 N loading conditions. The magnitude of loading had little effect on the predicted cell concentrations in the remainder of the defect (Fig. 4.20).

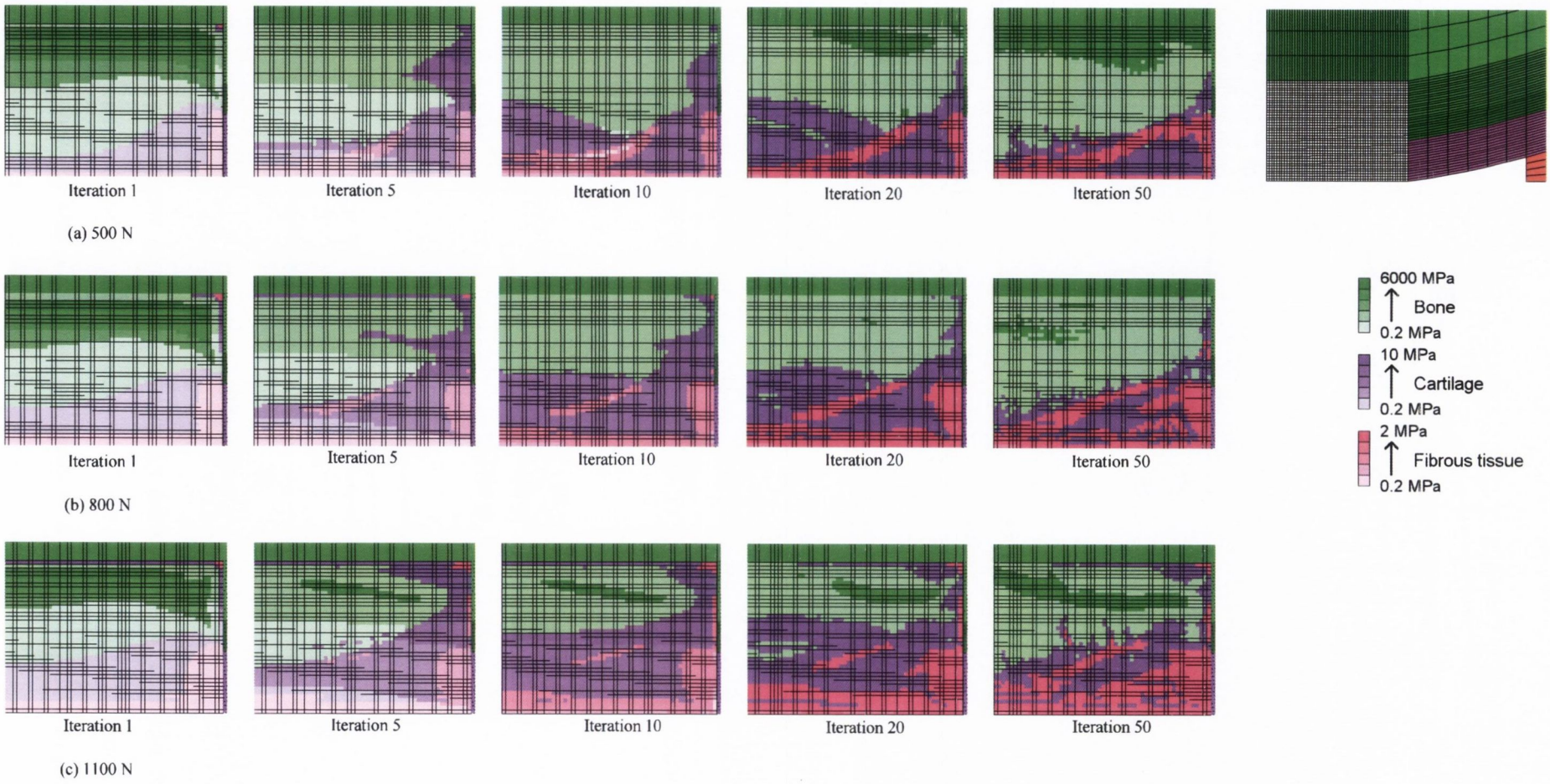

Fig. 4.16. *Predicted patterns of tissue differentiation in 7 mm defect during simulation of different loading conditions.*

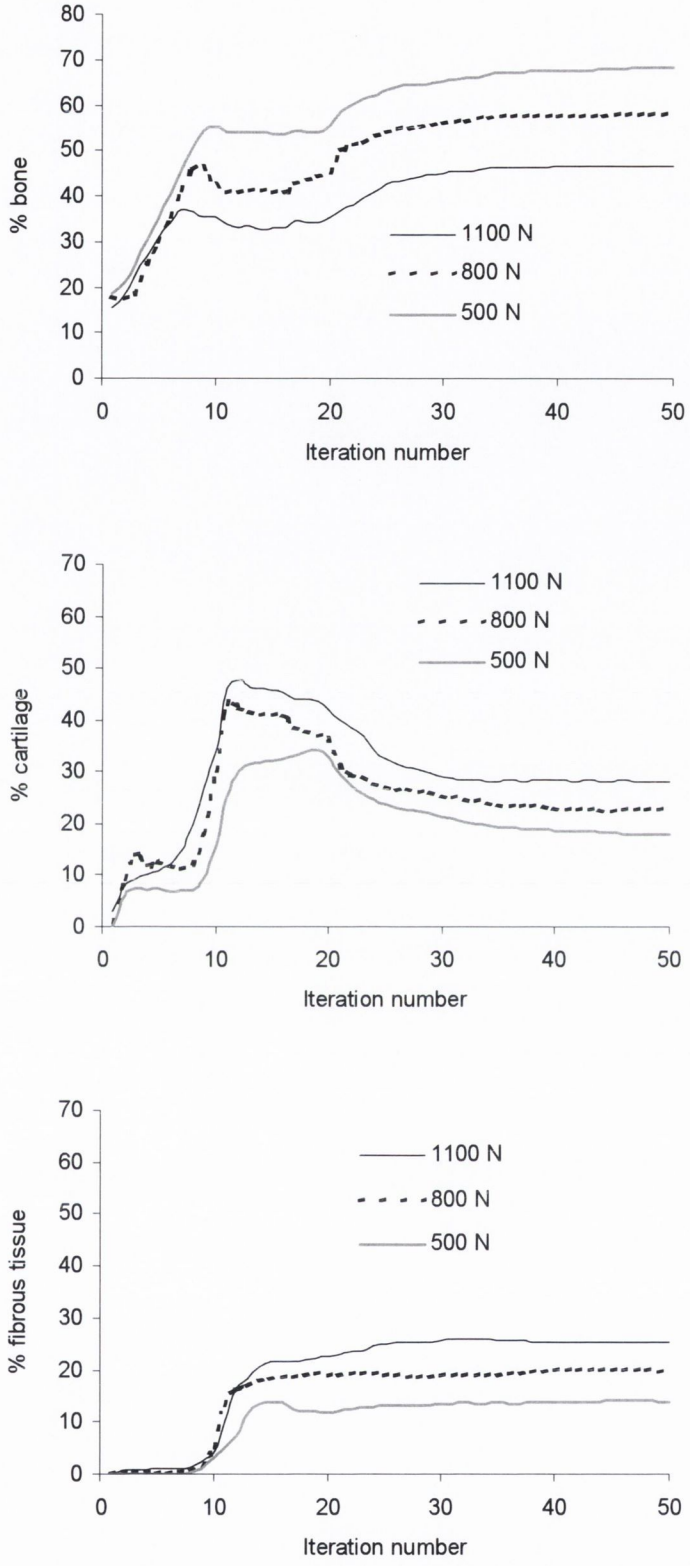

Fig. 4.17. *Comparisons of the amounts of (a) bone tissue (b) cartilage tissue and (c) fibrous tissue predicted to form in the 7 mm defect under different loads. For the purposes of this illustration granulation tissue is assumed to persist within an element until the total cell concentration exceeds 50.*

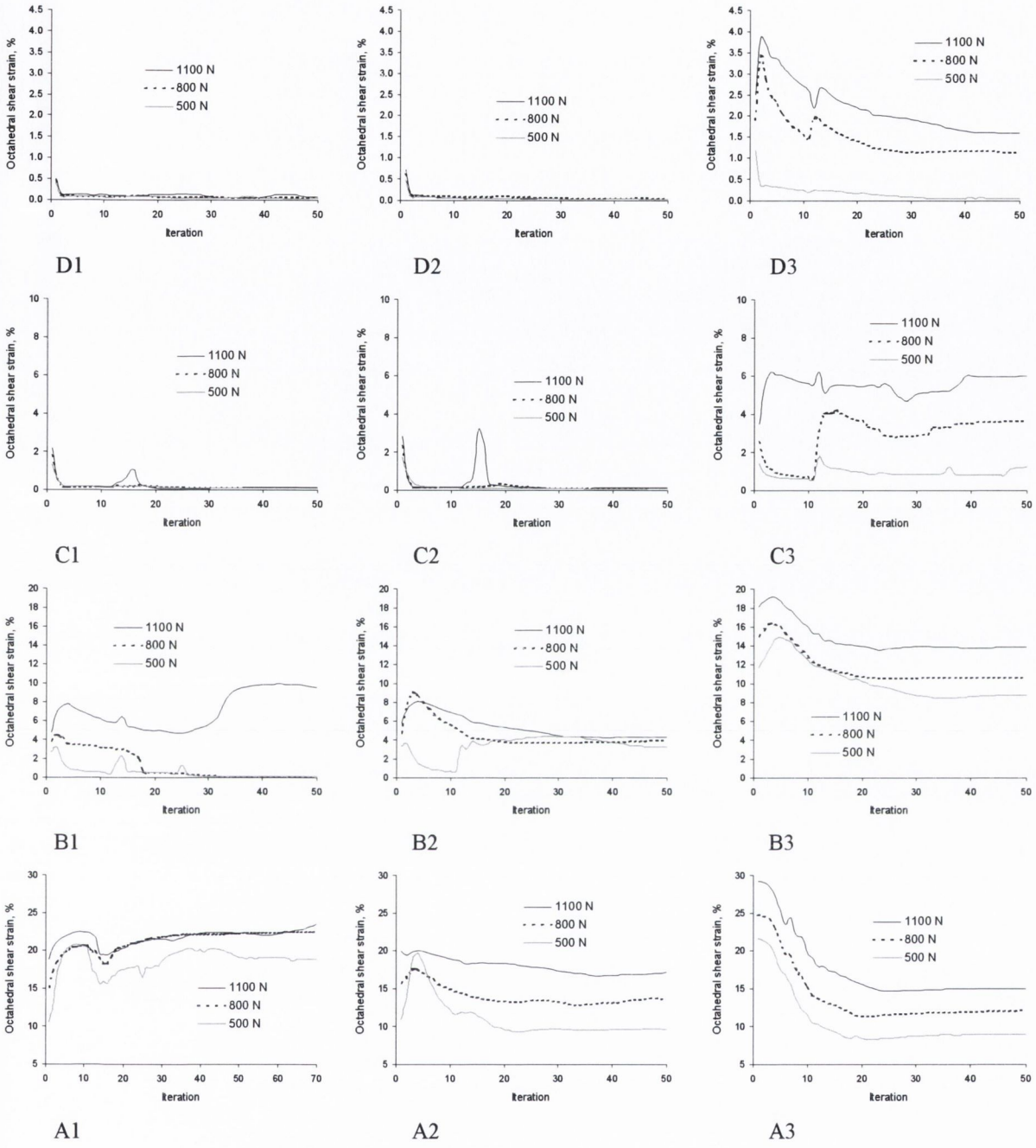

Fig. 4.18. *Predictions of octahedral shear strain in different elements within the 7 mm defect throughout the simulation for the 500 N, 800 N and 1100 N loading condition. The location of each element in the defect is indicated by the black dots in Fig. 4.12 (a).*

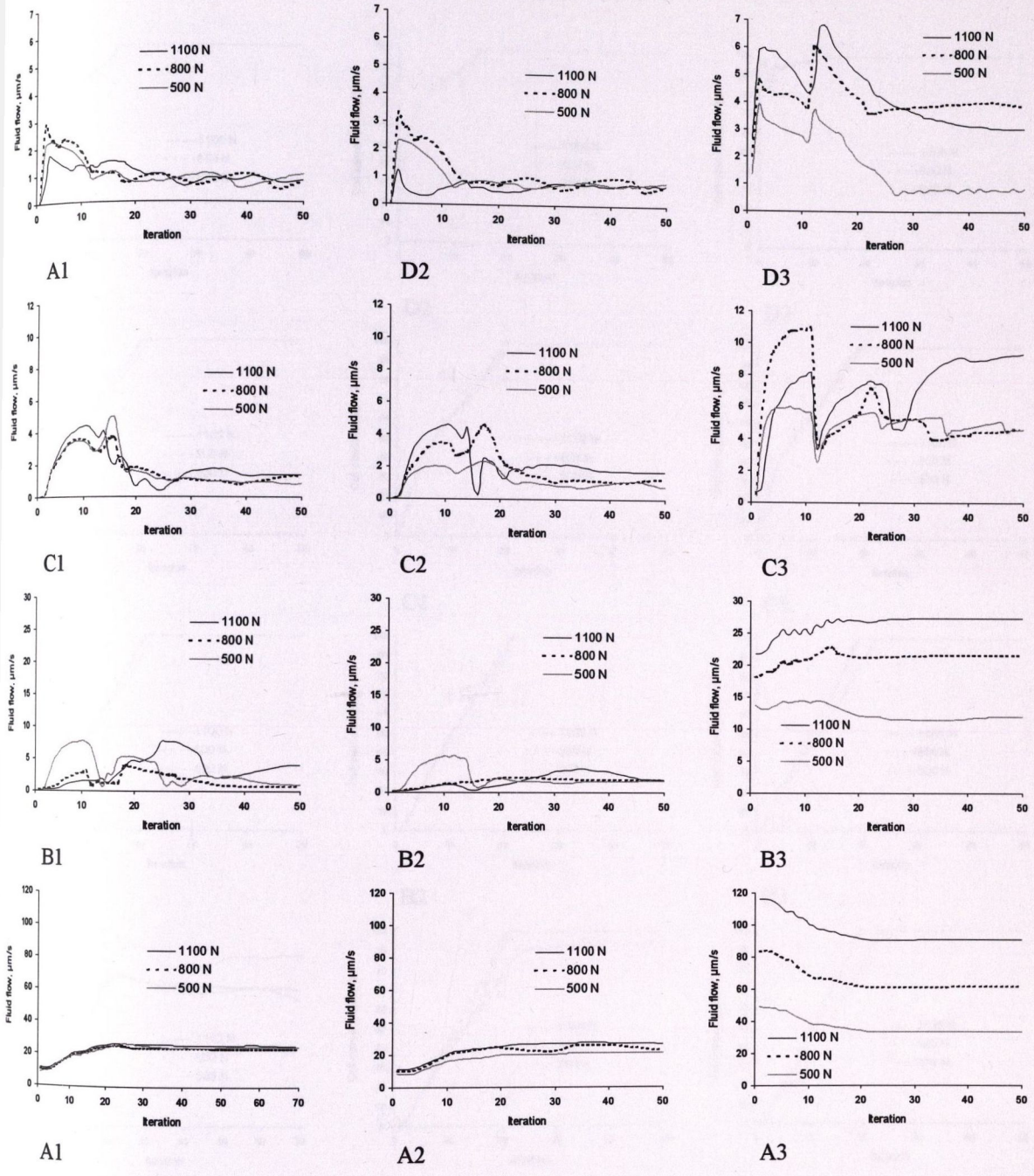

Fig. 4.19. *Predictions of interstitial fluid flow in different elements within the 7 mm defect throughout the simulation for the 500 N, 800 N and 1100 N loading condition. The location of each element in the defect is indicated by the black dots in Fig. 4.12 (a); therefore the graph in the top left hand corner represents the interstitial fluid flow in the element marked by the black dot in top left hand corner of Fig. 4.12.*

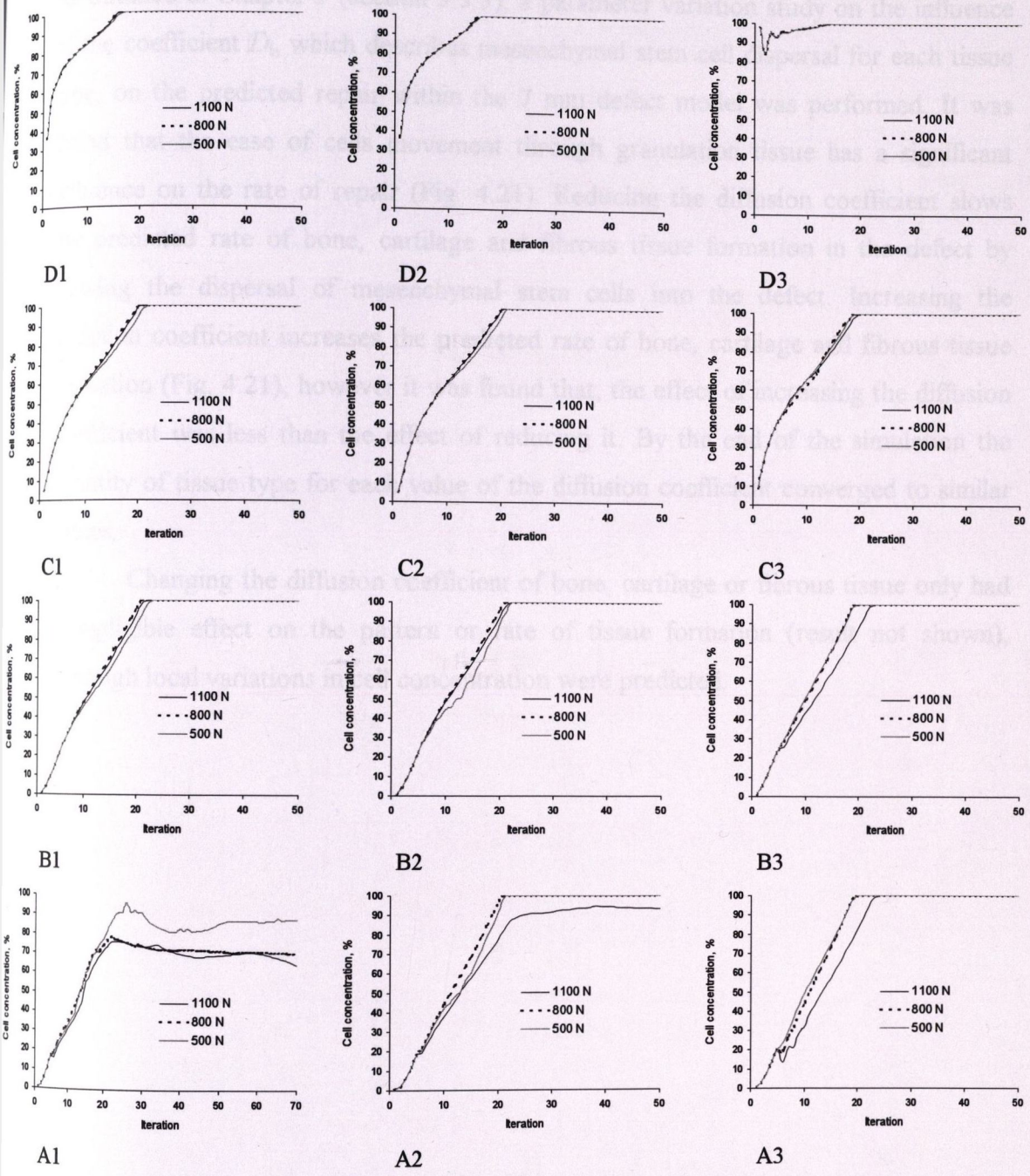

Fig. 4.20. *Predictions of total cell concentration in different elements within the 7 mm defect throughout the simulation for the 500 N, 800 N and 1100 N loading condition. The location of each element in the defect is indicated by the black dots in Fig. 4.12 (a); therefore the graph in the top left hand corner represents the total cell concentration in the element marked by the black dot in top left hand corner of Fig. 4.12.*

4.2.4 Parameter variation study of diffusion coefficients

As outlined in Chapter 3 (section 3.3.3), a parameter variation study on the influence of the coefficient D_i, which describes mesenchymal stem cell dispersal for each tissue type, on the predicted repair within the 7 mm defect model was performed. It was found that the ease of cells movement through granulation tissue has a significant influence on the rate of repair (Fig. 4.21). Reducing the diffusion coefficient slows the predicted rate of bone, cartilage and fibrous tissue formation in the defect by slowing the dispersal of mesenchymal stem cells into the defect. Increasing the diffusion coefficient increases the predicted rate of bone, cartilage and fibrous tissue formation (Fig. 4.21), however it was found that, the effect of increasing the diffusion coefficient was less than the effect of reducing it. By the end of the simulation the quantity of tissue type for each value of the diffusion coefficient converged to similar values.

Changing the diffusion coefficient of bone, cartilage or fibrous tissue only had a negligible effect on the pattern or rate of tissue formation (result not shown), although local variations in cell concentration were predicted.

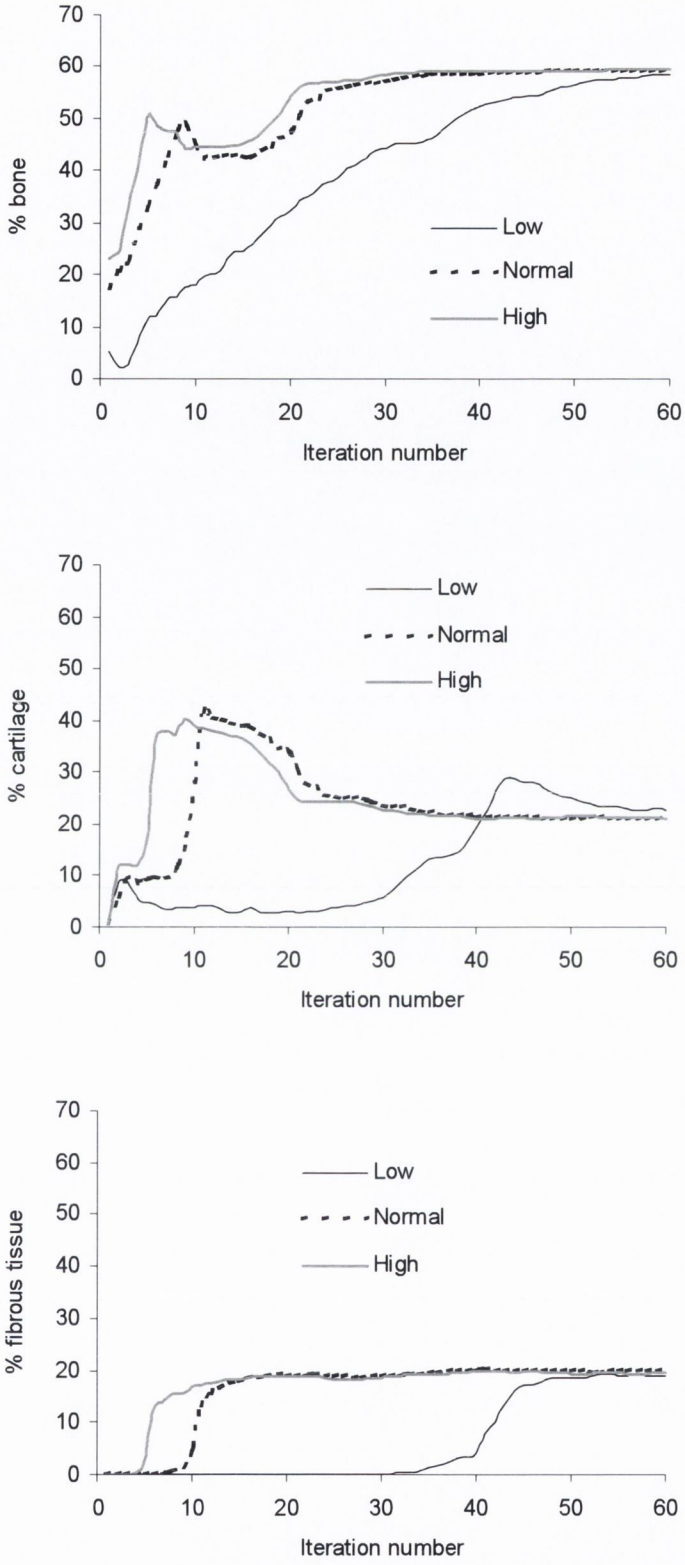

Fig. 4.21. *Influence of granulation tissue diffusion coefficient on the amounts of bone tissue, cartilage tissue and fibrous tissue predicted to form in the 7mm defect. For the purposes of this illustration granulation tissue is assumed to persist within an element until the total cell concentration exceeds 50.*

4.2.5 Influence of repair tissue integration

The importance of integration between the repair tissue and the natural tissue was studied by changing the interface conditions between the repair tissue and the surrounding tissue in the finite element model. Surprisingly only small differences in the patterns of repair were predicted between the completely integrated model and the poorly integrated model (Fig. 4.22). A region of cartilage formation persists in the base of the defect when the repair tissue is modelled as poorly integrated whereas this is not predicted to form when the repair tissue is modelled as completely integrated. Overall, modelling the repair tissue as poorly integrated to the surrounding tissue increases slightly the amount of fibrous tissue formation predicted to form within the defect, while reducing the predicted amount of ossification (Fig. 4.23). The amount of cartilage formation predicted to form is independent of how the repair tissue integration is modelled (Fig. 4.23).

Mechanical stimuli

Modelling the repair tissue as poorly integrated with the surrounding normal tissue reduces the magnitude of octahedral shear strain predicted at the interface between the repair tissue and the normal tissue from the base of the defect to the superficial layer (Fig. 4.24). A similar trend is not observed in the predicted magnitudes of interstitial fluid flow (Fig. 4.25). The magnitudes of octahedral shear strain and interstitial fluid flow throughout the remainder of the defect are largely unaffected by how repair tissue integration is modelled (Fig. 4.24 and Fig. 4.25).

Cell concentration

Except in a region of high strain at the articular surface (Fig. 4.26-A1), cell concentration throughout the defect is predicted to be independent of repair tissue integration (Fig. 4.26).

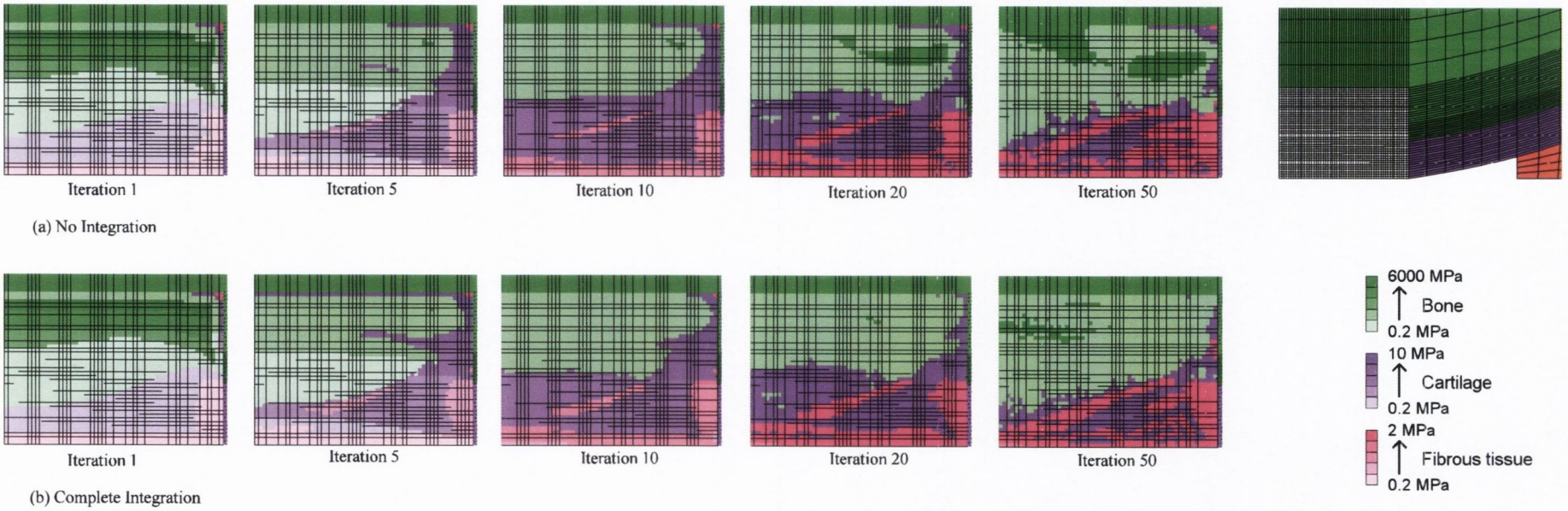

Fig. 4.22. *Predicted patterns of tissue differentiation in 7 mm defect during simulation of different repair tissue integration conditions.*

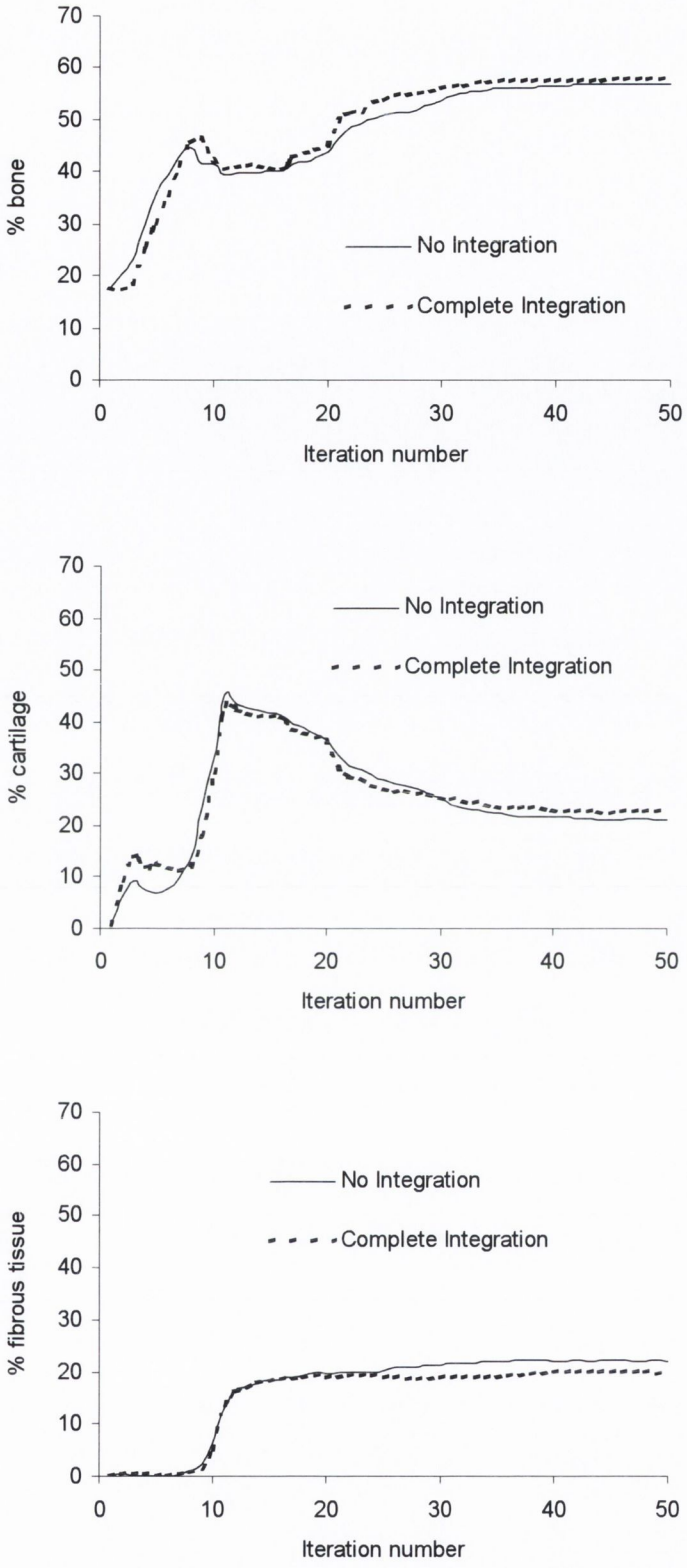

Fig. 4.23. *Comparisons of the amounts of bone tissue, cartilage tissue and fibrous tissue predicted to form in the 7 mm defect under different repair tissue integration conditions.*

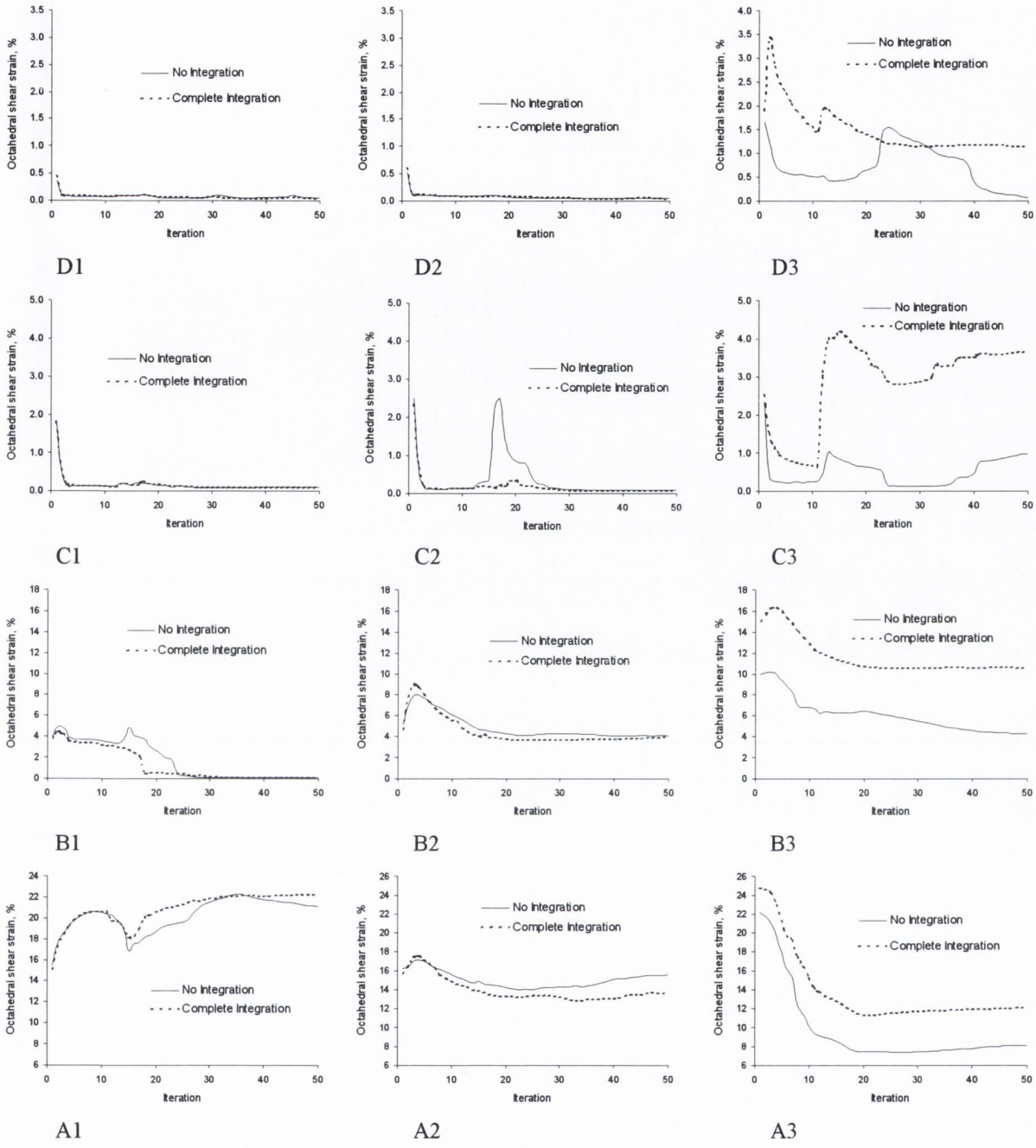

Fig. 4.24. *Predictions of octahedral shear strain in different elements within the 7 mm defect throughout the simulation assuming either complete or no integration between the repair tissue and the surrounding tissue. The location of each element in the defect is indicated by the black dots in Fig. 4.12 (a).*

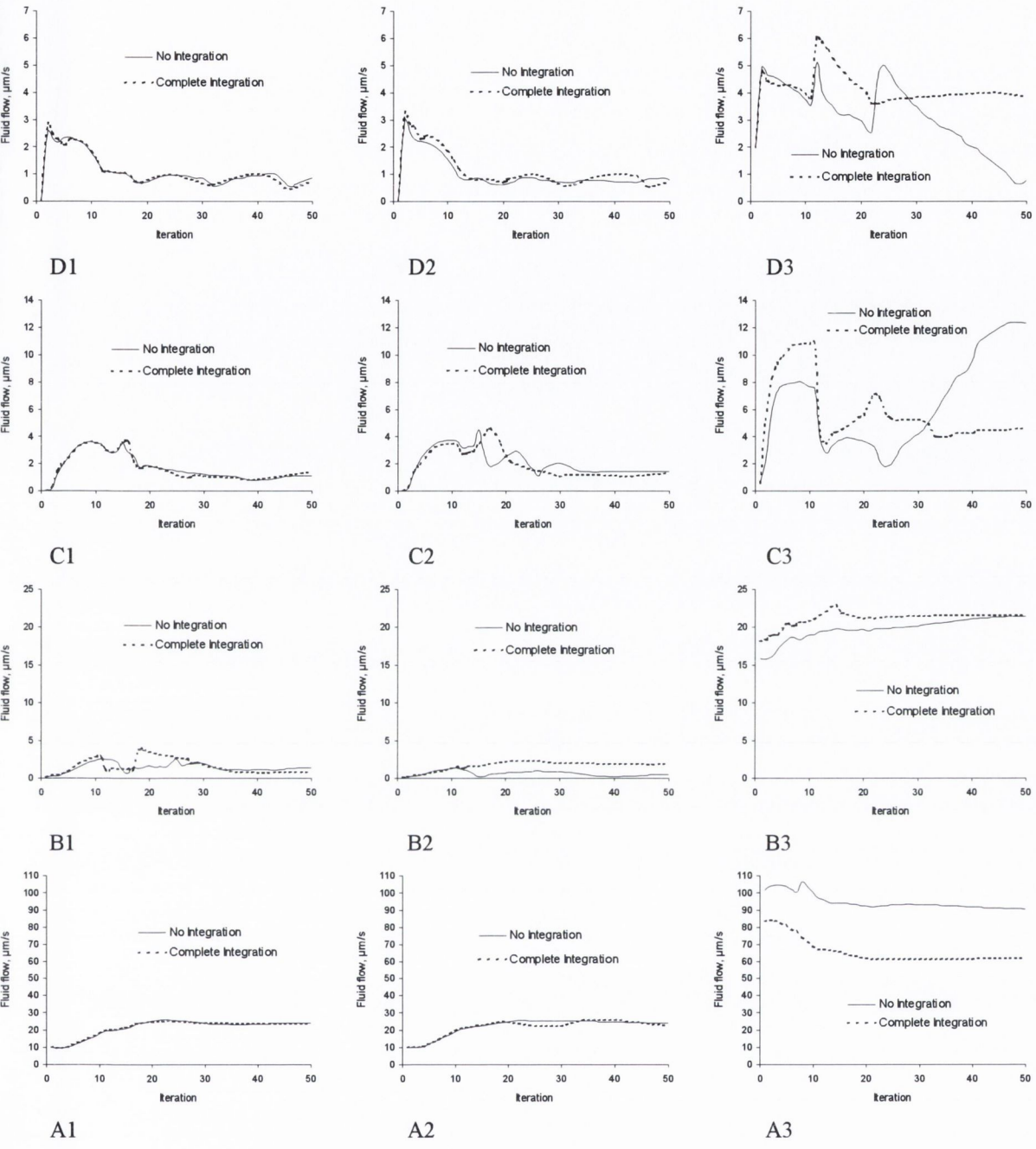

Fig. 4.25. *Predictions of interstitial fluid flow in different elements within the 7 mm defect throughout the simulation assuming either complete or no integration between the repair tissue and the surrounding tissue. The location of each element in the defect is indicated by the black dots in Fig. 4.12 (a).*

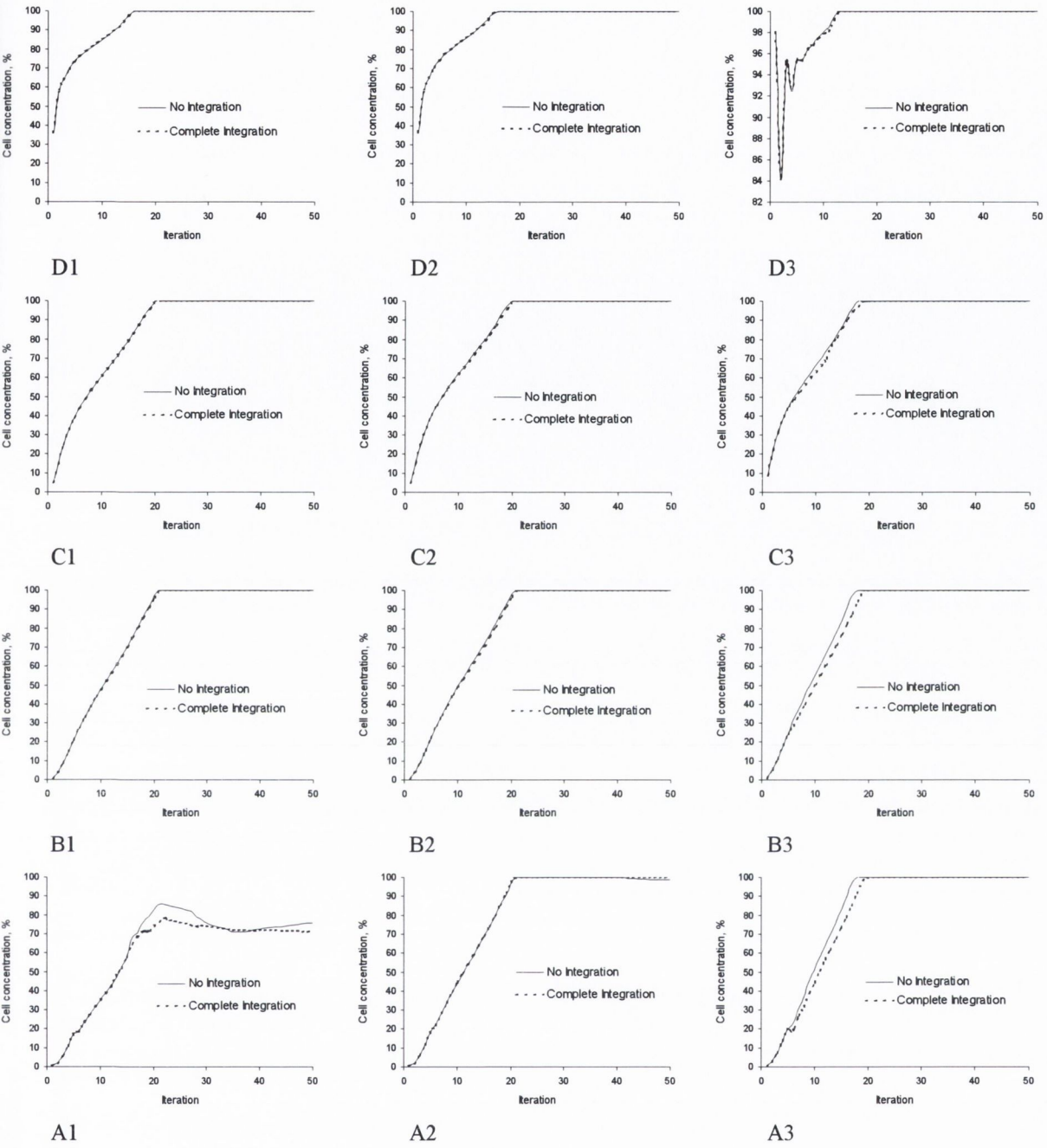

Fig. 4.26. *Predictions of cell concentration in different elements within the 7 mm defect throughout the simulation assuming either complete or no integration between the repair tissue and the surrounding tissue. The location of each element in the defect is indicated by the black dots in Fig. 4.12 (a).*

4.2.5 Influence of cellular mitosis

Three different models of cellular mitosis are compared. The standard model where mitosis is independent of cell concentration, where the rate of change in the number of cells is described as

$$\frac{dn^i}{dt} = D^i \nabla^2 n^i + P^i(S)n^i - K^i(S)n^i, \qquad \text{(Eqn 4.1)}$$

a second model where cell mitosis is removed after 30 iterations

$$\frac{dn^i}{dt} = D^i \nabla^2 n^i - K^i(S)n^i, \qquad \text{(Eqn. 4.2)}$$

and a third model where mitosis is dependent on cell concentration

$$\frac{dn^i}{dt} = D^i \nabla^2 n^i + \frac{(n^{max} - n^{tot})}{n^{max}} P^i(S)n^i - K^i(S)n^i. \qquad \text{(Eqn. 4.3)}$$

Removing cell proliferation after 30 iterations of the simulation had no effect on the ensuing tissue differentiation within the defect (Fig. 4.27). Introducing cell concentration dependent mitosis had the effect of slowing the rate of endochondral ossification within the defect, with greater amounts of cartilage formation and less bone formation predicted between iterations 15 and 35 when concentration dependant mitosis is introduced. After 35 iterations the different mitosis models converge to similar values. No significant difference is observed in fibrous tissue formation between the different cell mitosis models.

Mechanical stimuli

Removing cell proliferation after 30 iterations had a negligible effect on the mechanical stimuli predicted within the defect (Fig. 4.28 and Fig. 4.29). Increases in shear strain, and particularly fluid flow (Fig. 4.29), were predicted in the bony region of the defect with the concentration dependant mitosis model, resulting in the increased cartilage formation predicted between iterations 15 and 35 of the simulation.

Cell concentration

The rate of increase in cell concentration is significantly reduced throughout the defect when cell concentration dependent mitosis was introduced into the model (Fig. 4.30). Careful analysis of the results also reveals that in certain regions of the defect cell concentration does not reach 100%, or falls from 100% concentration in the case when cell mitosis is removed after 30 iterations (Fig. 4.30 - B1, B2, C2). This lowering in cell concentration in certain regions of the defect is not due directly to strain induced cell death, but rather due to migration of cells towards the articular surface where cell concentration is low due to strain induced cell death.

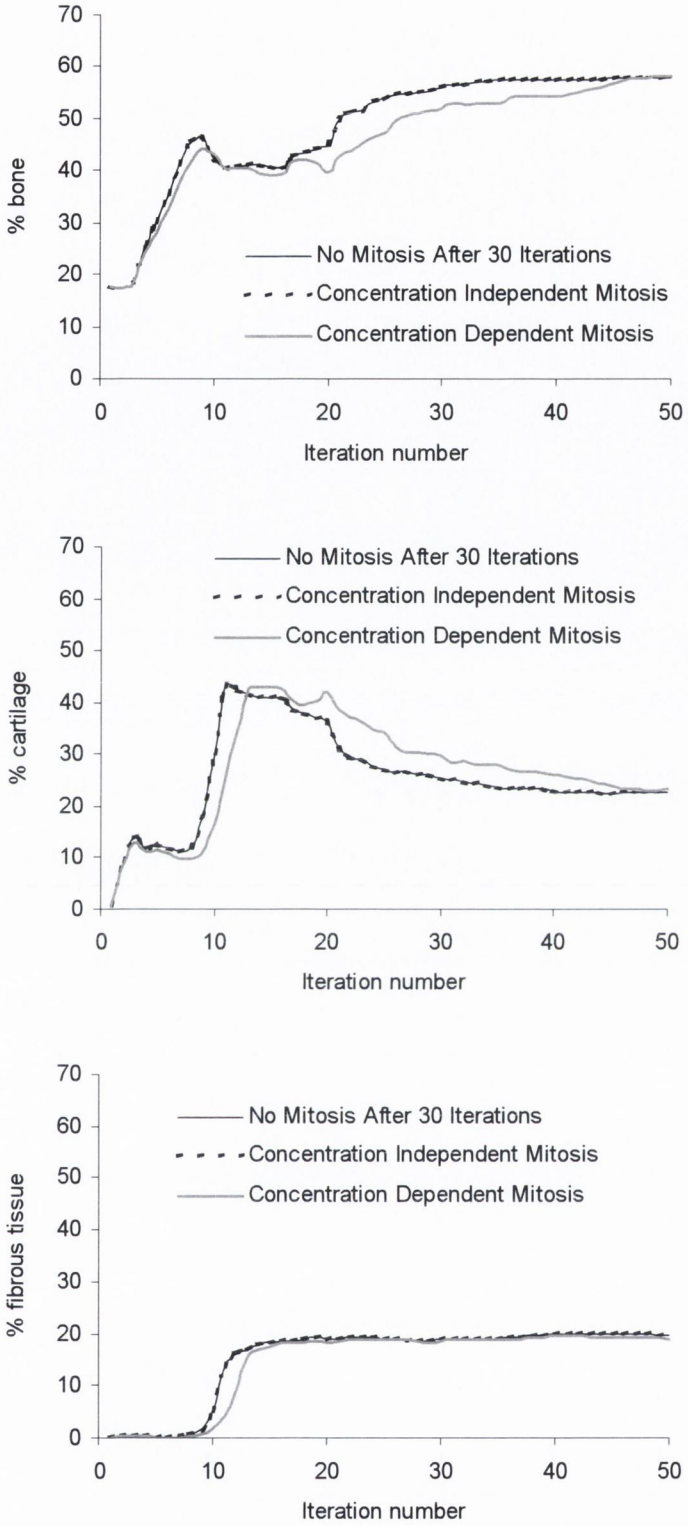

Fig. 4.27. *Comparisons of the amounts of (a) bone tissue (b) cartilage tissue and (c) fibrous tissue predicted to form in the 7 mm defect under different cell mitosis conditions.*

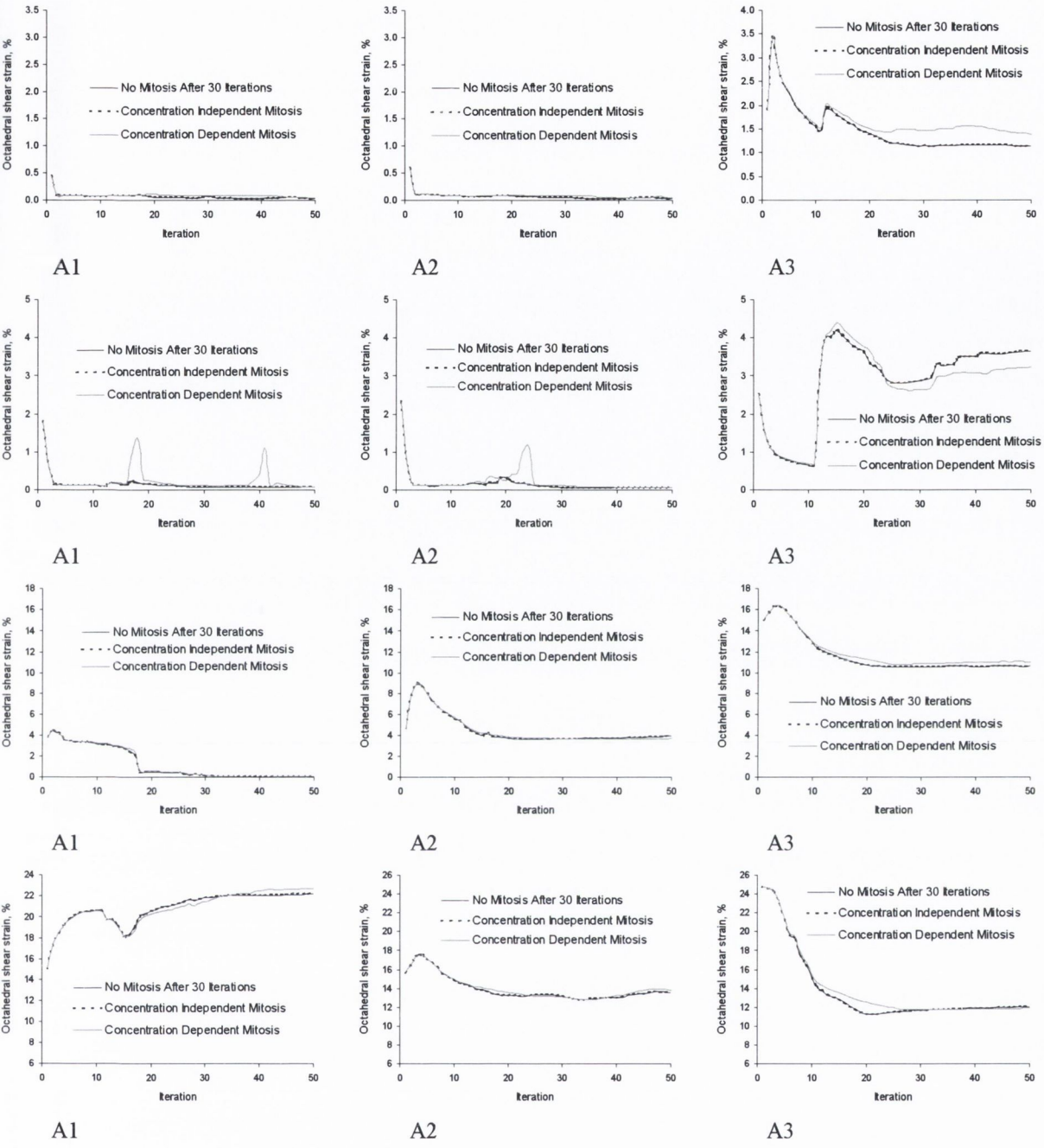

Fig. 4.28. *Predictions of octahedral shear strain in different elements within the 7 mm defect throughout the simulation assuming either concentration dependent mitosis, concentration independent mitosis or no mitosis after 30 iterations. The location of each element in the defect is indicated by the black dots in Fig. 4.12 (a).*

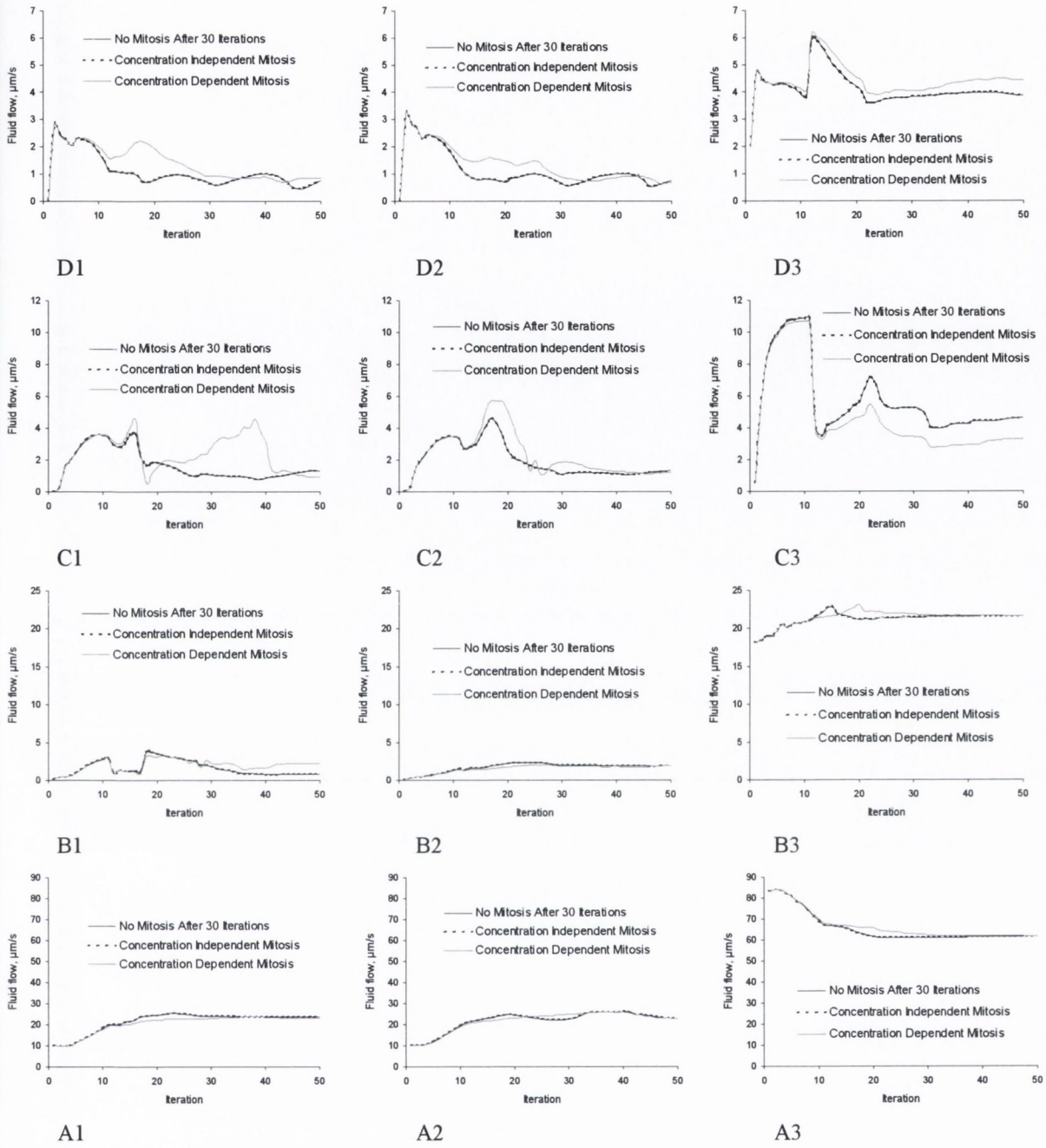

Fig. 4.29. *Predictions of interstitial fluid flow in different elements within the 7 mm defect throughout the simulation assuming either concentration dependent mitosis, concentration independent mitosis or no mitosis after 30 iterations. The location of each element in the defect is indicated by the black dots in Fig. 4.12 (a).*

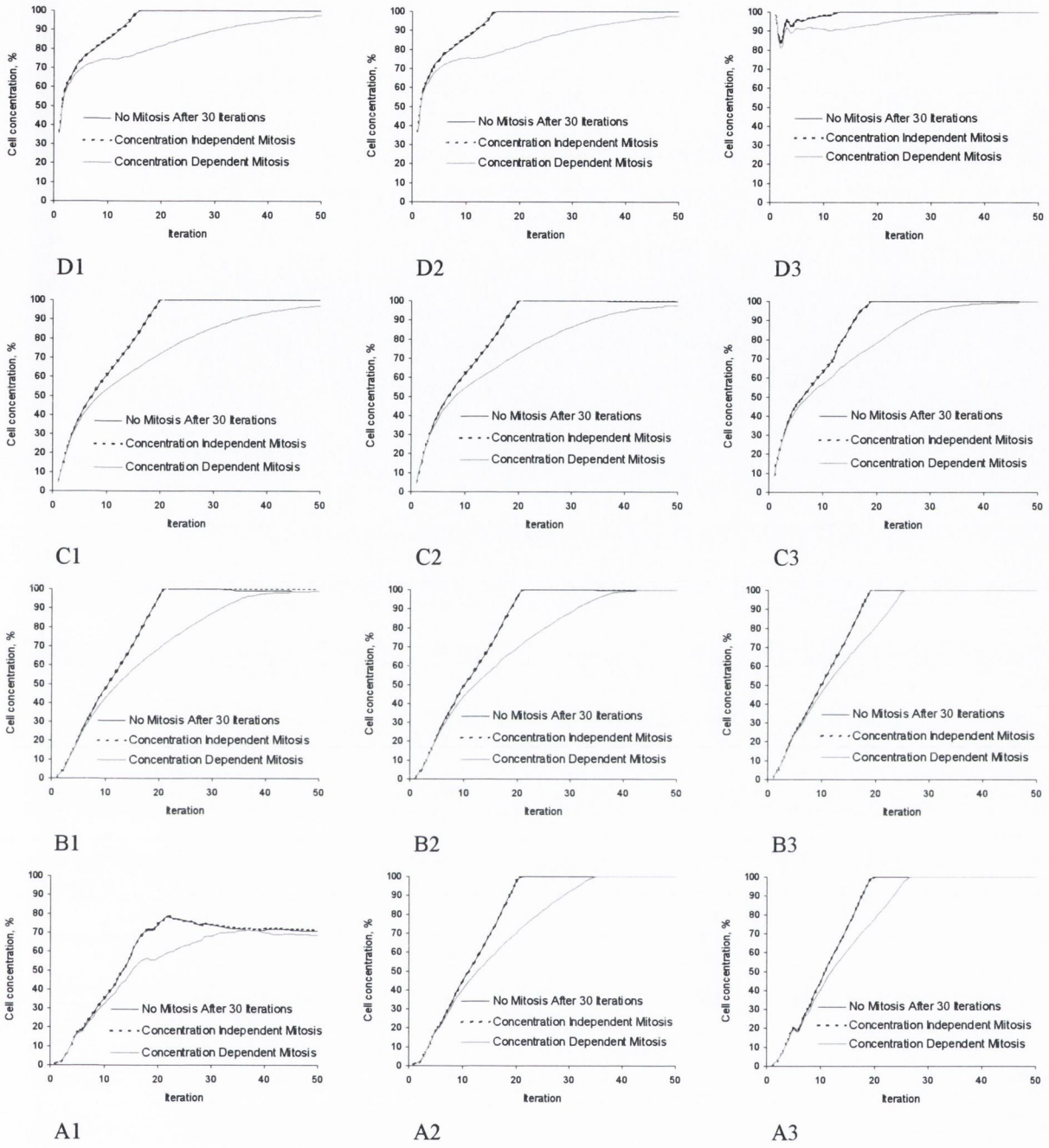

Fig. 4.30. *Predictions of total cell concentration in different elements within the 7 mm defect throughout the simulation assuming either concentration dependent mitosis, concentration independent mitosis or no mitosis after 30 iterations. The location of each element in the defect is indicated by the black dots in Fig. 4.12 (a).*

4.3 Mechanical properties of tissue engineered cartilage

In this section the results of the compressive tests of tissue engineered cartilage described in Section 3.4 of the methods chapter will be presented. The equilibrium aggregate modulus of constructs seeded with different numbers of cells will be first compared. Next the results of culturing tissue engineered constructs for a 12 week period will be presented. Finally the influence of different *in vitro* culture conditions on the mechanical properties of tissue engineered cartilage after different periods of *in vivo* development will be compared.

4.3.1 Influence of cell seeding density

The compressive modulus of tissue engineered cartilage constructs seeded with either 2 million, 4 million, 8 million or 16 million cells was determined (Table 4.1). The mean compressive modulus for each level of cell concentration used is plotted in Fig. 4.31. One way ANOVA was used to test for differences between the mean moduli of all levels of cell density used, however no one mean modulus was statistically different from the group ($p = 0.11$). Low sample numbers and large variability in the results meant that statistically significant results were not obtained. T-tests are used to compare different sets of results, however it should be noted that the overall trend is not statistically significant. The trend in the results suggests that the modulus of tissue engineered cartilage increases with increasing cell seeding density up to a certain seeding density value or range, above which the modulus reduces. A two sample t-test assuming unequal variance revealed that the mean modulus of scaffolds seeded with 4 million cells was different to those seeded with 8 million ($p = 0.024$) or 16 million ($p = 0.015$) cells, but not statistically different to scaffolds seeded with 2 million cells ($p = 0.123$).

Sample	2 million	4 million	8 million	16 million
1	9.75	19.58	8.47	13.64
2	13.47	12.46	4.95	6.68
3	5.77	14.68	5.4	4.33
4	8.45	13.73	4.52	6.43
5	7.89	17.2	7.03	4.8
6	29.684	29.304	26.513	21.602
7	22.898	14.473	11.15	12.086
8	-	32.556	18.912	16.909
Mean	13.98743	19.24788	10.86813	10.80963
Std Dev	8.938419	7.584976	7.885348	6.298004

Table 4.1. *Equilibrium aggregate modulus of tissue engineered cartilage constructs seeded with different numbers of cells.*

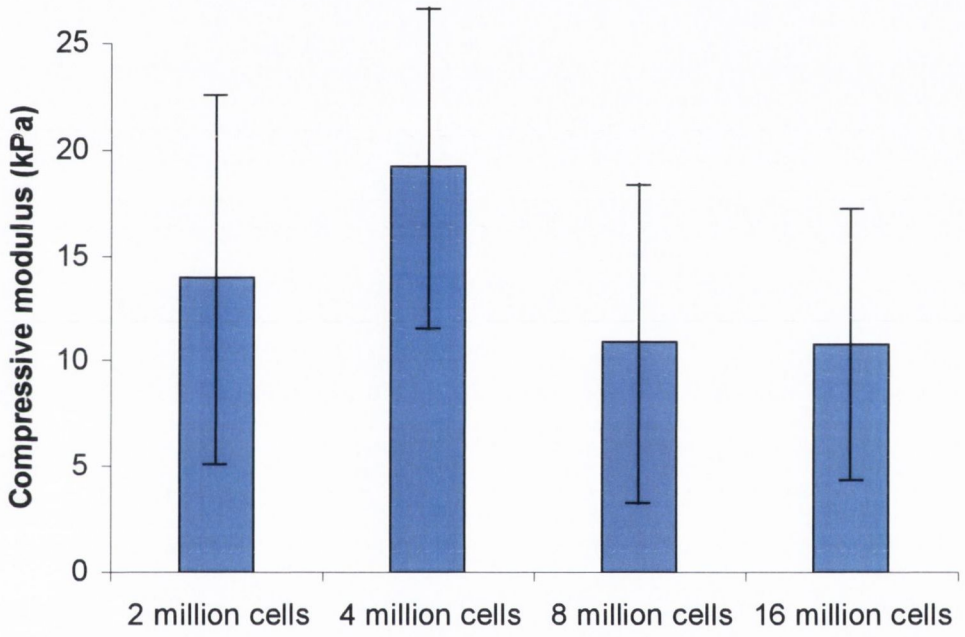

Fig. 4.31. *Mean equilibrium aggregate modulus of tissue engineered cartilage constructs seeded with different numbers of cells. (Error bars: ± Standard deviation.)*

4.3.2 Influence of long-term culture

After 12 weeks in culture, the compressive modulus and Young's modulus of tissue engineered cartilage approaches that of normal articular cartilage (Fig. 4.32). The mean compressive modulus was calculated to be 0.23 MPa, while the Young's modulus was calculated to be 0.19 MPa. From Eqn. 3.27, the mean Poison's ratio of tissue-engineered cartilage after 12 weeks in culture is calculated as 0.24.

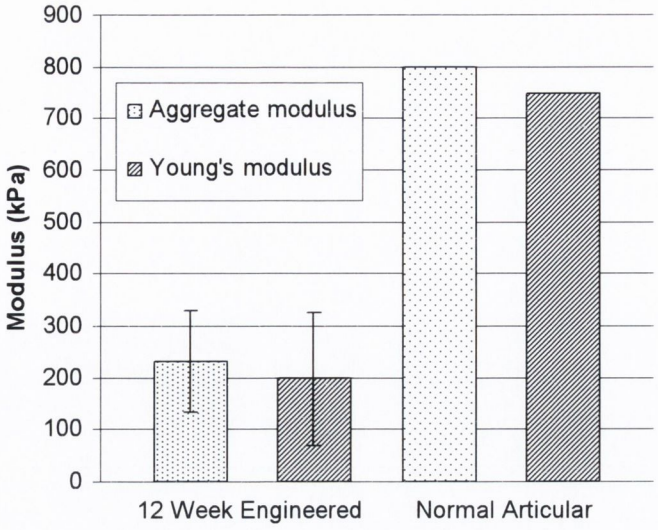

Fig. 4.32. *Comparison of the equilibrium aggregate and Young's modulus of normal articular cartilage and 12-week tissue engineered cartilage constructs. (Error bars: ± Standard deviation. Values for normal cartilage taken from Mow et al., 1980).*

4.3.3 Influence of in vitro pre-culture on in vivo development

Constructs seeded at the higher cell seeding density had a higher mean equilibrium aggregate modulus after 6 weeks *in vivo* with pre-culture in both the proliferating media ($p = 0.043$) and the differentiating media ($p = 0.189$), see Fig. 4.33. No obvious difference was observed between the proliferating media and the differentiating media. This trend of higher equilibrium moduli with a higher cell seeding density was also observed after 8 weeks, see Fig. 4.34. The mean equilibrium moduli of constructs seeded at the lower cell seeding density was higher when pre-cultured in differentiating ($p = 0.065$) and proliferating media ($p = 0.071$) compared to constructs implanted without pre-culture. The effect of pre-culture on constructs seeded at the higher cell seeding density is less significant, with constructs pre-cultured with the differentiating media having the highest equilibrium aggregate modulus.

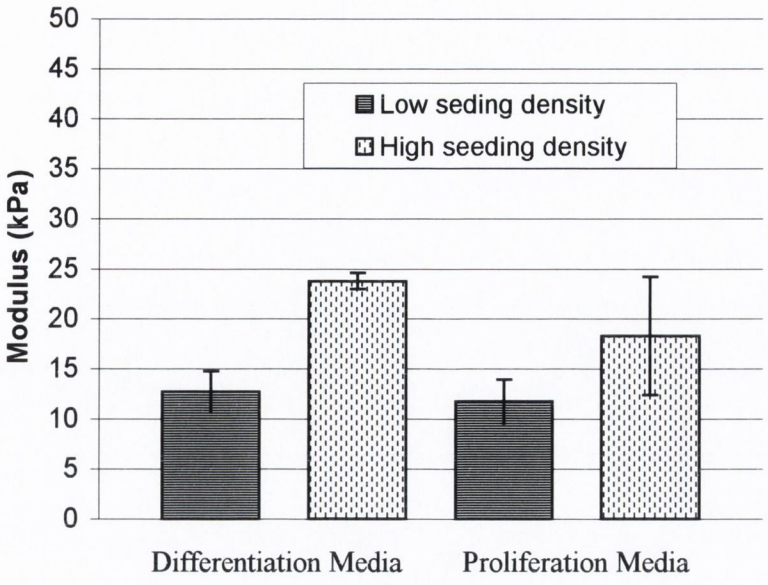

Fig. 4.33. *Comparison of the equilibrium aggregate modulus of tissue engineered cartilage constructs pre-cultured in different media after 6 weeks in vivo.*

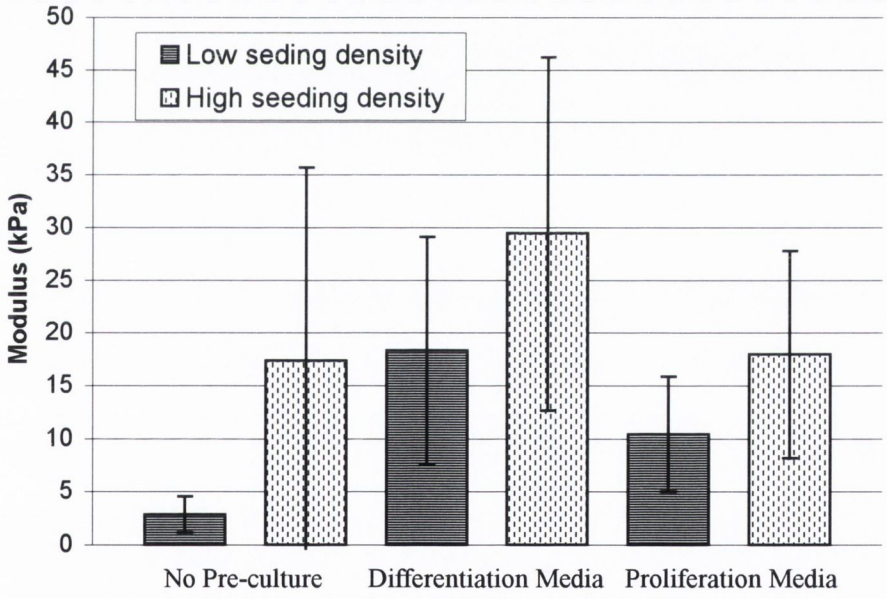

Fig. 4.34. *Comparison of the equilibrium aggregate modulus of tissue engineered cartilage constructs pre-cultured in different media after 8 weeks in vivo.*

4.4 Influence of engineered tissues on defect repair

The predicted patterns of tissue differentiation in an empty 7 mm defect (*spontaneous repair*) are compared to those in a 7 mm defect implanted with either a *low stiffness*, *medium stiffness* or *high stiffness* engineered cartilage tissue. The *low stiffness* and *medium stiffness* constructs correspond to the immature 40 day engineered cartilage and the mature 12 week engineered cartilage, while the *high stiffness* engineered cartilage corresponds to a hypothesised high stiffness engineered tissue, see section 3.5.2 of the methods chapter for details.

Dedifferenaition of this engineered cartilage tissue into a fibrous tissue is predicted to occur as early as iteration 5 regardless of the maturity of the engineered tissue, primarily at the articular surface (Fig. 4.35). Between iterations 5 and 20 significant endochondral ossification of the engineered-cartilage is predicted. By iteration 20 the pattern of tissue differentiation predicted in the empty defect and the defects implanted with either an *low stiffness* or *medium stiffness* engineered cartilage are remarkably similar. By iteration 50 each of the chondral regions of these defects has become a mixture of cartilage tissue and fibrous tissue. Only in the defect implanted with the *high stiffness* engineered cartilage is there a definite region of cartilage tissue predicted to persist within the defect, and even in this case a layer of fibrous tissue is predicted to form at the articular surface.

After 50 iterations of the simulation, the amount of bone tissue predicted to form in defects implanted with either the *low stiffness*, *medium stiffness* or *high stiffness* engineered tissue is almost identical (Fig. 4.36). A similar amount of fibrous and cartilage tissue is predicted to form with either the *low stiffness* or *mature* engineered tissues. Implanting the stiffer *optimal* construct was predicted to increase the amount of cartilage formation and reduce the amount of fibrous tissue formation within the defect.

Mechanical stimuli

The *high stiffness* engineered construct is predicted to reduce the magnitude of the octahedral shear strain at the articular surface (Fig. 4.37) and generally increase the magnitude of the interstitial fluid flow (Fig. 4.38). The high stiffness engineered cartilage is also generally predicted to reduce the magnitude of shear strain

throughout the remainder of the chondral part of the defect, explaining the reduced amounts of fibrous tissue predicted with the *high stiffness* engineered tissue.

Cell concentration

Cell concentration is not predicted to depend on engineered cartilage maturity, except in regions of cell death at the articular surface, where less cell death is predicted with greater engineered tissue maturity (result not shown).

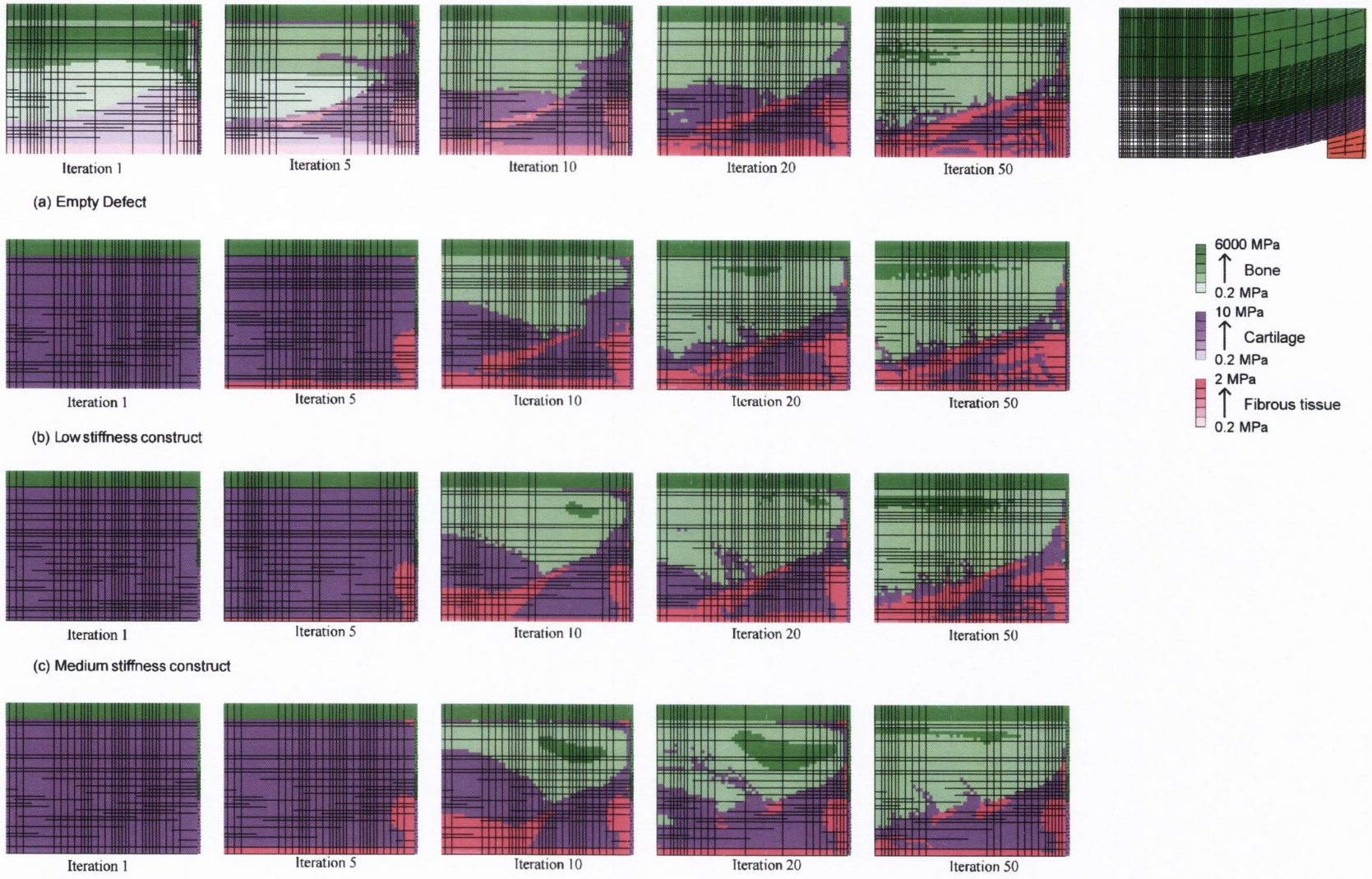

Fig. 4.35. *Predicted patterns of tissue differentiation in 7 mm defect during simulation of repair after implantation of an engineered tissue.*

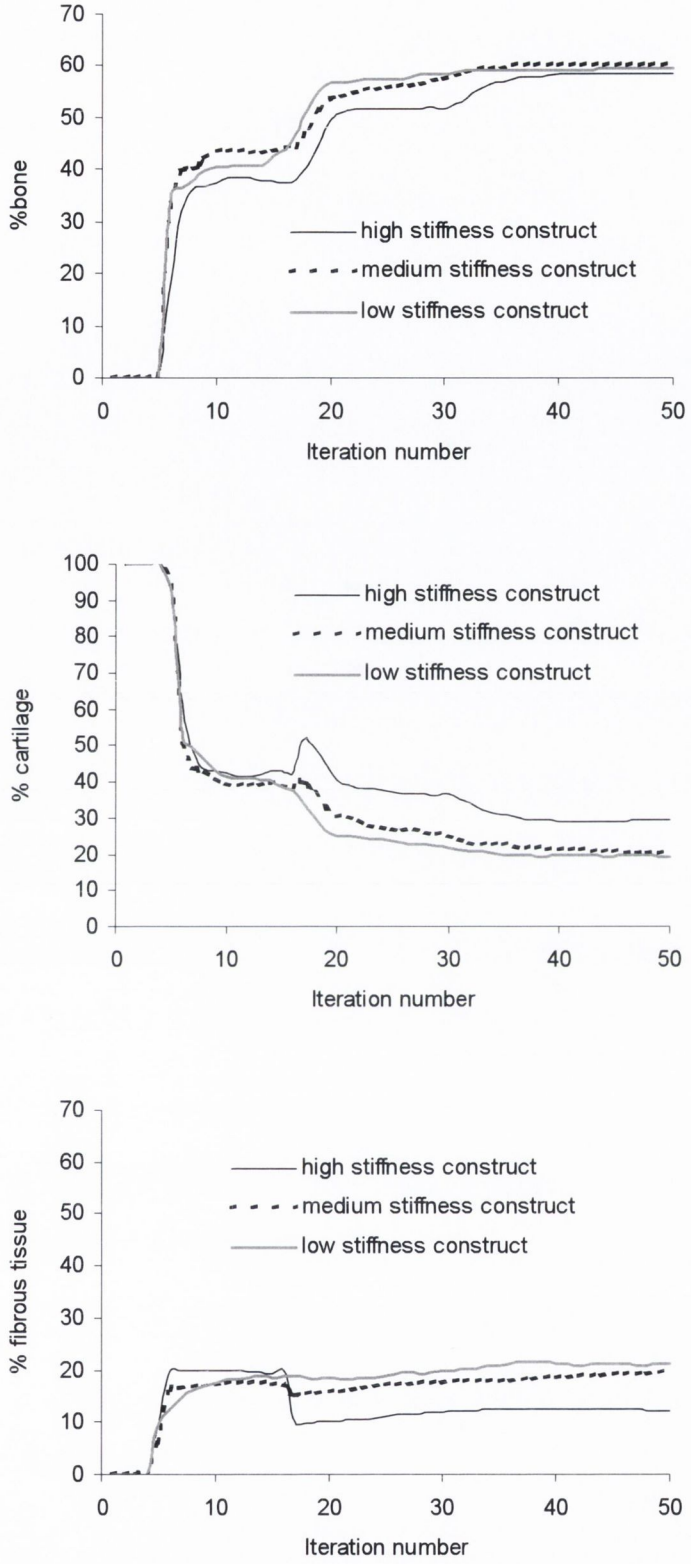

Fig. 4.36. *Comparisons of the amounts of (a) bone tissue (b) cartilage tissue and (c) fibrous tissue predicted to form in a 7 mm defect implanted with tissue engineered cartilage.*

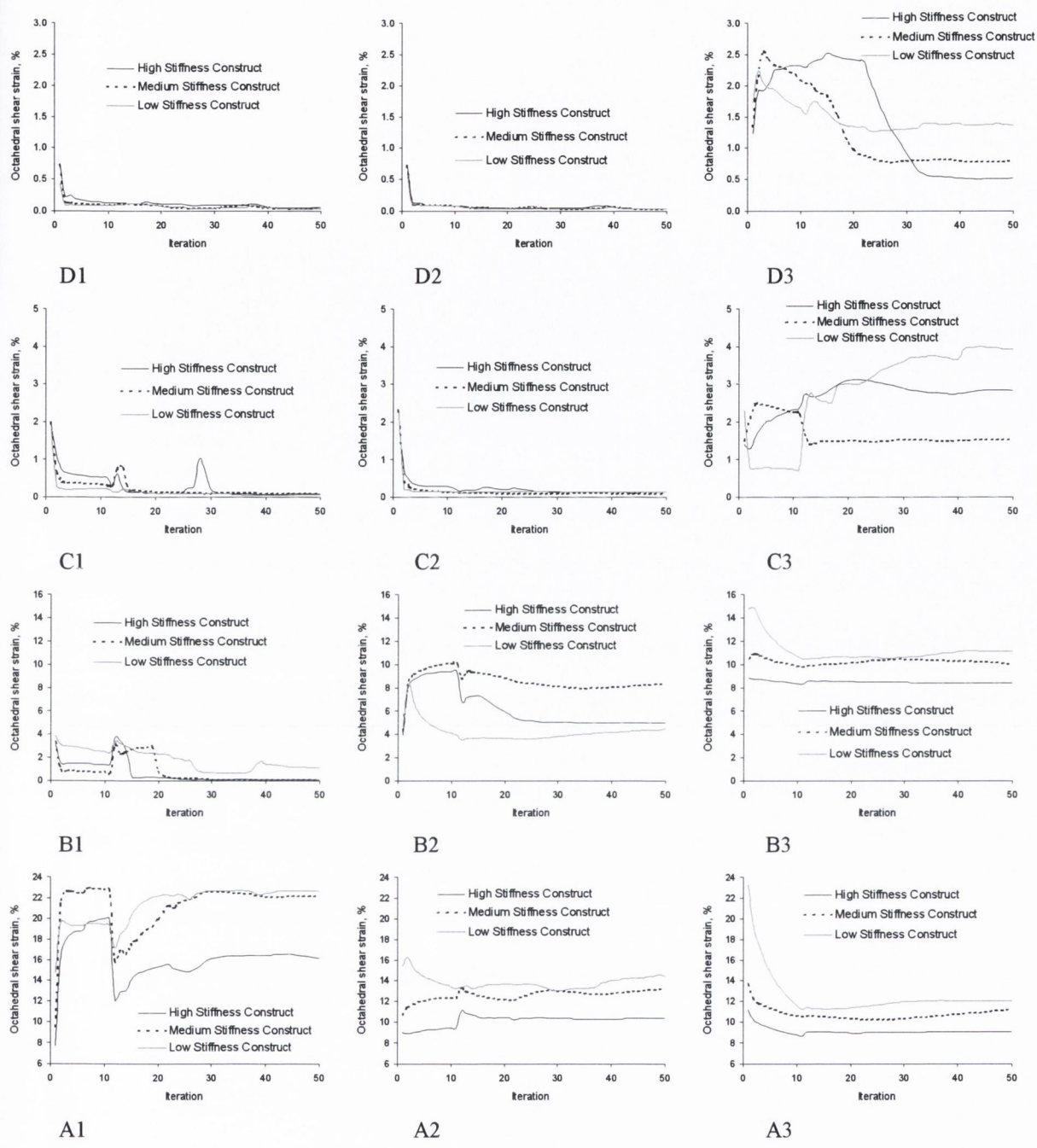

Fig. 4.37. *Predictions of octahedral shear strain in different elements within the 7 mm defect throughout the simulation with tissue engineered cartilage implanted. The location of each element in the defect is indicated by the black dots in Fig. 4.12 (a).*

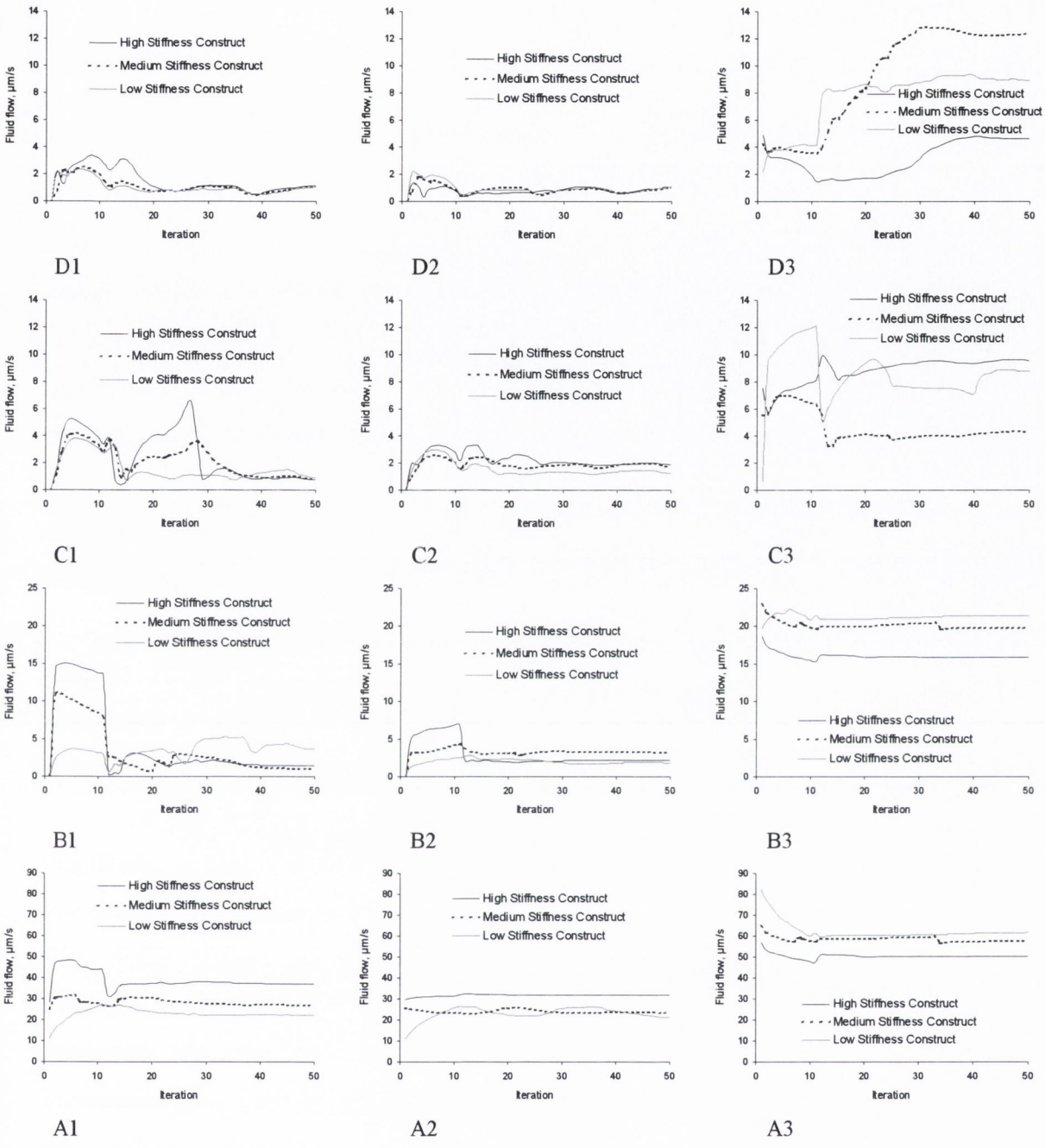

Fig. 4.38. *Predictions of interstitial fluid flow in different elements within the 7 mm defect throughout the simulation with tissue engineered cartilage implanted. The location of each element in the defect is indicated by the black dots in Fig. 4.12 (a).*

4.5 Influence of scaffolds on defect repair

The patterns of tissue differentiation in a 7mm defect implanted with a homogenous scaffold (Young's modulus = 10 MPa; permeability = 1e-14 N/ms^{-4}) are compared to those in an empty defect. The scaffold is predicted to support early chondrogenesis, with the chondral region of the defect consisting primarily of immature cartilage tissue after 5 iterations. Increased cartilage formation is predicted as the simulation of defect repair progresses, with a significantly greater proportion of the defect consisting of cartilage tissue after 10 iterations. By iteration 20 endochondral ossification is observed that continues until the bony region of the defect consists primarily of bone, apart from a pocket of cartilage tissue persisting in the upper corners of the defect. A remarkably uniform band of fibrous tissue persists at the articular surface, however the remainder of the chondral part of the defect consists nearly exclusively of cartilage tissue (Fig. 4.39).

For the majority of the simulation, the defect implanted with a scaffold consists of less bone tissue and greater amounts of cartilage tissue (Fig. 4.40). Implanting a scaffold is also predicted to reduce the amount of fibrous tissue formation within the defect by almost half (Fig. 4.40) by the end of the simulation.

At the articular surface, implanting a scaffold is predicted to reduce the magnitude of the octahedral shear strain compared to the empty defect (Fig. 4.41), however the magnitude of the interstitial fluid flow is predicted to be generally higher (Fig. 4.42). Within the centre of the chondral region of the defect, the scaffold functions to stabilise the mechanical stimuli, supporting a stimulus for cartilage formation. The stimuli within the bony region of the defect are generally higher after impanation of a scaffold, particularly at early time points, which helps explain why the scaffold is predicted to support early chondrogenesis within the regenerating defect.

The rate of increase in cell concentration is slightly higher in the presence of scaffold (Fig. 4.43). The scaffold also functions to prevent cell death at the articular surface (Fig. 4.43 A1).

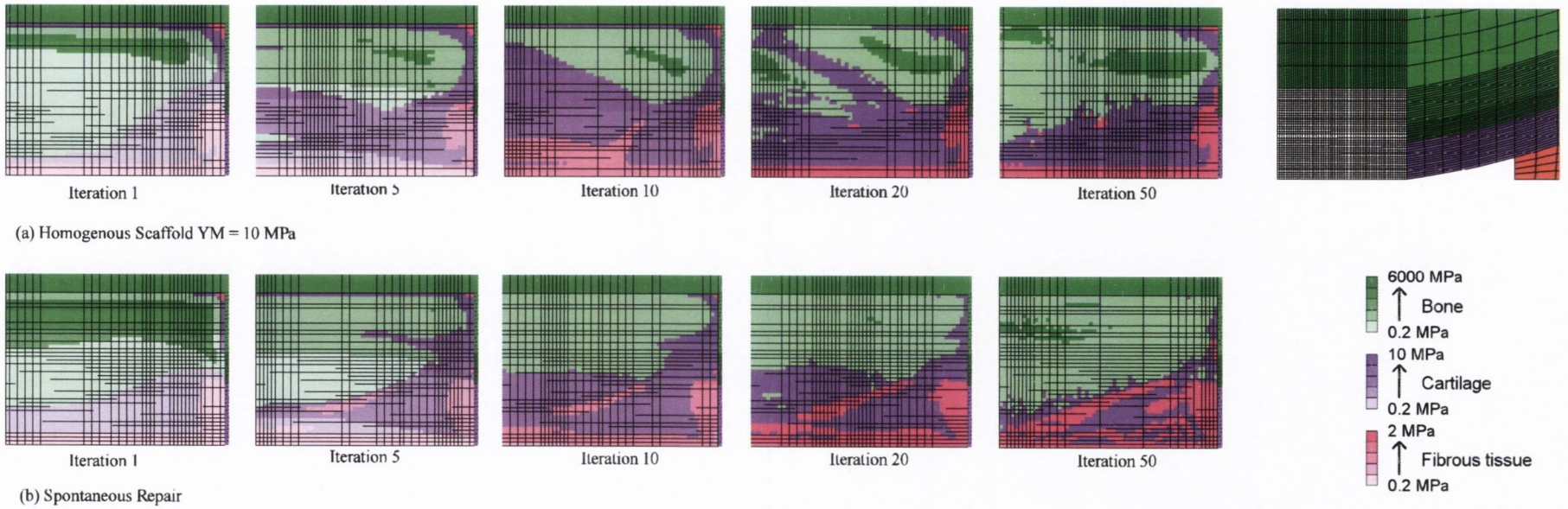

Fig. 4.39. *Predicted patterns of tissue differentiation in 7 mm defect with and without an implanted homogenous scaffold.*

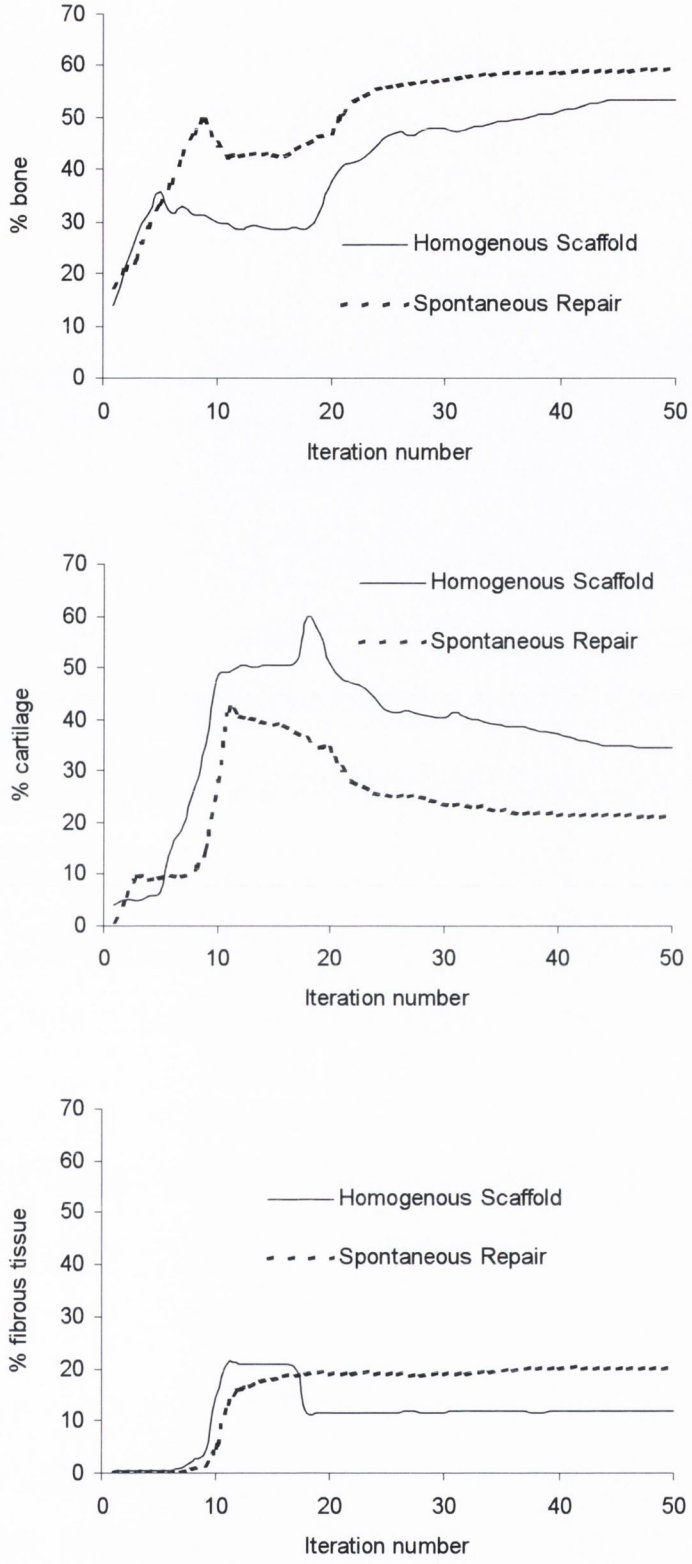

Fig. 4.40. *Comparisons of the amounts of bone tissue, cartilage tissue and fibrous tissue predicted to form in the 7 mm defect implanted with a homogenous scaffold.*

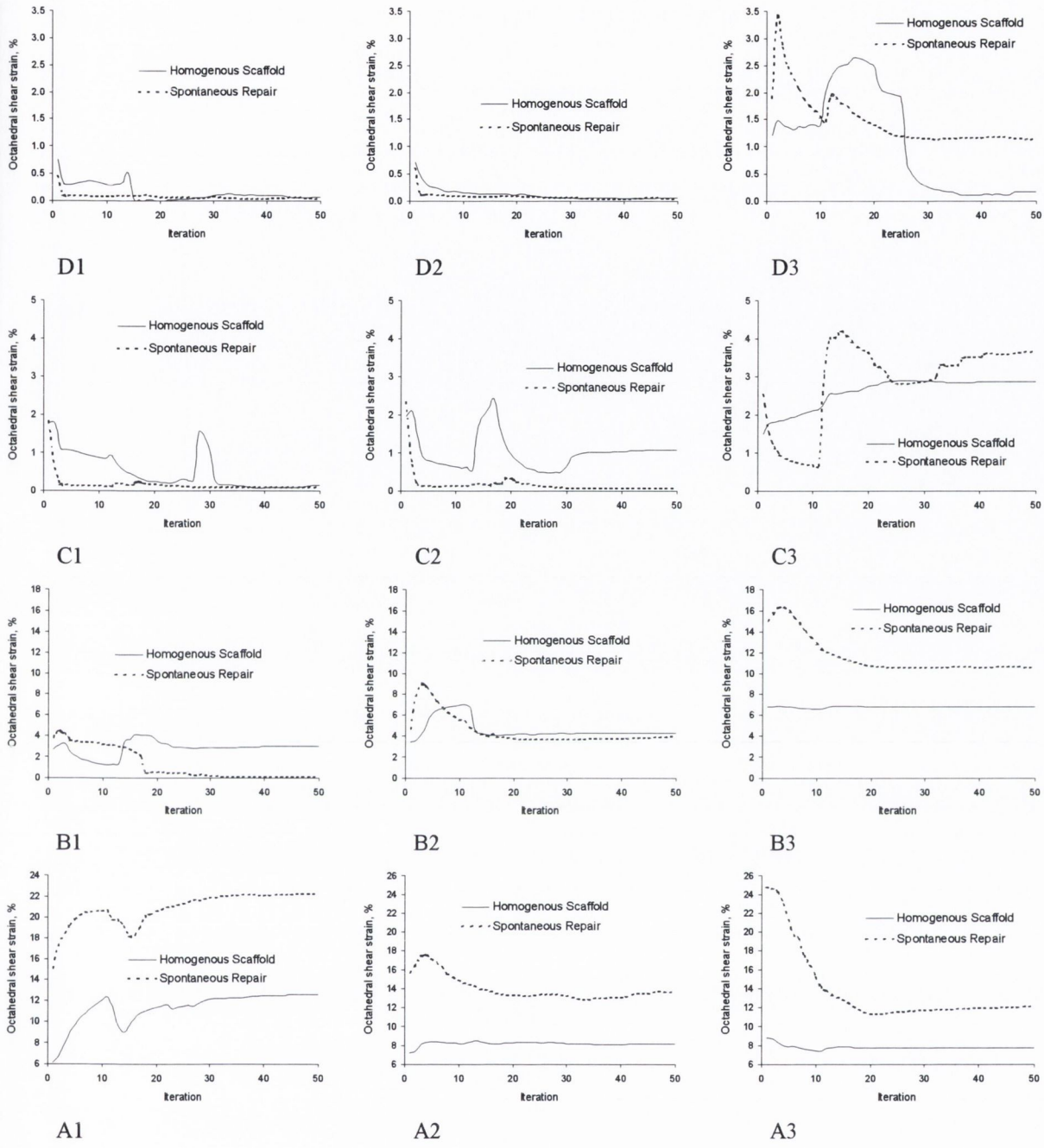

Fig. 4.41. *Predictions of octahedral shear strain in different elements within the 7 mm defect throughout the simulation with and without an implanted homogenous scaffold. The location of each element in the defect is indicated by the black dots in Fig. 4.12 (a).*

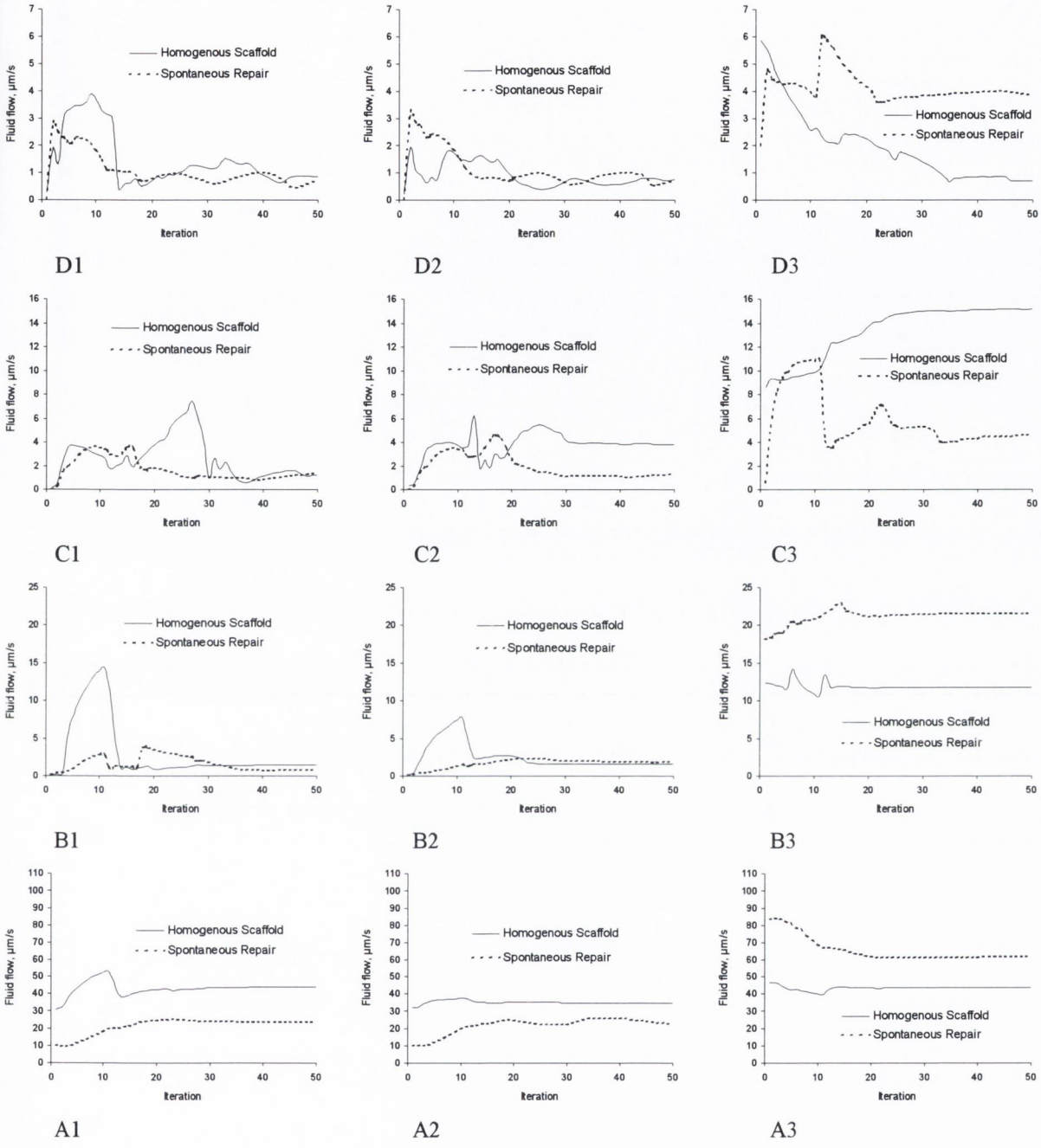

Fig. 4.42. *Predictions of interstitial fluid flow in different elements within the 7 mm defect throughout the simulation with and without an implanted homogenous scaffold. The location of each element in the defect is indicated by the black dots in Fig. 4.12 (a).*

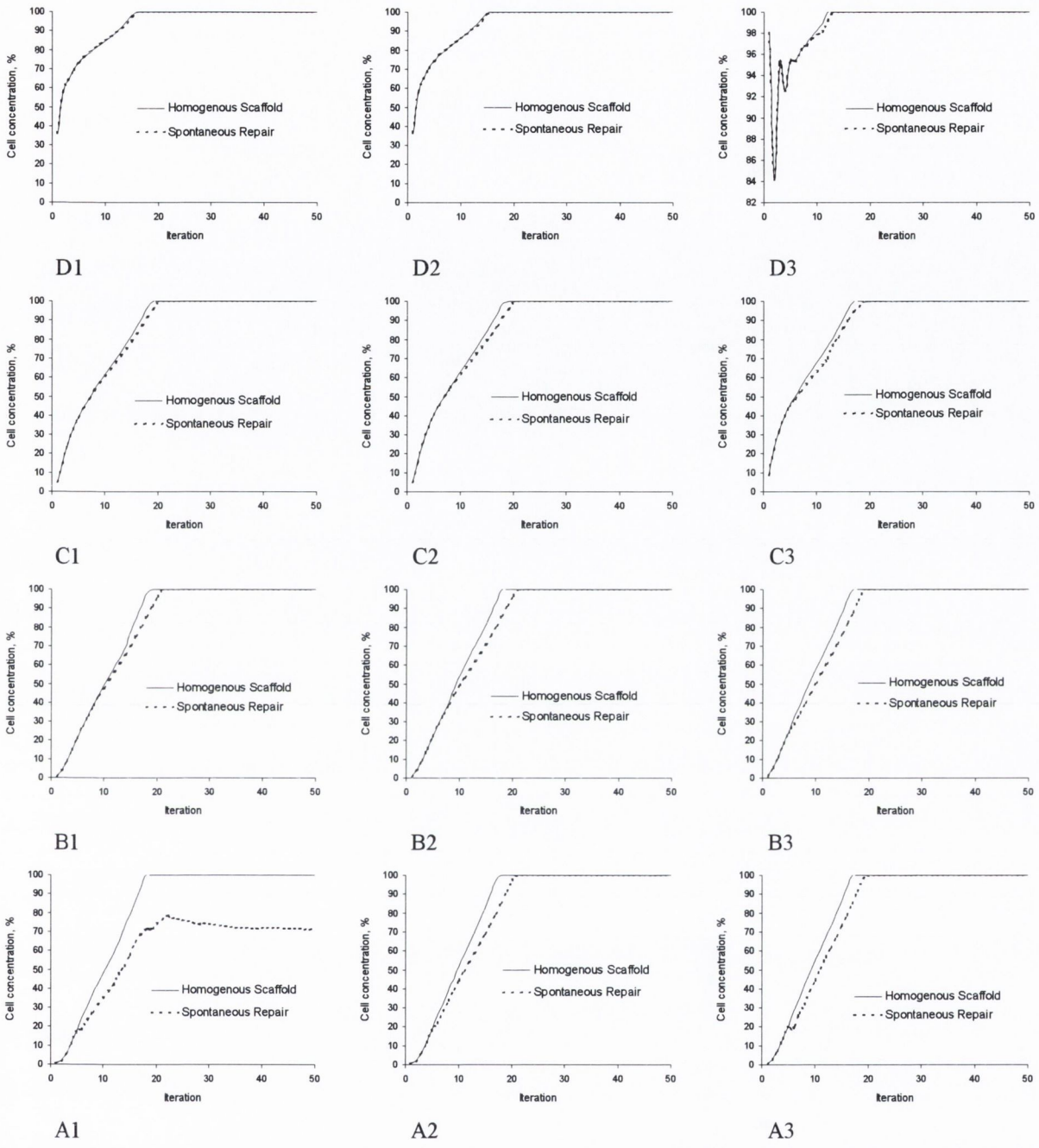

Fig. 4.43. *Predictions of total cell concentration in different elements within the 7 mm defect throughout the simulation with and without an implanted homogenous scaffold. The location of each element in the defect is indicated by the black dots in Fig. 4.12 (a).*

Influence of scaffold material properties: Young's modulus

The Young's modulus of the scaffold has a significant effect on the patterns of tissue differentiation and the amounts of each tissue type predicted to form within the defect. The most noticeable difference between the 5 MPa scaffold and the 20 MPa is the thicker layer of fibrous tissue predicted at the articular surface with the stiffer scaffold (Fig. 4.44). This trend continued when the modulus of the scaffold was increased to 50 MPa. Reducing the modulus of the scaffold to 1 MPa resulted in increased bone formation, reduced cartilage formation and increased fibrous tissue formation, similar in fact to that observed in an empty defect (Fig. 4.45). Interestingly increasing the modulus of the scaffold to 50 MPa was predicted to have a similar effect on the amounts of each tissue type within the defect as reducing the modulus to 1 MPa, with increased amounts of bone and fibrous tissue formation and reduced amounts of cartilage formation predicted to form within the defect (Fig. 4.45), however the patterns of tissue differentiation predicted using the two scaffolds were different (Fig. 4.44), with regions of cartilage predicted to persist in the base of the defect with the stiffer scaffolds. The 5MPa scaffold was predicted to produce the most uniformly thick layer of cartilage tissue.

The octahedral shear strain, interstitial fluid flow and cell concentration are plotted for 15 different locations throughout the defect. Increasing the modulus of the scaffold was predicted to reduce the magnitude of octahedral shear strain within the defect (Fig. 4.47). This reduction in strain was not accompanied by a reduction in the magnitude of interstitial fluid flow within the defect, with lager magnitudes of flow predicted within the centre of the chondral region of the defect (Fig. 4.48). These higher magnitudes of fluid flow were responsible for the increased amounts of fibrous tissue formation predicted when the modulus of the scaffold was increased. The modulus of the scaffold did not greatly affect the predicted cell concentrations within the defect, with no cell death predicted after implanting a scaffold with a modulus greater than 5 MPa (result not shown).

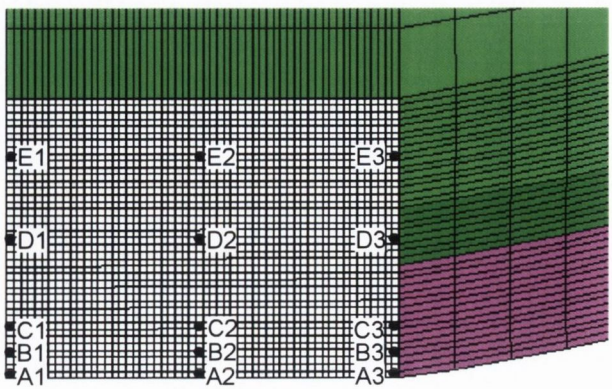

Fig. 4.46

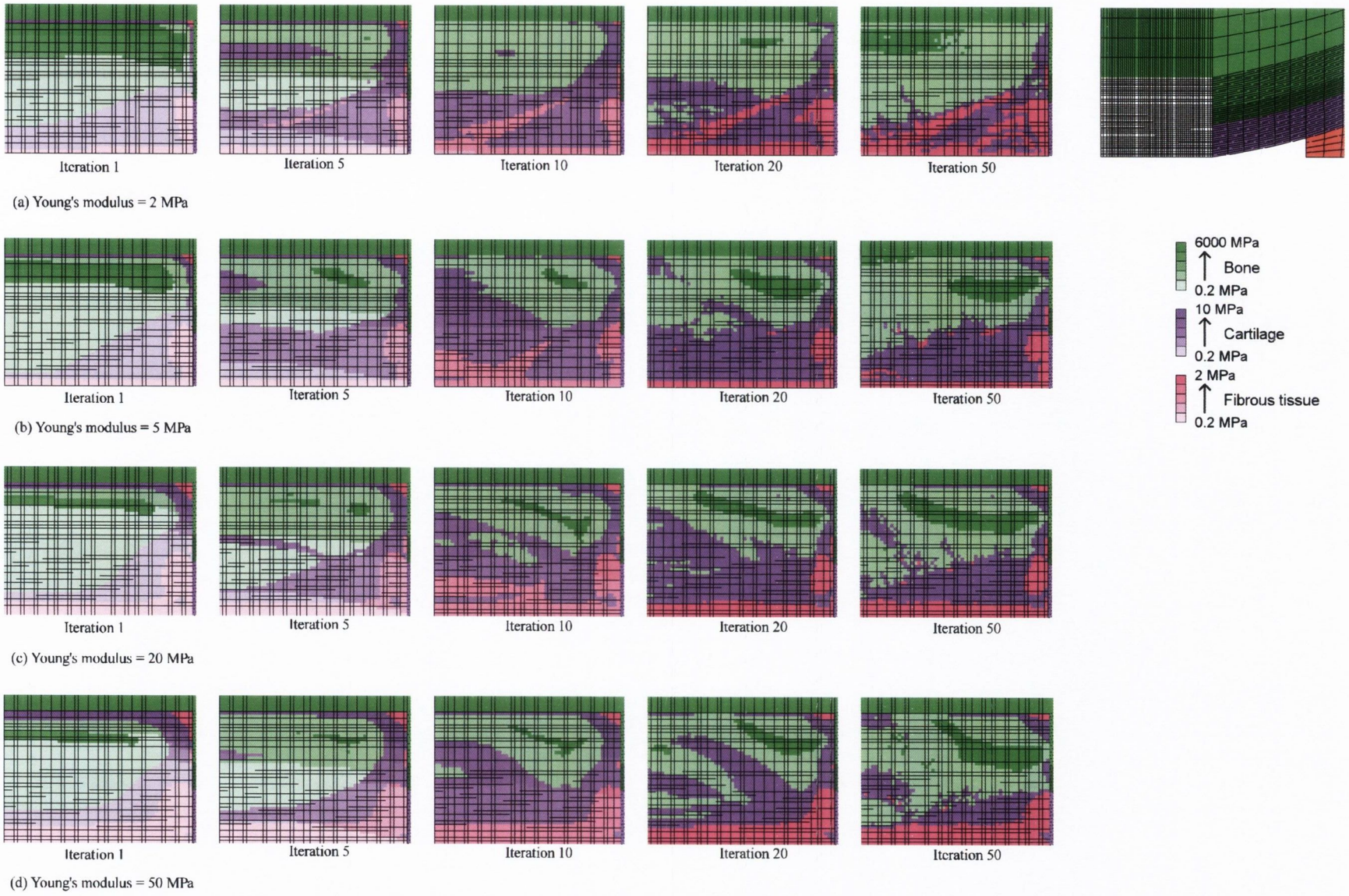

Fig. 4.44. *Predicted patterns of tissue differentiation in 7 mm defect with and without an implanted homogenous scaffold.*

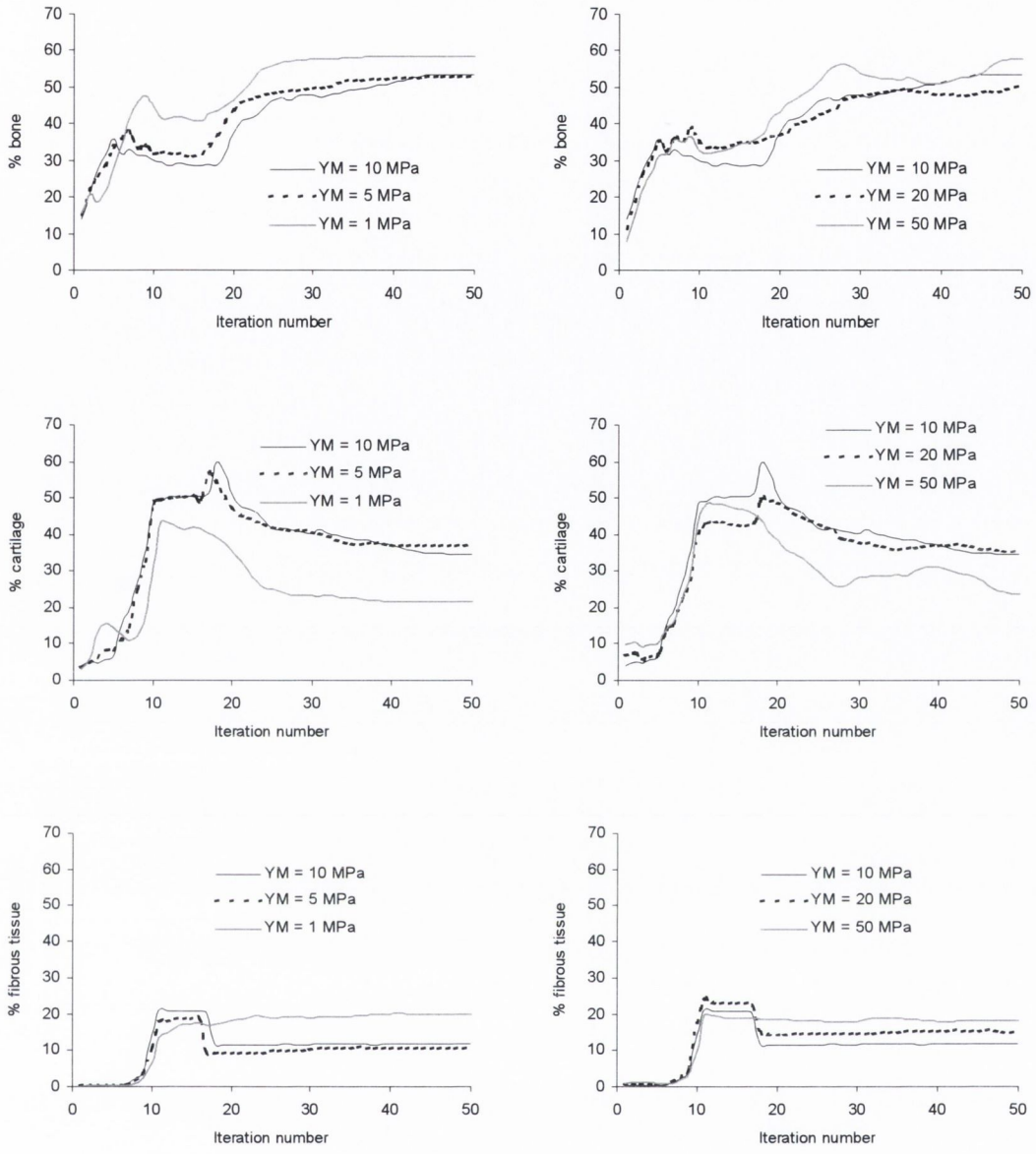

(a) Reducing E (b) Increasing E

Fig. 4.45. *Comparisons of the amounts of bone tissue, cartilage tissue and fibrous tissue predicted to form in the 7 mm defect implanted with a homogenous scaffold. (a) Influence of reducing the Young's modulus of the scaffold. (b) Influence of increasing the Young's modulus of the scaffold.*

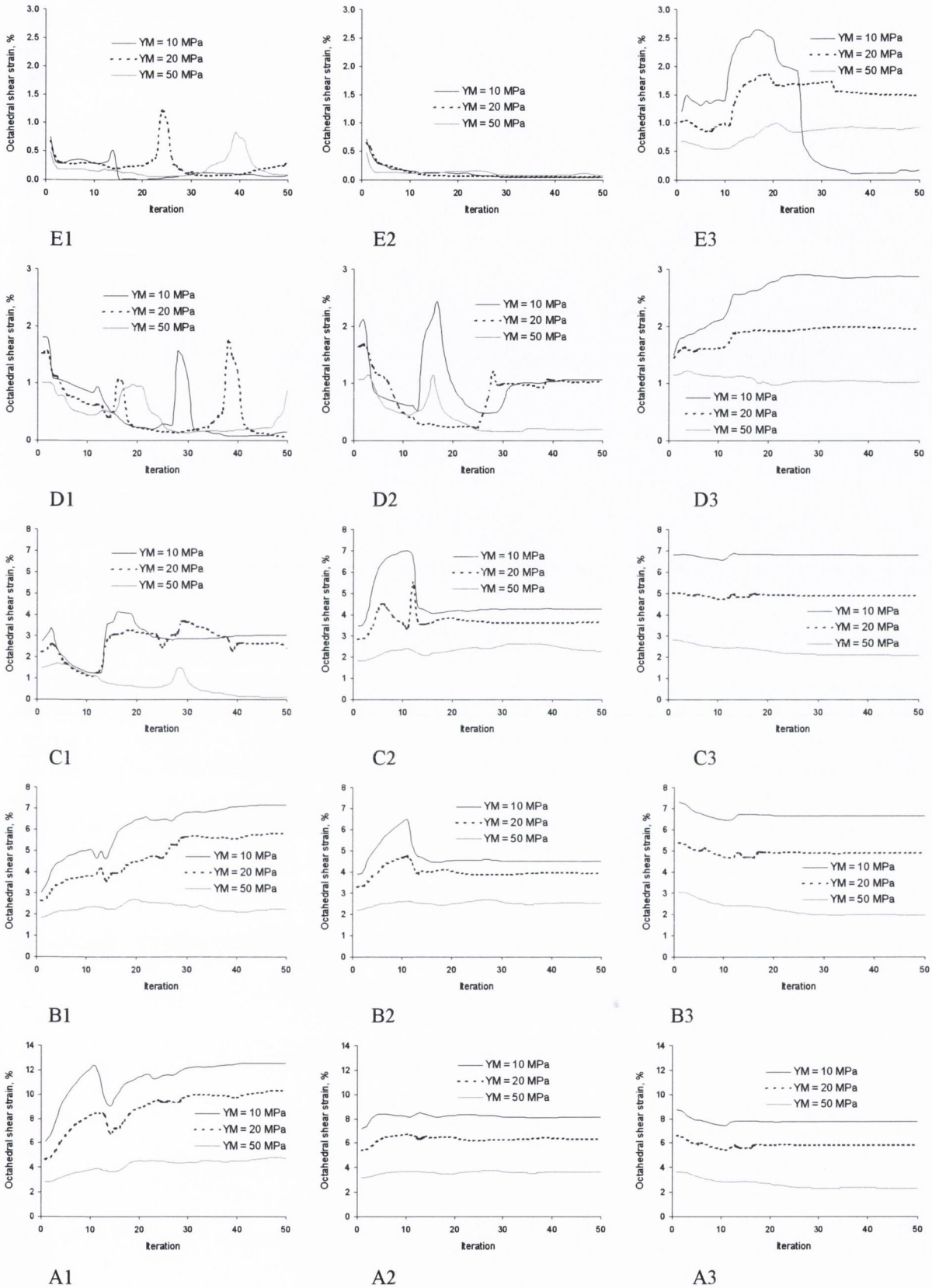

Fig. 4.47. *Predictions of octahedral shear strain in different elements within the 7 mm defect throughout the simulation with and without an implanted homogenous scaffold. Location of each element given in Fig.4.46.*

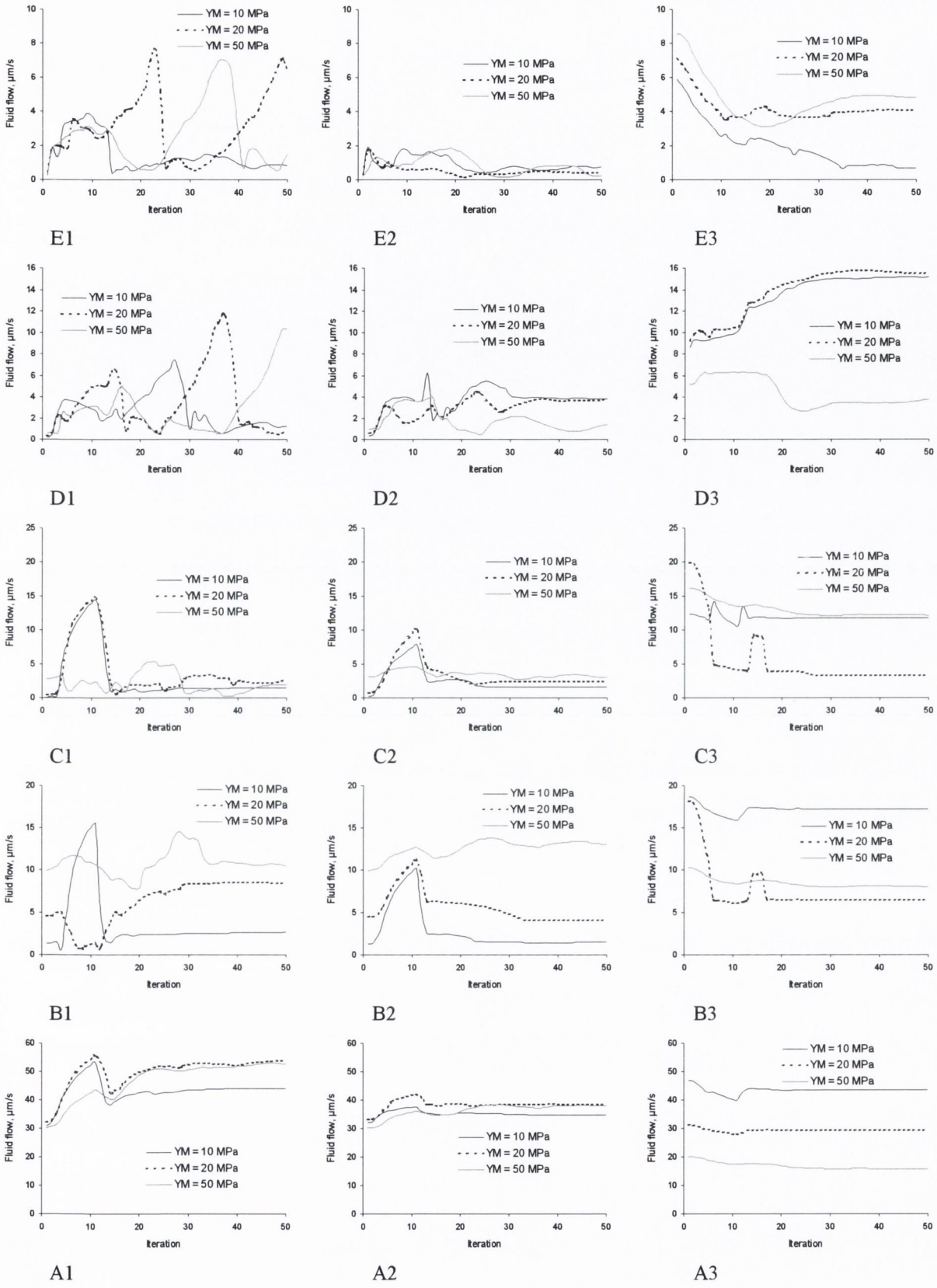

Fig. 4.48. *Predictions of interstitial fluid flow in different elements within the 7 mm defect throughout the simulation with and without an implanted homogenous scaffold. Location of each element given in Fig.4.46.*

Influence of material properties: Permeability

Reducing the permeability of the scaffold from 5e-15 m^4/Ns to 1e-15 m^4/Ns had a significant effect on the pattern of repair predicted within the defect (Fig. 4.49). The pattern of repair predicted when the permeability of the scaffold is reduced 5e-15 m^4/Ns is similar to that predicted with the baseline permeability (1e-14 m^4/Ns); intramembranous bone formation occurs at early time points in the base of the defect, increased cartilage formation in the centre of the defect as it begins to support load, and eventually endochondral ossification of cartilage resulting in near complete healing of the bony part of the defect. However when the permeability is reduced to 1e-15 m^4/Ns, the increased cartilage formation that is usually predicted between iterations 5 and 20 is not observed, and instead larger amounts of bone formation occur primarily from direct intramembranous ossification.

For scaffolds with a low permeability, bone formation increases continuously form iteration 1 to 10, after which bone formation stabilises (Fig. 4.50). A similar trend is predicted for cartilage formation, indicating little or no endochondral bone formation. However with scaffolds of a higher permeability, bone formation is predicted to increase initially, stabilise, and then increase again due to endochondral ossification. By the time the model has converged, larger amounts of bone formation, and smaller amounts of cartilage formation, are predicted as the permeability of the scaffold is reduced, to the point where the final thickness of the chondral region is less than that of the surrounding normal tissue. A scaffold permeability of 1e-15 m^4/Ns was predicted to produce the most uniformly thick layer of cartilage tissue. Down to a certain threshold value, reducing the permeability is also predicted to reduce the amount of fibrous tissue within the defect, below which fibrous tissue formation either levels off or increases.

Reducing the permeability of the scaffold is generally predicted to increase the magnitude of octahedral shear strain at the articular surface, and reduce the magnitude of stain, and the rate at which the magnitude of strain decreases, in the bony part of the defect (Fig. 4.51). Reducing the permeability of the scaffold is also predicted to reduce the magnitude of interstitial fluid flow throughout the defect during the simulation (Fig. 4.52). The higher magnitudes of strain predicated at the articular surface when the permeability of the scaffold was reduced led to significant cell death, particularly when the permeability was reduced to 5e-16 m^4/Ns (result not shown).

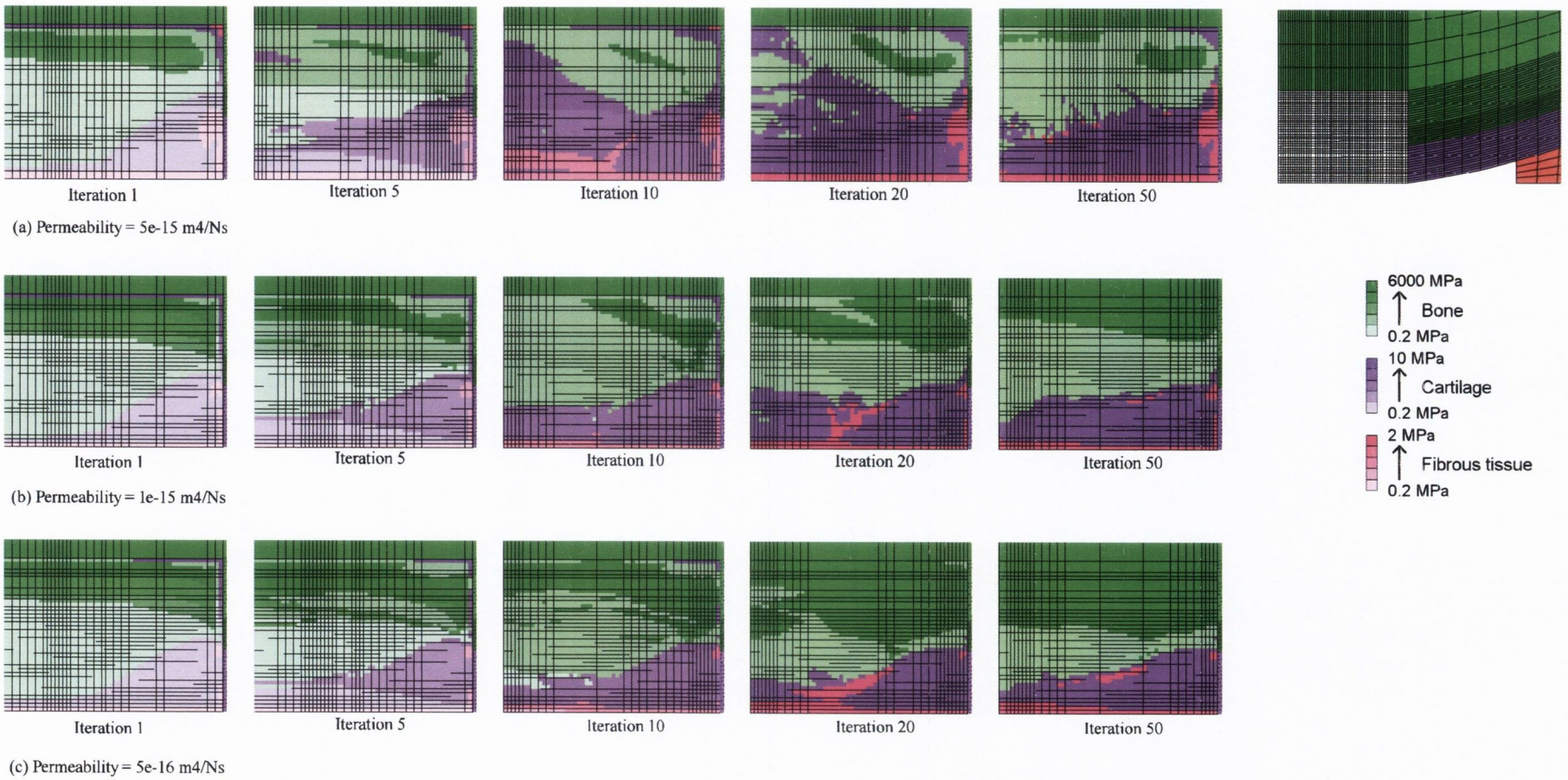

Fig. 4.49. *Predicted patterns of tissue differentiation in 7 mm defect after implantation of a homogenous scaffold.*

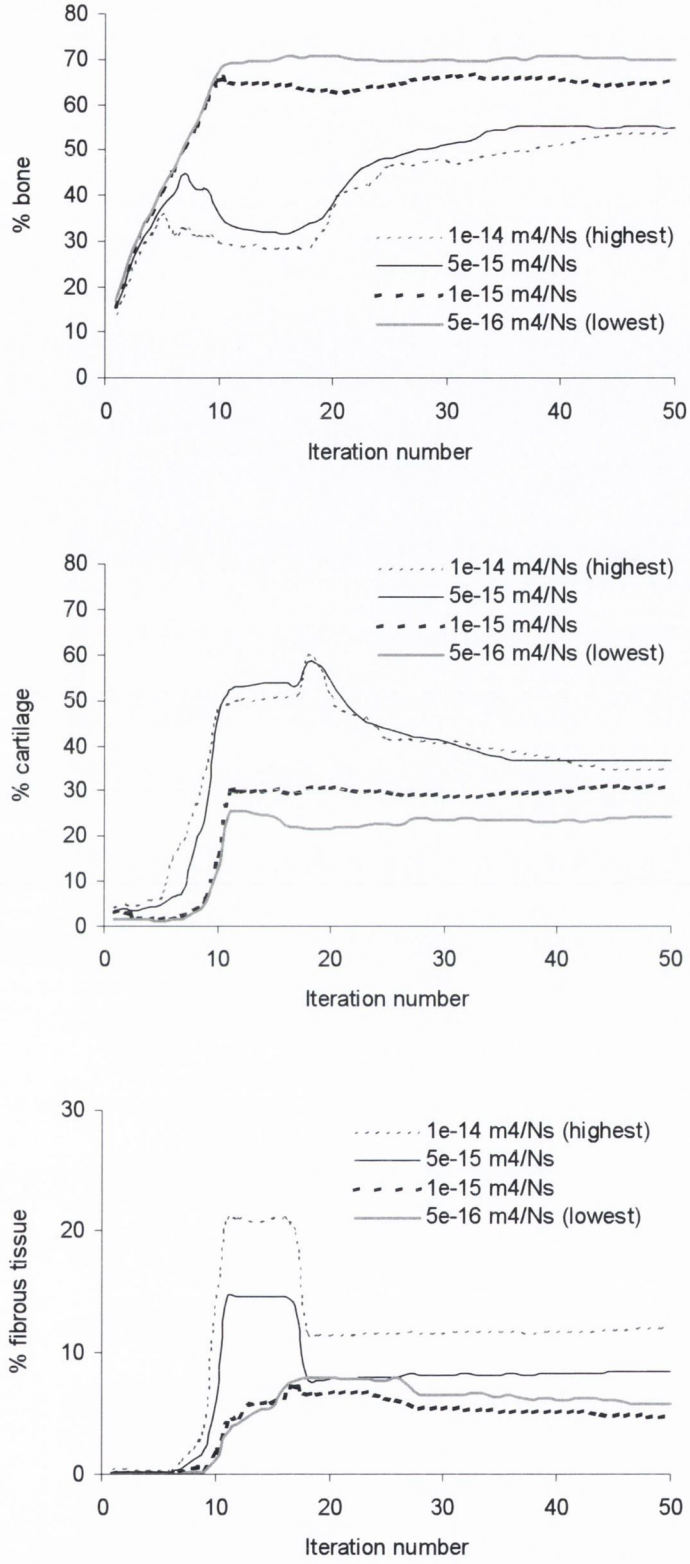

Fig. 4.50. *Comparisons of the amounts of bone tissue, cartilage tissue and fibrous tissue predicted to form in the 7 mm defect implanted with a homogenous scaffold of various permeabilities.*

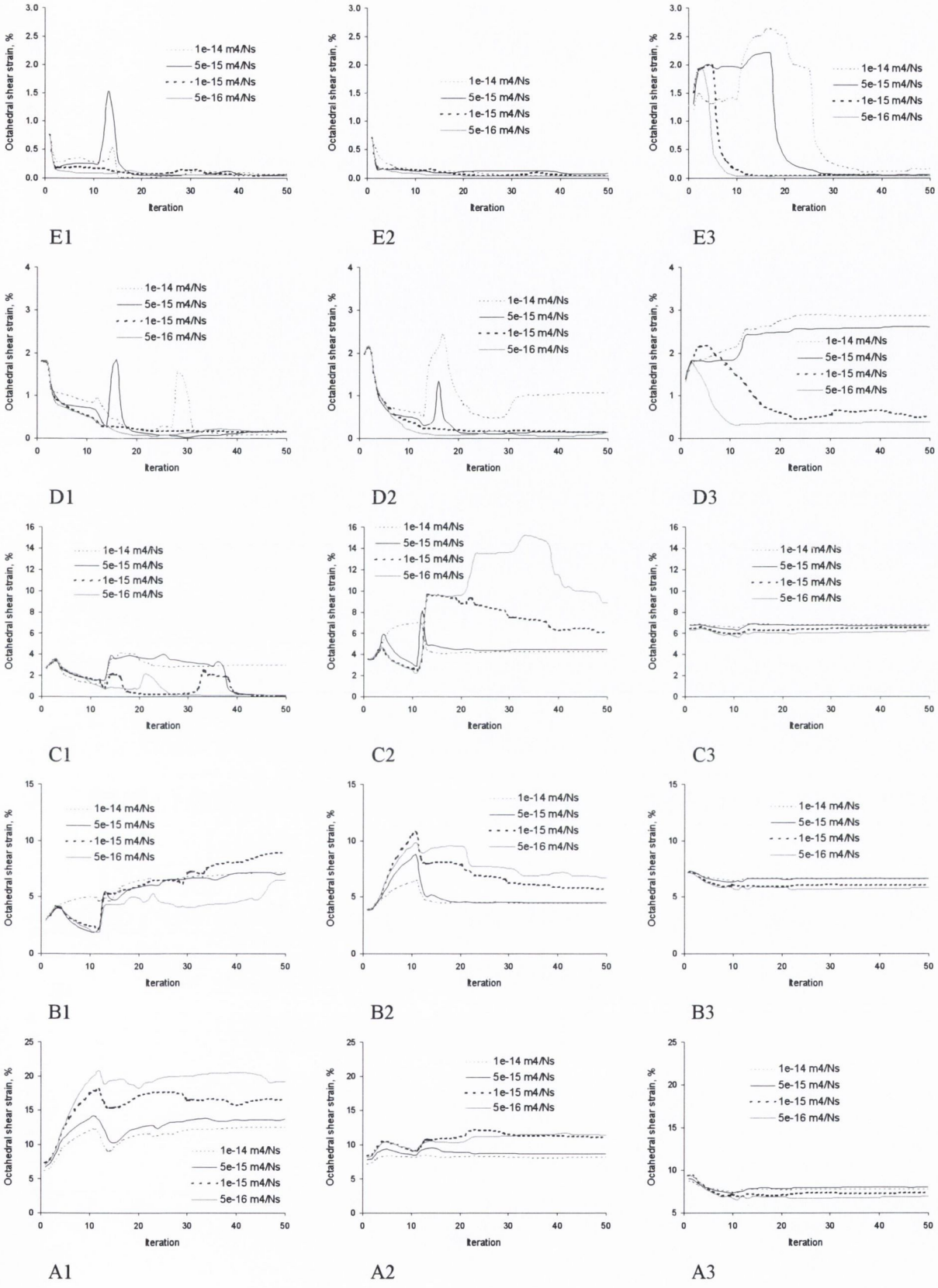

Fig. 4.51. *Predictions of octahedral shear strain in different elements within the 7 mm defect throughout the simulation with and without an implanted homogenous scaffold.*

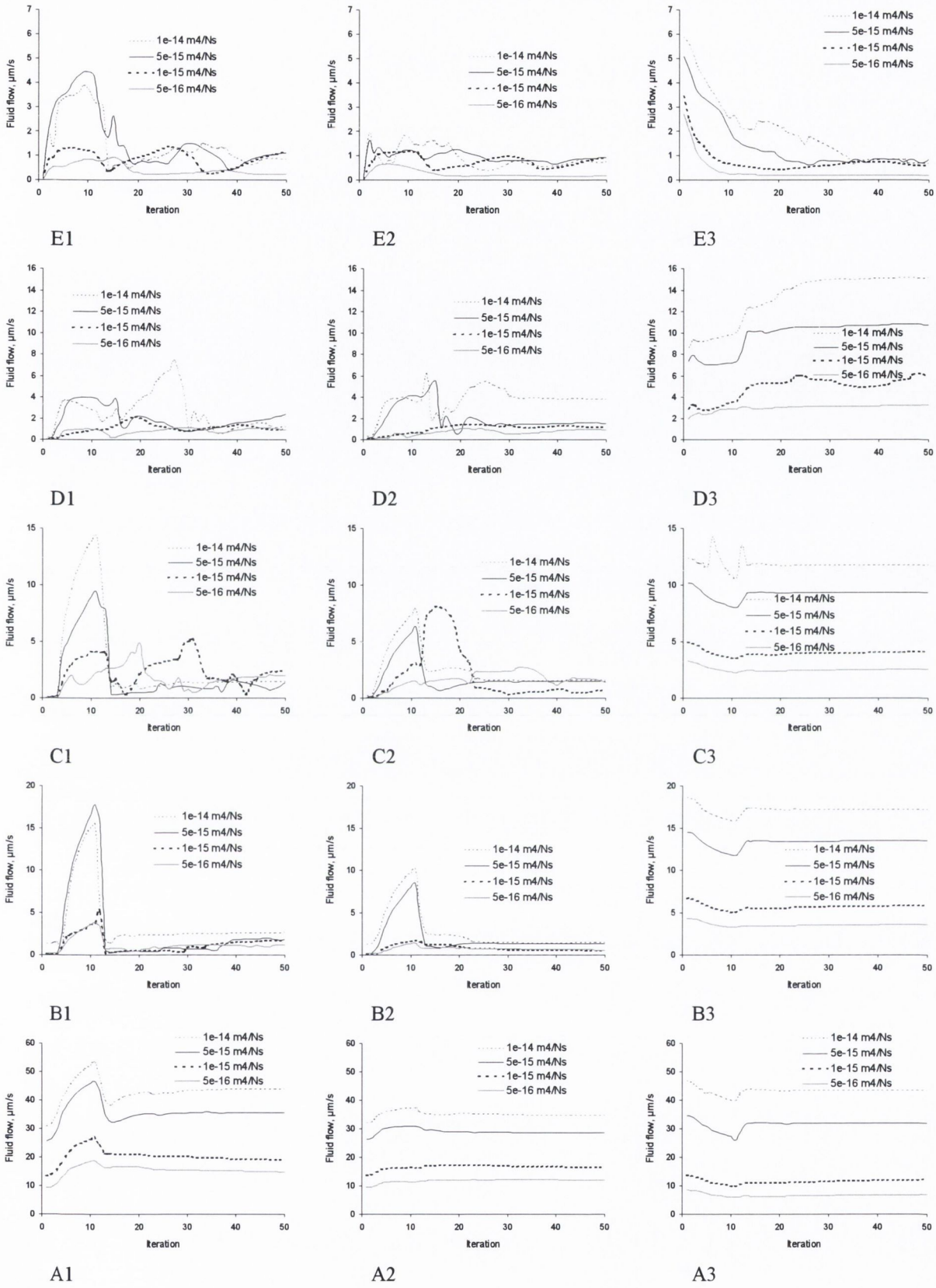

Fig. 4.52. *Predictions of interstitial fluid flow in different elements within the 7 mm defect throughout the simulation with and without an implanted homogenous scaffold.*

Influence of superficial phase of multiphase scaffold

Fibrous tissue formation was predicted at the articular surface or the repair tissue regardless of the Young's modulus used for the superficial layer of the scaffold (Fig. 4.53). Either increasing the modulus of the superficial layer to 30 MPa, or reducing it to 2 MPa, was predicted to increase the amount of fibrous tissue formation within the defect, mainly at the expense of reduced cartilage formation (Fig. 4.54). Although the stiffer superficial layer reduced the magnitude of the octahedral shear strain at the articular surface (Fig. 4.55 A), the reduction was not sufficient enough to prevent fibrous tissue formation at the articular surface (Fig. 4.53), and it also led to increased magnitudes of strain and fluid flow in other regions of the chonrdal part of the defect (Fig. 4.55 B and Fig. 4.56 B), which in turn led to the increased amounts of fibrous tissue formation predicted in these regions (Fig. 4.53). The increased amounts of fibrous tissue formation predicted within the chondral part of the defect after implantation of a multiphase scaffold with a 2 MPa superficial layer (Fig. 4.53) was due to larger magnitudes of fluid flow (Fig. 4.56). Increasing the stiffness of the superficial layer was also predicted to reduce slightly the predicted amount of bone formation within the defect (Fig. 4.54). The magnitudes of strain predicted at the articular surface were predicted to increase with reducing superficial layer stiffness, leading to cell death at the articular surface (result not shown).

Reducing the permeability of the superficial layer of the scaffold had little effect on the predicted patterns of tissue differentiation within the defect (Fig. 4.57). The amount of bone formation predicted to form within the defect was generally unaffected (Fig. 4.58). Down to a certain threshold value, reducing the permeability of the scaffold is also predicted to reduce the amount of fibrous tissue formation at the articular surface (Fig. 4.57), below which fibrous tissue formation increases. Although the magnitudes of strain predicted at the articular surface were predicted to increase with reducing superficial phase permeability, the increases were not great enough to cause cell death at the articular surface (result not shown).

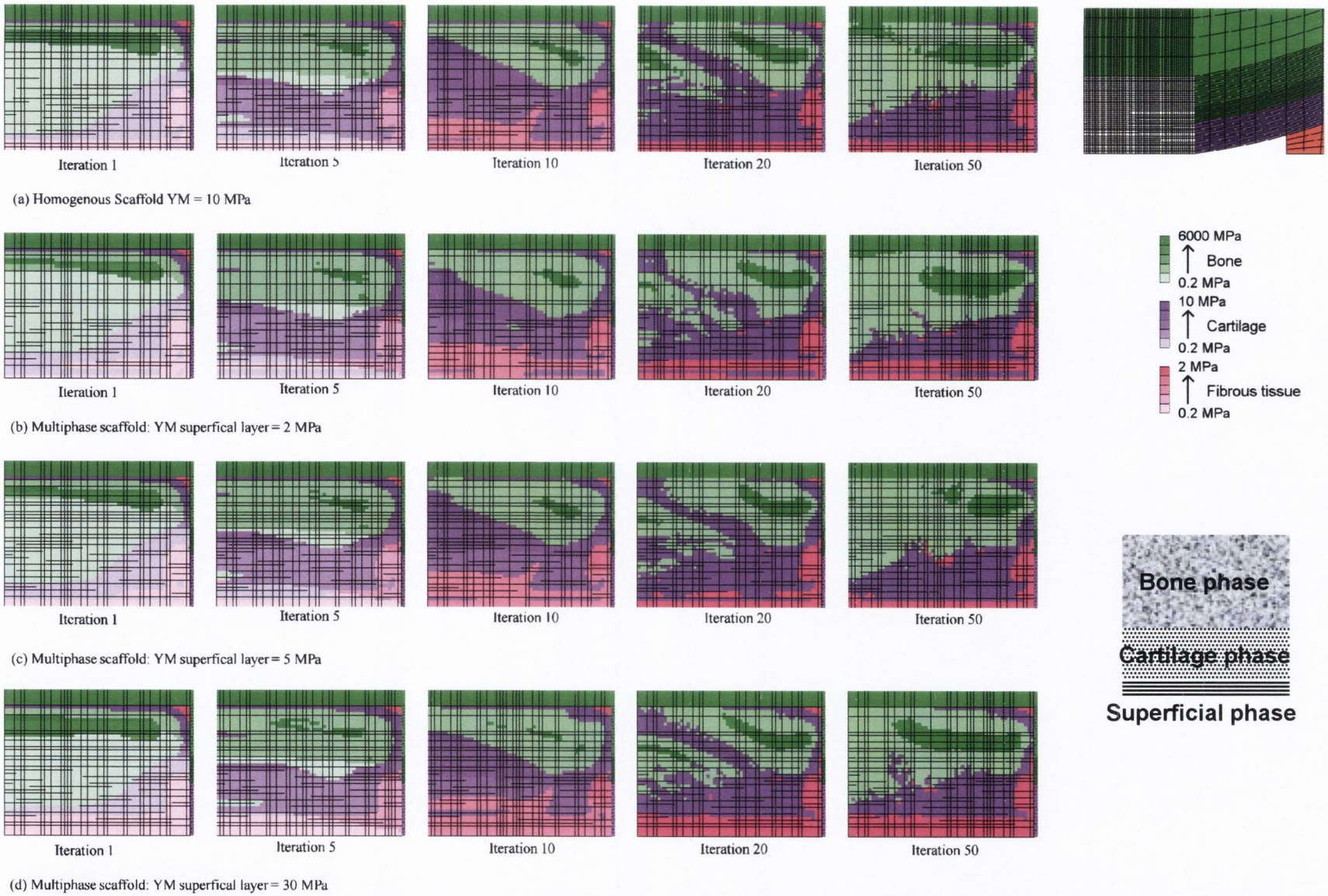

Fig. 4.53. *Predicted patterns of tissue differentiation in 7 mm defect after implantation of a multiphase scaffold. Influence of Young's modulus of superficial phase.*

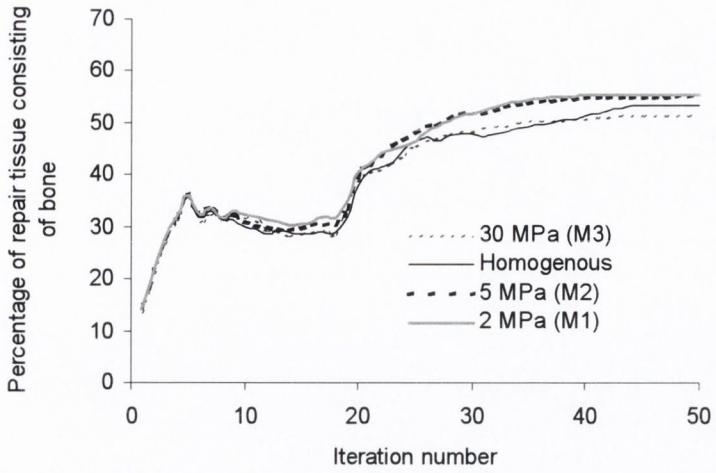

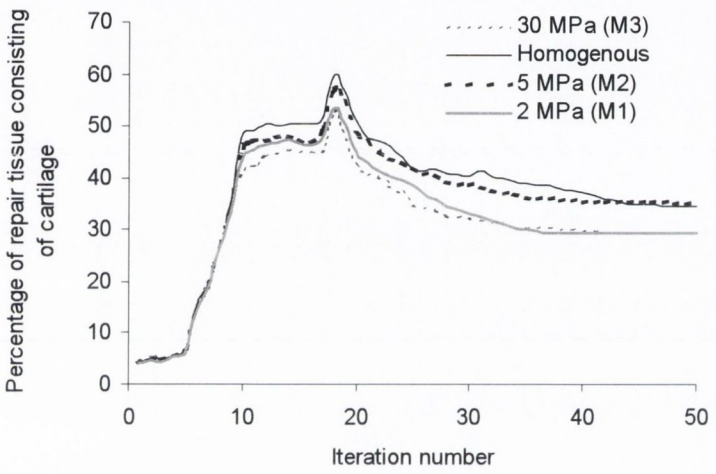

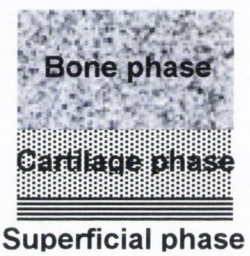

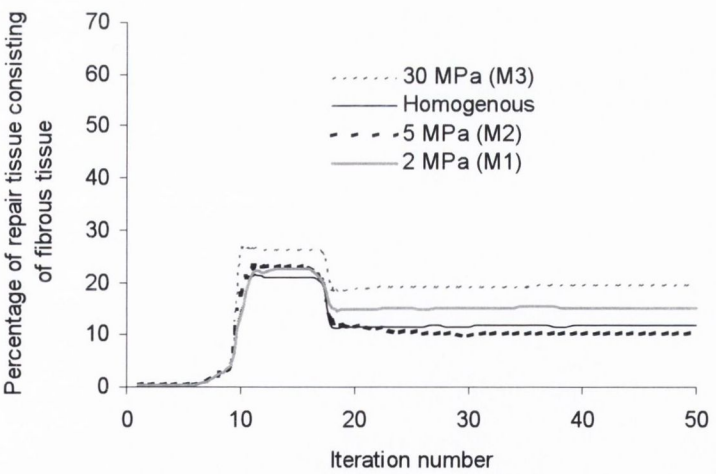

Fig. 4.54. *Comparisons of the amounts of bone tissue, cartilage tissue and fibrous tissue predicted to form after implantation with a multiphase scaffold, where the material properties of superficial phase are varied.*

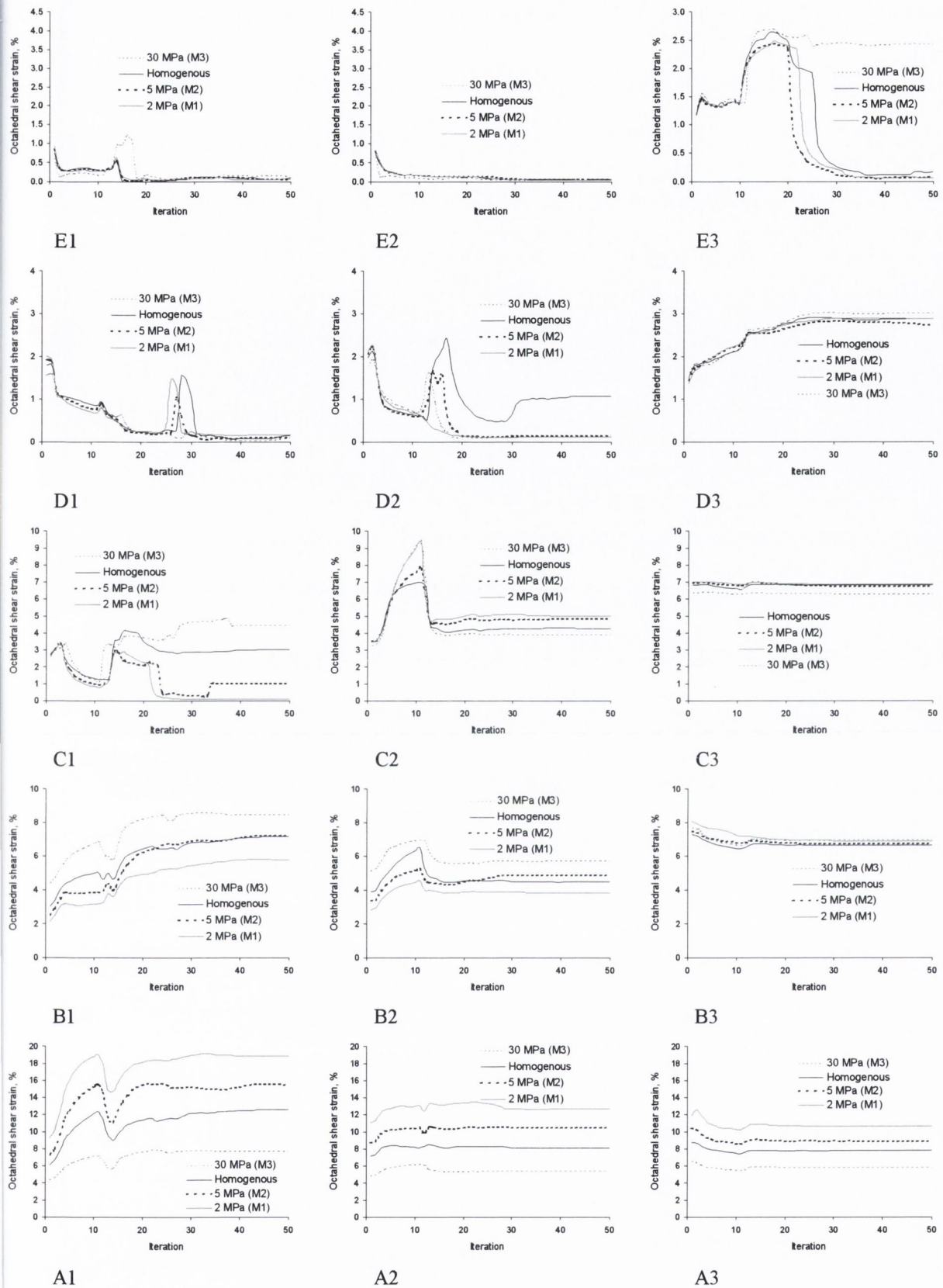

Fig. 4.55. *Predictions of octahedral shear strain in different elements within a defect implanted with a multiphase scaffold, where the material properties of the superficial phase of the scaffold are varied.*

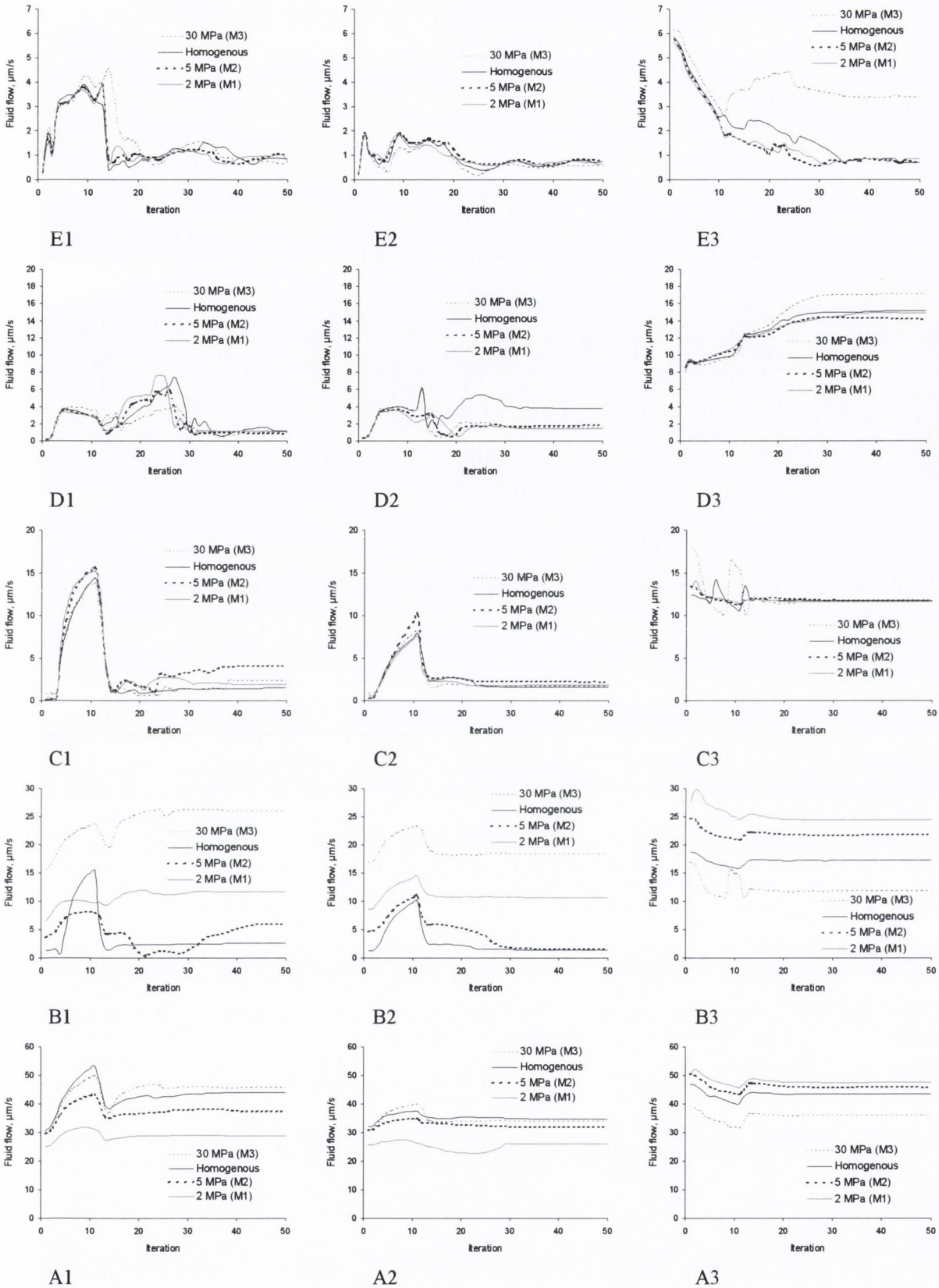

Fig. 4.56. *Predictions of interstitial fluid flow in different elements within a defect implanted with a multiphase scaffold, where the material properties of the superficial phase of the scaffold are varied.*

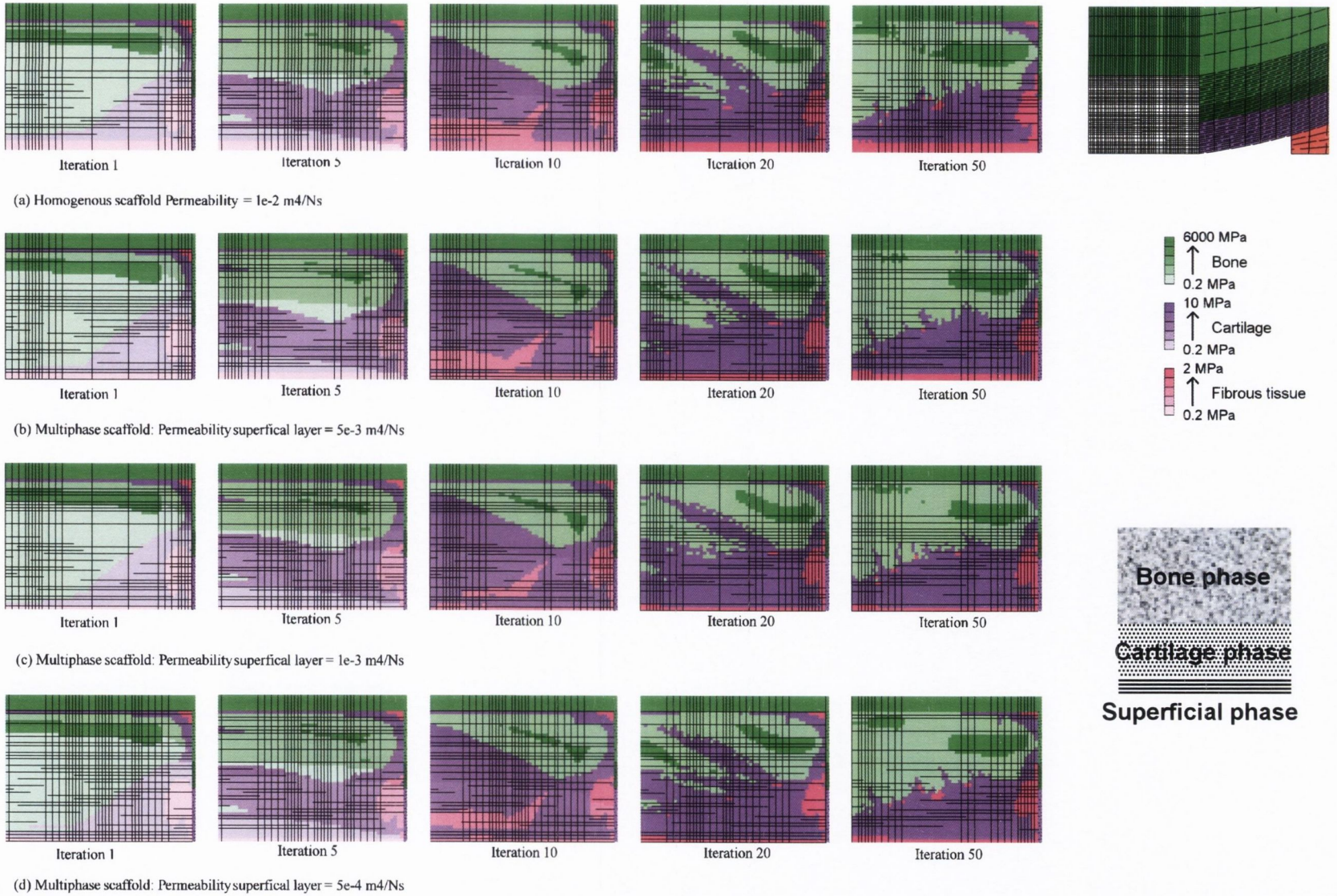

Fig. 4.57. *Predicted patterns of tissue differentiation in 7 mm defect after implantation of a multiphase scaffold. Influence of Permeability of superficial phase.*

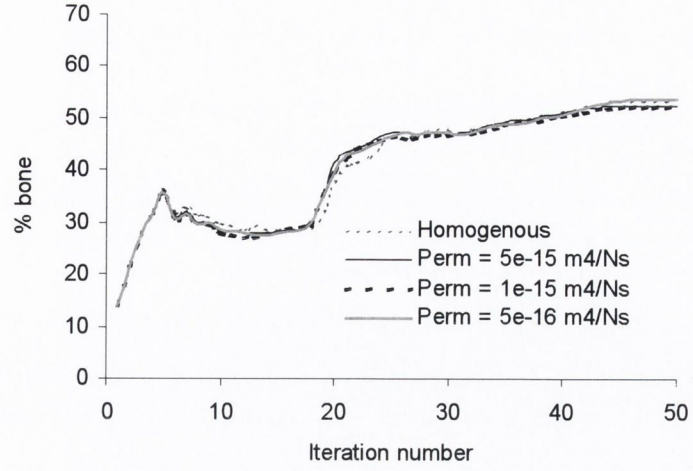

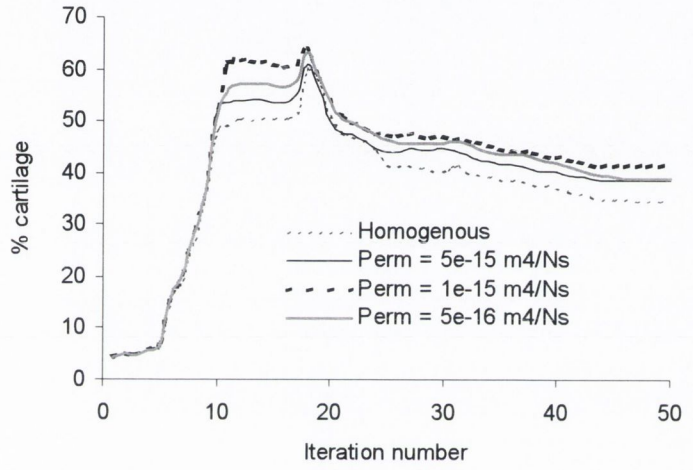

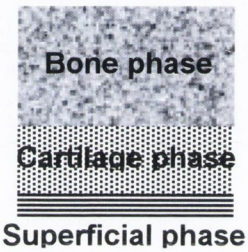

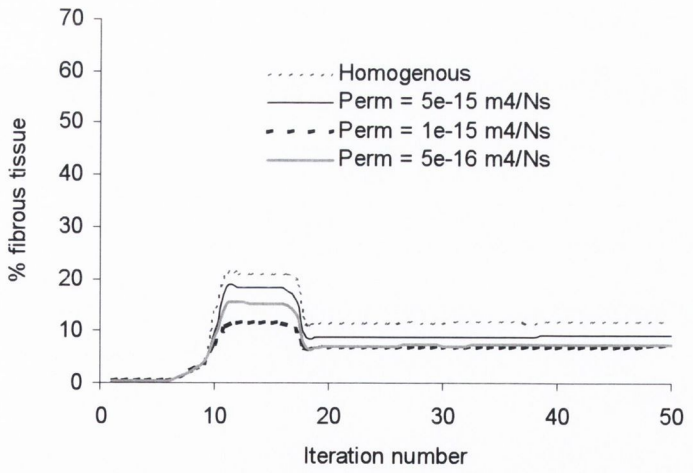

Fig. 4.58. *Comparisons of the amounts of bone tissue, cartilage tissue and fibrous tissue predicted to form after implantation with an multiphase scaffold, where the permeability of the superficial phase is varied.*

Influence of bone phase of multiphase scaffold

Bone formation is predicted to increase by either increasing the stiffness or reducing the permeability of the bone phase of the scaffold, resulting in the bony region of the defect consisting almost entirely of bone once healing has completed (Fig. 4.59). Reducing the permeability of the of the bone phase of the scaffold leads to increased bone formation primarily through direct intramembranous ossification (Fig. 4.60), with little endochondral ossification predicted, while reducing the modulus of the bone phase leads to an increase in cartilage formation, with bone formation predicted through a mixture of intramembranous and endochondral ossification. The amount of fibrous tissue formation is not significantly affected by the modulus or permeability of the bone phase of the scaffold.

Influence of chondral phase of multiphase scaffold

Reducing the modulus of chondral phase of the scaffold increases the amount of fibrous tissue within the defect (Fig. 4.61). Increasing the modulus also leads to an increase in fibrous tissue formation, and promotes regions of cartilage formation within the bony part of the defect. Reducing the permeability of the chondral phase of the scaffold reduces the amount of cartilage formation and promotes increased amounts of bone formation through direct intramembranous ossification (Fig. 4.62).

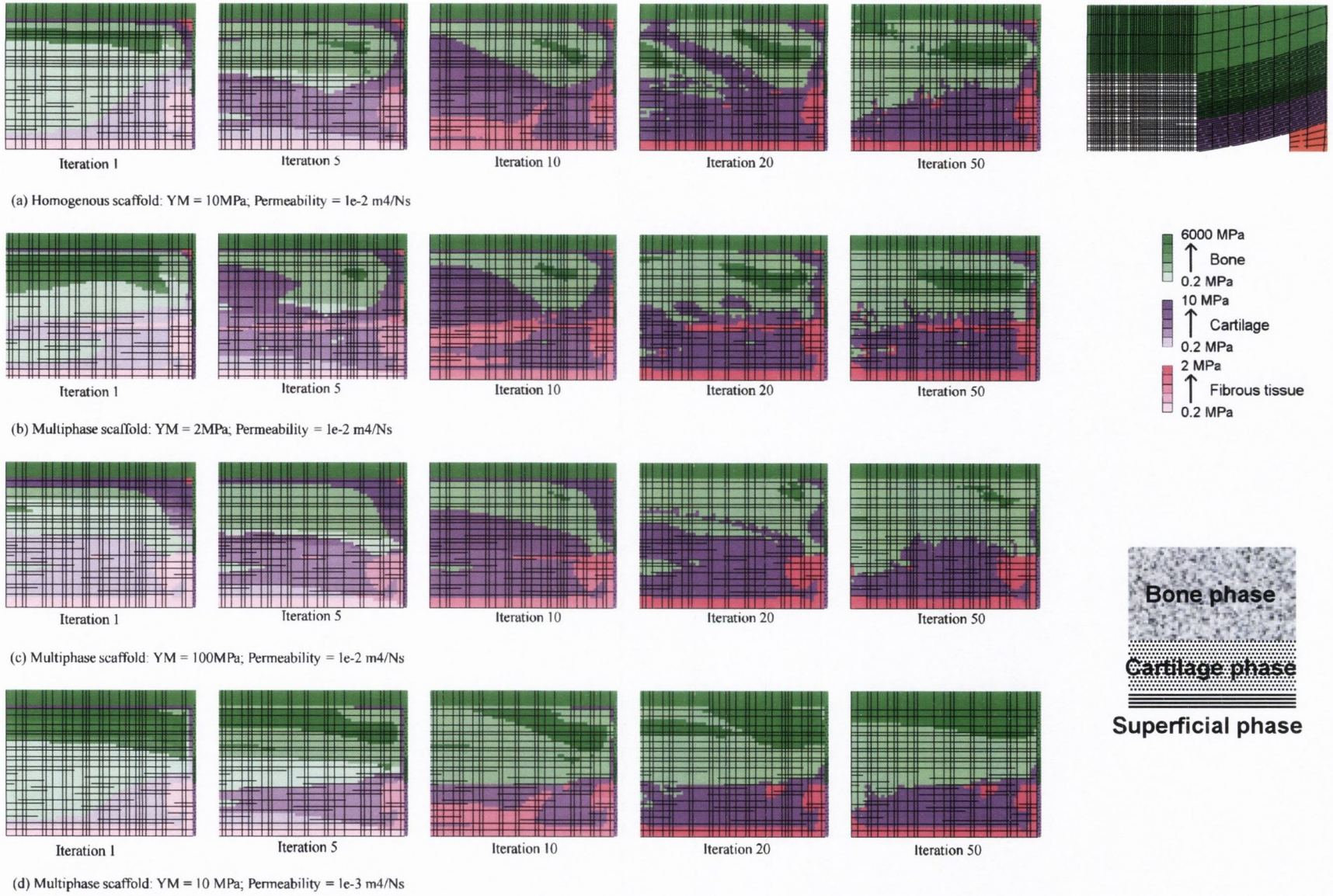

Fig. 4.59. *Predicted patterns of tissue differentiation in 7 mm defect after implantation of a multiphase scaffold. Influence of material properties of bony layer.*

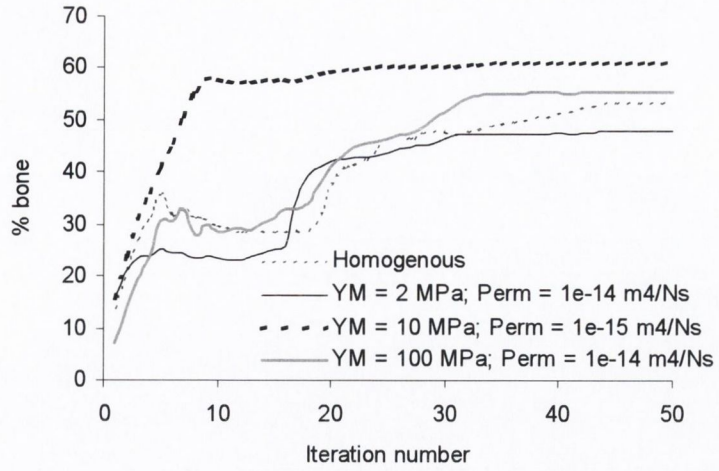

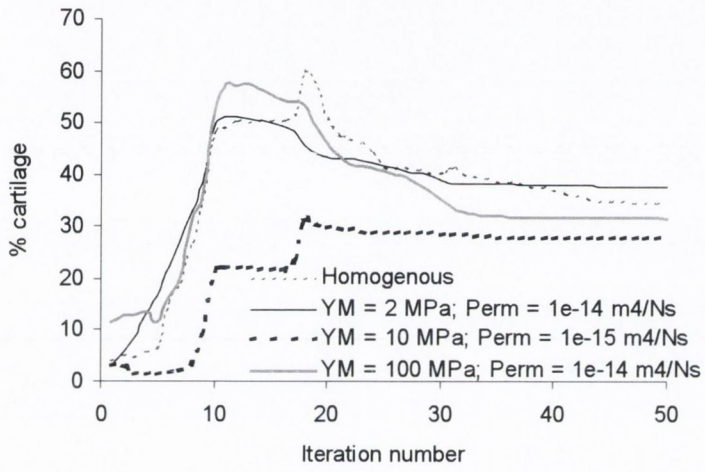

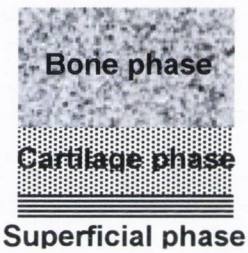

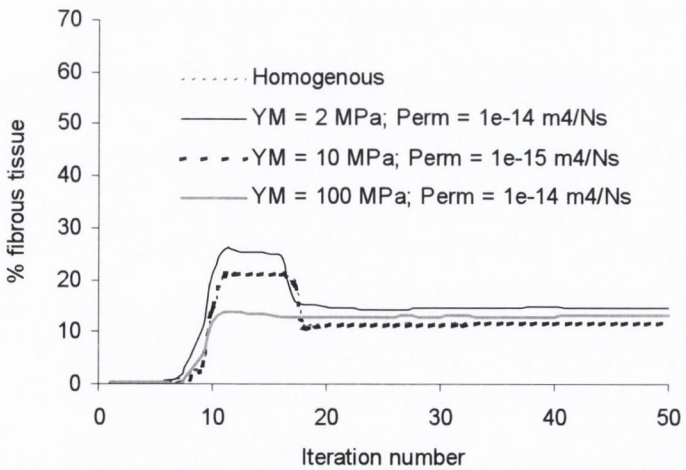

Fig. 4.60. *Comparisons of the amounts of bone tissue, cartilage tissue and fibrous tissue predicted to form after implantation with an inhomogenous scaffold, where the material properties of the bone phase is varied.*

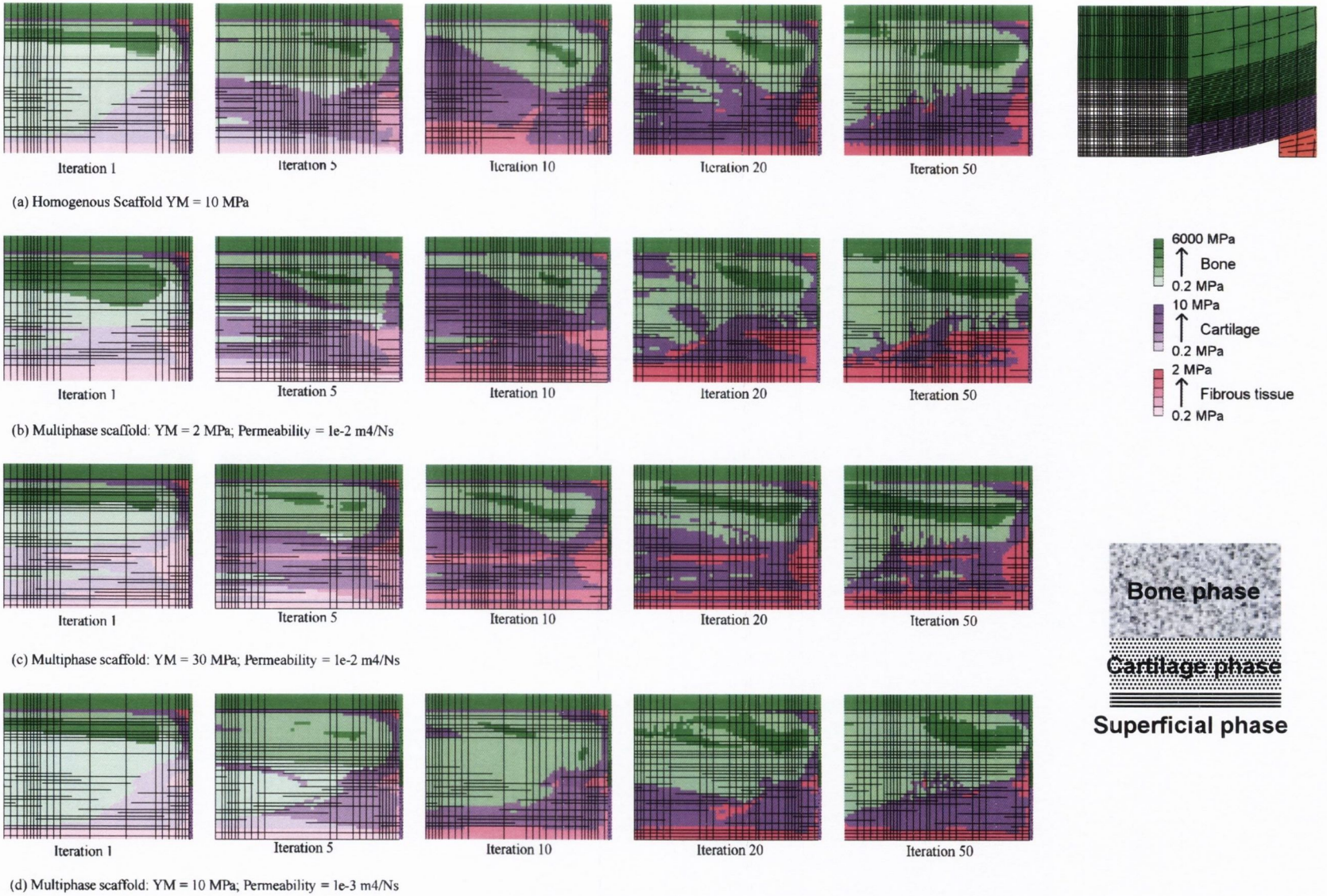

Fig. 4.61. *Predicted patterns of tissue differentiation in 7 mm defect after implantation of a multiphase scaffold. Influence of material properties of chondral layer.*

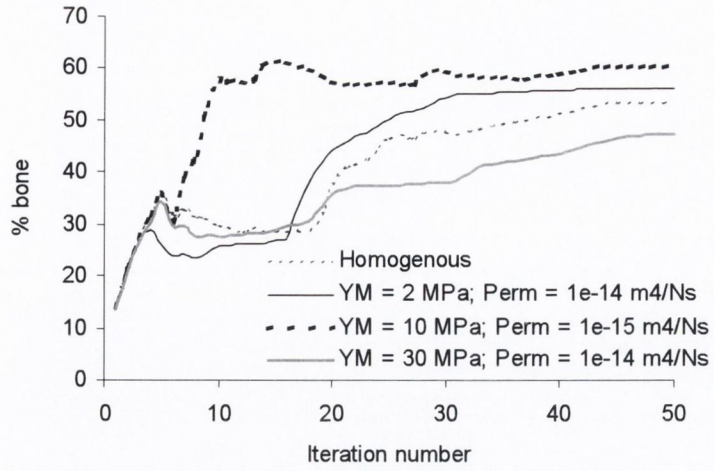

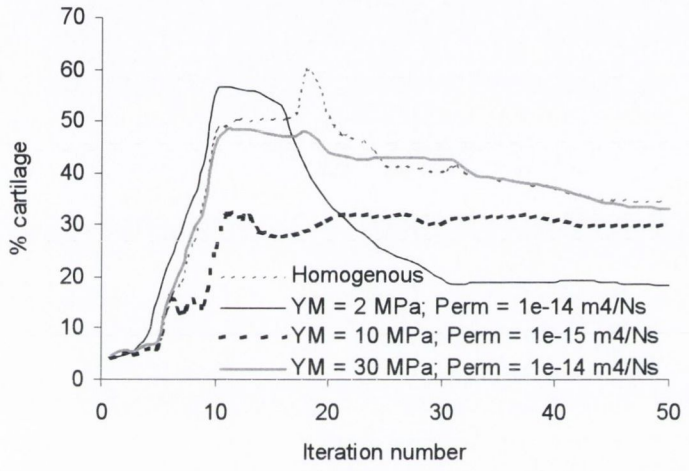

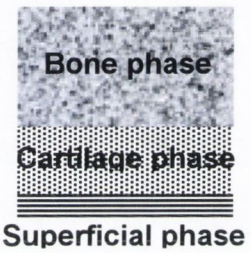

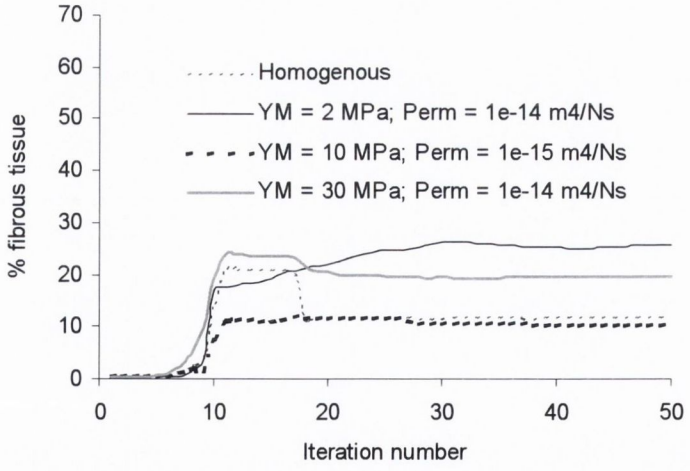

Fig. 4.62. *Comparisons of the amounts of bone tissue, cartilage tissue and fibrous tissue predicted to form after implantation with an inhomogenous scaffold, where the material properties of the chondral phase is varied.*

Chapter 5

Discussion

Contents

5.1 Introduction **154**

5.2 Assumptions and limitations of this study **154**

5.2.1 Dispersal of cells *154*

5.2.2 Mitosis and cell death *155*

5.2.3 Tissue differentiation *156*

5.2.4 The finite element model *158*

5.3 Simulating osteochondral repair: A test of the mechano-regulation concept **158**

5.3.1 General aspects of defect repair predicted by model *158*

5.3.2 Influence of defect size and loading *159*

5.3.3 Influence of repair tissue integration *162*

5.3.4 A hypothesis for repair tissue degradation *162*

5.4 Can tissue engineering improve osteochondral defect repair? **165**

5.4.1 Determining the properties of tissue engineered cartilage *165*

5.4.2 The influence of engineered tissues on defect repair *166*

5.4.3 Influence of scaffolds on defect repair *166*

5.4.4 The multiphase scaffold *169*

5.4.5 A blueprint for the optimal scaffold *169*

5.5 Conclusions **173**

5.1 Introduction

The primary objective of this thesis was to further develop our understanding of stem cell mechanobiology. This was done by developing a mechano-regulation model for what I considered to be fundamental features of stem cell biology – namely migration, proliferation, and death of stem cells, and their differentiation. In the previous chapter the predictions of this mechano-regulation model in simulating osteochondral defect repair were presented.

In this chapter the assumptions and limitations of the mechano-regulation model will be first discussed, with possible improvements suggested. Next the results of the simulations will be compared to what has been observed experimentally. An attempt will then be made to use the predictions of the mechano-regulation model to give a biomechanical explanation as to why spontaneous osteochondral defect repair is usually unsuccessful. Finally, based on the predictions of this model the benefits that tissue engineering can bring to osteochondral defect repair are discussed, and the potential of the mechano-regulation model as a tool for tissue engineering design will be evaluated.

5.2 Assumptions and limitations of this study

5.2.1 Dispersal of cells

The repair of osteochondral defects is mediated wholly by the dispersal, proliferation and subsequent differentiation of mesenchymal cells that originate from the underlying bone marrow (DePalma *et al.*, 1966; Shapiro *et al.*, 1993). In this study the dispersal of cells into the defect is modelled using a diffusion equation. The diffusion process assumes that each individual cell moves around in a random way resulting in some form of gross regular motion of the group of cells. Of course the migration of cells within an osteochondral defect is probably not a simple diffusion process; for example it has been hypothesised by Shapiro *et al.* (1993) that the strands of granulation tissue that form after the creation of an osteochondral defect form a scaffolding along which the mesenchymal cells orientate themselves. Regardless of the exact mechanism by which cells travel, the outcome seems to be that cells disperse from a region of high cell density, the marrow, into a region of low cell density, the defect, in a somewhat regular fashion. By measuring tritiated thymidine

uptake DePalma *et al.* (1966) were able to chart the dispersal and proliferation of mesenchymal cells within an osteochondral defect during the first 2 weeks of healing, showing that initially proliferating cells were confined to the marrow, but that over time these cells migrated into the defect, initially with a higher concentration in the base of the defect, until a homogenous distribution of cells was observed in the defect. For this reason, the author feels that the diffusion equation used in this study satisfactorily models this dispersal of cells observed during the early stages of healing.

A logical progression of this idea was that the diffusion coefficient, which determines the speed at which cells disperse, would be different for each cell type and also depend on the tissue type the cell was moving through. Implementing this idea required an estimation to be made for the diffusion coefficient for each tissue type, as no experimental measurements exists for the speed at which mesenchymal stem cells disperse through different tissues *in vivo*. A parameter variation study of the diffusion coefficients revealed that the coefficient used for granulation tissue had a particularly strong influence on the rate of repair within the tissue; however the simulations converged with similar predictions of tissue phenotype and cell concentration. One could conclude form this result that a scaffold used in the treatment of osteochondral defects should not impede the movement of cells through the defect, as this is predicted to slow the rate of repair.

5.2.2 Mitosis and cell death

As cells disperse throughout the defect, they can also potentially increase in number due to mitosis (cell proliferation), or decrease in number due to cell death. In this model it was assumed that a non-linear relationship exists between mitosis/cell death and the magnitude of the octahedral shear strain experienced by cells. Whether such a relationship exists has yet to be proved or refuted experimentally. While mitosis has been shown to increase at certain strain levels for certain cell types (Jones et al., 1991; Brighton et al., 1991), to the authors knowledge no single study has examined the influence of strain on cellular proliferation for different cell types across a wide range of strain magnitudes.

Similarly experiments measuring cell death in cartilage explants subject to different magnitudes of load have shown cell death to increase with increasing

magnitude of applied load, however no exact relationship could be quantified, presumably due to the difficulties in quantifying the levels of strain actually experienced by chondrocytes embedded in a non-linear, bi-phasic inhomogeneous tissue. Therefore as the relationship between strain and mitosis and cell death has yet to be determined experimentally (if such a relationship actually exists), we hypothesised a quadratic relationship between strain and cellular mitosis and death. In the future such relationships will need to be more accurately defined using well designed *in vitro* experiments.

5.2.3 Tissue differentiation

Prendergast *et al.* (1996) suggested that tissue differentiation is potentially regulated by two mechanical stimuli, tissue shear strain and interstitial fluid flow. This hypothesis has already been partially confirmed by computational simulations that have accurately predicted tissue differentiation patterns at bone-implant interfaces (Huiskes et al., 1997) and during fracture healing (Lacroix and Prendergast, 2000). The choice of strain and interstitial fluid flow as regulators of tissue differentiation differs from the ideas of Carter et al. (1998) and Pauwells (1980), who believe that both hydrostatic stress and the distortional (octahedral shear) stress or strain are regulators of tissue differentiation. In support of Carter's theory, Giori *et al.* (1995) used a linear elastic finite element model and concluded that patterns of tissue differentiation reported at bone-cement interfaces correlated with distributions of hydrostatic stress and distortional strain. They argued that hydrostatic stress in their linear elastic analysis represented the fluid pressure. It would seem therefore that the primary difference between the hypothesis of Prendergast *et al.* (1996) used in this thesis and that of Carter *et al.* (1998) and Pauwels (1980) is whether fluid pressure or interstitial fluid flow is a controlling variable for tissue differentiation. Since both distributions of fluid pressure and fluid flow have been related to patterns of tissue differentiation, what evidence exists to believe that fluid flow, rather than fluid pressure, is in fact a regulator of tissue differentiation?

Yuan *et al.* (2000) showed that the fluid pressure predicted by a finite element model within the differentiating tissues at implant-bone interfaces is largely independent of the tissue properties. It would seem unlikely that a regulator of tissue differentiation would be independent of the properties of the tissue type it is meant to

be regulating. Whether or not the mechanical stimuli used in this study, i.e. tissue shear strain and interstitial fluid flow, are in fact regulators of tissue differentiation in an osteochondral defect will be determined in the next section of this chapter when the predictions of the mechano-regulation model are compared to patterns of tissue differentiation observed experimentally.

Assuming that shear strain and fluid flow are indeed regulators of tissue differentiation, an obvious limitation of this study is that the boundaries of the mechano-regulation diagram (Fig. 3.7) have yet to be determined experimentally. With the advances that are currently being made in experimental and computational mechanobiology (van der Meulen and Husikes, 2002), accurately determining such values may soon become a possibility. Other biological questions regarding tissue differentiation, which will have a large bearing on how it is modelled, have also yet to be fully answered. Do cells transdifferentiate from one cell type to another, or do they die and get replaced by new mesenchymal cells which differentiate according to the local mechanical stimuli? For example, during endochondral ossification it is believed that chondrocytes become hypertropic, begin expressing a new genetic program, and finally apoptose when the cartilage tissue calcifies and is invaded by capillary vessels and bone-forming cells (Lefebvre *et al.*, 2001). In the mechano-regulation model this is modelled by directly replacing chondrocytes with osteoblasts. Perhaps it would be more appropriate to model this process by introducing a calcified cartilage phase into the mechano-regulation diagram, where all chondrocytes in the tissue undergo apoptosis, allowing for either new mesenchymal cells or osteoblasts to migrate into the calcified tissue from the surrounding bone. If transdifferentiation from one cell type to another occurs it will be important to determine the time it takes for this process to occur. At the moment it is assumed that cells differentiate after a single iteration. Also the rate at which differentiated cells synthesise new matrix, and hence regulate the mechanical properties of the repair tissue, could potentially be determined experimentally and incorporated into an improved model of tissue differentiation. The present model also assumes that once a group of cells has differentiated into a particular phenotype that these cells will synthesise a uniform isotropic tissue. A more plausible hypothesis would be that the mechanical stimuli that act on cells to regulate tissue differentiation would also influence the orientation and amount of matrix macromolecules such as collagen type I and II that are synthesised by the cells, and hence the mechanical properties of the new tissue. Possible implementation of these

ideas is discussed in the future work section of Chapter 6. Finally no attempt has been made to model the influences of growth factors such as TGF-β and BMP's, which have been shown to be possible regulators of tissue differentiation in a mathematical model of fracture healing (Bailón-Plaza and van der Meulen, 2001).

5.2.4 The finite element model

The finite element model used to determine the mechanical stimuli within an osteochondral defect is rather simplified relative to reality. Firstly modelling the geometry of the chondyle and meniscus as axi-symmetric is obviously a simplification. In reality the geometry is more complex. The tibial plateau is modelled as a rigid contact layer, which is obviously a simplification because the tibia is covered by an elastic cartilage layer. Secondly a constant load is applied to the model throughout the simulation. In reality the magnitude and orientation of the load varies throughout the gait cycle and also as the patient increases weight bearing as healing progresses. Thirdly the tissues were modelled using linear poroelastic isotropic elements. In reality the tissues, and particularly the soft tissues, are anisotropic and non-linearly elastic. Because of the charged nature of articular cartilage and the electrolytes dissolved in the interstitial fluid, articular cartilage also exhibits complex electrochemical properties including charge-dependent osmotic swelling pressures that influence the mechanical behaviour of the tissue. These properties have not been incorporated in the constitutive model used for cartilage. Finally, apart from the engineered cartilage, the mechanical properties of the tissues were estimated based on the literature data, and not determined experimentally by the author.

5.3 Simulating osteochondral repair: A test of the mechano-regulation concept.

5.3.1 General aspects of defect repair predicted by model

The simulations predict that, initially, the osteochondral defect is shielded from load by the surrounding intact tissue and that the stimulus within the defect is low. This low level of mechanical stimulus favours early bone formation through intramembranous ossification in the base of the defect. As the repair tissue begins to stiffen it starts to take more load, and chondrogenesis is favoured within the centre of

the defect. Fibrous tissue formation is predicted at the articular surface due to high magnitudes of strain and fluid flow in this region. This formation of soft tissues further stabilises the defect, allowing for a further increase in bone formation due to endochondral ossification. Further reductions in the amount of cartilage tissue within the defect are also predicted due to replacement of cartilage by fibrous tissue. Regions of fibrous or cartilage tissue persisted at the interface between the repair tissue and the normal tissue due to higher than average magnitudes of fluid flow in these areas.

To argue for the validity of the mechano-regulation model it must first be shown that the predictions of the model correspond with experimental observations. Metsäranta *et al.* (1996) analysed osteonectin and collagen type I, II and III expression in order to characterise the cell phenotypes in the repair tissue of osteochondral defects. At early time points, high levels of type I collagen and osteonectin expression, indicating bone formation, were observed in the base of the defect, while superficially undifferentiated mesenchymal cells expressed type III collagen. It was not until later time points that collagen type II expression, an indicator of chondrogenesis, was observed. This pattern of early bone formation within the base of the defect (~ iterations 1-10), followed by increased chondrogenesis at later time points (~ iterations 10-20), is predicted by the computational model. This correspondence between experimental and model predictions suggests that the model is correctly capturing some features of the tissue differentiation process, and that these process are in some way regulated by their mechanical environment.

The model also successfully predicts the distribution of different tissue phenotypes within the defect. Shapiro *et al.* (1993) observed bone formation through both endochondral and direct intramembranous ossification in the base of the defect, cartilage formation in the centre of the defect, and fibrous tissue formation superficially. This pattern of repair is also observed in the model, suggesting that the high strain and fluid flow environment at the articular surface does in fact provoke fibrous tissue formation and inhibit chondrogenesis.

5.3.2 Influence of defect size and loading

Another way to corroborate the model is to determine whether or not it predicts the effects of changes in defect size, or changes in loading, similar to experiments.

Increasing the size of the defect increased the amount of fibrous tissue formation and reduced the amount of bone formation. The soft tissues predicted to form in larger defects do not stabilise the defect sufficiently to allow endochondral ossification to occur. This is consistent with the observations of Convery *et al.* (1972), who observed, in horses, complete repair in small 3mm diameter defects, but an irregular mixture of fibrous tissue, fibro-cartilage, hypercellular cartilage and bone in defects larger than 9mm in diameter. The higher magnitudes of fluid flow predicted when the size of the defect was increased, rather than significant increases in octahedral shear strain, was the mechanism behind this prediction. Therefore, since increased fibrous tissue formation as the size of the defect is increased is also observed experimentally (Convery *et al.*, 1972), this result provides further indirect evidence that fluid flow is in fact a stimulus for differentiation.

It might also have been expected that cell death would have been greater in larger sized defects, but this was not predicted. This suggests that unsuccessful repair in larger sized defects is not related to massive cell death, but rather due to high magnitudes of strain and fluid flow within the defect reducing bone formation and increasing the amount of soft tissues forming. One could therefore hypothesise that there is two different mechanisms for repair tissue degradation:

(i) In small defects below a certain critical size, the repair tissue succeeds in successfully healing the bony region of the defect and filling the chondral region of the defect with a mixture of cartilage and fibrous tissue that may or may not degrade slowly over time (A hypothesised mechanism for this degradation process will be presented in Section 5.3.4 below).

(ii) In defects larger than a certain critical size successful repair does not occur, even in the short term, due to a high strain and fluid flow environment preventing ossification within the defect. This hypothesis is depicted in Fig. 5.1.

Increasing the magnitude of the applied load also increased the amount of fibrous tissue formation and reduced the amount of bone formation within the defect. Reducing the magnitude of the applied load has the opposite effect. It would seem that altering the magnitude of the applied load also changes the amount of intramembranous bone formation during the early stages of healing. To the authors knowledge no study to date has looked at the effects of loading magnitude on osteochondral defect repair, and therefore a comparison between the predictions of the model and experiment is not possible.

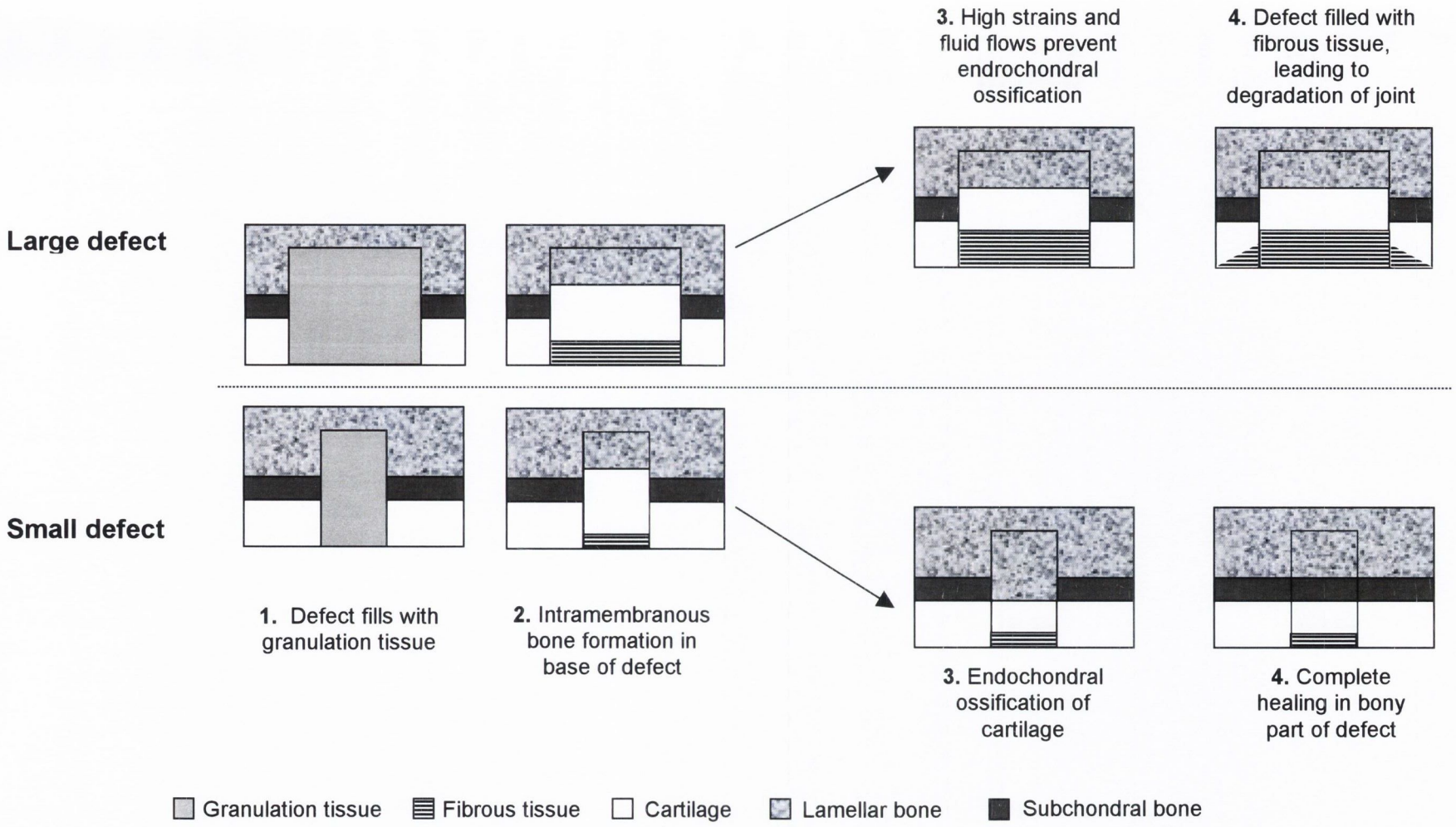

Fig. 5.1. *Illustration of the hypothesised differentiation processes in large and small defects, depicting the failure of the spontaneous repair process to satisfactory fill a large defect with the appropriate tissue types.*

5.3.3 Influence of repair tissue integration

Poor integration of the repair tissue with the normal residual tissue is often suggested as a possible contributor to repair tissue degradation. However the patterns of tissue differentiation predicted during the simulation are independent of the nature of the repair tissue integration. Although a slight increase in the amount of fibrous tissue formation is predicted when the repair tissue is modelled as poorly integrated to the repair tissue, it cannot be concluded based on this result that poor integration would result in poorer repair. The fact that the tibial plateau was modelled as rigid, therefore preventing any bulging of the tibial cartilage into the defect, may have lessened the effect of modelling the repair tissue integration, and may be the cause of this result.

5.3.4 A hypothesis for repair tissue degradation

Even if the spontaneous repair process is successful in completely healing the bony part of the defect and filling the chondral part of the defect with either a cartilage or fibrous-like tissue, the repair tissue is often observed to degrade over time (Shapiro *et al.*, 1993; Shahgaldi, 1998).

The present model can be used to help develop a hypothesis to explain this degradation process, based on the mechanical stimuli experienced by the cells. Firstly, fibrous tissue rather than hyaline-like cartilage forms at the articular surface. Mechanically this fibrous tissue is inferior to hyaline-like cartilage, and therefore it is unable to protect the fibroblasts that differentiate there and cell death results. While the cells underneath this superficial region maintain their proliferative ability, they provide a reserve of cells to replenish the cells lost due to mitosis. New mesenchymal stem cells might also be expected to invade the defect from the bone marrow. However as healing progresses, new bone formation occurs in the base of the defect, blocking the path of mesenchymal cells travelling from the bone marrow into the defect. It might also be hypothesized that this new bone formation hinders the diffusion of growth factors into the defect, thus reducing the proliferative ability of the remaining cells within the defect. Cell proliferation might also be expected to decrease in regions of high cell density due to limitations in space, nutrient diffusion or resources (Murray, 1993). In such a scenario this model predicts an overall reduction in the number of stem cells within the defect, as the rate of cell death now

exceeds the limited proliferative ability of the remaining cell population. This prediction is particularly obvious when the magnitude of loading applied to the finite element model is increased to 1100 N, where a reduction is cell concentration is predicted throughout the chondral part of the defect, see Fig. 5.2. This sequence, i.e. a repair tissue that is initially hypercellular followed by a reduction in cell number as time progresses, has been observed experimentally (Shapiro *et al.*, 1993; Mitchell and Shepard, 1976). In the early stages of healing, this large cell population may be able to remodel and repair the fibrous tissue at the articular surface. However as the surface strains increase and cell death proceeds, the reduced cell population is no longer able to maintain the new tissue, resulting in tissue damage at the articular surface and eventually complete degradation of the repair tissue. This sequence of events is depicted in Fig. 5.3.

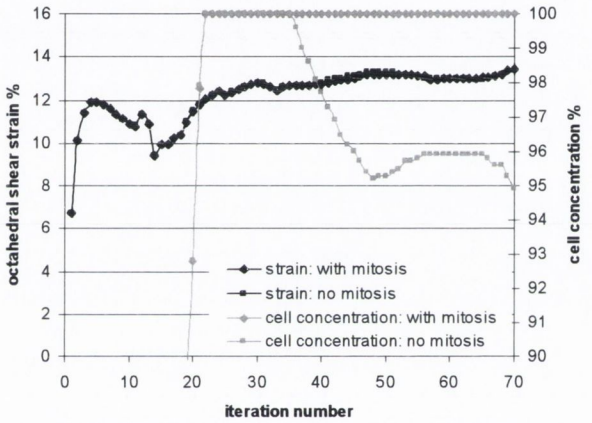

(b) element at the articular surface of defect

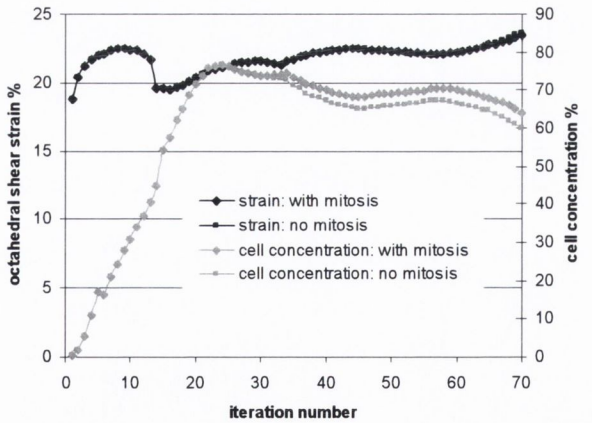

(a) element in middle of chondral region

Fig. 5.2. *Prediction of octahedral shear strain and interstitial flow in two different elements with and without cell mitosis after 30 iterations of the model for a 1100N loading.*

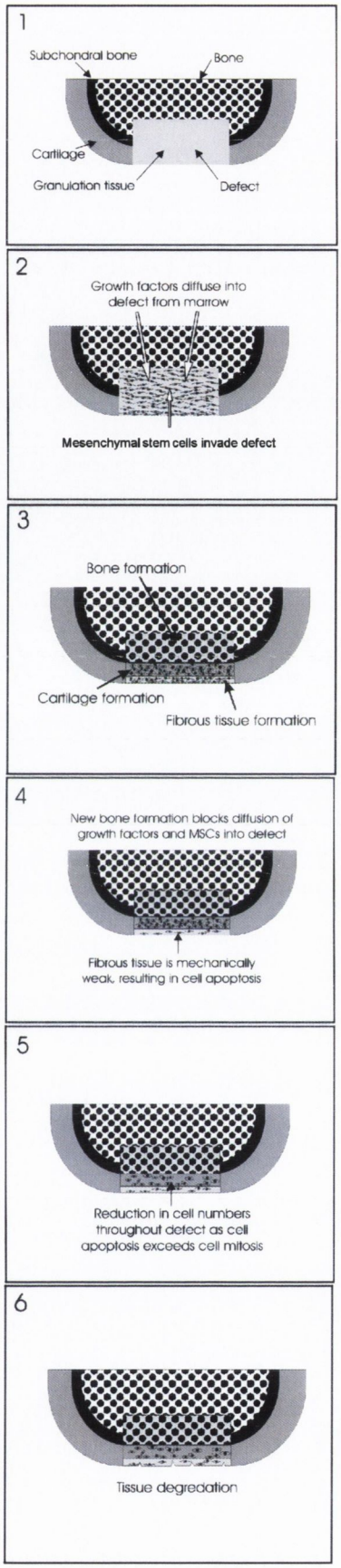

Fig. 5.3. *Illustration of the hypothesised degradation process that occurs in osteochondral defects.*

5.4 Can tissue engineering improve osteochondral defect repair?

5.4.1 Determining the properties of tissue engineered cartilage

A commonly cited goal of tissue engineering is to develop a functional tissue *in vitro* for implantation into the body. After 40 days in a static culture, and regardless of the cell seeding density used, the mechanical properties of tissue engineered cartilage were still only a fraction of normal articular cartilage (see Fig. 4. 31). It would seem that an optimal cell seeding density exists, and if this cell density is exceeded the mechanical properties of tissue engineered cartilage will actually decrease. This may be due to the fact that a higher cell seeding density will limit the diffusion of nutrients into the core of the engineered tissue, resulting in cell death. Increasing the time in culture from 40 days to 84 days (12 weeks) significantly increased the modulus of tissue. This raises the possibility that under the appropriate culture conditions it may be possible to engineer a tissue with mechanical properties matching that of normal articular cartilage.

Certain assumptions had to be made when determining the mechanical properties of tissue-engineered cartilage. The most important of these was to assume that the tissue-engineered construct was homogenous. However this was often not the case, with the tissue-engineered cartilage constructs usually consisting of an outer layer of cartilage and an inner core of either undeveloped cartilage or degrading scaffold material, due either to

(i) initial inhomogeneous seeding of the scaffold or

(ii) death of the cells in the centre of the scaffold as a result of an insufficient nutrient supply in a static culture.

The influence of this inhomogenity on the results of the confined compression test was the subject of a finite element study, which is presented as a separate scientific paper (see Appendix A). Briefly this finite element study predicted that higher volumes of degraded scaffold in the centre of the construct reduces the aggregate modulus calculated from the confined compression test and raises the estimate of tissue's permeability. It was concluded that more accurate estimations of the mechanical properties of tissue-engineered cartilage could be made using biphasic finite element models that account for the inhomogenity of the engineered constructs.

5.4.2. The influence of engineered tissues on defect repair

Implanting an engineered tissue into the defect was not predicted to significantly improve the quality of repair over the natural spontaneous repair process. This is primarily due to the fact that the mechanical properties of engineered cartilage, even after 12 weeks in culture, are still significantly lower that that of normal articular cartilage. This means that the matrix that has been synthesised during the culture period is lacking the mechanical characteristics to prevent dedifferentiation of the cartilaginous tissue into a fibrous-like tissue due to the high stain and fluid flow environment within a defect in an articulating joint. Increasing the modulus of the tissue-engineered cartilage, as can be expected if improvements in bioreactors and culture methods occur, was predicted to improve the quality of the repair. However a band of fibrous tissue still persisted at the articular surface. This result would suggest that engineering a cartilage tissue with the zonal characteristics of normal articular cartilage, and in particular engineering a superficial layer with a high tensile modulus and low permeability, would dramatically improve the quality of the repair. It is one of the main conclusions of this thesis that this should be the primary goal of tissue engineers attempting to culture a functional articular cartilage.

5.4.3 Influence of scaffolds on defect repair

The alternative tissue engineering approach to articular cartilage defect repair is to modulate or enhance the natural spontaneous repair process using a scaffold to help control the cellular environment within the defect. Traditionally the primary function of a scaffold in cartilage tissue engineering has been seen as a device to maintain the chondrogenic phenotype and provide a three dimensional structure for cells to lay down new matrix. Numerous types of scaffolds, such as fibrous polyglycolic acid, have successfully exhibited these properties *in vitro*. The question remains can a scaffold improve the quality of healing over the spontaneous repair process *in vivo*, and, if so, can the mechano-reguation model be used to determine the optimal mechanical properties for such a scaffold. In this case improved repair is defined as

(i) maximising the amount of bone tissue forming in the bony part of the defect, and

(ii) maximising the cartilage tissue forming in the chondral part of the defect, which equate to minimising fibrous tissue formation and producing a uniformly thick layer of cartilage repair tissue, and

(iii) preventing cell death within the defect.

In this study the predictions of spontaneous osteochondral defect repair were first compared to the predictions of spontaneous osteochondral defect repair in the presence of a homogenous scaffold. By modulating either the Young's modulus or permeability of the scaffold, it was predicted that a scaffold can be used to influence cellular differentiation, mitosis and death, and hence the quality of the repair. It would seem that a scaffold must have a certain minimum stiffness to reduce fibrous tissue formation within the defect; however if the scaffold is too stiff the amount of fibrous tissue formation predicted to form within the defect starts to increase (Fig. 5.4a). So while increasing the stiffness of the scaffold reduces the magnitude of octahedral shear strain within the defect (e.g. Fig. 4.46 B), it also increases the magnitude of fluid flow within the defect (e.g. Fig. 4.47 B), leading to a situation where the stimulus for fibrous tissue formation is increased due to increases in fluid flow. Increasing the stiffness of the scaffold is also predicted to reduce the thickness of the repair cartilage due to further progression of the osseous front. So it would seem that an optimal stiffness for a scaffold might exist. Similarly it was found that reducing the permeability of the scaffold would further reduce the amount of fibrous tissue formation within the defect, an obvious benefit, however if the permeability of the scaffold is to low the amount of fibrous tissue formation within the defect is again predicted to increase (Fig. 5.4b). In this case reducing the permeability of the scaffold beyond a certain threshold value lead to a slight increase in the stimulus for fibrous tissue formation due to increases in octahedral shear strain in the superficial region of the defect.

A scaffold with too low a permeability was predicted to have two further drawbacks. (i) Chondrogenesis within the centre of the scaffold reduced as the permeability of the scaffold was reduced, leading it a scenario whereby if the permeability of the scaffold was to low direct ossification was predicted in regions of the chondral part of the defect. (ii) Reducing the permeability of the scaffold resulted in higher magnitudes of strain at the articular surface, leading to increased cell death. Interestingly this region of high strain at the centre of the articular surface

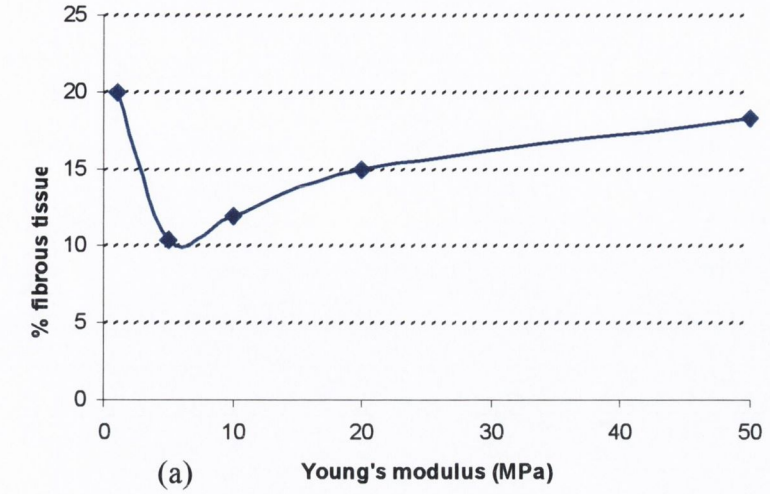

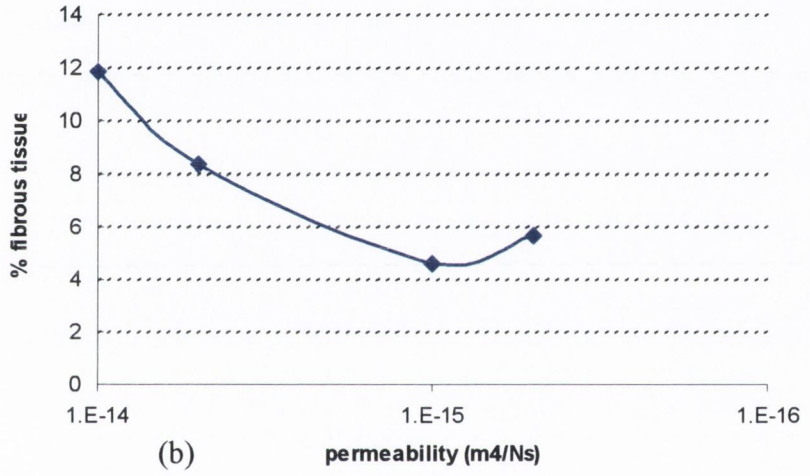

Fig. 5.4. *The influence of varying either (a) Young's modulus or (b) the permeability of the scaffold on the amounts of fibrous tissue predicted within the defect after 50 iterations of the simulation. (Note the log scale on the graph of permeability against fibrous tissue formation).*

correlates with the location of large vertical fissures observed by Niederauer *et al.* (2000) in defects implanted with polylacitide scaffolds (Fig. 5.5). These fissures originated at the articular surface, suggesting that the region of high strain at the centre of the articular surface can result in fracture of the repair tissue.

Based on this result another failure scenario for defect repair can be proposed. Suppose that the function of the superficial layer of normal articular cartilage, which consists primarily of collagen fibres aligned parallel to the articular surface, is to

increase the fracture toughness of the tissue. Since the superficial layer in repair cartilage is absent, or at best in an early stage of development, the fracture toughness of the repair tissue will be much lower than normal articular cartilage, leaving it susceptible to fissures developing in regions of high strain at the articular surface.

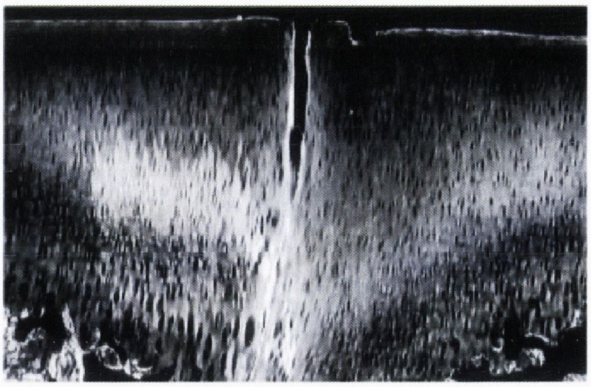

Fig. 5.5. *Fissure in an osteochondral defect implanted with a scaffold. Adapted from Niederauer et al. (2000).*

5.4.4 The multiphase scaffold

The idea behind the multiphase scaffold is that the conditions required to induce osteogenesis within the bony part of the defect are different from the conditions to induce chondrogenesis within the chondral part of the defect. Either reducing the permeability or increasing the modulus of the bony phase of the scaffold will help induce osteogeneisis in the bony part of the defect. The idea behind the superficial layer of the scaffold is to prevent fibrous tissue formation within this region of the defect. Increasing the stiffness of the superficial layer had a positive effect on chondrogenesis; however if the layer was too stiff, dedifferentiation of chondrocytes into fibroblasts was predicted in other regions of the defect. A similar effect was predicted by reducing the permeability of the superficial layer.

5.4.5 A blueprint for the optimal scaffold

In this thesis it has been predicted that varying the mechanical properties of the scaffold can be used to modulate differentiation in different regions of the defect. If this is true then the optimal design for a scaffold used in osteochondral defect repair will indeed be multiphase. The following criteria can be listed:

(i) The bony phase of the scaffold should provide sufficient rigidity to stabilise the defect, and process a sufficiently low permeability to reduce the large magnitudes of fluid flow responsible for preventing osteogenesis at the interface between the defect and the residual bone.

(ii) The superficial layer of the scaffold should be sufficiently rigid and impermeable to prevent fibrous tissue formation and cell death at the articular surface. The superficial layer should not induce dedifferentiation of chondrocytes into fibroblasts in other regions of the defect. This could be achieved by gradually reducing the stiffness and increasing the permeability of the scaffold from the superficial layer to the base of the chondral phase.

This study therefore comes to what would seem to be an obvious conclusion regarding the design of scaffolds for osteochondral defect repair, that the mechanical properties of the scaffold should mimic the mechanical properties of the extracellular matrix of the tissue it intends to replace.

To test this concept, a final simulation was performed where the mechanical properties were varied from the superficial layer through the depth of the scaffold, similar to normal articular cartilage. As outlined in Section 2.3.3, the tensile modulus of normal articular cartilage can be 6-20 times greater in the superficial zone of the tissue than in the middle-deep zone of the tissue (Akizuki *et al.*, 1986). In the model, the Young's modulus of the chondral phase of the scaffold decreases from 60 MPa in the superficial layer to 10 MPa in the base of the chondral phase of the scaffold. The permeability of the chondral phase increases from 1e-16 m^4/Ns in the superficial layer to 2e-15 m^4/Ns in the base of the chondral phase of the scaffold. The bone phase of the scaffold has a uniform stiffness of 50 MPa and a permeability of 2e-15 m^4/Ns. Both the Young's modulus and the permeability were then varied between these upper and lower limits throughout the depth of the chondral phase of the scaffold until the amount of fibrous tissue formation predicted to from using the model was minimised. This *optimisation* procedure was performed manually, but one could envisage a more sophisticated, computer optimised, procedure being possible in the future. The resulting scaffold design developed using this *optimisation* is given in Fig. 5.6.

The amount of fibrous tissue predicted to form with this optimised scaffold is significantly lower than that observed during spontaneous repair or repair in the presence of a homogenous scaffold (Fig. 5.7). Fibrous tissue formation is even prevented at the articular surface.

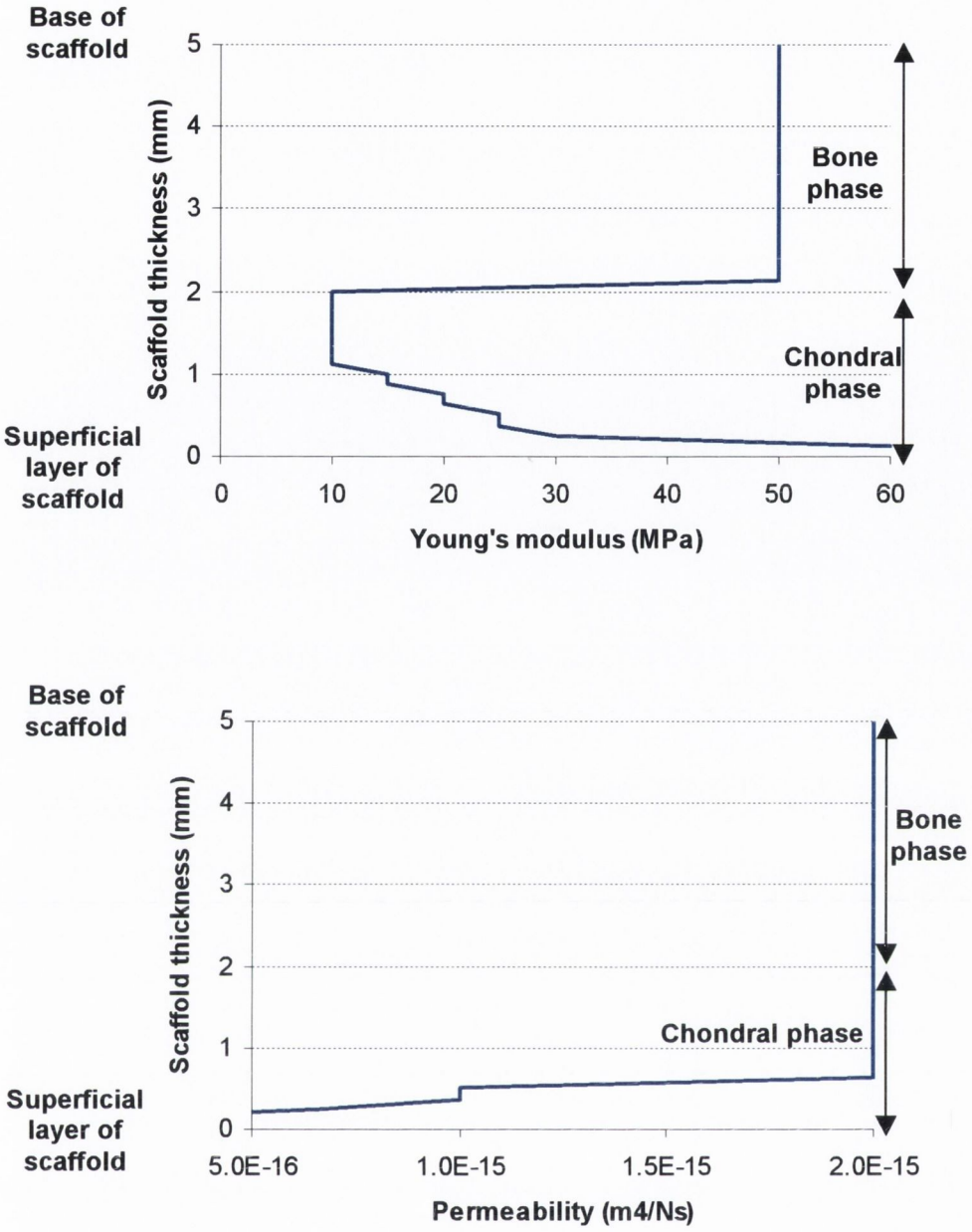

Fig. 5.6. Variation in the Young's modulus and permeability of a computer optimised scaffold.

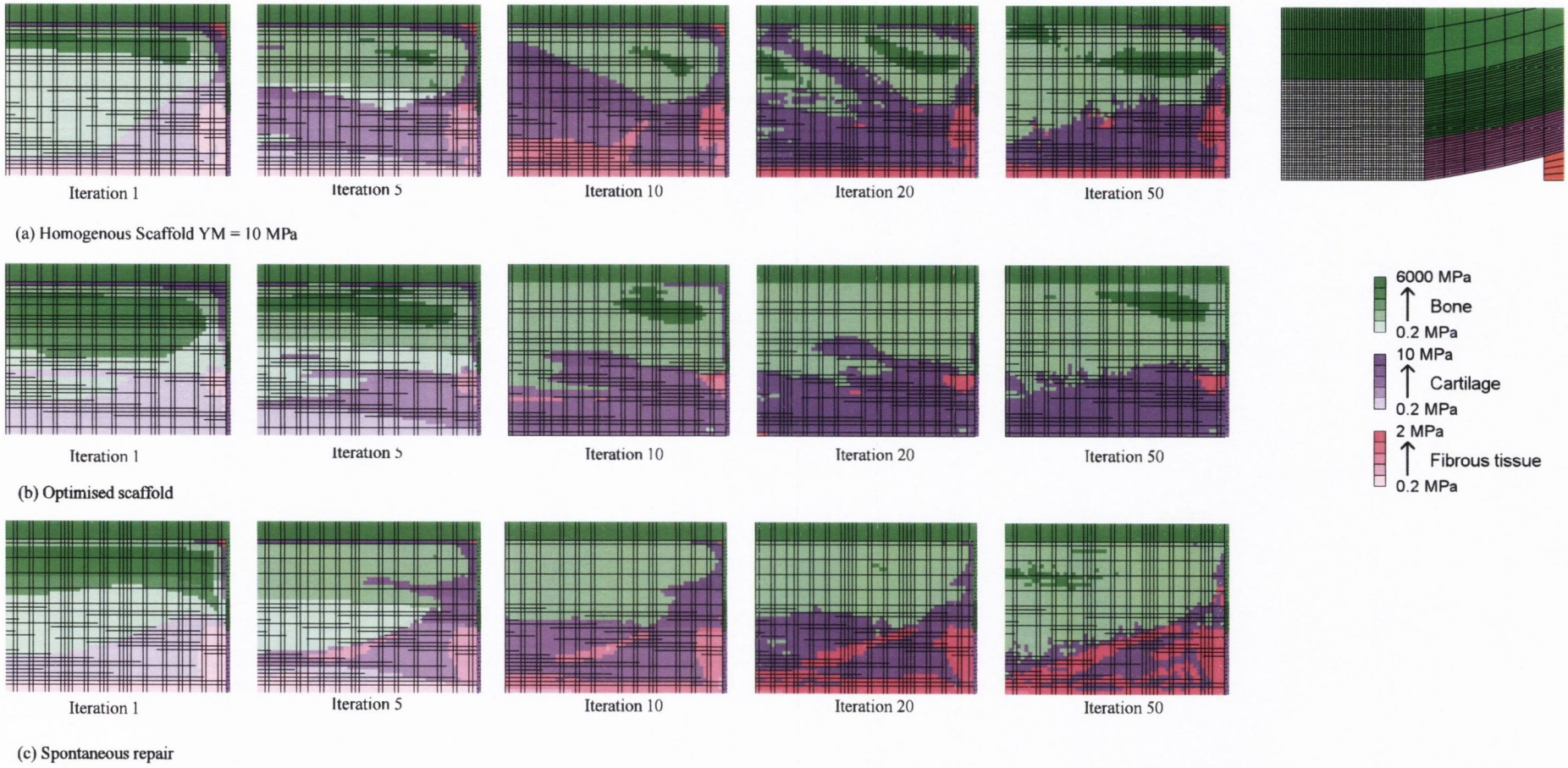

Fig. 5.7. *Comparison of the predicted patterns of tissue differentiation in 7 mm defect during spontaneous repair, repair in the presence of a homogenous scaffold, and repair in the presence of a computer optimised scaffold.*

5.5 Conclusions

Despite the simplifications and assumptions made in the finite element model of the osteochondral defect and in developing a mechano-regulation model of tissue differentiation, the model has successfully predicted may features of the tissue differentiation process observed during osteochondral defect repair. This provides evidence to confirm the hypotheses on which the stem cell mechanobiology theory was based. The evidence is by no means conclusive, and the model will have to be continually tested by attempting to simulate tissue differentiation in different circumstances; however it does strongly suggest that the mechano-regulation model can be used as a tool to evaluate tissue-engineering strategies. Furthermore, such models ultimately require experimental corroboration at the cellular level. Such experiments are ongoing in the Trinity Centre for Bioengineering under the supervision of Dr. Veronica Campbell.

The model has been used to study the optimal design for a scaffold used in osteochondral defect repair. It has been concluded that an optimal scaffold can indeed be designed. The further applications of an accurate mechano-regulation model are immense, and could be used for example in predicting tissue differentiation around orthopaedic implants or bone defect healing in the presence of an engineered tissue. New insights into mechano-biology will increase the predictive power of computational models such as that presented here, making them an invaluable tool in the future design of traditional orthopaedic and tissue engineered implants.

Chapter 6

Conclusions

Contents

6.1 Main results of this thesis **175**

6.2 Future work **176**

6.1 Main results of this thesis

The aim of this thesis was to develop a mechano-regulation model for tissue differentiation. Different aspects of cell biology involved in the tissue differentiation process, also thought to be partially mechano-regulated, such as migration, mitosis and cell death, were incorporated into the model. This model was then tested by attempting to simulate tissue differentiation during osteochondral defect repair. The main conclusions of this study are as follows:

1. The patterns of tissue differentiation predicted by the mechano-regulation model are similar to those observed experimentally during osteochondral defect repair, thereby giving confirmation to the theory that shear strain and interstitial fluid flow are regulators of mesenchymal stem cell differentiation.
2. The model predicted cell death at the articular surface, leading to the conclusion that repair tissue degradation is initiated at the articular surface and is could be a mechano-regulated process.
3. Increasing the size of the defect is predicted to cause more fibrous tissue formation. In very large defects the strain remains high and complete healing of even the bony part of the defect is prevented, with soft tissues persisting.
4. The rate of stem cell invasion (diffusion coefficient) within the granulation tissue significantly influences the rate of repair in the defect.
5. Poor integration between the repair tissue and the normal tissue was predicted to cause increased amounts of fibrous tissue formation within the defect, however the differences were not significant.
6. Incorporating cell-concentration dependent mitosis into the model significantly slows the rate of repair.
7. The mechanical properties of *in vitro* tissue engineered cartilage do not yet match those of normal articular cartilage. As a consequence of this, the tissue-engineered cartilage mechanically tested in this thesis is not predicted to improve significantly the quality of the repair. It is predicted that a more mature engineered cartilage, with mechanical properties approaching that of normal articular cartilage, and perhaps incorporating the inhomogeneity of articular cartilage, is required to significantly improve the quality of repair.
8. The mechanical properties of a scaffold used in the treatment of osteochondral defects will influence the quality of the repair tissue.

9. A multiphase scaffold is predicted to improve the quality of repair over a homogenous scaffold, and the proposed mechano-regulation model can be used to determine the optimal mechanical properties of such a scaffold.
10. Based on the results of this thesis, the author would propose that future tissue engineering strategies should concentrate on controlling the repair response *in vivo* with the use of scaffolds as regulators of the mechanical environment rather than attempting to engineer a tissue *in vitro*.

6.2 Future work

The flowing recommendations are made for future work on the subject of this thesis:

- Introduce a calcified cartilage phase into the mechano-regulation model for tissue differentiation between the bone phase and the cartilage phase. This new phase should model apoptosis of chondrocytes and facilitate the migration of new mesenchymal stem cells or osteoblasts.
- In the present model, changes in the Young's modulus depend on the number of cells and the tissue phenotype. The rate at which cells synthesise new matrix and hence alter the mechanical properties should be incorporated in the model. Such evolution equations have been put forward by Prendergast *et al.* (2003).
- Soft tissues are often much stiffer in tension than in compression due to collagen fibres that reinforce the tissue in tension. This anisotropy should be introduced into the model by introducing a stimulus, perhaps octahedral shear strain or maximum principle tensile strain, that controls the synthesis of collagen fibres and hence the mechanical properties of the soft tissue in tension.
- Further validation of the mechano-regulation hypothesis by attempting to simulate different natural and experimental models of tissue differentiation. For example, simulations could be performed of bioreactor studies of tissue differentiation (e.g. Altman *et al.*, 2002).
- Experimental calculations of cell proliferation and diffusion coefficients. Similar work has already begun in the Trinity Centre for Bioengineering measuring cell locomotion on different substrates (Prina Mello *et al.*, 2003).

REFERENCES

Akizuki, S., Mow, V.C., Müller, F., Pita, J.C., Howell, D.S., Manicourt, D.H., 1986. Tensile properties of human knee joint cartilage: I. Influence of ionic conditions, weight bearing, and fibrillation on tensile modulus. *J. Ortho. Res.*, 4: 379-392.

Altman, G.H., Horan, R.L., Martin, I., Farhadi, J., Stark, P.R.H., Volloch, V., Richmond, J.C., Vunjak-Novakovic, G., Kaplan, D.L., 2001. Cell differentiation by mechanical stress. *FASEB Journal,* 15 (14): U99-U111.

Bailon-Plaza, A., van der Meulen, M.C.H., 2001. A mathematical framework to study the effects of growth factor influences on fracture healing. *J. Theor. Biol.*, 212: 191-209.

Benya, P.D., Brown, P.D., 1986. Modulation of chondrocyte phenotype in vitro. In *Articular Cartilage Biochemistry*. K.E. Kuettner and R. Schleyerbach, editors. Raven Press, New York: 219-233.

Bianco, P., Robey, P.G., 2000. Marrow stromal stem cells. *J. Clin. Invest.*, 105(12): 1663-1668.

Biot, M.A., 1941. General theory of three-dimensional consolidation. *J. Appl. Phys.*, 12: 155-164.

Brighton, C.T., Strafford, B., Gross, S.B., Leatherwood, D.F., Williams, J.L., Pollack, S., 1991. The proliferative and synthetic response of isolated calvarial bone cells of rats to cyclic biaxial mechanical strain. *J. Bone Joint Surg.*, 73-A: 320-331.

Buschmann, M.D., Gluzband, Y.A., Grodzinsky, A.J., Hunziker, E.G., 1995. Mechanical compression modulates matrix biosynthesis in chondrocyte/agarose culture. *J. Cell Sci.*, 108:1497-1508.

Caplan, A.I., 1994. The mesengenic process. *Clin. Plast. Surg.*, 21: 429-435.

Carter, D.R., Blenman, P.R., Beaupré, G.S., 1988. Correlations between mechanical stress history and tissue differentiation in initial fracture healing. *J. Ortho. Res.*, 6: 736-748.

Carter, D.R., Beaupré, G.S., 2001. In *Skeletal Function and Form.* Cambridge University Press.

Claes, L., Heigele, C.A., 1999. Magnitudes of local stress and strain along bony interfaces predict the course and type of fracture healing. *J. Biomech.*, 32, 255-266.

Clarke, I.C., 1971. Articular cartilage: a review and scanning electron microscope study. 1. The interterritorial fibrillar architecture. *J Bone Joint Surg.*, Br. 53:732-50.

Clark, J.M., 1991. Variation of collagen fiber alignment in a joint surface: a scanning electron study of the tibial plateau in dog, rabbit, and man. *J. Ortho. Res.*, 9:246-57.

Convery, F.R., Akeson, W.H., Keown, G.H., 1972. The repair of large osteochondral defects: An experimental study in horses. *Clin. Ortho.*, 82:253-262.

Cowin, S.C., 2001. (Ed.) *Bone Mechanics Handbook.* CRC Press.

Dell'Accio, F., Vanlauwe, J., Bellemans, J., Neys, J., De Bari, C., Leyten, F.P., 2003. Expanded phenotypically stable chondrocytes persist in the repair tissue and contribute to cartilage matrix formation and structural integration in a goat model of autologous chondrocyte implantation. *J. Ortho. Res.*, 21:123-131.

DePalma, A.F., McKeever, C.D., Subin, D.K, 1966. Process of repair of articular cartilage demonstrated by histology and autoradiography with tritiated thymidine. *Clin. Ortho.*, 48:229-242.

Fermor, B., Gundle, R., Evans, M., Emerton, M., Pocock, A., Murray, D., 1998. Primary human osteoblast proliferation and prostaglandin E_2 release in response to mechanical strain in vitro. *Bone*, 22, 6: 637-643.

Freed, L.E., Vunjak-Novakovic, G., 1998. Culture of organised cell communities. *Adv. Drug Deliv. Rev.*, 33: 15-30.

Furukawa, T., Eyre, D.R., Koide, S., Glimcher, M.J., 1980. Biochemical studies on repair cartilage resurfacing experimental defects in the rabbit knee. *J. Bone Joint Surg.*, 62-A: 79-89.

Goiri, N.J., Beaupre, G.S., Carter, D.R., 1993. Cellular shape and pressure may mediate mechanical control of tissue composition in tendons. *J. Ortho. Res.*, 11(4): 581-91.

Goiri, N.J., Ryd, L., Carter, D.R., 1995. Mechanical influences on tissue differentiation at bone-cement interfaces. *J. Arthop.*, 10(4): 514-22.

Gruler, H. Bultmann, B.D., 1984. Analysis of cell movement. *Blood cells* 10, 61-77.

Hasler, E.M., Herzog, W., Wu, J.Z., Muller, M., and **Wyss, U., 1999**. Articular cartilage biomechanics: theoretical models, material properties, and biosynthetic response. *Crit. Rev. Biomed. Eng.*, 27(6): 415-488.

Hillam, R.A., 1994. Regional differences in bone strain. *Bone Miner.* (Suppl 1); 32.

Hunziker, E., 1992. Articular cartilage structure in humans and experimental animals. In: *Articular Cartilage and Osteoarthritis*, New York, Raven Press, 183-199.

Hunziker, E.B., 1999. Articular cartilage repair: are the intrinsic biological constraints undermining this process unsurpassable? *Osteoarthritis Cartilage*, 7:15-28.

Huiskes, R., Chao, E.Y.S, 1983. A survey of finite element analysis in orthopaedic biomechanics: the first decade. *J. Biomech.*, 16: 385-409.

Huiskes, R., van Driel, W.D., Prendergast, P.J., Søballe, K., 1997. A biomechanical regulatory model of peri-rosthetic tissue differentiation. *J. Mater. Sci. Mater. Med.*, 8: 785-788.

Ikenoue, T., Trindale, M.C.D., Lee, M.S., Lin, E.Y., Schurman, D.J., Goodman, S.B., Smith, R.L., 2003. Mechanoregulation of human articular chondrocyte aggrecan and type II collagen expression by intermittent hydrostatic pressure in vitro. *J. Orthop. Res.*, 21: 110-116.

Jones, D.B., Nolte, H., Scholübbers, J.G., Turner, E., Veltel, D., 1991. Biochemical signal transduction of mechanical strain in osteoblast-like cells. *Biomaterials*, 12: 101-110.

Kasper, D., Seidl, W., Neidlinger-Wilke, C., Beck, A., Claes, L., Ignatius, A., 2002. Proliferation of human-derived osteoblast-like cells depends on the cycle number and frequency of uni-axial strain. *J. Biomech.*, 35: 873-880.

Kim, H.K.W, Moran, M.E., Salter, R.B., 1991. The potential for regeneration of articular cartilage in defects created by chondral shaving and subchondral abrasion. *J. Bone Joint Surg.*, 73-A,:1301-1305.

Korhonen, R.K., Laasanen, M.S., Toyras, J., Rieppo, J., Hirvonen, J., Helminen, H.J., Jurvelin, J.S., 2002. Comparison of the equilibrium response of articular cartilage in unconfined compression, confined compression and indentation. *J. Biomech.*, 35: 903-909.

Kuiper, J.H., Richardson, J.B., Ashton, B.A., 2000. Computer simulation to study the effect of fracture site movement on tissue formation and fracture stiffness restoration. In *European Congress on Computational Methods in Applied Sciences and Engineering* (ECCOMAS), 1-6.

Kurz, B., Jin, M., Patwari, P., Cheng, D.M., Lark, M.W., Grodzinsky, A.J., 2001. Biosynthetic response and mechanical properties of articular cartilage after injurious compression. *J. Orthop. Res.*, 19: 1140-1146.

Lacroix, D., Prendergast, P.J., 2002(a). A mechano-regulation model for tissue differentiation during fracture healing: analysis of gap size and loading. *J. Biomech.*, 35: 1163-1171.

Lacroix, D., Prendergast, P.J., 2002(b). Three dimensional simulation of fracture healing in the human tibia. *Comput. Methods Biomech. Biomed. Engin.*, 5:369-376

Lacroix, D., Prendergast, P.J., Li, G., Marsh, D., 2002. Biomechanical model to simulate tissue differentiation and bone regeneration: application to fracture healing. *Med. Biol. Eng. Comp.*, 40: 14-21.

Lee, D.A., Noguchi, T., Knight, M.M., O'Donnell, L., Bently, G., Bader, D.L., 1998. Response of chondrocyte subpopulations cultured within loaded and unloaded agarose. *J. Orthop. Res.*, 16:726-733.

Lefebvre, V., Behringer, R.R., de Crombrugghe, B., 2001. L-Sox5, Sox6 and Sox9 control essential steps of the chondrocyte differentiation pathway. *Osteoarthritis Cartilage* 9: S69-S75 Suppl. A.

Liu, Y., Chen, F., Liu, W., Cui, L., Shang, Q., 2002. Repairing large porcine full-thickness defects of articular cartilage using autologous chondrocyte-engineered cartilage. *Tissue Eng.*, 8: 709-721.

Loboa, E.G., Beaupré, G.S., Carter, D.R., 2001. Mechanobiology of initial pseudarthrosis formation with oblique fractures. *J. Ortho. Res.*, 19: 1067-1072.

Loening, A.M., James, I.E., Levenston, M.E., 2000. Injurious Mechanical Compression of Bovine Articular Cartilage Induces Chondrocyte Apoptosis. *Arch. Biochem. Biophys.*, 381, 2: 205-212.

Ma, P.X., Langer, R., 1999. Morophology and mechanical function of long-term in vitro engineered cartilage. *J. Biomed. Mater. Res.*, 44: 217-221.

Mankin, H.J., 1982. Current concepts review. The response of articular cartilage to mechanical injury. *J. Bone Joint Surg.*, 64-A: 460-466.

Martin, I., Démarteau, O., Braccini, A., 2002. Recent advances in cartilage tissue engineering: From the choice of cell sources to the use of bioreactors. *JSME International Journal,* 45(4): 851-861.

Martin, I., Obradovic, B., Treppo, S., Grodzinsky, A.J., Langer, R., Freed, L.E., Vunjak-Novakovic, G., 2000. Modulation of the mechanical properties of tissue engineered cartilage. *Biorheology,* 37 (1-2): 141-147.

Martini, F.H., Ober, W.C., Garrison, C.W., Welch, K., Hutchings, R.T.. *Fundementals of Anatomy and Physiology*. Prentice Hall, New Jersey, fifth edition.

Mello, A.P., Volkov, Y., Kelleher, D. & Prendergast, P.J., 2003. Comparative locomotory behaviour of T lymphocytes and T lymphoma cells on flat and grooved surfaces. *Ann. Biomed. Eng.*, 31: 1106-1113.

Metsaranta, M., Kujala, U.M., Pelliniemi, L., Osterman, H., Aho, H., Vuorio, E., 1996. Evidence of insufficient chondrocytic differentiation during repair of full-thickness defects of articular cartilage. *Matix Biology*, 15:39-47.

Mow, V.C., Guo, X.E, 2002. Mechano-electrochemical properties of articular cartilage: their inhomogeneities and anisotropies. *Annu. Rev. Biomed. Eng.* 4:175-209.

Mow, V.C., Holmes, M.H., Lai, W.M., 1984. Fluid transport and mechanical properties of articular cartilage: a review. *J. Biomech.* 26:709-23.

Mow, V.C., Kuei, S.C., Lai, W.M., Armstrong, C.G., 1980. Biphasic creep and stress relaxation of articular cartilage: theory and experiments. *J. Biomech. Eng.*, 102: 73-84.

Mow, V.C., Lai, W.M., 1980. Recent developments in synovial joint mechanics, *SIAM Rev.*, 22: 275-317.

Muir, H., Bullough, P., Maroudas, A., 1970. The distribution of collagen in human articular cartilage with some of its physiological implications. *J. Bone Joint Surg.*, Br. 52:554-63.

Murray, J.D., 1989. *Mathematical Biology*. Springer-Verlag.

Nerem, R.M., 2002. Tissue engineering. Challenges and opportunities. Course run in Limerick Ireland, January 30th.

Niederauer, G.G., Slivka, M.A., Leatherbury, N.C., Korvick, D.L., Harroff, H.H., Ehler, W.C., Dunn, C.J., Kieswetter, K., 2000. Evaluation of multiphase

implants for repair of focal osteochondral defects in goats. *Biomaterials*, 21: 2561-2574.

O'Driscoll, S.W., Keeley, F.W., Salter R.B., 1986. The chondrogenic potential of free autogenous periosteal grafts for biological resurfacing of major full-thickness defects in joint surfaces under the influence of continous passive motion. *J. Bone Joint Surg.*, 68-A (7): 1017-1034.

Palmoski, M.J., Brandt, K.D., 1984. Effects of static and cyclic compressive loading on articular cartilage plugs in vitro. *Arth. Rhuem.*, 27:675-81.

Parkkinen, J.J., Lammi, M.J., Helminen, H.J., Tammi, M., 1992. Local stimulation of proteoglycan synthesis in articular cartilage explants by dynamic compression in vitro. *J. Ortho. Res.*, 10:610-20.

Pauwels, F., 1941. Grundrieß einer Biomechanik der Fracturheiling. In 34e Kongress der Deutschen Orthopädischen Gesellschaft, pp. 464-508. Stuggart: Ferinand Engke. (Translated by P. Manquet and R. Furlong as Biomechancis of the locomotor apparatus, pp.106-137. Springer-Verlag.)

Pauwels, F., 1980. Gesammelte Abhendlungen zur Funktionellen Anatomie des Bewegungsapparates (Translated by P. Manquet and R. Furlong as Biomechancis of the locomotor apparatus.) Springer-Verlag.

Perren, S.M., Cordey, J., 1980. In *Current concepts of internal fixation of fractures.* Springer, Berlin, p. 65.

Perren, S., Rahn, B.A, 1980. Biomechanics of fracture healing. *Can. J. Surg.*, 23(3): 22-32.

Prendergast P.J., 1997. Finite element models in tissue mechanics and orthopaedic implant design. *Clin. Biomech.*, 12 (6): 343-366.

Prendergast, P.J., Kelly, D.J., McGarry, J.G., 2003. Modelling the response of cells to mechanical stimulation. In Press: *Modelling in Biomechanics (Institute of Fundemental Technology Research, Polish Acadeemy of Sciences).*

Prendergast P.J., Huiskes, R., Søballe, K., 1997. Biophysical stimuli on cells during tissue differentiation at implant interfaces. *J. Biomech.* 30 (6):539-548.

Prendergast, P.J., van Driel, W.D., and Kuiper, J.H., 1996. A comparison of finite element codes for the solution of biphasic poroelastic problems. *Proc. Inst. Mech. Rng.* H., 210: 131-136.

Quinn, T.M., Allen, R.G., Schalet, B.J., Perumbuli, P., Hunziker, E.B, 2001. Matrix and cell injury due to sub-impact loading of adult bovine articular

cartilage explants: effects of strain rate and peak stress. *J. Orthop. Res.*, 19: 242-249.

Rahfoth, B., Weisser, J., Sternkopf, F., Aigner, T., von der Mark, K., 1998. Transplantation of allograft chondrocytes embedded in agarose gel into cartilage defects in rabbits. *Osteoarthritis Cartilage*, 6: 50-65.

Risbud, M.V., Sittinger, M., 2002. Tissue Engineering: Advances in in vitro cartilage generation. *Trends Biotechnol.*, 20(8): 351-356.

Roux, W. (1895). Gesammelte Abhandulgen uber Entwicklungsmechanic der Organismen. Leipzig, Wilhelm Engelmann.

Schaefer, D., Martin, I., Jundt, G., Seidel, J., Heberer, M., Grodzinsky, A., Bergin, I., Vunjak-Novakovic, G., Freed, L.E., 2002. Tissue-engineered composites for the repair of large osteochondral defects. *Arthritis Rheum.*, 46 (9): 2524-2534.

Schingal, R.M., Gurskis, D., Chen, A.C., Sah, R.L., 1997. Depth dependent confined compression modulus of full-thickness bovine articular cartilage. *J. Ortho. Res.*, 15(4): 499-506.

Schreiber, R.E., Ilten-Kirby, B.M., Dunkelman, N.S., 1999. Repair of osteochondral defects with allogeneic tissue engineered cartilage implants. *Clin. Ortho. Relat. Res.*, (367), S382-S395.

Shapiro, F., Koide, S., Glimcher, M.J., 1993. Cell origin and differentiation in the repair of full-thickness defects of articular cartilage. *J. Bone Joint Surg.*, 75-A: 532-533.

Slivka, M.A., Leatherbury, N.C., Kieswetter, K., Niederauer, G.G., 2000. In vitro compression testing of fiber-reinforced, bioabsorbable, porous implants. In: Agrawal CM, Parr JE, Lin ST, editors. Synthetic Bioabsorbable Polymers for Implants, ASTM STP 1396. American Society for Testing and Materials, West Conshohocken, PA. 124–35.

Søballe, K., Hansen., E.S., B-Rasmussen, H., Jørgensen, P.H., Bunger, C., 1992. Tissue ingrowth into titanium and hydroxyapapite coated implants during stable and unstable mechanical conditions. *J. Ortho. Res.*, 10: 285-299.

Soltz, M.A., Ateshian, G.A, 1998. Experimental verification and theoretical prediction of cartilage interstitial fluid pressurization at an impermeable contact interface in confined compression. *J. Biomech.*, 31:927-34.

Spilker, R.L., Suh J.K., Mow, V.C., 1992. A transversly isoptropic biphasic finite element model of the meniscus. *J. Biomech.*, 25(9), 1027-1045.

Terzaghi, K., 1925. Erdbaumechanik auf Bodenphysikalischer Grundlage (Leipzig F. Deuticke, 1925), "Principle of soil mechanics", Eng. News Record.

Van der Meulen, M.C.H., Huiskes, R., 2002. Why mechanobioloby? A survey article. *J. Biomech.*, 35, 404-414.

Van der Meulen, M.C.H., Prendergast, P.J., 2000. Mechanics in skeletal development, adaptation and disease. *Philos. T. Roy. Soc. A.*, 358 (1766), 565-578.

Van Lankveld, M., 1994. *The Mechanical Behaviour of the Tibiofemoral Joint*. PhD thesis, Eindhoven University of Technology.

Vunjak-Novakovic, G., Martin, I., Obradovic, B., Treppo, S., Grodzinsky, A.J., Langer, R., Freed, L.E., 1999. Bioreactor cultivation conditions modulate the composition and mechanical properties of tissue-engineered cartilage. *J. Orthop. Res.*, 17: 130-138.

Wakitani, S., Goto, T., Pineda, S.J., 1994. Mesenchymal cell-based repair of large, full-thickness defects of articular cartilage. *J. Bone Joint Surg.*, 76-A:579-592.

Wakitani, S., Goto, T., Young, R.G., Mansour, J.M., Goldberg, V.C., Caplan, A.C., 1998. Repair of large full-thickness articular cartilage defects with allograft articular chondrocytes in a collagen gel. *Tissue Eng.*, 4:429-444.

Waldman, S.D., Spiteri, C.G., Grynpas, M.D., Pilliar, R.M., Kandel, R.A., 2003a. Long-term intermittent shear deformation improves the quality of cartilaginous tissue formed in vitro. *J. Orthop. Res.*, 21(4), 590-596.

Waldman, S.D., Grynpas, M.D., Pilliar, R.M., Kandel, R.A., 2003b. The use of specific chondrocyte populations to modulate the properties of tissue-engineered cartilage. *J. Orthop. Res.*, 21(1), 132-138.

Wilson, W., van Rietbergen, B., van Donkelaar, C.C., 2003. Pathways of load induced cartilage damage causing cartilage degeneration in the knee after meniscectomy. *J. Biomech.* 36(6): 845-851.

Wong, M., Wuethrich, P., Eggli, P., Hunziker, E.B., 1996. Zone-specific cell biosynthesis activity in mature bovine articular cartilage: A new method using confocal microscopic stereology and quantitive autoreadiography. *J. Ortho. Res.*, 14:424-32.

APPENDIX A

Special Section: Biomechanical Interactions in Tissue Engineering and Surgical Repair (BITES)

Effect of a degraded core on the mechanical behaviour of tissue-engineered cartilage constructs: a poro-elastic finite element analysis

D. J. Kelly **P. J. Prendergast**

Centre for Bioengineering, Department of Mechanical Engineering, Trinity College, Dublin, Ireland

Abstract—*The structure and functionality of tissue-engineered cartilage is determined by the tissue culture conditions and mechanical conditioning during growth. The quality of tissue-engineered cartilage can be evaluated using tests such as the confined compression test. Tissue-engineered cartilage constructs usually consist of an outer layer of cartilage and an inner core of either undeveloped cartilage or degrading scaffold material. A biphasic poro-elastic finite element model was used to demonstrate how such a core influences the reaction force–time curve obtained from a confined compression test. The finite element model predicted that higher volumes of degraded scaffold in the inner core would reduce the aggregate modulus calculated from the confined compression test and raised the estimate of tissue permeability. The predicted aggregate modulus reduced from 0.135 MPa, for a homogenous construct, to 0.068 MPa, for a construct that was only 70% cartilaginous. It was found that biphasic poro-elastic finite modelling should be used in preference to a one-dimensional model that assumed homogeneity in estimating the properties of tissue-engineered cartilage.*

Keywords—*Tissue engineering, Cartilage, Confined compression, Biomechanics*

Med. Biol. Eng. Comput., 2003, **42**, 9–13

Redacted

Redacted

Redacted

Redacted


Redacted

APPENDIX B

Drawings of confined and unconfined compression rigs.

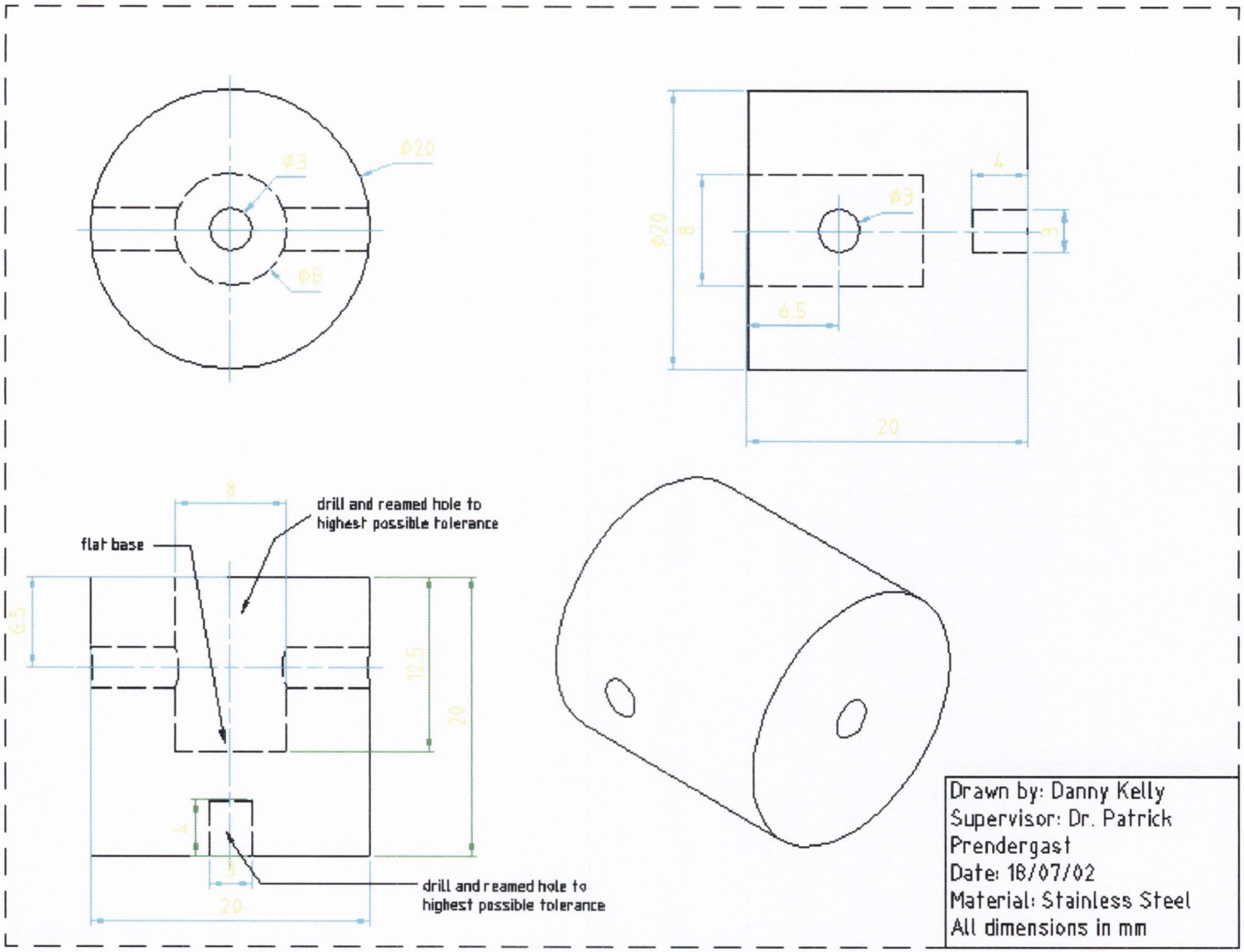
ø3
ø20
ø8
ø20
8
ø3
4
3
6.5
20
8
drill and reamed hole to highest possible tolerance
flat base
8
12.5
20
4
3
drill and reamed hole to highest possible tolerance
20
Drawn by: Danny Kelly
Supervisor: Dr. Patrick Prendergast
Date: 18/07/02
Material: Stainless Steel
All dimensions in mm

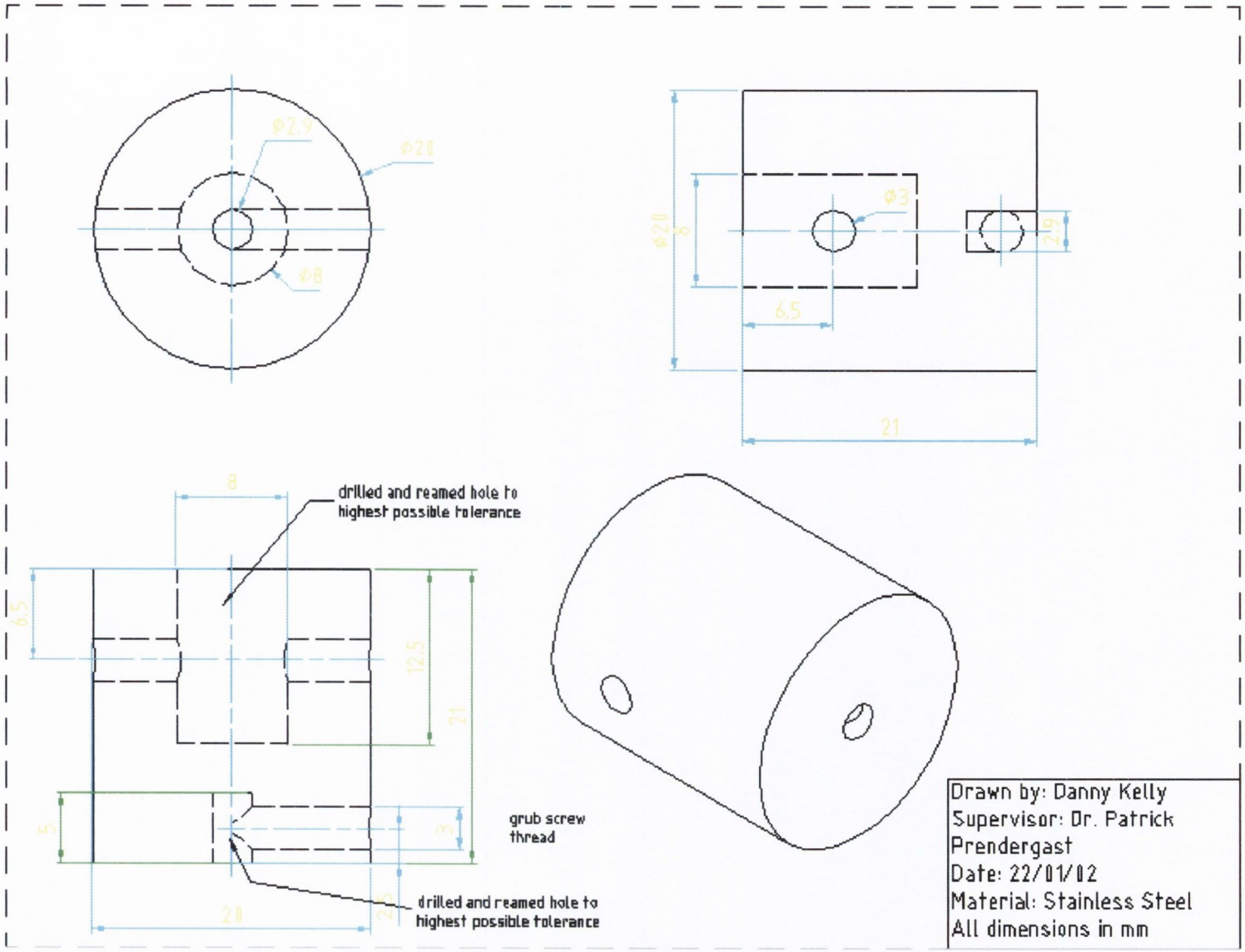
ø2.9
ø21
ø8
ø3
ø20
ø9
6.5
21
8
drilled and reamed hole to highest possible tolerance
6.5
12.5
21
5
3
grub screw thread
20
drilled and reamed hole to highest possible tolerance
Drawn by: Danny Kelly
Supervisor: Dr. Patrick Prendergast
Date: 22/01/02
Material: Stainless Steel
All dimensions in mm

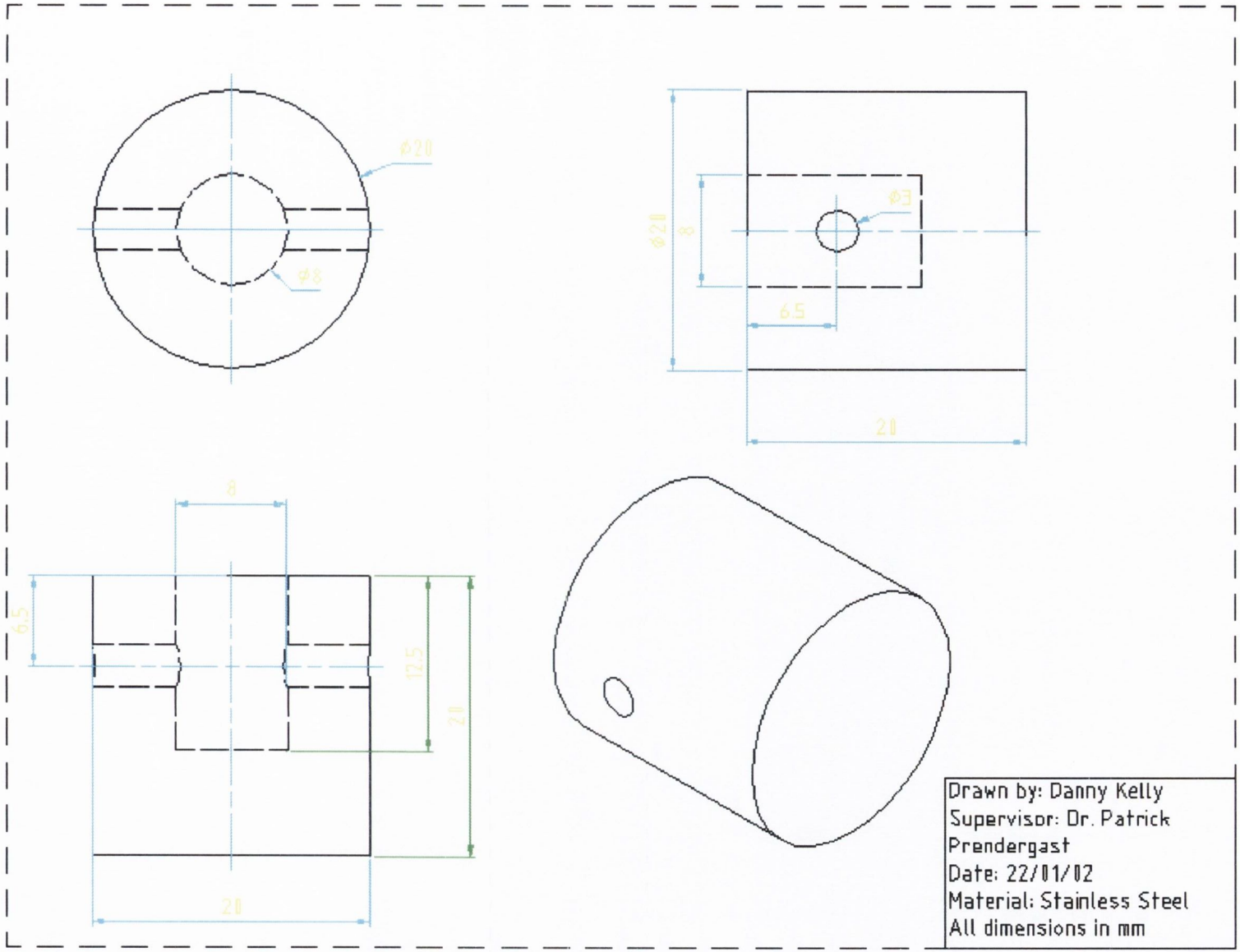
ø20
ø8
ø21
8
ø3
6.5
20
8
6.5
12.5
21
20
Drawn by: Danny Kelly
Supervisor: Dr. Patrick Prendergast
Date: 22/01/02
Material: Stainless Steel
All dimensions in mm

APPENDIX C

Data from Aegis Advanced Materials (www.aegis-ceramics.co.uk) for porous sintered bronze used for filter elements in confined compression test.

Materials	SINTERED BRONZE	SINTERED STAINLESS STEEL
Tensile strength	21-28 MPa	10-180 MPa
Density (g/cc)	4.5-5.6 (51-64%)	5.2-5.8 (67-72%)
Oxidising temp	200°C	530°C
Max operating temp	480°C	800°C
Chemical composition	89-96% Cu, bal. Sn	316L (18Cr, 8Ni, 2Mo)

Standard Porosity Grades[a]

Grade	Material	Particle Removal size (Microns)	Bubble Point[b] (in. water)	Pressure Drop[c] (PSI for 1 CFM/in² air)	Maximum Pore Size (Microns)
F30	Bronze	65-110	1.1	0.04-0.07	200-300
F40	Bronze	50-70	1.7	0.07-0.17	150-210
F60	Bronze	30-45	2.9	0.12-0.26	90-130
F100	Bronze	15-25	6.1	0.43-0.9	45-72
FCR25	Stainless	15-25	6.1	2-8	56-65
FCR510	Stainless	5-15	11.7	4-12	30-35
FCR1020	Stainless	3-10	20.7	10-21	16-19
FCR2030	Stainless	2-5	31.9	17-28	10-13

[a] Other grades available

[b] Air pressure required on one side of a sample saturated in isopropyl alcohol to form air bubbles on the other side

[c] Actual Permeability controlled by part density